

TOWARDS PRECISION MEASUREMENTS WITH A
LONG-BASELINE CLOCK ATOM INTERFEROMETER

A DISSERTATION
SUBMITTED TO THE DEPARTMENT OF APPLIED PHYSICS
AND THE COMMITTEE ON GRADUATE STUDIES
OF STANFORD UNIVERSITY
IN PARTIAL FULFILLMENT OF THE REQUIREMENTS
FOR THE DEGREE OF
DOCTOR OF PHILOSOPHY

Yijun Jiang
May 2025

Abstract

Clock atom interferometry is an emerging tool in precision measurements and fundamental physics tests. The use of narrow optical clock transitions permits long-baseline sensors beyond the table-top scale and exceptionally efficient atom optics. The 10-meter strontium interferometer at Stanford University and the MAGIS-100 detector currently under construction at Fermilab are two of the first instruments in this new class of devices. This dissertation presents the key features of these two sensors, with a focus on the 10-meter interferometer that is about to be completed at Stanford University and serves as a prototype for MAGIS-100. This dissertation documents the design and construction of this interferometer, highlighting a novel magnetic shield that screens the Earth's field over the entire length of the apparatus, and innovative strategies to transport ultracold atoms over large distances using optical lattices. Additionally, this dissertation reports on the study of laser frequency errors in narrowband clock atom interferometers and shows that they can support a sensitivity enhancement of 10^4 through large momentum transfer.

Acknowledgments

The path to a Ph.D. is rarely linear and often filled with unexpected challenges. I am deeply aware that reaching this milestone would not have been possible without the collective support of the incredible people around me.

First and foremost, I would like to express my sincere gratitude to my advisor, Jason Hogan, for his invaluable guidance, patience, and encouragement throughout my research. His mentorship has been fundamental to both my academic and personal growth. I am also grateful to my reading committee members, Mark Kasevich and Leo Hollberg, who have offered me great inspiration and support over my Ph.D. years.

I am especially thankful to Ben Garber, Megan Nantel, and Mahiro Abe, with whom I have worked closely on the development of our experimental apparatus. Their collaboration, insights, and camaraderie made the tough days easier and the good days more rewarding. I would also like to thank my labmates Jan Rudolph, Michael Van de Graaff, TJ Wilkason, Hunter Swan, Sam Carman, Rachel Barcklay, Indra Periwal, Nicholas Entin, Dhruv Tandon, Healey Kogan, and all the master, undergraduate, and visiting students in the lab. It has been a privilege to work alongside these brilliant individuals, to learn from them, and to call them friends.

My deepest thanks go to my parents, Yonglin and Ruxin, whose unconditional love and unwavering belief in me have sustained me throughout this journey. I am also extremely fortunate and grateful to have met my wife, Yi, at the start of my time at Stanford. Over the past eight years, she has been my greatest companion and strongest source of support. None of my Ph.D. achievements would be possible without her by my side. Finally, I must acknowledge the two most adorable cats that I have encountered. I appreciate the smoothness of Tangyuan and the fluffiness of Fantuan, as well as their long-time accompany, which has brought countless laughter to my life.

To everyone who stood by me during this journey – mentors, friends, family – thank you. This dissertation is as much yours as it is mine.

Contents

Abstract	iv
Acknowledgments	v
1 Introduction	1
2 Clock Atom Interferometry	3
2.1 Light-Atom Interaction	4
2.2 Atom Interferometry	9
2.2.1 Mach-Zehnder Interferometer	10
2.2.2 Large-Momentum-Transfer (LMT) Technique	11
2.3 Gradiometer Configuration	12
2.3.1 Common-Mode Noise Cancellation	12
2.3.2 Phase-Shear Readout	12
2.3.3 Triple-Source Design for MAGIS-100	12
2.4 Choice of Atom	13
2.4.1 Strontium Properties	14
2.4.2 Comparison between Clock and Multi-Photon Interferometry	16
2.5 Fundamental Physics Measurements	17
2.5.1 Gravitational Waves	17
2.5.2 Dark Matter	18
2.5.3 Quantum Science	19
3 The Stanford 10-m Strontium Interferometer	22
3.1 Atom Sources	23
3.1.1 Generation of Cold Atomic Beam	23
3.1.2 3D-MOT Chamber and Coils	26
3.1.3 Polarity-Reversal Circuit for MOT Coils	27
3.2 Connection Nodes	37

3.2.1	Pump-out Tree	37
3.2.2	Optical Access	37
3.3	Interferometer Sections	40
3.3.1	Vacuum Tubes	40
3.3.2	Electrode Chamber	43
3.3.3	Bake-Out Equipment and Linear Bearing System	52
3.3.4	Magnetic Field System Overview	58
3.3.5	Mechanical Structure	59
3.3.6	Lifting	63
3.4	Interferometry Laser Delivery	68
3.4.1	Specifications for the Interferometry Laser	68
3.4.2	In-Vacuum Laser Delivery System	72
3.4.3	Rotation Compensation System	75
3.4.4	Broadband Interferometry Option	76
3.5	Adaptations to MAGIS-100	77
4	Magnetic Field System	80
4.1	Magnetic Field Requirements	80
4.2	Magnetic Shield	82
4.2.1	Mu-Metal Properties	82
4.2.2	Challenges from a Large Aspect Ratio	83
4.2.3	Magnetic Shield Geometry	86
4.2.4	Magnetic Shield Assembly	90
4.3	Active Field Control	94
4.3.1	Transverse Bias Coil Bars	94
4.3.2	Longitudinal Bias Solenoid	102
4.3.3	Compensation Coils	104
4.4	Magnetic Field Characterization	106
4.4.1	External Magnetometry	106
4.4.2	Annealing the Vacuum Components	107
4.4.3	Degaussing the Magnetic Shield	108
4.4.4	Internal Magnetometry	108
4.5	Adaptations to MAGIS-100	117
4.5.1	Sectional Shield and Bias Coil Bars	117
4.5.2	Couplers and Longitudinal Compensation Coils	120
4.5.3	Magnetometry	120

5 Optical Lattice Transport	123
5.1 Optical Lattice Basics	124
5.1.1 Periodic Optical Potential	124
5.1.2 Bloch States and Band Structure	126
5.1.3 Atoms in an Accelerating Lattice	128
5.2 Shuttle Lattice Design	129
5.2.1 Long-Distance Transport Strategies	130
5.2.2 Double Lattice Geometry	131
5.2.3 Orthogonal Degrees of Freedom	133
5.2.4 Loss Calculation	137
5.3 Shuttle Lattice Realization	139
5.3.1 Optical System	139
5.3.2 RF System	142
5.3.3 Fiber Noise Cancellation	143
5.3.4 Shuttle Lattice Test	145
5.4 Launch Lattice	146
5.4.1 Launch Lattice Geometry	146
5.4.2 Adjustment of Launch Angle	147
5.4.3 Alignment of Lattice Beams	152
6 Cumulative Fidelity in LMT Interferometers	155
6.1 Sequence Structure of LMT Interferometers	156
6.1.1 Narrowband Interferometers	156
6.1.2 Broadband Interferometers	158
6.1.3 Double-Diffraction Narrowband Interferometers	160
6.2 Interferometer Fidelity and Contrast	162
6.3 Parasitic Interferometer Paths	168
6.3.1 Parasitic Amplitude Bound	168
6.3.2 Parasitic Path Counting	173
6.4 Laser Frequency Noise	178
6.4.1 Frequency Noise Transfer Function	178
6.4.2 Laser Stability Requirements	182
6.5 Discussion	183
7 Outlook	186
A Drawings for Custom Machining	188
B Schematics for Custom PCBs	200

List of Tables

2.1	Several important strontium transitions and their usage in the experiment	15
2.2	Summary of stable isotopes of strontium	16
3.1	Laser beams used in the AOSense cold atomic beam system	26
3.2	List of parts that are used in the polarity-reversal box	35
3.3	Components of the electrode chamber	46
3.4	Locations of thermocouples along the upper and lower sections	54
4.1	All mu-metal pieces in the shield sections to enable the staggered geometry	88
4.2	Labor split between a team of three to prepare a cable loop for internal magnetometry	111
4.3	List of electronics used in the internal magnetometry measurement	112
6.1	Dependence of the dimensionless relative position Q on the first error index j_1 . . .	176

List of Figures

2.1	Rabi oscillations and Bloch-sphere representation	7
2.2	Damped Rabi oscillation	9
2.3	Space-time diagram of a Mach-Zehnder interferometer	10
2.4	Space-time diagram of an LMT gradiometer	13
2.5	Energy level diagram of strontium	14
2.6	Projected strain sensitivity for MAGIS-100 and follow-on detectors	18
2.7	Sensitivity of dark matter coupling to electron mass and fine structure constant for MAGIS-100 and follow-on detectors	19
2.8	Sensitivity of dark matter coupling to $B - L$ for MAGIS-100 and follow-on detectors	20
3.1	Rendering of the tower CAD model	24
3.2	Geometry of the atom source	25
3.3	Illustration of an H-bridge	28
3.4	IGBT connection inside a half-bridge module	29
3.5	LTspice simulation of quenching the IGBT in a coil circuit	30
3.6	Polarity reversal circuit comparison	31
3.7	Polarity reversal box and its components	33
3.8	Oscilloscope trace of the polarity reversal circuit	36
3.9	CAD model of the connection node and the pump-out tree	38
3.10	CAD model of the in-vacuum lens triplet	41
3.11	Two completed tower sections side by side	42
3.12	Roller support structure to bear the weight of a long vacuum tube	44
3.13	CAD model of the electrode chamber	45
3.14	Procedure to assemble the electrode chamber	47
3.15	Procedure to connect the electrode chamber to the vacuum tubes	50
3.16	Lower tower section with heat tapes and thermocouples	53
3.17	Wrapping the thermal insulation around a tower section	55
3.18	Zoom-in view of the thermal insulation around the electrode chamber	56

3.19	The shield scaffolding and the linear bearing structure	57
3.20	The upper table that supports the upper tube section	60
3.21	The bottom part of the upper table with I-beam connections	61
3.22	The lower table that supports the lower tube section	62
3.23	Stress simulation of the double crown and the H-plate	64
3.24	The 80/20 structure on the mezzanine	65
3.25	The chain host used to lift the tower	66
3.26	The upper tower section and its strongback	67
3.27	The tower lifted vertically and translated to the desired location	69
3.28	Cross section of the beam delivery tube	73
3.29	CAD model of the five-way cross at the top of the tower	74
3.30	The tip-tilt mirror system CAD model at the bottom of the tower	76
3.31	Cross section of the broadband bottom beam delivery tube	78
4.1	<i>B</i> - <i>H</i> curve of the mu-metal alloy	83
4.2	Simulation of a cylindrical shield in the presence of a longitudinal magnetic field	85
4.3	Simulation of a cylindrical shield in the presence of a transverse magnetic field	86
4.4	Longitudinal structure of the magnetic shield	88
4.5	Transverse cross section of the magnetic shield and its support structure	89
4.6	Simulation of a cylindrical shield stacked by mu-metal sheets in the presence of a longitudinal magnetic field	91
4.7	Simulation of a cylindrical shield stacked by mu-metal sheets in the presence of a transverse magnetic field	92
4.8	Shield scaffolding ribs that form the periodic octagonal structural support	93
4.9	Simulation of the bias field generated by a set of four wires placed in the optimal azimuthal location	99
4.10	The procedure for winding the bias coil bar	101
4.11	The solenoid around the bottom tube	103
4.12	CAD model of the compensation coil box at the connection node	104
4.13	Simulation of edge effect suppression at the upper connection node	105
4.14	Vacuum annealing of the stainless steel components	107
4.15	Degaussing of the magnetic shield by connecting the bias coil bars to form a coil loop	109
4.16	The magnetometry cart and its enclosed electronics	113
4.17	The internal magnetometry setup	115
4.18	Internal magnetometry result of the lower shield section	118
4.19	Internal magnetometry result of the upper shield section	119
4.20	Magnetic shield coupler at the shield gap of a non-atom-source connection node	121

5.1	The band structure of an optical lattice	127
5.2	The first band gap as a function of the trap depth	128
5.3	Trajectory of the atoms in the toss-and-catch double lattice	132
5.4	Safety factors c_1 , c_2 , and c_3 as functions of θ	134
5.5	Optical diagram of the shuttle lattice	135
5.6	Ray tracing of the shuttle lattice delivery setup	136
5.7	Effects of non-adiabatic loading and unloading	138
5.8	Optical diagram of the double-pass chirping AOMs and fiber noise cancellation	140
5.9	The shuttle lattice delivery module	141
5.10	A simplified diagram of the shuttle lattice RF system	143
5.11	Fiber noise cancellation scheme with orthogonal polarizations	144
5.12	The shuttle lattice test setup	145
5.13	CAD model of the launch lattice in the connection node	148
5.14	CAD model of the launch lattice module	149
5.15	The custom optomechanics for the pair of prism mirrors	150
5.16	Ray tracing of the launch lattice delivery setup	151
5.17	The connection node with the launch lattice optics and alignment tools installed	153
5.18	The alignment target on a linear actuator	154
6.1	Momentum-time and space-time diagrams of a Mach-Zehnder interferometer	158
6.2	Momentum-time and space-time diagrams of a narrowband $4\hbar k$ interferometer	159
6.3	Momentum-time and space-time diagrams of a broadband $7\hbar k$ interferometer	161
6.4	Bloch sphere representation and space-time diagram of a narrowband LMT interferometer, showing the parasitic paths	163
6.5	Space-time diagram of a broadband LMT interferometer, showing the parasitic paths	164
6.6	Momentum-time and space-time diagrams of the main upper arm of a narrowband $4\hbar k$ interferometer	169
6.7	Momentum-time and space-time diagrams of even-order parasitic paths in the upper arm of a narrowband $4\hbar k$ interferometer	170
6.8	Momentum-time and space-time diagrams of odd-order parasitic paths in the upper arm of a narrowband $4\hbar k$ interferometer	171
6.9	Counting and upper-bounding the parasitic paths	174
6.10	Laser frequency noise transfer function and fidelity of an augmentation zone	181
6.11	LMT enhancement of a clock interferometer in the presence of laser frequency noise	184
A.1	Drawing of the polarity-reversal box	189
A.2	Drawing of the water-cooling plate for the polarity-reversal box	190
A.3	Drawing of the “double crown” flange adapter	191

A.4	Drawing of the “H-plate” adapter	192
A.5	Drawing of the magnetic shield base plate	193
A.6	Drawing of the magnetic shield supporting “rib”	194
A.7	Drawing of the magnetic shield pressure plate	195
A.8	Drawing of the shuttle lattice delivery breadboard	196
A.9	Drawing of the block that extends from the shuttle lattice delivery breadboard	197
A.10	Drawing of the CF 2.75" viewport adapter for shuttle lattice delivery optics	198
A.11	Drawing of the CF 1.33" viewport adapter for launch lattice delivery optics	199
B.1	Full schematic diagram of the H-bridge driver circuit	201
B.2	PCB layout generated by EAGLE from the schematic diagram in Figure B.1	202
B.3	Full schematic diagram of the magnetometry circuit inside the cart	203
B.4	PCB layout generated by EAGLE from the schematic diagram in Figure B.3	204
B.5	Full schematic diagram of the magnetometry circuit on the laser distance sensor side	205
B.6	PCB layout generated by EAGLE from the schematic diagram in Figure B.5	206

Chapter 1

Introduction

Over recent years, the rapid advancement of quantum sensing has demonstrated immense potential to transform measurement science, surpassing the constraints of classical technologies. In particular, precision measurements based on coherent light-atom interactions have progressed to a level where physical quantities can be measured with extraordinary precision [1–22]. Building on this technological evolution, long-baseline atom interferometry, whose sensitivity benefits significantly from the large-momentum transfer (LMT) technique [23–37], has become a powerful method for probing fundamental physics. Clock atom interferometry, which employs long-lived optical transitions in alkali-earth(-like) atoms, holds the promise of fully leveraging the advantages of LMT enhancement [35, 38, 39].

My Ph.D. has been devoted to the understanding and development of long-baseline clock atom interferometry detectors, whose broad scientific potential has been widely recognized by the community [40–42]. Most of my work has been focused on the design and construction of a 10-meter strontium atom interferometer located in the sub-basement of the Physics and Astrophysics Building of Stanford University. However, the design principles and techniques can be easily transferred to even larger atom interferometer sensors such as the MAGIS-100 detector currently under construction at Fermilab [43]. Therefore, I am writing this dissertation not only as a summary of my own Ph.D. but also as a technical guidebook for the design of several systems in MAGIS-100 and similar detectors.

The outline of this dissertation is as follows. I will start with a general overview of matter-wave interferometry in Chapter 2, focusing on understanding some important concepts and features of clock atom interferometry and gradiometry over a baseline. Chapter 3 is a comprehensive description of the Stanford 10-meter strontium atom interferometer¹. My labmate Ben Garber and I have been collaborating together for years on the 3D modeling and simulation of almost every aspect of this intricate machine. During the second half of my Ph.D., I worked closely with Megan Nantel and

¹The full length of this apparatus is 8.8 m, but we colloquially refer to it as “the 10-meter tower”.

Mahiro Abe on the assembly of the structural, magnetic, and vacuum systems of this interferometer. Thus, this chapter contains knowledge of both the design and the realization phase of the apparatus.

Among all components of the interferometer, I spent the most time on the magnetic field system and the optical lattices, which are complicated enough that they deserve their own chapters. Chapter 4 focuses on the design, assembly, and characterization of the magnetic shield and bias coils. Chapter 5 is devoted to my optical lattice work in two applications: the shuttle lattice that transports the atoms from the cooling chamber to the interferometry region, and the launch lattice that accelerates the atoms vertically to initiate an atomic fountain.

Apart from the instrumental projects described in the previous chapters, I have developed a theoretical framework to treat population transfer errors in an LMT interferometer. This work is presented in Chapter 6, showing that pulse errors in an interferometer sequence accumulate linearly with the LMT order n , instead of quadratically, which is incorrectly claimed by a recent paper [44]. This chapter also introduces a way to bound the interference between the parasitic paths and the main interferometer at the output ports. With a thorough understanding of the accumulation of pulse errors, we derive an analytic expression of the laser frequency noise transfer function and verify the laser stability specification proposed for MAGIS-100 [43]. Finally, Chapter 7 concludes with an outlook towards future experiments that can be performed on the Stanford 10-meter strontium interferometer and the MAGIS-100 detector, as well as the broad potential of the long-baseline clock atom interferometry technology.

Chapter 2

Clock Atom Interferometry

It has long been known that matter exhibits wave and particle properties depending on experimental circumstances. In 1924, Louis de Broglie introduced his theory of electron waves in his Ph.D. dissertation [45], suggesting that an electron around a nucleus could be thought of as being a standing wave and that electrons and all matter could be considered as waves. The equation of motion for electron waves, now known as the wave function, was later developed by Erwin Schrödinger, forming one of the founding blocks of non-relativistic quantum mechanics. The wave nature of quantum mechanical objects was verified by subsequent experiments [46–51], among which the most famous is the electron double slit experiment [47], where the spatial distribution of probability to find an electron exhibits an interference pattern when no “which-way” information is revealed. The electron is considered to be in a quantum superposition of the two paths until an observation is made. Beyond electrons, heavier objects have been put under quantum superposition, and recently interference of a molecule as large as 25 kDa has been reported [52].

The improvement in our ability to manipulate the wave function of matter is enabled by the progression of modern laser technologies [53]. Light from a frequency-stabilized laser is a convenient source of coherent electromagnetic radiation, which can be coupled to the discrete energy levels of quantum mechanical objects and is at the heart of atomic, molecular, and optical physics. In particular, with the electronic states of neutral atoms as the quantum mechanical system of interest, light-matter interactions can be used to trap the atoms and reduce their temperature to approach absolute zero [54, 55], thus suppressing the random thermal motion, increasing their lifetime, and enhancing the signal-to-noise ratio of the measurement. Such an extremely low temperature permits the use of neutral atoms as quantum sensors, allowing precision measurements of extremely weak signals.

An atom interferometer is a type of quantum sensor that measures the phase difference between the atomic wave function along different paths [56, 57]. It is similar to a laser interferometer, but with the roles of matter and light reversed, that is, the beamsplitter and mirrors are light pulses while the

interfering object is matter. In this chapter, I will give an overview of atom interferometry and discuss how light-atom interaction can be used to create atom optics that generate delocalized superposition of matter waves, as well as how a differential phase can be accumulated between the two arms in an atom interferometer. To cancel common-mode noise, two or more atom interferometers can be arranged as a gradiometer that is sensitive to the gravity gradient instead of the absolute gravity [58–60]. I will then introduce clock atom interferometry that utilizes single-photon transitions in alkali-earth(-like) atoms, and compare the technical differences with multi-photon atom interferometry, such as Bragg or Raman.

A significant part of my Ph.D. has been devoted to the instrumental development of long-baseline atom interferometry sensors, including the 10-meter tower at Stanford and MAGIS-100 at Fermilab. Therefore, towards the end of this chapter, I will discuss the broad scientific motivation of these long-baseline detectors in fundamental physics searches.

2.1 Light-Atom Interaction

The electronic state of an atom, whose structure depends on the specific element, is known to be quantized in discrete levels given by the eigenfunctions of the time-independent Schrödinger equation

$$\hat{H}_0 |\psi_n(\mathbf{r})\rangle = E_n |\psi_n(\mathbf{r})\rangle \quad (2.1)$$

where E_n is the energy of the state $|\psi_n(\mathbf{r})\rangle$ ¹. Here, the levels are labeled with a generic subscript n . In reality, many hierarchical quantum numbers are used to label the principle, angular momentum, and spin state of an atom. A general notation of an atomic state is $n^{2s+1}L_j$, where n is the principle quantum number, s is the total spin quantum number, L is the total orbital angular momentum quantum number, and j is the total angular momentum quantum number. However, for the discussion of this section, we abstract away these details and simplify the atom as a two-level system. The ground state, usually taken as the eigenstate with the lowest energy or a state with a long lifetime, is denoted as $|g\rangle$. The excited state, whose energy is higher than that of the ground state, is denoted as $|e\rangle$. The energy difference² between the two states is denoted as $\omega_a \equiv (E_e - E_g)/\hbar$.

When a laser with an angular frequency ω is blazed on the atom, the induced light-atom interaction can be written as a time-dependent Hamiltonian \hat{H}_1 . For an optical laser, the electric dipole approximation can be applied, where spatial variation over the size of an atom is neglected³.

¹Note that here I have used the Dirac notation instead of the traditional wave function notation.

²Here I use “energy” and “angular frequency” interchangeably. They are directly related by a multiplier \hbar .

³The atomic radius of a strontium atom is typically considered to be 0.215 nm, much smaller than the wavelength of the optical transitions, which are hundreds of nm.

Treating the laser classically, we can express the interaction as^{4,5} [54]

$$\hat{H}_1(t) = -e\mathbf{E}(\mathbf{r}, t) \cdot \mathbf{r} \quad (2.2)$$

With the origin set at the atom, the electric field operator can be written as

$$\mathbf{E}(t) = E_0 \hat{\epsilon} \cos \omega t = \frac{1}{2} E_0 \hat{\epsilon} (e^{i\omega t} + e^{-i\omega t}) \quad (2.3)$$

where E_0 is the intensity and $\hat{\epsilon}$ is the polarization of the electric field. The coupling strength is usually written as a Rabi frequency defined as

$$\Omega \equiv -\frac{eE_0}{\hbar} \langle \text{e} | \mathbf{r} \cdot \hat{\epsilon} | \text{g} \rangle \quad (2.4)$$

which simplifies the light-atom interaction as

$$\hat{H}_1 = \frac{1}{2} \hbar (\Omega | \text{e} \rangle \langle \text{g} | + \Omega^* | \text{g} \rangle \langle \text{e} |) (e^{i\omega t} + e^{-i\omega t}) \quad (2.5)$$

The Hamiltonian in the interaction picture is

$$\hat{H}_{1,\text{int}} = e^{i\hat{H}_0 t / \hbar} \hat{H}_1 e^{-i\hat{H}_0 t / \hbar} \quad (2.6)$$

$$= \frac{1}{2} \hbar \Omega | \text{e} \rangle \langle \text{g} | (e^{i(\omega+\omega_a)t} + e^{-i(\omega-\omega_a)t}) + h.c. \quad (2.7)$$

where *h.c.* denotes the Hermitian conjugate. We define the detuning as $\Delta \equiv \omega - \omega_a$. In the scenario where $|\Delta| \ll \omega + \omega_a$, the Hamiltonian can be simplified with the rotating-wave approximation (RWA), which drops the fast oscillating term at $\omega + \omega_a$ due to time-averaging. We can further eliminate the time dependence by transforming to a rotating frame with $\hat{U} = e^{i\Delta t | \text{e} \rangle \langle \text{e} | / \hbar}$,

$$\hat{H} = \hat{U} \hat{H}_{1,\text{int}}^{\text{RWA}} \hat{U}^\dagger + i\hbar \partial_t \hat{U} \hat{U}^\dagger \quad (2.8)$$

$$= -\hbar \Delta | \text{e} \rangle \langle \text{e} | + \frac{1}{2} \hbar \Omega | \text{e} \rangle \langle \text{g} | + \frac{1}{2} \hbar \Omega^* | \text{g} \rangle \langle \text{e} | \quad (2.9)$$

Written in the matrix form with basis $\{| \text{g} \rangle, | \text{e} \rangle\}$,

$$\mathcal{H} = \frac{1}{2} \hbar \begin{pmatrix} 0 & \Omega^* \\ \Omega & -2\Delta \end{pmatrix} \quad (2.10)$$

whose eigenvectors represent the new energy eigenstates of the driven two-level system, also known

⁴I try to use the most common convention in the coming up derivation. Some readers may find different conventions in other literature that are completely equivalent. The readers can also trust that the signs, Hermitian conjugates, and factors of two in my derivation are self-consistent.

⁵Here, a generic electron coordinate \mathbf{r} is used and $-e\mathbf{r}$ is known as the electric dipole operator. For multi-valence atoms, one can more accurately write $\mathbf{d} = -e \sum_i \mathbf{r}_i$ as the dipole operator.

as the “dressed states”. A generic state $|\psi(t)\rangle = c_g(t)|g\rangle + c_e(t)|e\rangle$ evolves under \mathcal{H} according to the matrix Schrödinger equation $i\partial_t(c_g, c_e)^\top = \mathcal{H}(c_g, c_e)^\top$, and the population oscillates between the ground and excited states, neither of which are the energy eigenstates. For example, the excited state probability for an atom starting in the ground state at $t = 0$ is given by

$$P_e(t) = |c_e(t)|^2 = \frac{\Omega^2}{\Omega^2 + \Delta^2} \sin^2 \frac{\sqrt{\Omega^2 + \Delta^2} t}{2} \quad (2.11)$$

$$= \frac{\Omega^2}{2\Omega'^2} (1 - \cos \Omega' t) \quad (2.12)$$

where we rewrite the complex Rabi frequency as $\Omega e^{i\phi_L}$ so that $\Omega \in \mathbb{R}$ represents its amplitude, and define $\Omega' \equiv \sqrt{\Omega^2 + \Delta^2}$ as the generalized Rabi frequency. As shown in Figure 2.1, $P_e(t)$ oscillates periodically and reaches the maximum value at $t = (2n+1)\pi/\Omega'$, where $n \in \mathbb{Z}$. The peak probability of driving an atom to the excited state increases with smaller Δ , and becomes unity at $\Delta = 0$, or in other words, when the laser drive is on resonance with the atomic levels. In this scenario, the oscillation period is $T = 2\pi/\Omega$ and longer than driving off resonance. By choosing the length of the laser pulse, we can terminate the Rabi oscillation at a fraction of the period and achieve any population ratio between the ground and excited states in the resulting superposition state. In particular, a resonant pulse with length $t_{\pi/2} = \pi/(2\Omega)$ achieves an equal superposition between the ground and excited states by applying the following unitary matrix to the initial state vector,

$$\mathcal{U}_{\pi/2} = e^{-i\mathcal{H}t_{\pi/2}/\hbar} = \frac{1}{\sqrt{2}} \begin{pmatrix} 1 & -ie^{-i\phi_L} \\ -ie^{i\phi_L} & 1 \end{pmatrix} \quad (2.13)$$

where ϕ_L originates from the phase of the laser. A resonant pulse with length $t_\pi = \pi/\Omega$ fully transfers the population from the ground to the excited state and vice versa by applying the following unitary matrix to the initial state vector,

$$\mathcal{U}_\pi = e^{-i\mathcal{H}t_\pi/\hbar} = \begin{pmatrix} 0 & -ie^{-i\phi_L} \\ -ie^{i\phi_L} & 0 \end{pmatrix} \quad (2.14)$$

These two special pulses are known as the $\pi/2$ -pulse and the π -pulse, respectively, and are the building blocks of light-pulse atom interferometry, as is discussed in detail in Section 2.2.

Any pure state of a two-level system can be geometrically represented by a unitary vector to the surface of a Bloch sphere. The laser drive defines a torque vector about which the state vector precesses. As shown in Figure 2.1, the effect of a resonant $\pi/2$ -pulse and a π -pulse can be recognized as rotating a state on one of the two poles to the equator and to the other pole, respectively, about a torque vector on the equator. An off-resonant drive, on the other hand, has a torque vector off the equator plane, and thus cannot achieve complete population transfer.

The Rabi oscillation is a continuous periodic evolution between the ground and excited states,

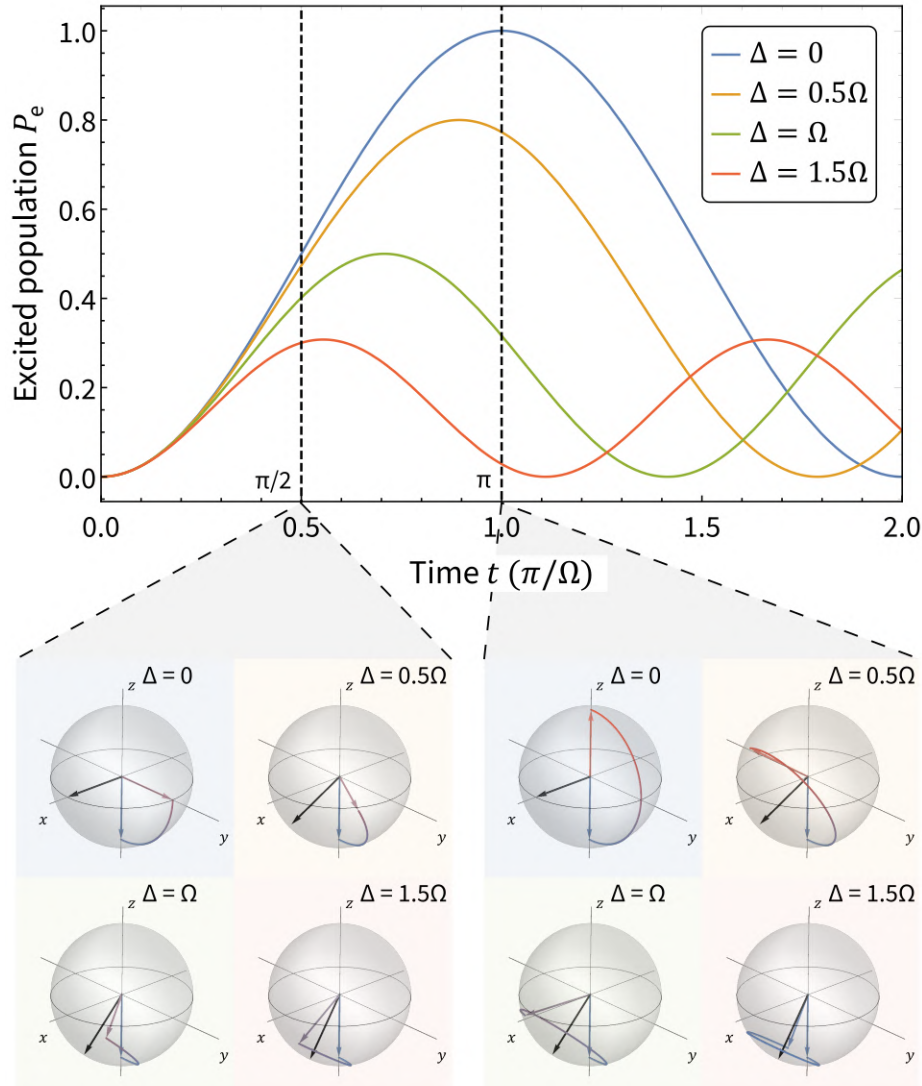


Figure 2.1: Rabi oscillations of an atom driven by a monochromatic laser with detuning Δ , measured as the angular frequency difference between the drive and the oscillator. Full-contrast oscillation only occurs at $\Delta = 0$, that is, when the laser is on resonance with the atom. In this case, the Bloch sphere picture depicts a state vector of the atom that precesses about a torque vector in the equator plane at rate given by the Rabi frequency Ω . Starting from the ground state, the atom evolves to an equal superposition between the ground and excited states at $t_{\pi/2} = \pi/(2\Omega)$, and to the excited state at $t_\pi = \pi/\Omega$. When a nonzero detuning is introduced, the maximum excited state population is reduced. In the Bloch sphere picture, the state vector of the atom precesses about a torque vector that is off the equator plane, at a faster rate given by the generalized Rabi frequency $\Omega' = \sqrt{\Omega^2 + \Delta^2}$.

where two phenomena known as light absorption and stimulated emission occur alternatively. Although we derive the Rabi oscillation from a classical treatment of the electromagnetic field, these two events can be better understood with a quantized view of light, where a quantum of the electromagnetic field known as a photon interacts with the atom. In light absorption, a ground-state atom absorbs a photon and is excited to the excited state. In stimulated emission, an excited-state atom returns to the ground state by emitting a photon with the same frequency, polarization, and direction as the driving electromagnetic field. In either case, since the photon being absorbed or emitted carries momentum $p = \hbar k$, according to momentum conservation, the atom receives a momentum recoil of the same magnitude. This is important in atom interferometry and allows for the momentum separation between different parts of the atomic wave function.

Up to this point, the discussion assumes that an atom can stay in the excited state infinitely. However, a quantum mechanical process known as spontaneous emission limits the lifetime of the excited state. The rate of this process is determined by the atomic level structure and the density of electromagnetic modes of the environment, but not by the strength of the external drive, with the following expression

$$\Gamma = \frac{\omega^3 \mu^2}{3\pi\epsilon_0\hbar c^3} \quad (2.15)$$

where $\mu = -e \langle e|\mathbf{r}|g \rangle$ is the transition dipole moment. The lifetime of the excited state is given by $\tau = 1/\Gamma$. Since spontaneous emission is a stochastic process that can emit a photon into any electromagnetic mode, it leads to heating and decoherence of the atom and results in loss of population. Taking spontaneous emission into account, the amplitude of the Rabi oscillation is reduced over time, as shown in Figure 2.2.

The population dynamics in the presence of spontaneous emission can be described with the optical Bloch equations on the density matrix. In the steady state, a finite portion of the total population remains in the excited state, given by

$$\rho_{ee} = \frac{s_0/2}{1 + s_0 + (2\Delta/\Gamma)^2} \quad (2.16)$$

where $s_0 = 2\Omega^2/\Gamma^2$ is the dimensionless saturation parameter and proportional to the laser intensity I . It is often convenient to express the laser intensity as $I = s_0 I_{\text{sat}}$, where I_{sat} is the saturation intensity that is a property of the transition and independent of the drive. In terms of the transition parameters,

$$I_{\text{sat}} = \frac{\pi\hbar c}{3\lambda^3\tau} \quad (2.17)$$

When the laser is detuned from atomic resonance, the energies of the dressed states are perturbed from the undriven scenario, commonly referred to as the AC Stark shift. In particular, by diagonalizing Equation (2.10) with the assumption $|\Delta| \gg \Omega$, the energy of the dressed ground state

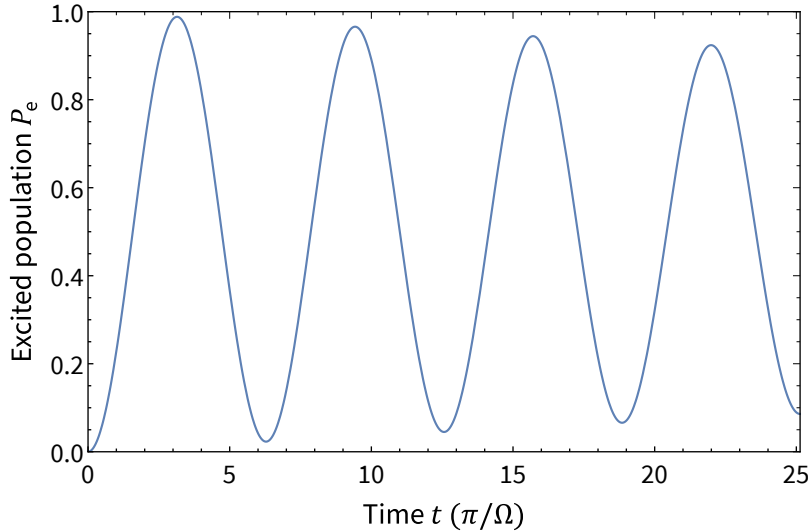


Figure 2.2: A damped Rabi oscillation where $\Delta = 0$ and $\Gamma = 0.01 \Omega$. The time evolution is obtained by numerically solving the optical Bloch equations.

is proven to be shifted by

$$\Delta E_g = \frac{\hbar\Omega^2}{4\Delta} \propto \frac{I}{\Delta} \quad (2.18)$$

Thus, a spatially dependent intensity profile leads to a potential landscape and thus to a force $F = -\nabla(\Delta E_g(\mathbf{r}))$. This is the basics of optical traps and is discussed in detail in Section 5.1 with a focus on optical lattices. The steady-state population of the excited state, according to Equation (2.16), is approximately $\Omega^2/(4\Delta^2)$ in the limit $|\Delta| \gg \Omega, \Gamma$. As a result, a proportional increase in both Δ and I maintains the same trap depth but reduces the population in the excited state, which is a common strategy to suppress spontaneous emission loss in the trap.

2.2 Atom Interferometry

Atom optics that generate delocalized superposition of matter waves are at the heart of atom interferometry. The terminology “atom optics” refers to light pulses with specific durations that manipulate the two-level system of an atom in the same way as optical elements manipulate the two arms of a light interferometer. Specifically, the $\pi/2$ -pulse and the π -pulse described by Equations (2.13) and (2.14) are commonly referred to as a “beamsplitter” and a “mirror” because of their functional similarities. Apart from changing the internal states, the atom optics also impart photon momentum to the atoms. By arranging the direction of the pulses and the resonant condition with one or both of the interferometer arms, the two arms of the interferometer can be separated in space-time and

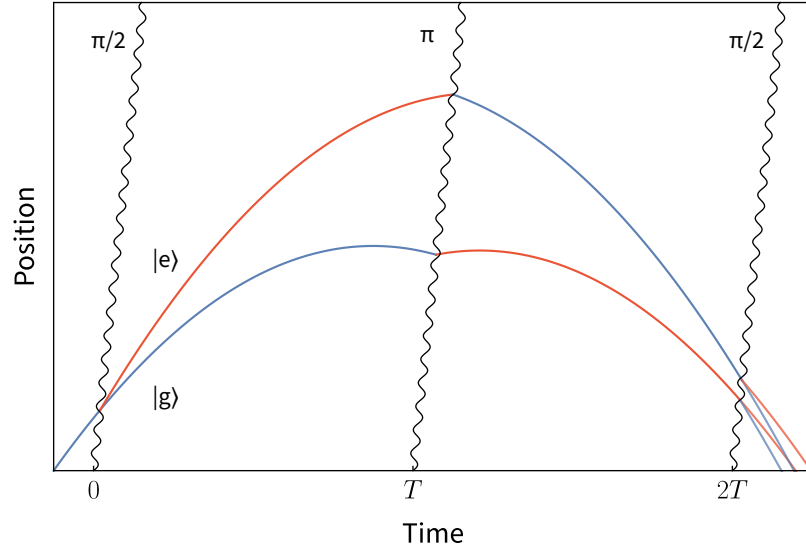


Figure 2.3: The space-time diagram of an atom Mach-Zehnder interferometer freely falling under gravity. The matter wave interacts with three atom optics separated by an interrogation time T . The first and last are $\pi/2$ -pulses that act as beam splitters, and the middle is a π -pulse that acts as a mirror. Blue and red colors denote the ground and excited states of the atom.

then brought back to each other, which allows the wave function to overlap and interfere at read-out. The interferometer phase, explicitly manifested as the fraction of the population in the ground and excited states, encodes the differential time evolution between the two arms and is sensitive to different types of signal.

2.2.1 Mach-Zehnder Interferometer

An atom Mach-Zehnder interferometer, similar to its optical counterpart, uses three atom optics as shown in Figure 2.3. The first beam splitter pulse splits the wave function in an equal superposition between the ground and excited states, where the excited state receives a momentum recoil and is spatially separated from the ground state. After an interrogation time T , a mirror pulse flips both the internal levels and the momentum states of the two arms. At time $2T$, the two arms spatially overlap each other, and a second beam splitter pulse is applied. This beam splitter separates the ground and excited states of the interfered wave function into two distinct output ports, which can be individually imaged to extract the interferometer phase.

The phase of an atom interferometer has been thoroughly studied [56, 57] and I will not attempt to re-derive the equations. To summarize, it can be decomposed into a laser phase that is imprinted on the wave function during light-atom interaction, a propagation phase due to the time evolution

of the wave function between the pulses, and a separation phase when the two arms of the interferometer do not exactly intersect at the final beamsplitter. We consider a clock atom Mach-Zehnder interferometer where each pulse is a single photon with wave vector k in the atomic frame. For such an interferometer freely falling under gravity, its phase arises from the time difference between the two arms spent in the excited state and can be categorized as the propagation phase, which depends on the finite speed of light compared to the free-fall distance. The leading order phase is

$$\phi_{\text{MZ}} = \frac{\omega_a}{c} g T^2 \quad (2.19)$$

Although this expression resembles the phase of a two-photon interferometer where $\phi_{\text{MZ,2ph}} = k_{\text{eff}} g T^2$, the origin of the phase is different. Here, $k_{\text{eff}} = |\mathbf{k}_1 - \mathbf{k}_2|$ is the effective momentum imparted to the atom by the two-photon atom optics. The interferometer phase arises from the laser phase fronts of the two photons that constitute the atom optics, rather than the action integral of the excited-state atom over time.

2.2.2 Large-Momentum-Transfer (LMT) Technique

According to Equation (2.19), the phase of an atom interferometer can be increased by a prolonged interrogation time T , which is fundamentally limited by the lifetime of the atoms and the vertical extent of the experiment. Another method of increasing the interferometer phase is known as large momentum transfer (LMT), where instead of a single-photon recoil, the two arms of the interferometer are separated in momentum space by $n\hbar k$. This is achieved by a sequence of additional π -pulses from alternating directions after the initial $\pi/2$ -pulse, and the detailed sequence structure is analyzed in Section 6.1. The phase of the interferometer is enhanced by the LMT order n ,

$$\phi_{\text{LMT}} = n \frac{\omega_a}{c} g T^2 \quad (2.20)$$

As the number of pulses increases, pulse errors from various sources accumulate and affect the phase contrast C of the interferometer. In reality, one needs to balance the loss of contrast and the gain of the interferometer phase when deciding an optimal LMT order. A useful metric is the LMT enhancement defined as the product nC . A practical LMT sequence should also consider the π -pulse length to ensure that the sequence can fit within the free-fall duration. A detailed analysis on this topic can be found in Chapter 6.

2.3 Gradiometer Configuration

2.3.1 Common-Mode Noise Cancellation

The enhancement in sensitivity from long interrogation times and large momentum transfer makes atom interferometers a promising tool for precision measurement applications. However, technical limitations such as laser frequency errors and vibrations of the apparatus can introduce noise to the measured interferometer phase. To mitigate these noise sources, both the Stanford tower and MAGIS-100 are arranged in a gradiometer configuration. As shown in Figure 2.4, in this configuration, multiple atom interferometers are separated by a baseline distance L and operated with the same laser pulses. Therefore, the phase front of the laser pulse, which contains noise due to instability of the laser source or vibration of the deliver optics, is imprinted on all of the interferometers. A differential measurement between the interferometers thus cancels this laser noise as a common mode. The resulting phase difference is

$$\delta\phi = n \frac{\omega_a}{c} a_1 T^2 - n \frac{\omega_a}{c} a_2 T^2 \quad (2.21)$$

$$\approx n \frac{\omega_a}{c} g_{zz} L T^2 \quad (2.22)$$

where a_1 and a_2 are the local acceleration at the two interferometers. The gradiometer is thus sensitive to the acceleration gradient g_{zz} but not to the absolute acceleration g . This is because the gradiometer does not rely on a stable phase reference. Instead, one interferometer acts as the phase reference for the other. The excited-state population of one interferometer as a function of the other traces an elliptical diagram whose ellipticity encodes the relative phase between the two interferometers [35].

2.3.2 Phase-Shear Readout

When a transverse phase gradient is introduced to the atom cloud, the differential phase between multiple interferometers can also manifest itself as an offset of the transverse fringe pattern [61, 62]. This is known as the phase-shear readout and is achieved by introducing a transverse component

$$k_x = k \sin \delta\theta \quad (2.23)$$

to the interferometry laser, where $\delta\theta$ is a small angle that can be applied to the upward-propagating pulses by the retro mirror at the bottom of the apparatus discussed in Section 3.4.3.

2.3.3 Triple-Source Design for MAGIS-100

MAGIS-100 has not two but three interferometers, located at the top, middle, and bottom of the apparatus. When all three interferometers are operated simultaneously, correlations can be measured

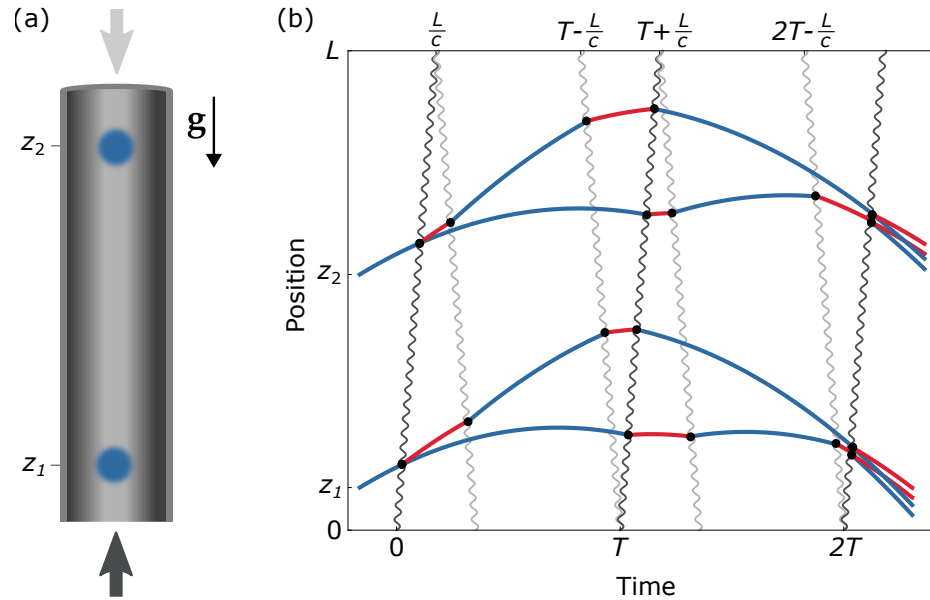


Figure 2.4: A gradiometer arranged by two atom interferometers separated by a baseline $\Delta z = z_2 - z_1$. Both interferometers are addressed by the same atom optics so their differential phase is not affected by common-mode noises. The gradiometer is compatible with the LMT technique and this figure shows the case where $n = 2$.

across more than two sources distributed along the vertical baseline. This allows characterization and suppression of Newtonian gravity gradient noise (GGN), which otherwise limits terrestrial detectors at low frequencies [63].

2.4 Choice of Atom

A clock atom interferometer relies on optical couplings from the ground state to metastable excited states. The alkali-earth and alkali-earth-like families of atoms are especially suitable thanks to the two valence electrons in their outermost shell. The spin states of the two electrons can be arranged in a symmetric or anti-symmetric configuration, leading to a singlet and a triplet in their level structure,

$$\text{singlet} \quad |0,0\rangle = (|\uparrow\downarrow\rangle - |\downarrow\uparrow\rangle)/\sqrt{2} \quad (2.24)$$

$$\text{triplet} \quad \begin{cases} |1,1\rangle = |\uparrow\uparrow\rangle \\ |1,0\rangle = (|\uparrow\downarrow\rangle + |\downarrow\uparrow\rangle)/\sqrt{2} \\ |1,-1\rangle = |\downarrow\downarrow\rangle \end{cases} \quad (2.25)$$

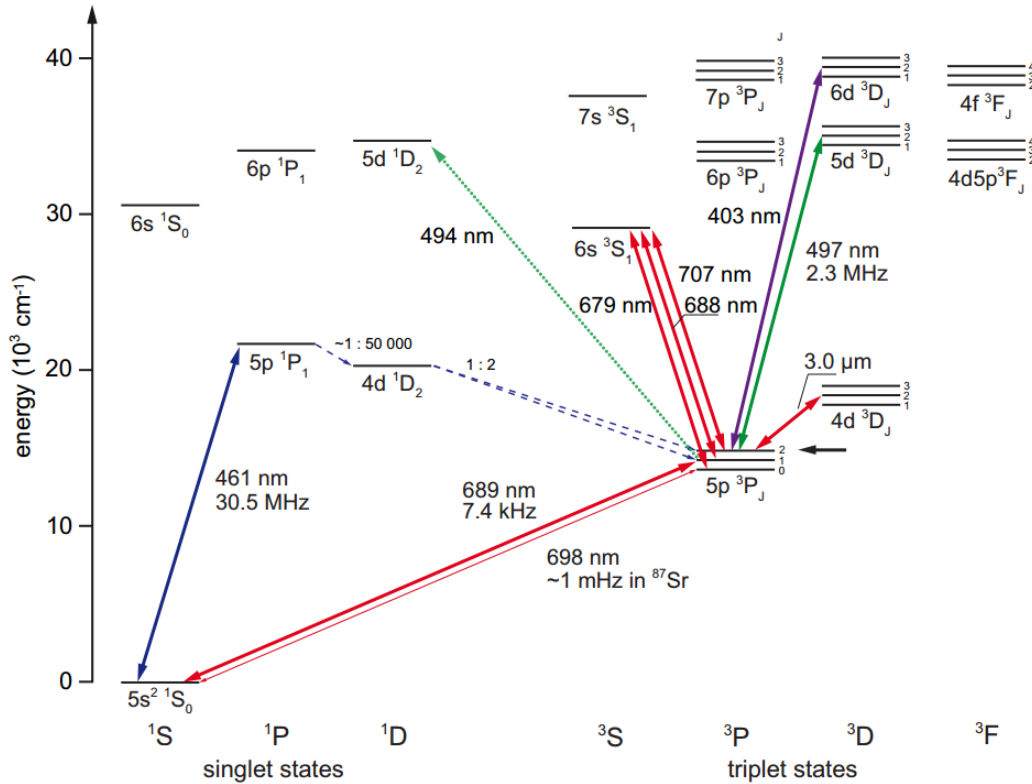


Figure 2.5: (Adapted from Ref. [81]) Energy level diagram of strontium.

The transition from the ground state, which is a singlet, to any triplet excited state is spin-forbidden ($s = 0 \leftrightarrow s = 1$). Moreover, the transition to the lowest fine structure state of the ^3P manifold is dipole-forbidden ($j = 0 \leftrightarrow j = 0$) but still weakly allowed in fermionic isotopes due to the nonzero nuclear spin, making it a metastable state with an exceptionally long lifetime [64, 65]. This is often referred to as the “clock transition” due to its important application in optical atomic clocks [64–77]. Both the Stanford tower and MAGIS-100 use strontium due to its unique properties discussed in the rest of this section. However, other elements such as ytterbium are also viable choices for long-baseline atom interferometry experiments and have their own advantages [14, 78–80].

2.4.1 Strontium Properties

The energy level diagram of strontium is shown in Figure 2.5, with the important transitions summarized in Table 2.1. The exact transition frequencies differ between various isotopes on the order of 100 MHz and can be bridged by acousto-optic modulators (AOMs).

Strontium has four stable isotopes, with properties summarized in Table 2.2. Among them, ^{88}Sr is the most abundant, making it a convenient choice for experiments like ours that benefit

Table 2.1: Several important strontium transitions and their usage in the experiment

Transition	Wavelength (nm)	Linewidth Γ (Hz)	Usage
$^1S_0 - ^1P_1$	461	2.01×10^8	Blue MOT, push, imaging
$^1S_0 - ^3P_1$	689	4.7×10^4	Red MOT, broadband interferometry
$^1S_0 - ^3P_0$	698	8.5×10^{-3}	Narrowband interferometry
$^3P_0 - ^3S_1$	679	8.9×10^6	Repump, dual-isotope Bragg
$^3P_2 - ^3S_1$	707	4.2×10^7	Repump

from an increasing number of atoms. In fact, all of the broadband interferometry work that we have so far accomplished are based on ^{88}Sr atoms [35, 39]. In addition to its abundance, ^{88}Sr is a boson with zero nuclear spin, which leads to the absence of a hyperfine structure and simplifies the laser configuration required for trapping and cooling. However, ^{88}Sr has a poor scattering length, which makes it almost impossible to thermalize in a trap. This has led to technical difficulties in the community when a Bose-Einstein condensate (BEC) is desired. Sympathetic cooling with a different isotope (^{87}Sr) is usually required to achieve a BEC with ^{88}Sr [81, 82], which complicates the experiment. On the other hand, ^{84}Sr has a convenient scattering length, which makes it favored in many BEC demonstrations [83, 84], but it suffers from a low natural abundance of 0.56%.

Although bosonic isotopes of strontium have a simpler level structure, the lack of nuclear spin forbids the $^1S_0 - ^3P_0$ clock transition from naturally occurring. This transition has to be induced by a strong external magnetic field [85]⁶, which has been demonstrated in an atom interferometer [38, 90], but the use case is limited by the field requirement. On the other hand, the nuclear spin $I = 9/2$ in the sole fermionic isotope ^{87}Sr allows the clock transition with a lifetime of 118 s [65], which is long enough to allow a few-second interferometer interrogated by $10^3 \sim 10^4$ pulses. This transition is thus the workhorse for many operation modes in the tower and MAGIS-100.

Our experiment is designed to be compatible with multiple strontium isotopes, including both bosons and fermions, to allow $^1S_0 - ^3P_1$ and $^1S_0 - ^3P_0$ to act as the interferometry transitions. Moreover, the apparatus will have the ability to operate two isotopes simultaneously, where Bragg transitions at 679 nm can be used to implement dual-isotope atom interferometry for equivalence-principle-type experiments.

Another feature of strontium, just like other alkaline-earth(-like) elements, is the magnetic field insensitivity of both the ground state and the clock state as a result of the zero total angular momentum quantum number. This relaxes the residual field specifications of the interferometer, which simplifies the magnetic shield and allows the use of 316L stainless steel as the material for

⁶Another way to drive the clock transition in bosonic isotopes without the strong magnetic field is through a three-photon process [86–89]. In particular, this excitation can be arranged in an interferometry-compatible collinear configuration [86, 87].

Table 2.2: Summary of stable isotopes of strontium

Isotope	Natural abundance (%)	Nuclear spin	Scattering length (a_0)
^{84}Sr	0.56	0 (Boson)	124
^{86}Sr	9.86	0 (Boson)	834
^{87}Sr	7.0	9/2 (Fermion)	97
^{88}Sr	82.58	0 (Boson)	-1

the vacuum chamber. However, this also means that ground-state strontium is not magnetically trappable and that optical traps must be used for matter-wave lensing and evaporative cooling to quantum degeneracy.

2.4.2 Comparison between Clock and Multi-Photon Interferometry

As discussed earlier, a clock atom interferometer utilizes single-photon optical transitions to couple the ground state to a metastable excited state in alkali-earth(-like) atoms such as strontium or ytterbium. However, this is not the only strategy to implement atom optics and impart momentum to the atomic wave function. In fact, because of the technical maturity of ultracold alkali atoms, historically multi-photon interferometry was first realized. In these interferometers, Bragg [24, 29] or Raman [91] atom optics are required, where a two-photon⁷ transition is induced between two long-lived states $|1\rangle$ and $|2\rangle$, with a third virtual excited state involved, which is practically not populated to avoid scattering loss. In a Bragg interferometer, the states $|1\rangle$ and $|2\rangle$ are the momentum states of the ground-state atom separated by the difference in kinetic energy. In a Raman interferometer, the states are usually taken as the hyperfine ground states of the alkali atom. In both cases, the two laser pulses need to have a high intensity and be far-detuned from the virtual state. This is because the scattering rate from the virtual state scales as

$$\Gamma P_e \propto \frac{I}{\Delta^2} \quad (2.26)$$

where P_e is the small occupancy of the virtual state. On the other hand, the effective two-photon Rabi frequency Ω_{eff} scales as

$$\Omega_{\text{eff}} \propto \frac{I}{\Delta} \quad (2.27)$$

Thus, proportionally increasing both I and Δ reduces scattering loss while maintaining the same Rabi frequency. Limited by practical laser power, the detuning is usually set around $\Delta \sim 5000\Gamma$, which can be on the order of 10 GHz for a typical D2 transition with a few-MHz linewidth.

In contrast, a clock atom interferometer does not suffer from scattering loss in the virtual state,

⁷More accurately, “an even number of photons” for the case of a Bragg interferometer.

and the atom optics can and should be tuned on resonance in the atomic frame. The fundamental limit comes from the intrinsic excited-state lifetime and does not scale with laser intensity. In strontium, the lifetime of the clock state is in principle long enough to support 10^4 pulses, which is not possible with multi-photon interferometers under current laser technologies.

Another advantage of clock atom interferometry is its superior cancellation of laser frequency noise as a common mode in differential readout as a gradiometer. In a Bragg or Raman interferometer, atom optics always involve two pulses from opposite directions, in order to impart a momentum recoil on the order of an optical photon to the atomic wave function. However, the phase front of these two pulses can only intersect at one specific height in the apparatus. Therefore, in the gradiometer configuration, the two interferometers experience a phase difference from the atom optics and are more susceptible to the associated laser noise [57, 59, 60]. In contrast, in a clock atom gradiometer, the exact same phase front is imparted to both interferometers, which allows greater noise suppression.

2.5 Fundamental Physics Measurements

Long-baseline clock atom interferometers, with their sensitivity enhanced by extended baseline, prolonged free-fall time, and the implementation of the LMT technique, are well suited for precision measurements in the field of fundamental physics. The MAGIS-100 detector, in particular, is expected to play a path-finding role for gravitational wave detection, act as a sensor for ultralight dark matter candidates, and test quantum mechanics on previously unexplored scales.

2.5.1 Gravitational Waves

Current gravitational wave observatories, such as LIGO, VIRGO, and KARGA, use terrestrial laser interferometry techniques. Due to seismic noise, these detectors are severely limited at low frequencies and only sensitive to gravitational waves between a few Hz and 10 kHz [92–95]. At much lower frequencies, the planned space-based LISA detector is targeted at $1 \sim 50$ mHz range [96–99]. The gap between the ranges of LIGO and LISA may carry important information about black hole or neutron star binaries as well as cosmological sources from the early universe [100–102], which can be filled by atom interferometer sensors [103, 104]. This “mid-band” frequency is also the optimal band for sky localization of the sources, where the signal from the binaries can last for months before the final merger. Observation at different times of the year allows for the use of Earth’s orbit as a baseline to identify the location of the source in the sky even by a single-baseline detector [105]. Atom interferometer detectors can thus send out early warning to other observatories, enabling multi-messenger astronomy.

Gravitational wave detection by MAGIS-100 relies on the change in light travel time between multiple interferometers in the detector when the baseline is modulated by a passing gravitational

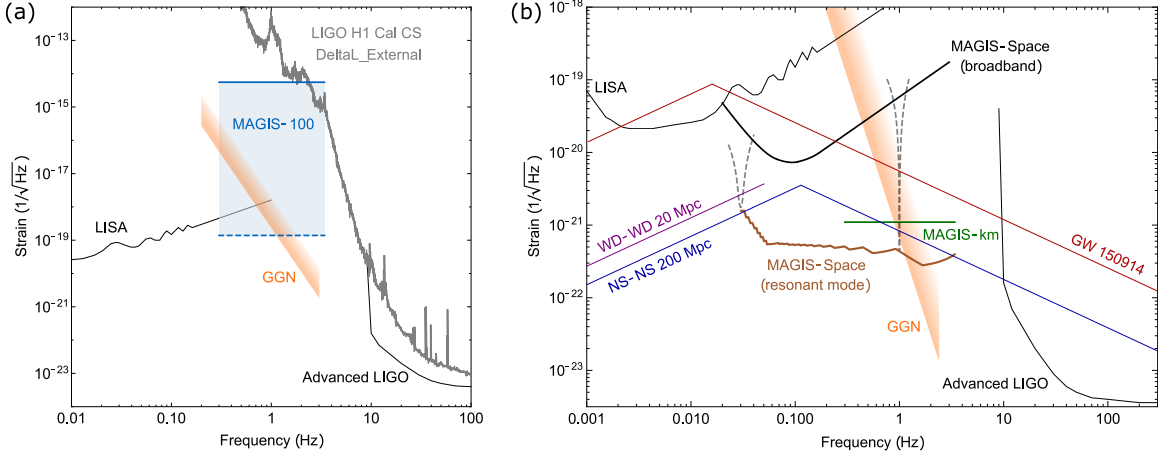


Figure 2.6: (Adapted from Ref. [43]) Projected gravitational wave strain sensitivity for MAGIS-100 and follow-on detectors. (a) Strain sensitivity of MAGIS-100. The solid blue line shows initial performance using current state-of-the-art parameters. The dashed line assumes parameters improved to their physical limits. LIGO low frequency calibration data (gray) is shown as an estimate for the state-of-the-art performance in the mid-band frequency range [108]. An estimate of gravity gradient noise (GGN) at the Fermilab site is shown as an orange band. (b) Estimated sensitivity of a future km-scale terrestrial detector (MAGIS-km, green) and satellite-based detector (MAGIS-Space, brown). The detector can be switched between both broadband (black, solid) and narrow resonant modes (black, dashed). The resonant enhancement Q can be tuned by adjusting the pulse sequence [106]. Two example resonant responses are shown targeting 0.03 Hz ($8\hbar k$ atom optics, $Q = 9$) and 1 Hz ($1\hbar k$ atom optics, $Q = 300$). The brown curve is the envelope of the peak resonant responses, as could be reached by scanning the target frequency across the band. Sensitivity curves for LIGO [109] and LISA [97] are shown for reference. Also shown are a selection of mid-band sources including neutron star (NS) and white dwarf (WD) binaries (blue and purple) as well as a black hole binary already detected by LIGO (red). The GGN band (orange) is a rough estimate based on seismic measurements at the SURF site [110].

wave [59, 60, 106, 107]. In the lowest order, the phase signal is proportional to the strain h ,

$$\delta\phi_{\text{GW}} \propto \omega_a \frac{Lh}{c} \quad (2.28)$$

The projected strain sensitivity for gravitational wave detection in MAGIS-100 and follow-on detectors is shown in Figure 2.6.

2.5.2 Dark Matter

Modern cosmological observations reveal that dark energy and dark matter together dominate the composition of the universe, yet their fundamental nature remains unknown. Unraveling the properties of these mysterious components is one of the most pressing challenges in modern physics, with implications that could reshape our understanding of the universe. Observational bounds allow a

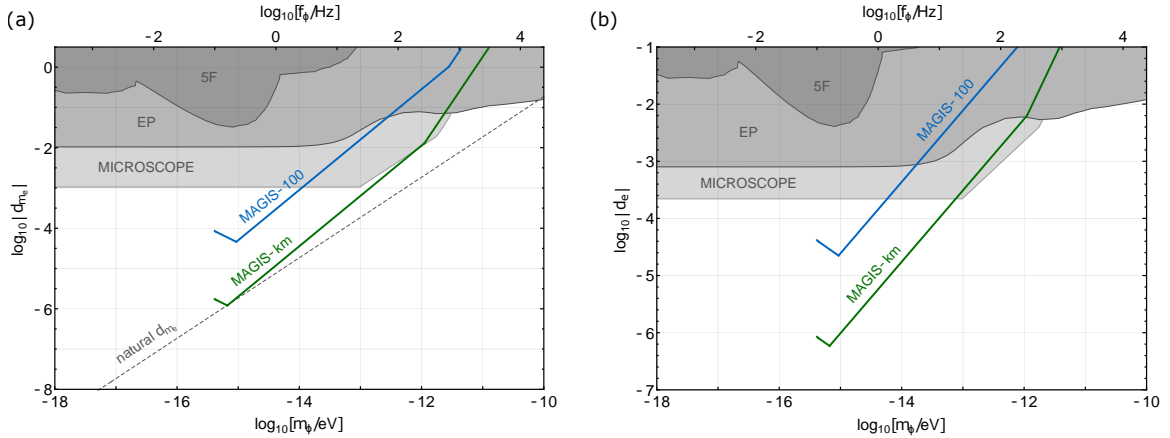


Figure 2.7: (Adapted from Ref. [43]) Sensitivity of MAGIS-100 to ultralight dark matter fields coupled to (a) the electron mass with strength d_{m_e} and (b) the fine structure constant with strength d_e , shown as a function of the mass of the scalar field m_ϕ or alternatively the frequency of the field [111]. The blue sensitivity curve assumes a shot noise limited phase resolution and corresponds to 1 year of data acquisition ($1000 \hbar k$ atom optics, $10^{-4} \text{ rad}/\sqrt{\text{Hz}}$ phase resolution). We assume a density of $0.3 \text{ GeV}/\text{cm}^3$ for each candidate dark matter field. The gray bands show existing bounds, derived from equivalence principle (EP) and fifth force (5F) tests [111], as well as the MICROSCOPE satellite EP experiment [112]. The green curve is the projected sensitivity of a future kilometer-scale detector.

10% fraction or more of dark matter to have a mass as low as 10^{-22} eV . Therefore, it is important to extend the search for dark matter to low-mass ranges, where the candidates are modeled as a classical field that oscillates at a frequency determined by their mass.

This oscillating dark matter field can show up as four different types of experimental signatures. The field can induce currents in circuits, exert accelerations on test masses, cause spin precession, and change the values of fundamental constants [113]. MAGIS-100 is sensitive to the latter three types of signatures, with dark matter candidates in the mass range between 10^{-22} eV and 10^{-15} eV [111, 114, 115]. For instance, dark matter candidates that couple to the electron mass or the fine-structure constant modulate the transition frequency ω_a , which is directly proportional to the interferometer phase [111]. The sensitivity of MAGIS-100 to these candidates is shown in Figure 2.7. As another example, dark matter candidates that couple to the mass of the atoms can exert equivalence-principle-violating forces to falling objects [115], thereby detectable by a dual-isotope interferometer measurement [10–13, 116, 117]. The $B - L$ coupled vector boson is such an example, and the sensitivity of MAGIS-100 to this dark matter candidate is shown in Figure 2.8.

2.5.3 Quantum Science

The Stanford tower and MAGIS-100 provide platforms to develop techniques that are broadly applicable to quantum information and quantum sensing, such as high-fidelity qubit manipulation and

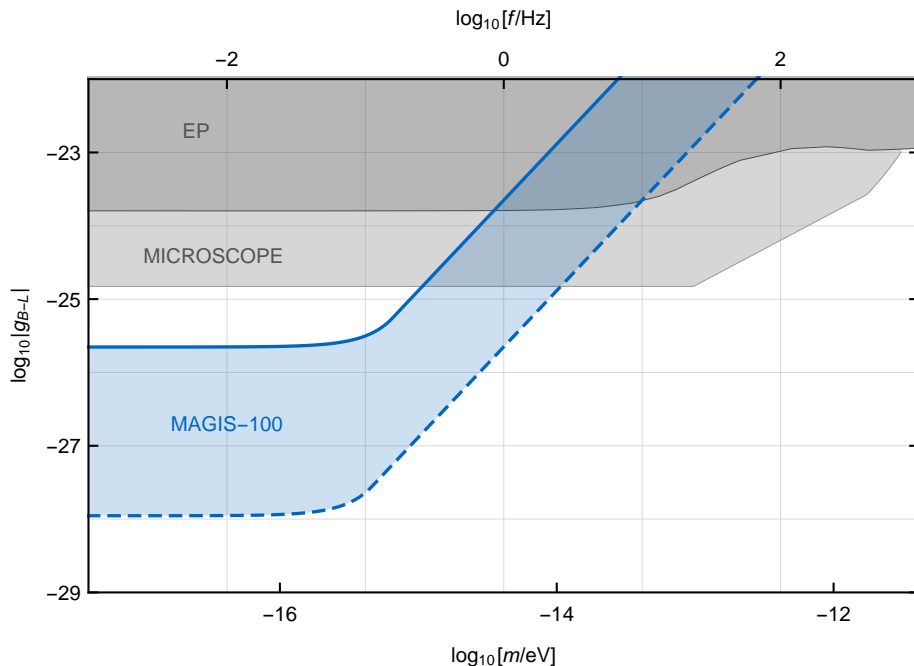


Figure 2.8: (Adapted from Ref. [43]) Dark matter sensitivity of MAGIS-100 for an ultralight vector field coupled to $B - L$. The initial (solid) curve is for $10^{-14} g/\sqrt{\text{Hz}}$ acceleration sensitivity (assumes 50 m launch, $100 \hbar k$ atom optics, 10^6 atoms/s flux, shot noise limited), while the upgraded (dashed) curve is for $6 \times 10^{-17} g/\sqrt{\text{Hz}}$ (assumes 100 m launch, $1000 \hbar k$ atom optics, 10^8 atoms/s flux, shot noise limited). At lower frequencies the detector sensitivity is likely limited by systematic errors (e.g., time-varying blackbody radiation or magnetic fields). We assume a density of $0.3 \text{ GeV}/\text{cm}^3$ for the $B - L$ field. The gray shaded regions show bounds from equivalence principle tests using torsion pendula (EP) [115, 118] and the MICROSCOPE satellite experiment [112]. Potential sensitivities of this detector method to general other dark matter candidates are discussed in Ref. [115].

advanced quantum control protocols. Moreover, long-baseline atom interferometers can be operated to test quantum mechanics itself. Advances in matter-wave interferometry already allow for the generation of quantum superposition states on meter scales [29, 119] and over many seconds [120, 121]. With recent progress in clock atom interferometry [35, 39, 86], longer free-fall times can be achieved, and delocalization of the atomic wave function over a few meters becomes possible. Such measurements have implications for a variety of proposed fundamental decoherence models [122–126]. Long-baseline atom interferometers may also search for non-linear corrections to the Schrödinger equation [41, 127] and measure phase shifts arising from higher-order variations in the gravitational potential across the wave function [128, 129].

Chapter 3

The Stanford 10-m Strontium Interferometer

As discussed in Chapter 2, the phase sensitivity of the interferometer scales quadratically with the interrogation time T . Thus, it is crucial to build a tall vacuum system to maximize the free-fall time of the atoms. Moreover, to achieve common-mode rejection of the laser phase noise, a gradiometer configuration is necessary, with multiple interferometers operating in parallel addressed by a common laser beam. This motivates us to design and construct a 10-meter-scale atom gradiometer at Stanford University, which I refer to as “the tower” for the rest of this dissertation, whose total length is limited by the maximum lifting height of the crane near the lab ceiling. Due to the double-story floor plan of the lab space, it is natural to divide the apparatus into two halves, each hosting an individual interferometer. We attach one of them to the first floor (sub-basement of Physics and Astrophysics Building, PAB) and the other to the second floor (basement of PAB). The whole tower fits into a pre-existing U-shaped opening on the second floor, and a mezzanine on the second floor was constructed around this opening space during lab renovation to allow access to the top of the tower.

Figure 3.1 shows an overview of the tower anchored to the lab. Despite the length difference in the interferometry region as a result of the floor heights, the two halves of the tower are identical. Loosely speaking, each half consists of an oven as well as cooling and trapping infrastructure known as the “atom source”, a launch and detection chamber known as the “connection node”, and a magnetically shielded vertical tube section for interferometry known as the “interferometer section”. To deliver the interferometry laser to the atoms from both directions, additional vacuum components and in-vacuum optics are attached to the top and bottom of the tower. In this section, I will introduce all the components of the tower mentioned above, with a special focus on the interferometer sections, which I have spent many years designing and assembling in collaboration with my labmates Ben

Garber, Megan Nantel and Mahiro Abe.

3.1 Atom Sources

Figure 3.2 shows the atom source where the strontium atoms are cooled and trapped. The vacuum system of the atom source consists of an AOSense cold atomic beam system¹, a Kimball Physics Multi-CF vacuum chamber², and vacuum pumps to maintain the ultrahigh vacuum (UHV) environment necessary for trapping and cooling. The weight of the vacuum system is supported by an aluminum extrusion frame³. This frame also rigidly supports several solid aluminum breadboards to mount the necessary optics to deliver cooling and trapping light to the atoms. A pair of circular, water-cooled coils inside the frame provide the magnetic field gradient for the magneto-optical trap (MOT) at the center of the chamber, and a set of six thinner coils form a rectangular box along the frame to compensate for the magnetic field of Earth and its gradient. Finally, the frame is enclosed by laser-safe panels to confine scattered light due to surface reflections and stabilize the environment around the optics.

Two identical atom sources, commonly referred to as “Frame One” and “Frame Two” by the lab members⁴, are built for the tower, with the intention that one of them will supply atoms to the upper interferometer and the other one to the lower interferometer.

3.1.1 Generation of Cold Atomic Beam

The atoms originate from an oven loaded with pure metallic strontium. The oven is heated to $410 - 430\text{ }^{\circ}\text{C}$ to produce vaporized strontium, which leaves the oven through an orifice as a thermal atomic beam. The divergence angle of this atomic beam is then reduced through a transverse cooling step, where light is shined perpendicular to the atomic beam and acts like an optical molasses in the transverse direction. A Zeeman slower laser is aligned into the atomic beam to slow down the atoms of a certain velocity class whose Doppler detuning compensates for the Zeeman effect caused by spatially variant permanent magnets in the system. The glass viewport of the Zeeman slower is heated to $350\text{ }^{\circ}\text{C}$ to reduce atom deposition. Two 2D-MOT stages further cool the transverse motion, and divert the atomic beam by 10° each, which further avoids coating the Zeeman slower viewport. The cold atomic beam system maintains 10^{-10} mbar pressure by a built-in ion pump.

The vacuum and magnetic components mentioned above are integrated and purchased as a commercially available product from AOSENSE, which is described in detail in Ref. [130]. The operation

¹AOSense Beam-RevC-Sr cold atomic beam system.

²Kimball Physics MCF800-ExtOct-G2C8 chamber.

³From [80/20 LLC](#), thus referred to as “80/20” for the rest of this dissertation. Our favorite distributor is G.A. Wirth and they have a 20% university discount.

⁴They are officially named as “Betty” and “Gordon” to express gratitude to one of our major funding sources.

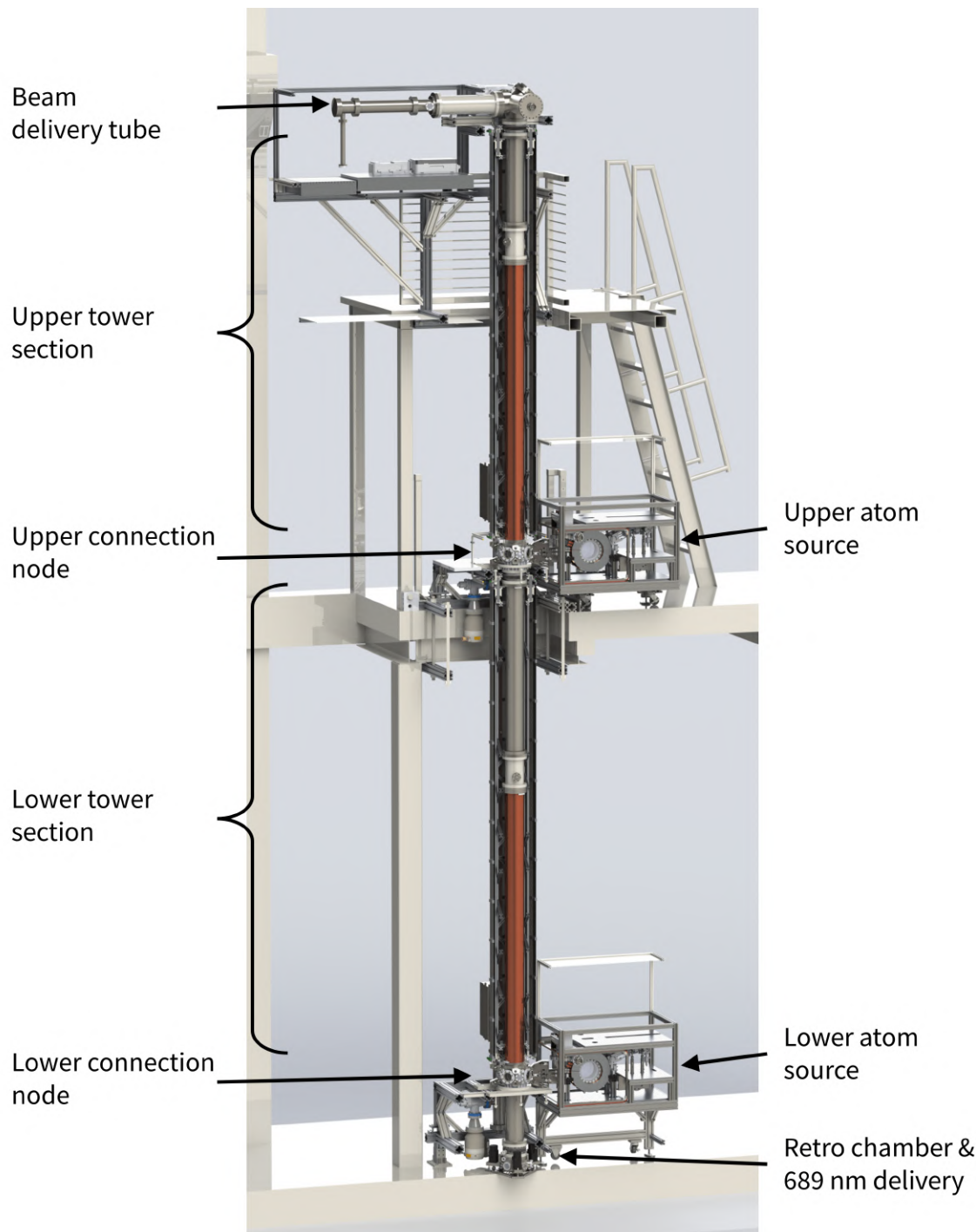


Figure 3.1: Rendering of the tower CAD model, with various components indicated. Note that the 689 nm delivery tube is out-of-date in this figure and should include two custom branches, one for a retractable mirror and the other for laser input.

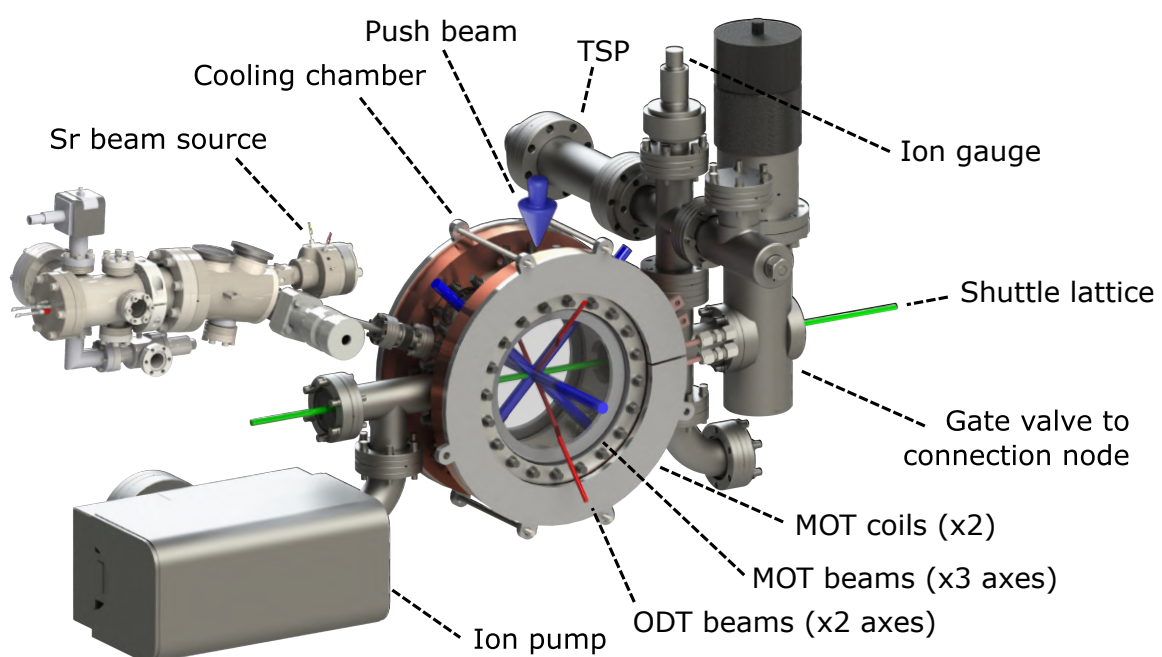


Figure 3.2: (Adapted from Ref. [43]) Geometry of the atom source. The 80/20 frame, bias coil box, and the optics breadboard are omitted for clarity.

of this system requires the delivery of 461 nm light of appropriate size, power, detuning, and polarization into designated glass viewports, which is summarized in Table 3.1.

Table 3.1: Laser beams used in the AOSense cold atomic beam system. The values on the two frames may be slightly different. The detunings are with respect to the $^1S_0 - ^1P_1$ resonance.

Functionality	Size	Power	Detuning	Polarization
Transverse cooling	5 mm × 5 mm	24 mW	-22.5 MHz	Linear
Zeeman slower	5 mm × 5 mm	75 mW	-500 MHz	Linear
2D-MOT 1	5 mm × 25 mm	5 mW	-22.5 MHz	Circular
2D-MOT 2	5 mm × 25 mm	5 mW	-22.5 MHz	Circular

3.1.2 3D-MOT Chamber and Coils

As indicated by Figure 3.2, after the two 2D-MOT stages, the cold atomic beam passes through a narrow tube and enters the 3D-MOT chamber. The tube allows differential pumping between the oven side and the chamber side, so that the pressure in the chamber can be maintained at 10^{-11} mbar, an order of magnitude lower than the pressure on the oven side. This UHV specification is typical for AMO labs that require the residual gas collision to not limit the MOT lifetimes. To achieve this pressure, a 75 L/s ion pump⁵ is connected via a tee to a CF 2.75" flange on the chamber. On the other side of the chamber, a CF 2.75" vacuum cross hosts a 90-degree valve with a roughing port, a titanium-sublimation pump (TSP)⁶, and an ion gauge⁷. An all-metal gate valve⁸ at the end of the vacuum cross allows future connection to the rest of the tower without breaking the vacuum in the 3D-MOT chamber. Details of this vacuum system can be found in my labmate TJ Wilkason's dissertation [131].

The 3D-MOT chamber, also referred to as the "atom source chamber" to emphasize its functionality in the tower, provides multiple optical access ports for cooling, trapping, and imaging of the atoms. A pair of CF 2.75" viewports in the vertical direction is used for the push beam to perform state-selective imaging in the chamber. Two pairs of CF 2.75" viewports at $\pm 45^\circ$ angles with respect to the vertical direction allow for input and retroreflection of the MOT beams along two perpendicular axes. The third axis of the MOT light enters the chamber horizontally through a pair of CF 8.00" viewports. These viewports are large enough to also provide oblique line of sights to the center of the chamber. This allows photodiode and camera detection of the fluorescence of the atoms at an oblique angle (horizontally diverted from the normal of the 8" viewport by 45°), and the implementation of a cross-dipole trap at $\pm 45^\circ$ in the vertical plane (red beams in Figure 3.2)

⁵Gamma Vacuum 75S-CVX-4D-SC-N-N 75 L/s Titan ion pump.

⁶Gamma Vacuum 360819 3-filament titanium sublimation pump.

⁷Pfeiffer Vacuum IKR270 compact cold cathode gauge.

⁸VAT 48132-CE44-AAM1 all-metal gate valve.

for matter-wave lensing [132] and evaporative cooling [81, 82, 133] if necessary. Furthermore, the chamber can be optically accessed along the horizontal axis from the CF 2.75" viewport above the ion pump to the CF 2.75" viewport on the gate valve (when opened). This axis is used to perform atom interferometry locally in the chamber before the tower is finalized and is reserved for a shuttle lattice in the tower.

Trapping and cooling of strontium atoms in a 3D-MOT generally require two stages using $^1S_0 - ^1P_1$ and $^1S_0 - ^3P_1$ transitions, commonly referred to as the “blue MOT” and the “red MOT” due to the color of the light. In the blue-MOT stage, three cm-sized circularly polarized laser beams are sent into the chamber and overlap at the center perpendicular to each other⁹. Each beam then passes a quarter waveplate and is retro-reflected to flip into the opposite-rotating polarization. The beams are about 10 mW in power and are detuned by -34 MHz from the $^1S_0 - ^1P_1$ transition. After 600 ms of loading, about 10^8 atoms are collected in the blue MOT at a temperature of 4 mK.

The three red-MOT beams are a few mm in size and overlap at the center of the blue MOT. They share the same delivery optics as the blue MOT, including the quarter waveplates, which function for both wavelengths. In the red-MOT stage, we first perform a broadband MOT, which modulates the laser frequency to allow more atoms to load from the blue MOT. Then the laser detuning is fixed at -0.2 MHz from the $^1S_0 - ^3P_1$ transition to allow a higher phase-space density. The laser power is also reduced from 9 mW to 300 μW . Eventually, approximately 1.8×10^6 atoms are cooled to 2.5 μK with a cloud size of 105 μm . Interested readers can refer to my labmate Megan Nantel’s dissertation for more details of the trapping and cooling sequence and the related laser system.

Additionally, both MOT stages require a magnetic field gradient to generate a spatially dependent Zeeman splitting across the magnetic substates. Typical values are 32 G/cm for the blue MOT and 3.2 G/cm for the red MOT, achieved by a pair of water-cooled coils mechanically interfaced with the flanges of the CF 8.00" viewports. When connected in the anti-Helmholtz configuration, the coils generate a gradient of 0.72 G/(cm·A) and 1.38 G/(cm·A) in the weak plane and along the strong axis, respectively, measured at the center of the coil pair which coincides with the center of the chamber¹⁰. The inductance of the coil pair is measured as 16.5 mH. When connected in the Helmholtz configuration, the coils generate a uniform magnetic field of 16.86 G/A near the center. The homogeneity of the field is estimated to be better than 1% within 1" from the center.

3.1.3 Polarity-Reversal Circuit for MOT Coils

The two MOT coils are arranged in the anti-Helmholtz configuration by default to create the magnetic field gradient necessary for the blue and the red MOT. However, there are certain scenarios

⁹Repump light at 679 nm and 707 nm is merged into the same beam path to deplete population in the 3P_2 and 3P_0 states.

¹⁰Note that due to geometric constraints it is not possible to measure the field at the center of the chamber *in situ*. This measurement was performed with a flux gate magnetometer when the coils were removed from the chamber but separated by the same distance. Thus, it did not capture the effect of the magnetization of the chamber.

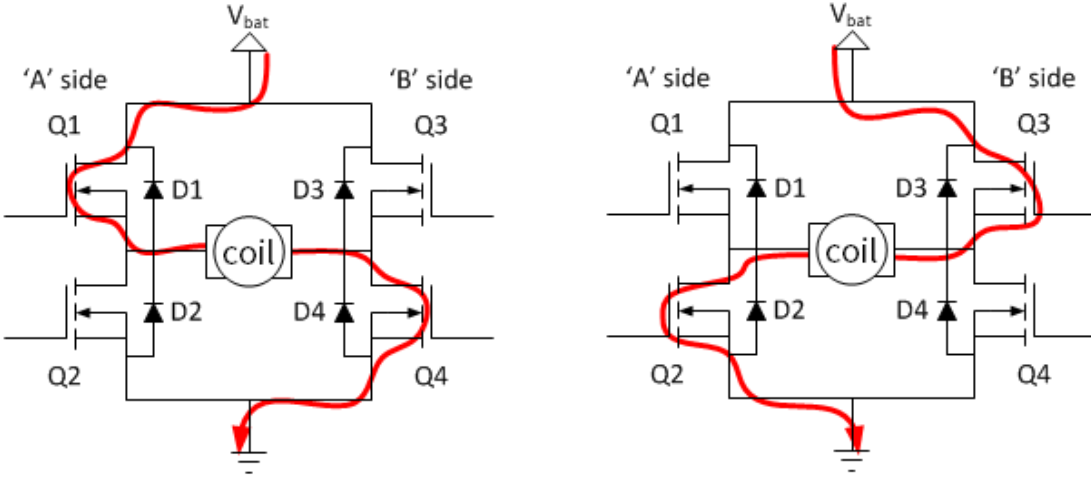


Figure 3.3: Illustration of an H-bridge.

where a uniform field is required, such as to break the degeneracy between different magnetic substates or to induce the forbidden $^1S_0 - ^3P_0$ transition in bosonic isotopes of strontium. These applications generally require the magnetic coil configuration to change within a few ms during a sequence. Therefore, I built a “polarity-reversal circuit” that acts as a fast switch on the polarity of one of the coils up on an external control signal. This subsection discusses my design and realization of the circuit.

H-bridge

The two coils are connected in series to guarantee a common current and a better impedance match to the power supply¹¹. The polarity-reversal circuit, based on an H-bridge configuration illustrated in Figure 3.3, allows one of the coils to be disconnected and reconnected in the opposite direction. Two dual IGBT modules¹² are used to form this H-bridge. Each module consists of two insulated-gate bipolar transistors (IGBTs) internally connected in the half-bridge configuration shown in Figure 3.4, that is, the emitter of the high-side IGBT connects to the collector of the low-side IGBT. The coil whose polarity needs to be flipped is connected in between the two half-bridges.

To turn on an IGBT, a voltage must be applied between the gate and the emitter to charge the gate capacitor, which is $1.5 \mu\text{F}$ for the ones we use. As a naive calculation, if we choose a gate resistor R_G of 10Ω and drive V_{GE} up to 15 V (thus initial charging current of 1.5 A), a time constant of $1 \mu\text{s}$ is obtained. However, this time scale should be considered as the turn on/off delay time, not the rise/fall time, which is observed in an LTspice simulation as the span of the green curve in

¹¹TDK-Lambda Genesys, Model Gen 40-60 DC power supply.

¹²Infineon FF150R17KE4 1700 V, 150 A dual IGBT module.

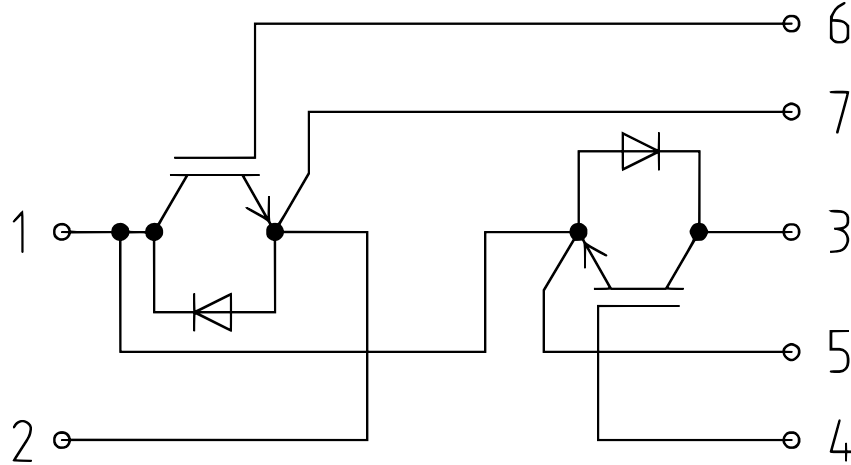


Figure 3.4: IGBT connection inside a half-bridge module.

Figure 3.5. In this simulation, we change R_G from $1\text{ k}\Omega$ to $10\text{ k}\Omega$ (both are unrealistically large but pedagogical values). It is observed that the turn on/off delay is prolonged from 0.013 ms to 0.13 ms . This is the time required to charge up/drain the gate capacitor to change the state of the IGBT. Once this phase is over, current across the coil begins to change, and the dynamics is dominated by the LR decay. This decay lasts for 0.6 ms and is independent of R_G , leading to a voltage spike $L \frac{dI}{dt} \sim 1.5\text{ kV}$ across the coil assuming the circuit is turned off at 57 A . Such a voltage spike is detrimental to the IGBT and its driver, and can be mitigated by reducing the amount of current before switching. Therefore, prior to polarity reversal, we quench the coils off using a snubber-snap circuit [131], and only allow switching when the current drops below a certain threshold¹³.

It is important to note that the IGBT has a body diode that always allows the current to flow in the reverse direction. Due to this, snubbing is not effective for L_2 in the circuit shown in Figure 3.6 (a). Experimentally, even when almost no current is measured through the coils, flipping polarity can still cause detrimental voltage spikes because there is non-negligible current through L_2 . This has killed multiple IGBTs. The simplest solution is to add diodes like in Figure 3.6 (b). Note that these diodes must have voltage ratings similar to those of the IGBTs. We choose the common anode diode module MD120A16D1-BP and the common cathode diode module MD120K16D1-BP.

Homemade PCB

The circuit discussed here is shown in Figure B.1. To control the IGBTs, we used the Analog Devices ADUM4223 isolated precision half-bridge driver. It is packaged in SOIC-16 and can drive the gates of two IGBTs connected in the half-bridge configuration mentioned above (that is, two chips for the

¹³For safety considerations we still choose components with $\sim\text{kV}$ ratings.

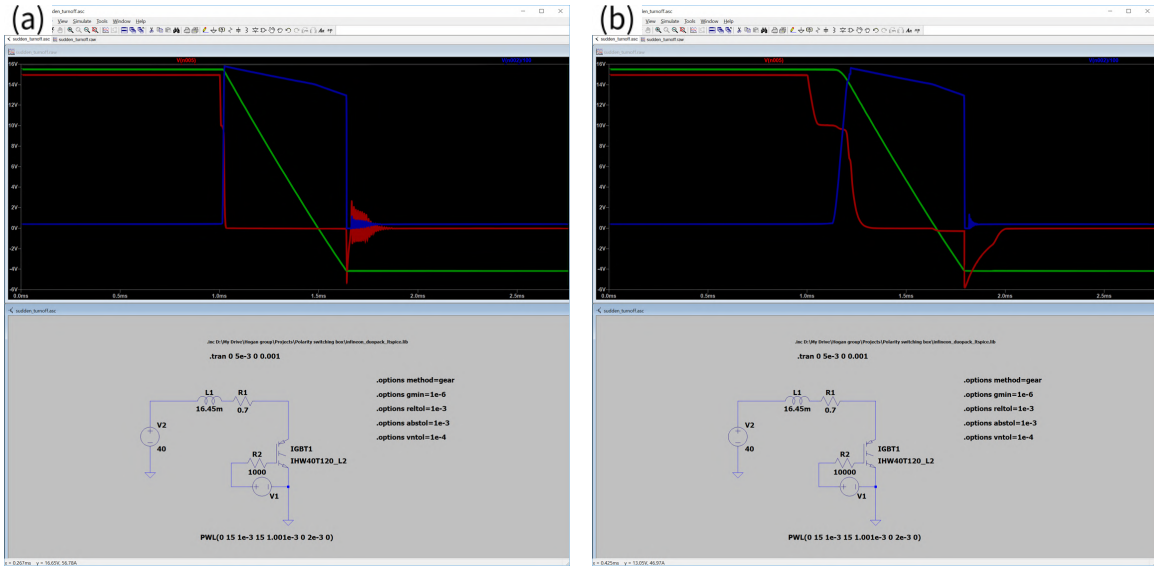


Figure 3.5: LTspice simulation of suddenly turning off the IGBT with 57 A of current in the circuit. The current decays within a few ms (green), much slower than the draining of the gate capacitor (red). Changing R_G from (a) 1 k Ω to (b) 10 k Ω only affects the draining rate of the gate capacitor, but not the current decay or the induced kV-level voltage spike (blue).

full H-bridge), providing 4 A current for each gate which is sufficient for our choice of $R_G = 100 \Omega$. The chip requires 5 V to power the primary end and two floating supplies up to 18 V to power the high and low sides on the secondary end. Notice that these two supplies on the secondary end should not refer to the common ground but to their respective emitters, and a traditional way to solve this problem is using a bootstrapping capacitor. For some unknown reason this attempt was unsuccessful. Instead, we used two isolating DC-DC converters¹⁴ per IC to power the secondary end.

The driver needs a 5 V TTL to change the state of the IGBTs. Instead of directly sending an external control signal, for safety considerations, a mechanism is necessary to reject this signal when there is a significant amount of current through the coils. Therefore, the real-time current is monitored and compared with a set value on a comparator¹⁵. Current measurement is provided by an UltraStab sensor¹⁶ in the snubber-snap circuit [131], in the form of a voltage up to about 8 V. We divide it by half to make maximum voltage within 5 V range, and compare it with the output of a tunable voltage divider across 5 V. This voltage divider consists of a 10 M Ω fixed resistor and a 25-turn 200 k Ω trimmer potentiometer in series, to achieve a variable set point up to 100 mV.

The output of the comparator goes to the “latch enable” (LE) pin of a D-type latch¹⁷. The input

¹⁴CUI PDS1-S5-S15-M-TR isolated module DC-DC converter.

¹⁵Texas Instruments LMV761MF precision comparator with shutdown.

¹⁶UltraStab IT 65-S 60 A current transducer.

¹⁷Texas Instruments SN74LVC1G373 single D-type latch with 3S output.

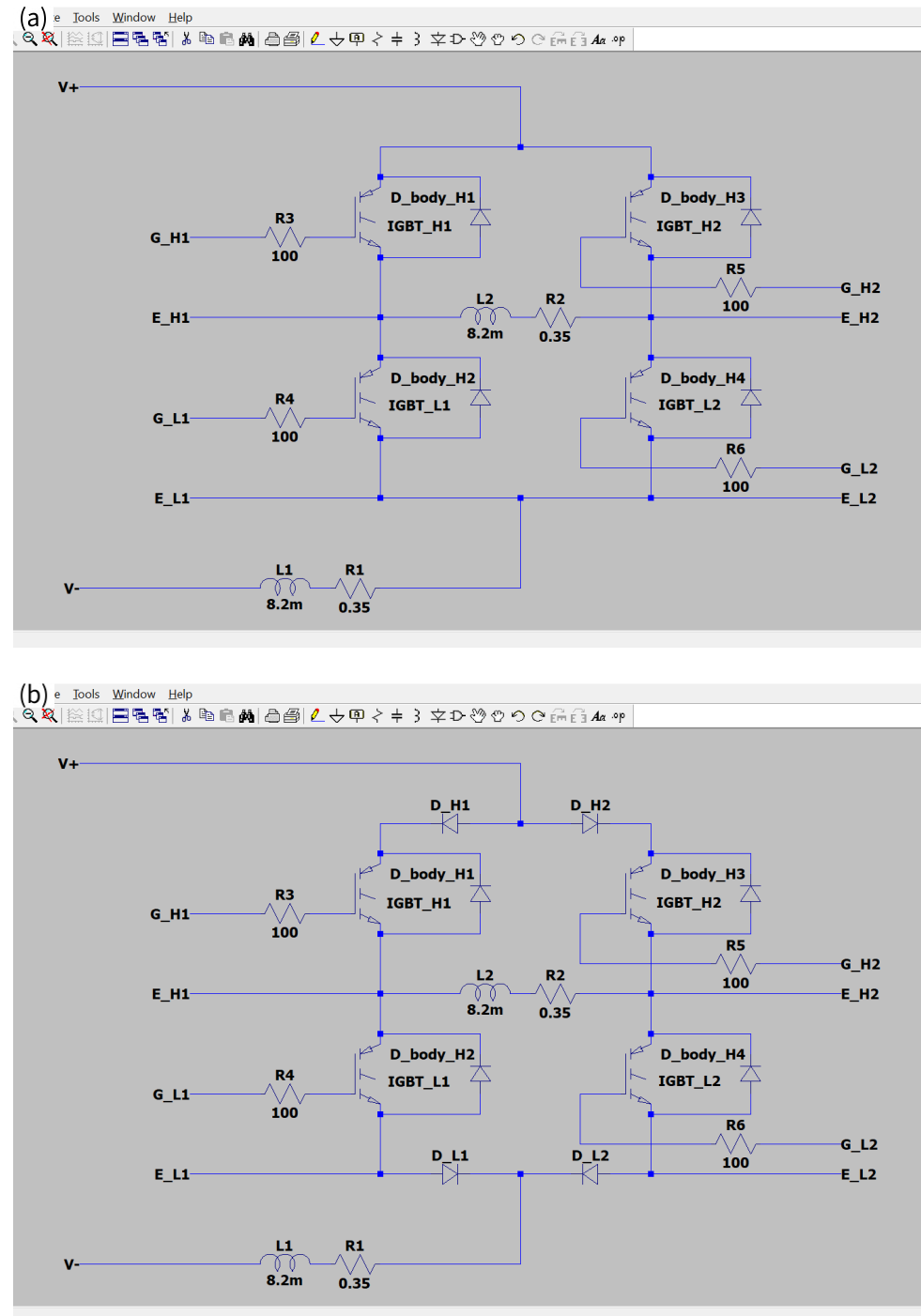


Figure 3.6: (a) A bad circuit: the body diodes create a path for the current in L_2 even in snubbing.
 (b) A good circuit: the extra diodes block the current back-flow path.

D of the latch receives the external control signal. The latch output Q follows the input pin D when LE is high (that is, the sensor output is low) and stays in its original state when LE is low. Thus, when there is almost no current flowing in the coils, the control TTL goes through the latch. On the other hand, when the current is higher than the threshold, the control TTL does not go through and the latch output keeps the old value. The latch output is then sent to the IGBT drivers. An inverter¹⁸ is used for channels that have a negative sign. The comparator, latch, and inverter are packaged in SOT-23-6.

It has been experimentally discovered that the set point voltage can pick up 100 mV spikes when attempting to flip the polarity with some amp-level current through the IGBT. The comparator may see a reference voltage that is different from what is determined by the voltage divider. It is dangerous because the safety circuit may accept a polarity flip when it should not. Adding a 10 nF capacitor across the set point solves this problem. This capacitor is not integrated into the first batch of printed circuit boards (PCBs) and has to be soldered separately.

The complete schematic diagram and the PCB layout that incorporate all the components mentioned above can be found in Appendix B and in my GitHub repository [134]. We ordered multiple unpopulated PCBs from JLCPCB and made two functional circuits, one for each atom source.

Installation

All electronic components are enclosed in an aluminum box mounted inside the atom source frame near the TSP. As shown in Figure 3.7 (a), the box is attached to a water cooling plate through four screws into tapped holes that we machined on the plate. The water cooling plate has slots to accommodate hex head bolts that are used to attach the IGBT modules and the diode modules. The slots make it such that the bolt heads are captured and cannot rotate (but can still wobble around). The electronic components can then be placed in the box, with the bolts aligned with the mounting holes. Due to the depth of the box, we used long coupling nuts to fasten the components, which can be tightened using a socket screwdriver without reaching deep into the tight space.

On one side of the box there are four strain reliefs for gauge 1/0 wires from the power supply and to the coils. The opposite side hosts the PCB. All other components are mounted on the floor. Note that with all the components in place, it is not possible to replace one of the two IGBT modules. The neighboring diode module needs to be removed to free up the space required to replace this IGBT module. Other components can be taken out of the box without conflict, as long as the copper bars are removed and the thick wires are out of the way (they are retractable through the strain reliefs). In order to electrically connect the components, which inevitably involves wire crossing, some wire lugs are raised in height by cylindrical copper spacers. M6 screws are used for the IGBT modules and M5 screws for the diode modules to make electrical connections. Some additional tips for part replacement are as follows (please also refer to Figure 3.7 (b)).

¹⁸Texas Instruments SN74LVC2G14 2-channel inverter with Schmitt-trigger inputs.

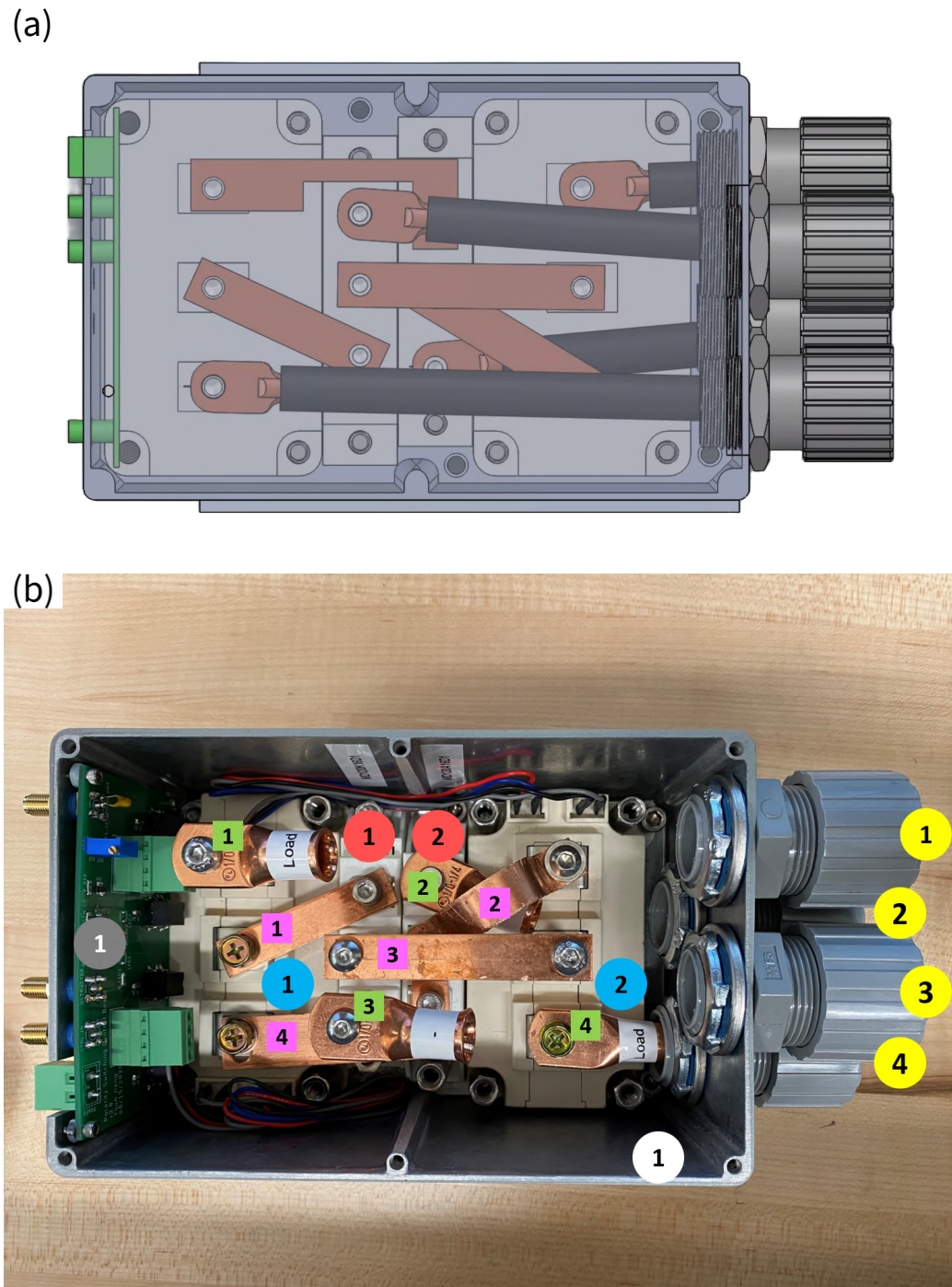


Figure 3.7: (a) CAD model of the polarity reversal box with its components, attached to a water cooling plate. (b) A photo of the actual box with the components labeled.

- To install or uninstall the wires, beware that the strain reliefs are very close to each other due to space limitations. The heads may slightly conflict with each other, but should still be turn-able.
- To replace a diode module, the copper on top of it must first be removed. Then the two coupling nuts need to be removed. Note that diode module 1 has a short coupling nut (custom machined) to avoid contact with connector 4. Reverse the procedure to install a new diode module.
- To replace IGBT module 2, the copper on top of it must first be removed. Then the four coupling nuts need to be removed. Remove lug 1 and the spacer underneath it to unplug the green connector from the PCB. Reverse the procedure to install a new IGBT module.
- To replace IGBT module 1, the copper on top of both itself and diode 1 must first be removed. Take out diode 1 and unplug the green connector from the PCB. Then take out the two coupling nuts holding the IGBT on the far side of the PCB. Take off the two fasteners on the close side of the PCB from the outside, leaving two free nuts on IGBT 1. Loosen the four screws inside the box that secure the box to the water cooling plate (no need to take them out completely). Now lift up the box from the water cooling plate, wiggle IGBT 1 until it comes out. Reverse the procedure to install a new IGBT module. For the two nuts on the close side of the PCB, use an alley key to stop them from moving while the fastener is being tightened from the outside.
- To replace the PCB, remove IGBT module 1 first.

Performance

We set the safety reference point at 12 mV, which can be monitored through one of the SMAs on the PCB. This translates to rejecting polarity flips as long as the UltraStab outputs more than 75 mV, or, equivalently, a current greater than 0.45 A. This means a wait time of less than 2.5 ms between snubbing off an anti-Helmholtz current of 4.2 A and flipping the coil polarity.

Figure 3.8 (a) is an oscilloscope trace in which the polarity flip is rejected. The sequence here is 4.2 A → snub → wait 2.1 ms → flip → wait 0.2 ms → turn on 20 A. We can identify that the polarity flip did not happen because the purple trace (UltraStab output) did not reach zero. On the other hand, with the wait time being 2.5 ms, Figure 3.8 (b) shows an oscilloscope trace in which the polarity flip is accepted. We can identify that the polarity flip happened because the purple trace (UltraStab) jumped to zero abruptly.

Table 3.2: List of parts that are used in the polarity-reversal box.

Description	Part number	Label in Fig. 3.7 (b)	Notes
Box	Hammond 1590EGY	White 1	See Figure A.1 for machining details.
Strain relief	McMaster-Carr 7529K193/7466K38	Yellow 1-4	Cut the rubber insert open for easy installation.
IGBT pair	Infineon FF150R17KE4	Blue 1-2	The two modules have opposite orientations.
Common-cathode diode pair	MCC MD120K16D1	Red 1	
Common-anode diode pair	MCC MD120A16D1	Red 2	
PCB	Custom from JLCPCB	Gray 1	Has four 4-40 screws as standoffs but is secured to the box via 3 through-hole SMAs.
Copper lugs	Size 1/0	Green 1-4	1, 4 = Load; 2 = V+; 3 = V-; The order matches the strain reliefs.
Copper connectors	Custom	Pink 1-4	Connector 2 is bent to allow lug 2 to pass underneath it.

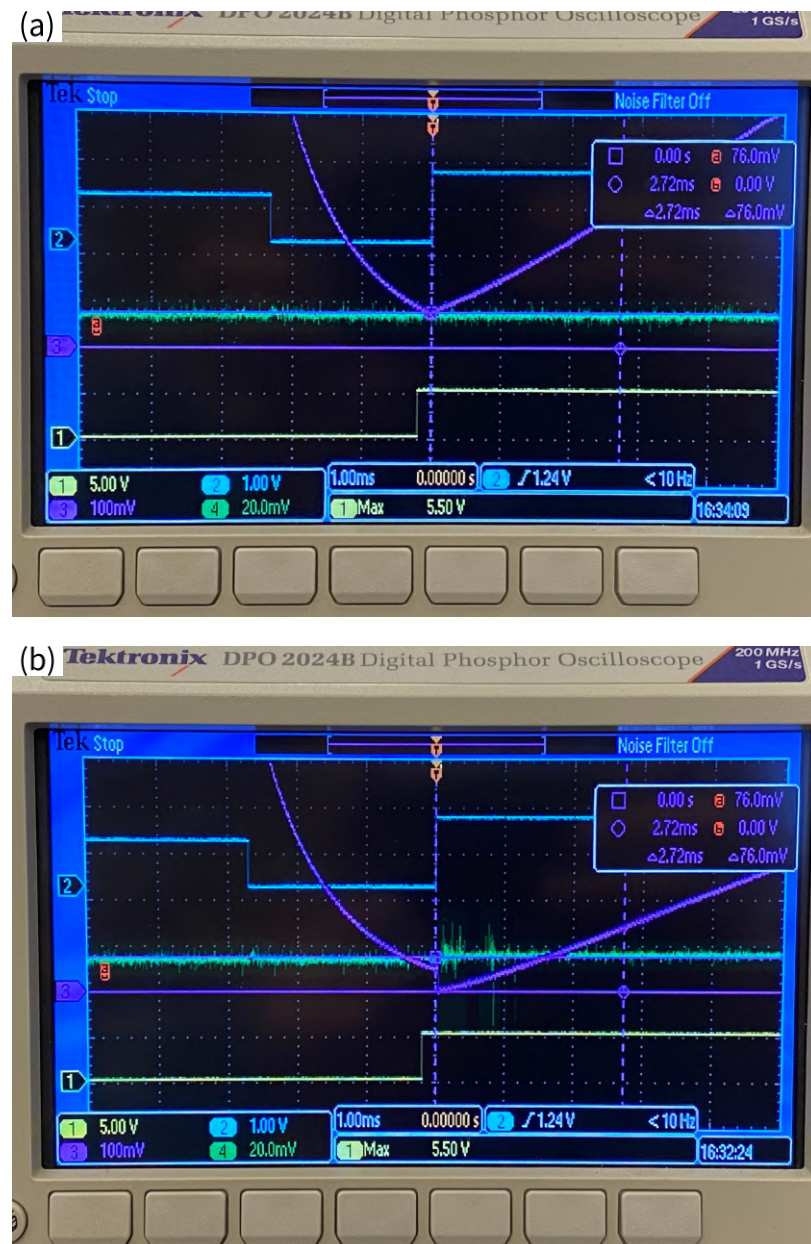


Figure 3.8: Oscilloscope trace of (a) a rejected polarity flip and (b) an accepted polarity flip. In both panels, yellow trace is the polarity (Low = anti-Helmholtz, High = Helmholtz), blue is coil on/off (second rise edge is set higher to trigger on it), purple is the UltraStab measurement, and green is the set point monitoring.

3.2 Connection Nodes

The connection nodes are two identical vacuum chambers that connect horizontally to the two atom sources and vertically to the interferometer sections. The purpose of each connection node is two-fold. First, it provides a high-conductance pump-out port that allows us to achieve the UHV pressure in the interferometry region. Second, it allows optical access for several important atomic physics procedures before and after the interferometry sequence.

3.2.1 Pump-out Tree

Our target UHV pressure in the interferometry region is 10^{-11} mbar, comparable to the Ye group's strontium optical lattice clock, where a vacuum lifetime of 91 s was reported in an optical dipole trap [135]. To maintain this pressure throughout the tower, ion pumps are distributed along the length. The permanent magnets on the ion pumps do not allow them to be installed inside or close to the magnetic shield. Therefore, a natural place to install these pumps is on each connection node, where the magnetic shield already has a gap for optical access. To further minimize the impact on magnetic shielding, the ion pump is installed on a custom pump-out tree that is 40 cm away from the axis of the interferometry tube. The magnet on the ion pump is arranged so that it faces away from the magnetic shield.

To reach the target pressure in the presence of the gas load in the tower, dominated by hydrogen from the atom source oven, and the remainder from the vacuum surface outgassing, it is estimated that a pump speed of 1000 L/s is required at each connection node. To achieve this requirement with a safety margin, we chose a 200 L/s ion pump in combination with a titanium sublimation pump (TSP). The TSP is mounted in a long 4" diameter tube (CF 6.00") at the bottom of the pump-out tree, and allows all the vacuum surface in its line of sight to contribute to the pump speed. It is estimated that a fresh titanium coating in this tube can achieve 1900 L/s of pumping.

As shown in Figure 3.9, the pump-out tree is attached to the connection node chamber by a conical expander welded to the chamber, which enlarges the CF 4.50" port on the chamber to CF 6.00". It has been calculated that sufficient pumping can be achieved in the connection node even with the limitation of conductance due to the conical expander. In addition to pumps, the pump-out tree also includes an ion gauge to monitor the pressure at the connection node.

3.2.2 Optical Access

Each connection node is equipped with 10 CF 1.33" viewports, 3 CF 2.75" viewports (including the one on the pump-out tree, which has a direct line of sight to the center of the chamber), and 4 CF 4.50" viewports¹⁹. The many optical accesses allow for multiple functionalities of the connection

¹⁹We initially purchased viewports from Torr Scientific but their viewport had coating issues. Then we switched to MPF viewports.

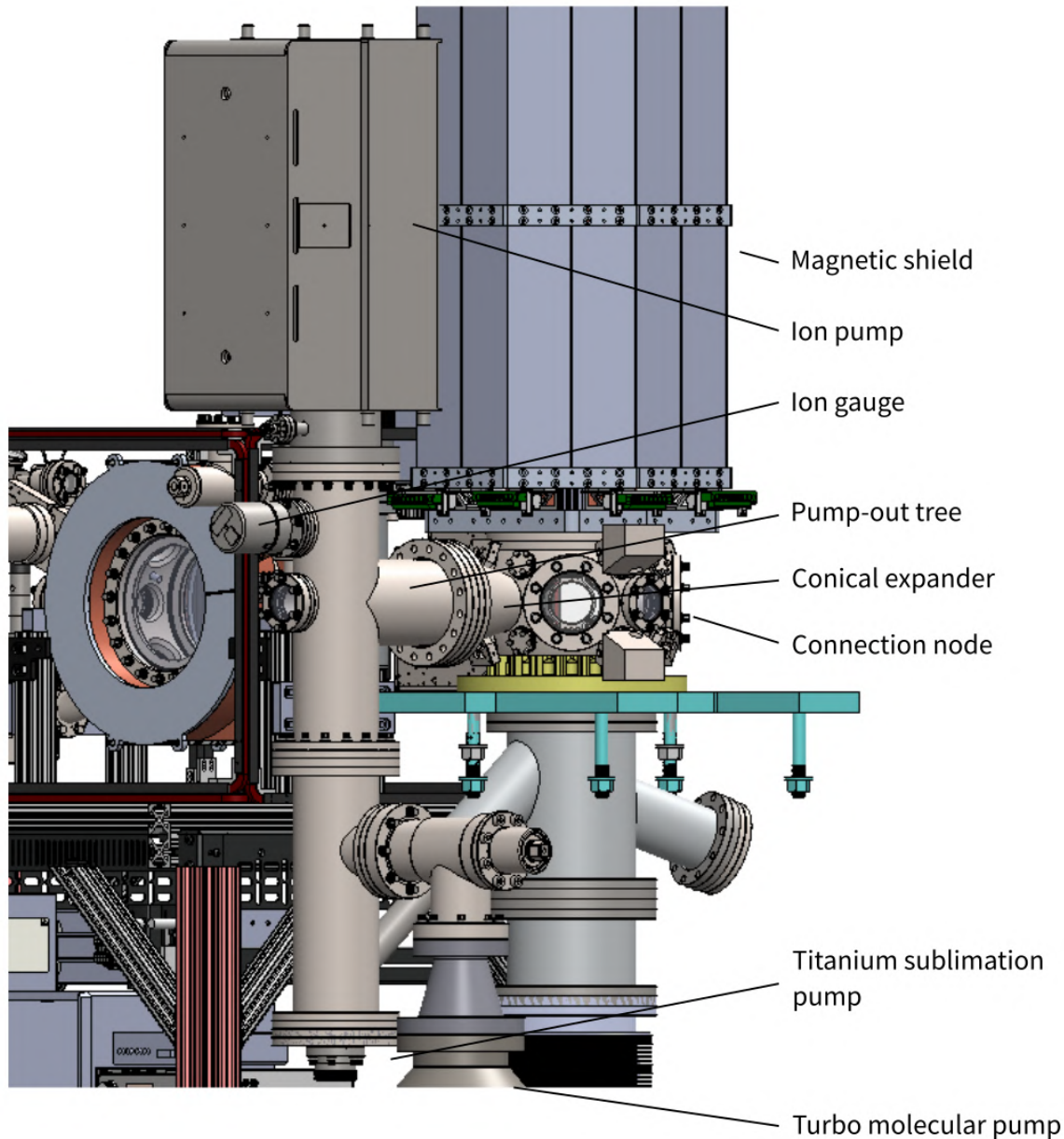


Figure 3.9: The connection node chamber and the pump-out tree attached to its side, showing the location of various pumps to achieve a target UHV pressure of 10^{-11} mbar in the interferometry region.

node chamber as follows.

Shuttle Lattice

After cooling, the atom ensemble is transferred from the atom source chamber to the connection node using a horizontally moving optical lattice referred to as the “shuttle lattice” [136]. The optical lattice light is blue-detuned from the $^1S_0 - ^3P_1$ transition to reduce spontaneous emission loss during transport [137, 138]. Details of the shuttle lattice are discussed in Section 5.2 and Section 5.3.

Launch Lattice

Once the atoms reach the center of the connection node chamber, the same shuttle lattice light is redirected to form a vertical optical lattice called the “launch lattice”. The atoms are loaded into this lattice and accelerated upwards into the interferometer region. To achieve the launch velocities needed for the desired free-fall times, the two laser beams forming the lattice must overlap over a sufficient vertical distance. This is achieved by an in-vacuum optical system, which is discussed in Section 5.4.

State Preparation

After atoms have been cooled to a sufficiently low temperature, they must be prepared in the proper internal state. For clock interferometry on the 698 nm transition, ensembles of ^{87}Sr atoms will be prepared in the $m_F = +9/2$ magnetic substate [66]. The choice to operate using both $m_F = +9/2$ and $m_F = -9/2$ states allows for simultaneous, co-located interferometers with opposite-sign linear Zeeman coefficients. Taking the average of the phase of these two m_F interferometers then suppresses magnetic field dependent phase shifts, while the phase difference between them can provide a magnetic field measurement that may be monitored or used for additional corrections.

Alternatively, for dual-isotope operations, Bragg transitions at 679 nm will be used to implement atom interferometry. This transition offers advantages for simultaneous interferometry with two isotopes, including reduced spontaneous emission and less sensitivity to isotope shifts. To operate in this mode, the atoms must first be transferred to the 3P_0 state. However, the bosonic isotopes have no natural coupling on the $^1S_0 - ^3P_0$ transition, so instead the atoms can be transferred via a coherent multi-photon Raman process, with 3P_1 and 3S_1 as intermediate levels, or a four-level STIRAP sequence such as in Ref. [139].

Atom Detection and Phase Extraction

After the interferometer closes, the atoms fall back to the connection node chamber and are imaged to read out the population in each output port, which is then converted to the interferometer phase. The atom cloud becomes dilute after the expansion during a long free-fall time; therefore,

it is important to design an imaging system that collects as much light as possible from the atom fluorescence while also resolving spatial features on the atom cloud. This is achieved by an in-vacuum lens triplet, which is positioned 2.2" away from the center of the chamber and has a diameter of 2". The resulting solid angle is thus 0.65 sr, much higher than any imaging system can achieve outside the vacuum chamber. The shapes and locations of the lenses were chosen to minimize aberrations using Zemax simulations, taking into account an identical triplet outside the chamber to form a $4f$ system. This imaging system is focused at the center of the chamber with the help of a retractable custom resolution chart shown in Figure 3.10. Interested readers should refer to my labmate Megan Nantel's dissertation [140] to learn about the details of the design, alignment, and characterization of the in-vacuum lens triplet.

To obtain information on the cloud from different perspectives, two in-vacuum lens triplets are installed 90° perpendicular to each other inside neighboring CF 4.5" viewports. The smaller CF 2.75" viewports can also be used for cameras outside the connection node for additional imaging and diagnostic purposes.

3.3 Interferometer Sections

As mentioned previously, the tower is modularized into two main sections, shown in Figure 3.11, which measure 129.4" and 155.8" in length. The length difference results from the different ceiling heights of the two floors in the lab. Each section consists of a UHV-compatible vacuum system, a pair of in-vacuum high-voltage electrodes, a magnetic shield, a set of bias coils for magnetic field control, and a mechanical support structure. The sections were assembled horizontally for convenience and then installed and planned to be operated in a vertical configuration. This section discusses the design choices of the interferometer sections and the assembly procedure we have developed, which can be transferred to MAGIS-100 as many of the features are shared.

3.3.1 Vacuum Tubes

The vacuum system for each section is made up of two 6" diameter vacuum tubes (referred to as the "top tube" and the "bottom tube" according to their location in the vertical configuration) and a chamber between them to house the in-vacuum electrodes. The bottom tubes for both sections have identical lengths (89"), so that the electrode chambers are positioned at the same relative height from the connection nodes. On one end of the bottom tube, the flange is custom ordered to have a double density fastener pattern with tapped and smooth interleaved holes. The tapped holes are used to secure two aluminum base plates which are part of the mechanical structure discussed in Section 3.3.5. The smooth holes are used for vacuum connection to the connection node.

A double-layer solenoid is wound around the bottom tubes to provide a uniform bias magnetic field along the tube, which is referred to as the longitudinal direction. We realized empirically

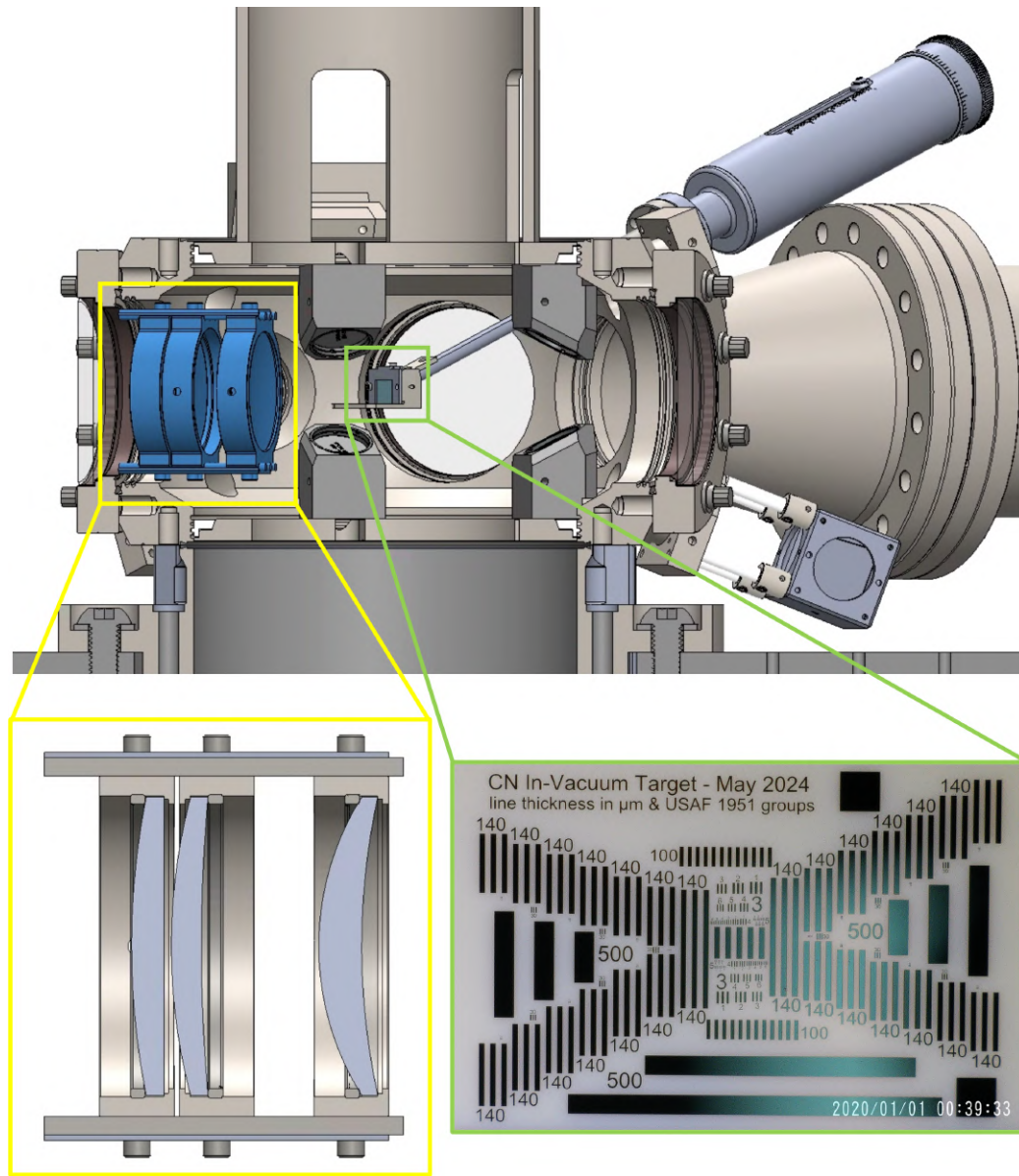


Figure 3.10: A 2" in-vacuum lens triplet highlighted in blue for final readout of the atom cloud. A resolution chart installed on a linear actuator can be moved to the center of the connection node to characterize the imaging optics. A cross section of the lens triplet and a microscope image of the resolution chart are shown in individual boxes. The connection node contains two identical lens triplets separated by 90°, but only one is shown here.

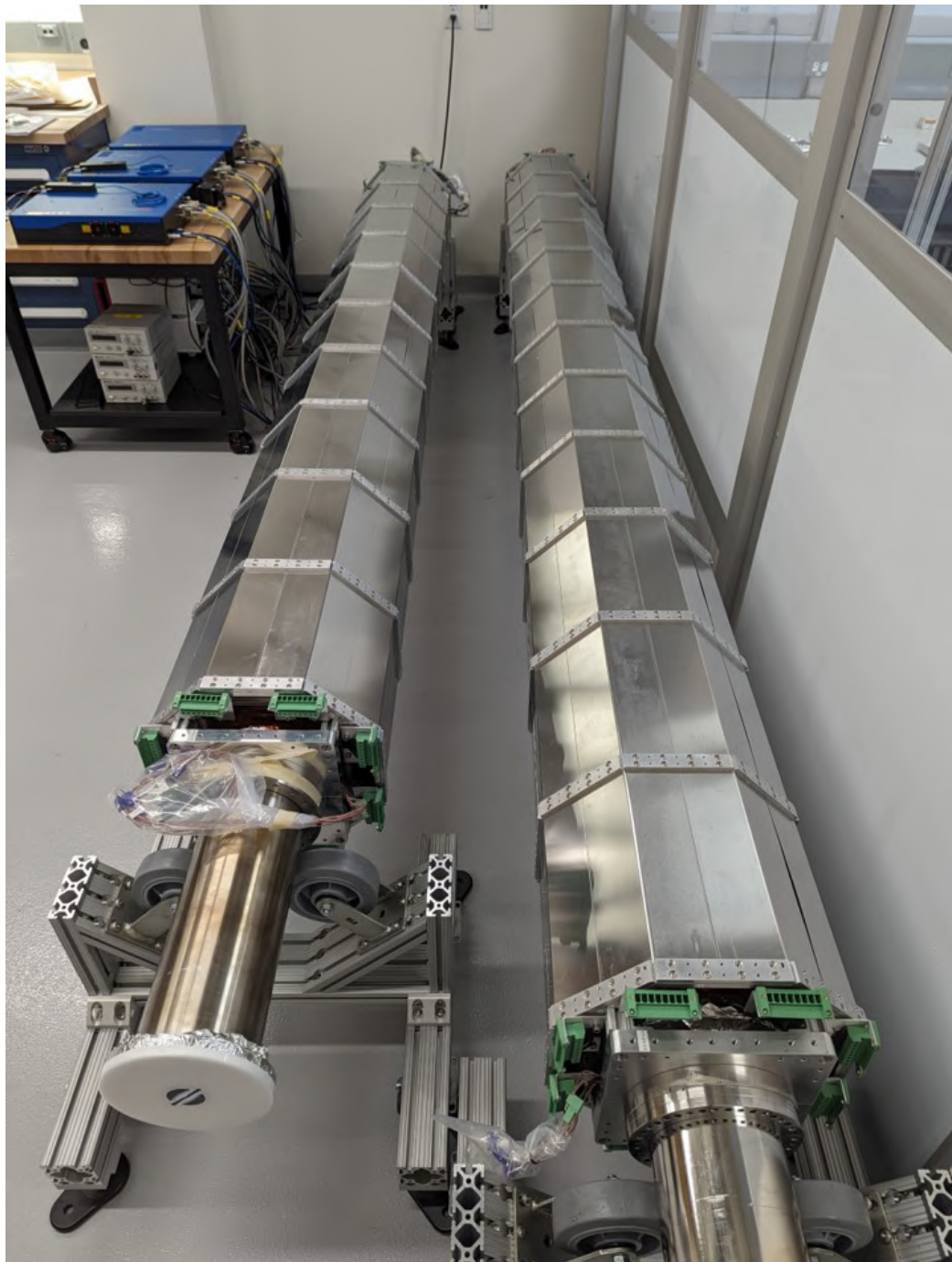


Figure 3.11: Two completed tower sections side by side. The shorter one is the upper, and the longer one is the lower tower section.

that the solenoid winding process requires continuous rotation of the tube, which causes vibrations that are detrimental to the integrity of the electrode stack (see Section 3.3.2). Therefore, it is recommended to wind the solenoid on the bottom tube before making the connection to the electrode chamber²⁰. The details of this solenoid are explained in Section 4.3.2.

To continuously rotate long vacuum components, we built four roller support structures out of 80/20 components shown in Figure 3.12 that allow a 6" diameter cylinder to rotate about its axis without sagging under gravity. The section under operation is usually connected to two short vacuum tubes on the ends, and these short tubes are placed on top of the rubber wheel pairs of two rollers separated by the length of the tube section. We nickname this structure a “rotisserie” due to its similarity to the roasting technique. We added casters underneath the 80/20 to move the tube section around and adjustable feet to fine-tune the height of the tube section for vacuum connection purposes.

3.3.2 Electrode Chamber

The high-voltage (HV) electrodes are designed for QMATCH, the atomic charge neutrality experiment [141, 142]. They are a pair of 25" long SS 316L tubes²¹ rigidly supported in vacuum by ceramic rods inside a custom vacuum chamber. They are designed to operate at $\pm 15\text{ kV}$ to perform a force-free measurement of the scalar Aharonov-Bohm phase induced by the residual charge on the atoms, if any, when the two interferometer arms experience this differential potential. The structure of the electrode chamber, shown in Figure 3.13, was developed by my labmate Ben Garber, with a careful choice of many design parameters based on extensive simulation [142]. After Ben’s work, I collaborated with Megan Nantel and Mahiro Abe to make modifications and iterate on the assembly procedure until we reached a mature design.

Assembly

The electrode chamber was assembled in a cleanroom environment and then connected to the rest of the vacuum system. Table 3.3 summarizes the components used in the electrode chamber. Many rounds of assembly were performed to address the mechanical, magnetic, and vacuum issues that we have identified, and the procedure to which we converged is as follows.

1. Figure 3.14 (a): Build a jig supported by 80/20 beams on which the electrode stack can be constructed. The jig was repurposed from a pair of spare base plates. Install wheels on the bottom of the 80/20 structure for mobility. Fasten the lower double density flange to the base

²⁰We did not follow this procedure for the first tower section and chipped the ceramic spacers in the electrode stack. We then had to remove the electrode chamber for repair.

²¹Despite of higher density, we choose stainless steel instead of aluminum due to its superior surface hardness. After machining, the surface was electropolished by a local service shop, Advanced Electropolishing Technologies, to remove high points that may cause discharge.



Figure 3.12: Roller support structure with rubber casters (80/20 2705) to bear the weight of a long 6" vacuum tube while allowing rotation about its axis. Four of these are built in order to support the two tower sections (one on each end).

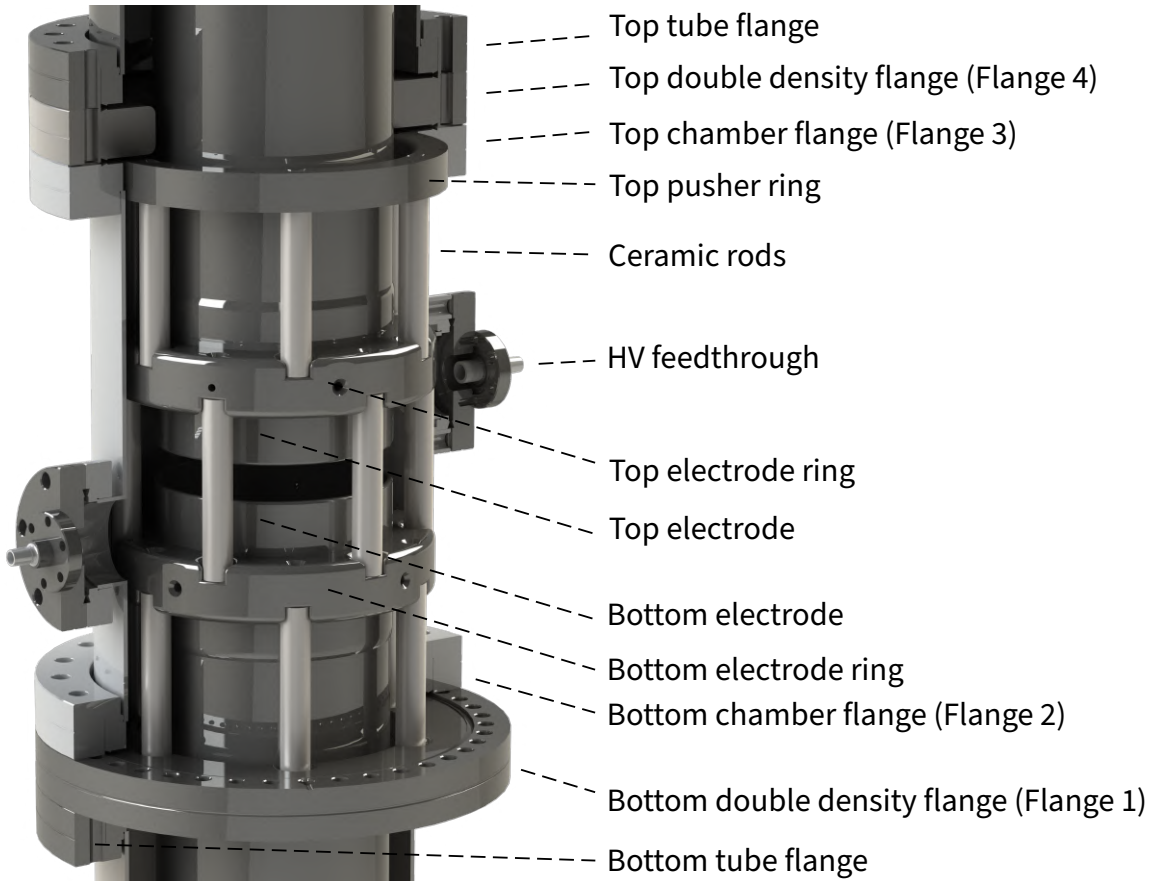


Figure 3.13: CAD model of the electrode chamber. The top and bottom tube flanges are also included. Only the electrodes and electrode rings will be charged to HV through the feedthrough. All other metal components will be at ground. Electrical insulation is realized through ceramic rod spacers and vacuum gaps. For the design details of this chamber, see my labmate Ben Garber's dissertation [142].

Table 3.3: Components of the electrode chamber. Their locations are indicated in Figure 3.14.

Component	Qty. per section	Description
Electrodes	2	SS 316L hollow tubes electropolished for a smooth surface. The electrodes have a slightly large diameter at the base to match the electrode rings.
Electrode rings	2	Provides mechanical interface to the ceramic spacers. Four fasteners and eight set screws secure the ring to the electrode and kill the large moment of tipping.
Double density flanges	2	Two distinct double-sided flanges to connect the electrode chamber to the tube sections. The top flange has holes for set screws (push) and pull screws (pull) to compress the electrode stack. The bottom flange has counterbores and serves as the base for the first layer of ceramic rods.
HV feedthrough	2	Non-magnetic CeramTec Mini HV feedthroughs (CF 2.75") rated to 15 kV. The HV wires are 0.032" copper (Ceramtec 18745-01) and crimped to terminal connectors (Ceramtec 16757-02-A). The free end of the wire is fastened to the electrode ring and the crimped end is connected to the feedthrough. The wires are insulated by alumina beads.
Ceramic rods	18	We initially tried Macor rods from McMaster-Carr and used fasteners to connect them to the electrode rings, which led to frequent chipping. We then switched to alumina rods for their superior strength and diameter tolerance. The rods measure 0.5" in diameter and 3" in height.
Electrode chamber	1	Custom chamber with one of the flanges rotated, which is important for the clocking of the top fasteners.

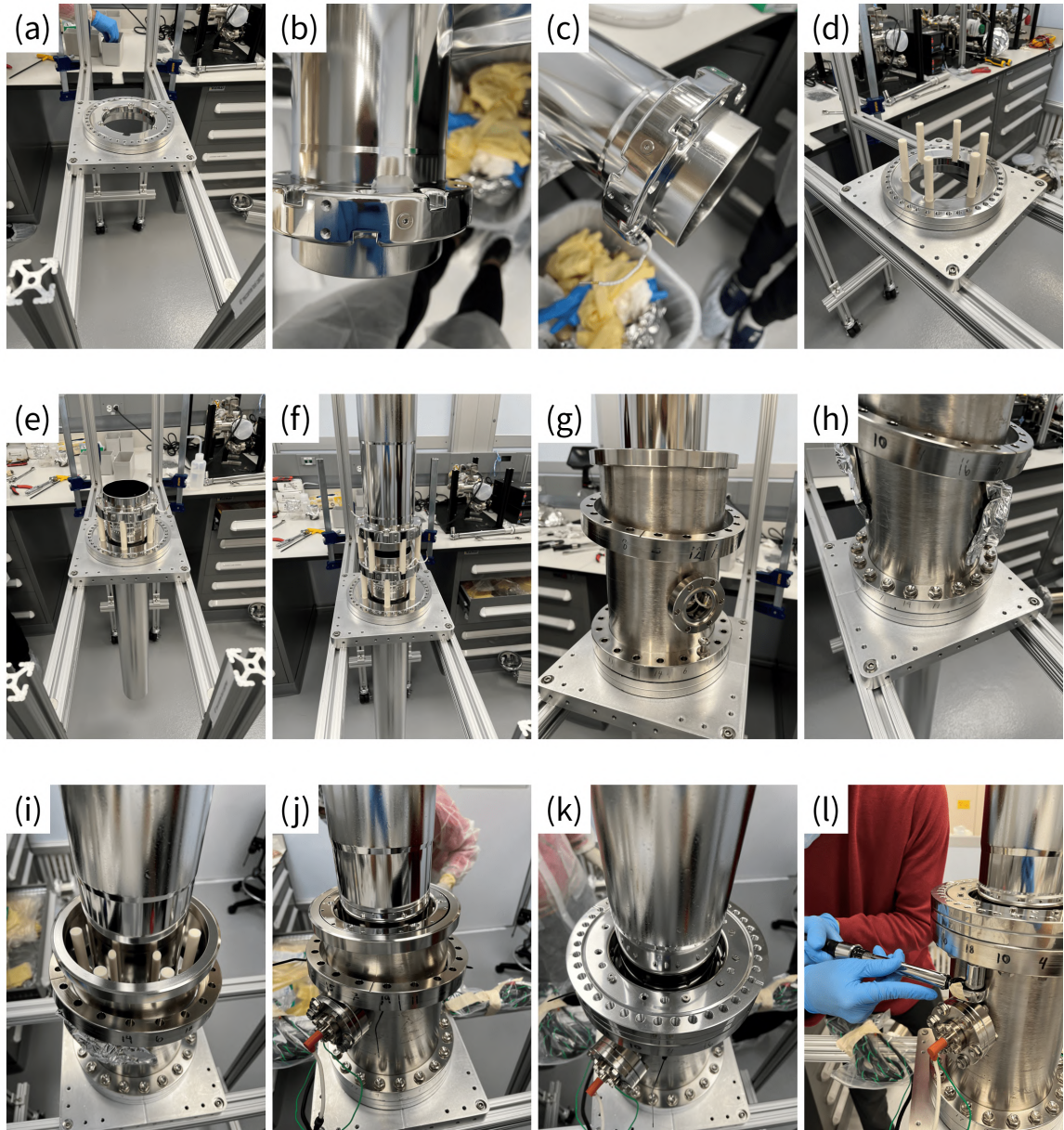


Figure 3.14: Procedure to assemble the electrode chamber. Refer to the text for detailed description of these steps.

plate with a copper gasket underneath to protect the knife edge. This gasket will not be used for the final vacuum seal, so it is acceptable to take a used gasket as long as it has been cleaned.

2. Figure 3.14 (b): Connect the electrode rings to the electrode. The electrode is not machined as an interference fit to the rings, leading to radial gaps around the edge. To address this issue, we cut out shims from Grade 316 stainless steel (SS 316) sheets. The shims were around 1" wide and slightly taller than the electrode ring. We punched a hole in the center of the shim so that it could be captured by the fasteners connecting the ring to the electrode²². We had a range of sizes from 0.001" to 0.004" and iteratively tried what would make the tightest fit. Once we were satisfied with the fit, we fastened the electrode to the ring and added set screws for additional stabilization.
3. Figure 3.14 (c): Prepare HV wires that connect the electrode ring and the electrode to the 2.75" feedthrough that will be mounted to the electrode chamber. These are bare copper wires bent into the proper shapes. Add insulating beads and attach these wires to the appropriate holes on both electrode rings.
4. Figure 3.14 (d): Put six clean alumina ceramic rods²³ in the countersunk holes on the lower double density flange. These rods will be under compression load only, so it is not necessary to use fasteners²⁴. Due to machining tolerance, these rods have a length distribution. If possible, try to choose ceramic rods of around the same length²⁵.
5. Figure 3.14 (e): Place the electrode and ring assembly on the ceramic stack so that the ceramic rods fit inside the countersunk holes in the electrode ring. It is useful to have three people to do this. One person lowers the electrode and two people ensure that the ceramic rods go smoothly into their holes. It is easy to break the ceramic rods if the rings hits them at an angle or if they get jammed.
6. Figure 3.14 (f): Add the middle layer of clean ceramic rods. Then place the top electrode and ring assembly over the middle layer of ceramic rods. Make sure the orientation is such that the two HV wires are about 180° apart.
7. Figure 3.14 (g): Clean a copper gasket²⁶ and load it on the double density flange that is secured to the jig. Then lower the electrode chamber onto the double density flange. Make sure the HV wires are tucked in so the chamber does not get caught on them when being lowered. Then

²²So that in case the shim slipped out, it would be caught by the fasteners and not fall onto the in-vacuum optics.
²³We cleaned the rods by soaking them in acetone and then wiping each rod using acetone and Kimwipes.

²⁴We could not use fasteners anyways as the ceramic rods became more fragile after being tapped. We also chose alumina instead of Macor for higher flexural strength. The rods were purchased from Coorkstek: Alumina High Purity > 99.6%. Tolerances: OD $\pm 0.001"$, straightness 0.003"/1.000".

²⁵Before assembly, we started by measuring the rods and sorted them by length in order to make this step easier.

²⁶Due to many vacuum leaks in our early attempts, we used a custom 2.35 mm gasket made by our local machinist Mehmet Solyali instead of an off-the-shelf 2 mm gasket for Flange 2 (bottom of electrode chamber) and Flange 3 (the top of the electrode chamber).

pull out the HV wires to make sure the chamber is oriented correctly and the wires can reach the 2.75" feedthroughs.

8. Figure 3.14 (h): Use titanium fasteners and Nord-Lock washers to make the vacuum seal between the chamber and the double density flange²⁷.
9. Figure 3.14 (i): Add the final layer of ceramic rods so that their heights are balanced. It is easier to determine the ceramic rod configuration before putting on the chamber in Step 7 (then the rods have to be removed but their locations should be recorded).
10. Figure 3.14 (j): Screw in two of the 6-32 pull fasteners into the top pusher ring. Use these fasteners as handles to lower the ring and thread it over the electrode. Note that in the photo the HV feedthroughs have been installed. This can be done at any convenient time after Step 7.
11. Figure 3.14 (k): Add a clean gasket and the top double density flange. One person needs to hold up the rotatable flange on the electrode chamber. Find the correct clocking of the double density flange with respect to the top electrode ring by probing with two 6-32 pull screws²⁸. Once we found the correct clocking, we dropped in all twelve to make sure they would engage with the threads, but we did not tighten them all the way. Then load the six compression set screws (1/4–20 × 0.75" cone point) but do not tighten all the way.
12. Figure 3.14 (l): Rotate just the rotatable flange to match up with the hole and fasten with titanium fasteners and Nord-Lock washers from 120 to 200 inch-lbs in steps of 20 inch-lbs. Tighten the set screws from 30 to 60 inch-lbs in steps of 10 inch-lbs. Tighten the pull screws to 30 inch-lbs. Finally, tighten the titanium fasteners on the flange to 250 inch-lbs in steps of 10 inch-lbs.

Then, to connect the electrode chamber to the vacuum tubes, we followed these steps:

1. Figure 3.15 (a): Make the connection between Flange 4 and the top tube. For the upper section, this tube was short enough (about 28") that we could make the entire connection and tighten the fasteners vertically using our consistent torque pattern. For the lower section with a longer top tube (about 54"), we had to attach a cart to the jig, flip the assembly horizontally, and then make the tube connection. We only tightened to 140 inch-lbs and then

²⁷Torque pattern: 120, 140, 160, 180, 200, 210, 220, 230, 240, 250 (triple rounds) inch-lbs in a 20-point star pattern. We chose titanium fasteners due to their non-magnetic properties and strength, and Nord-Lock washers (SS 316) due to their wedge-locking feature. Note that at this torque value the cheaper non-magnetic fastener option, silicon-bronze, may break under shear load. For historical reasons, the fasteners are coarse thread (5/16–18).

²⁸We placed two pull screws into their holes on the top flange and purposefully biased the top flange to be in the incorrect position. Then we rotated the flange and watched the fasteners fall into their threaded holes. We only used two fasteners for this task because we found if using all twelve, we could accidentally pull the top ring by over rotating when the fasteners fell into place. This would add additional, unwanted stress on the ceramic rods.

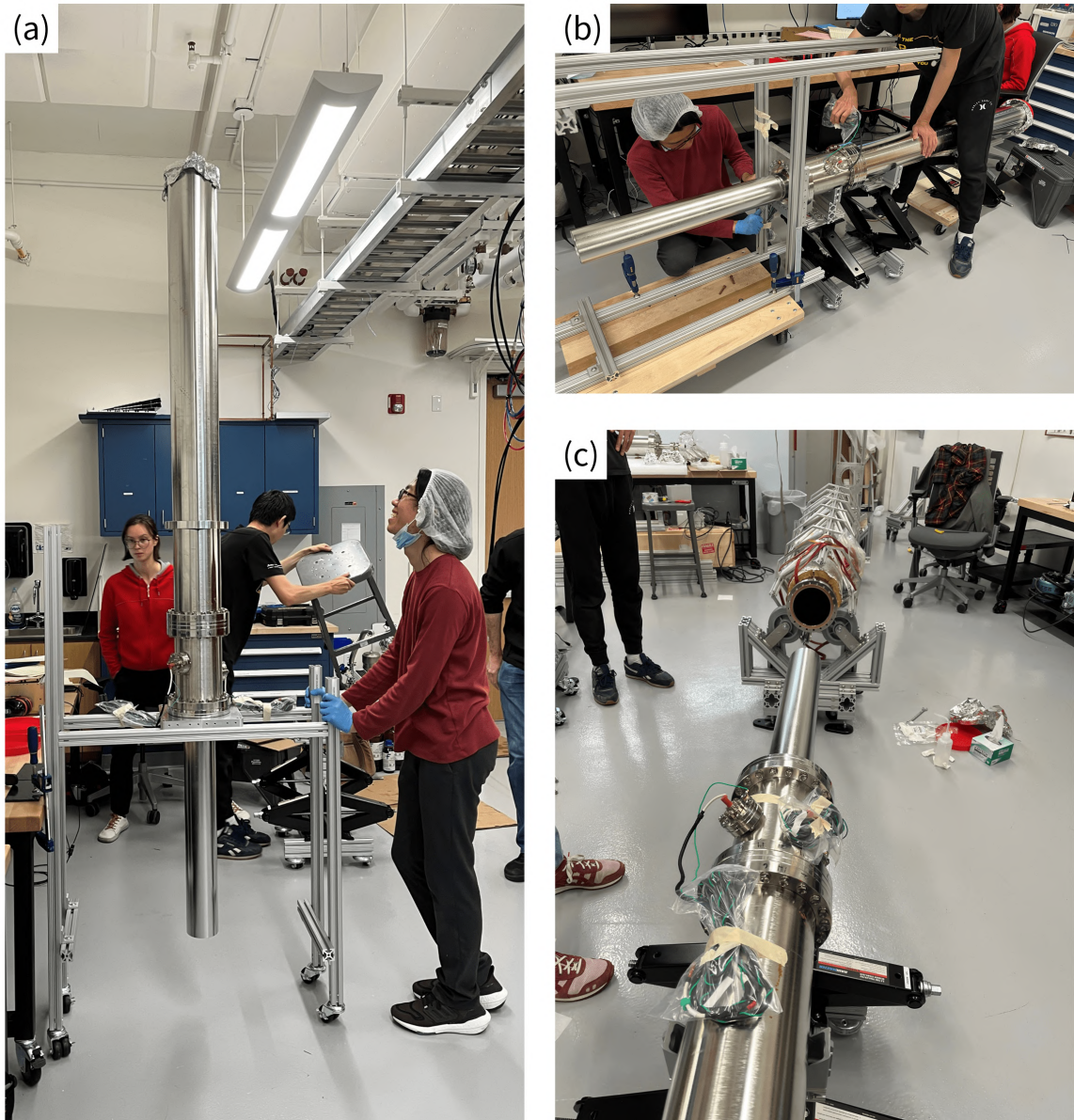


Figure 3.15: Procedure to connect the electrode chamber to the vacuum tubes. Refer to the text for detailed description of these steps. Note that panel (c) was during a repair of the electrode chamber. At that time the bottom tube was already wrapped with the bake-out equipment and an 80/20 shield scaffolding.

flipped it back vertically to finish tightening in the vertical configuration. This task requires four to five people to do it safely.

2. Figure 3.15 (b): The assembly was flipped horizontally and additional support was added to the tube and electrode chamber so that the construction jig could be removed.
3. Figure 3.15 (c): Vacuum connection was made between Flange 1 and the bottom tube.

After this procedure, the tube section was leak checked. For multiple times, we have come across irreparable leaks in the vicinity of Flange 1 and Flange 2 (they are too close to tell apart). This motivated our attempts to use custom thicker gaskets and tighten the flanges in the vertical configuration in a specific torque pattern. These measures were effective and we ended up without any leak in both the upper and lower tube sections. However, as a backup option, we applied Vacseal to Flanges 1 through 4.

Conditioning

When the electrodes are charged, the field concentration at high points along the surface of the electrodes and the walls of the vacuum tube may cause a breakdown at any voltage greater than 1 kV. To address this issue, we connected the feedthroughs to a homemade²⁹ HV power supply with commercial cables³⁰, then the electrodes were conditioned under vacuum at up to 18 kV to smooth the surfaces. To achieve this, we pumped the tube section to around 10^{-6} mbar and slowly increased the voltage on the electrode while paying attention to the current. A current greater than 1 μ A may occur during this process, indicating electric discharge. Such current spikes often do not persist, which is a sign of successful removal of the local surface roughness. In this case, the voltage can be increased further. However, if the current persisted and prevented the voltage from increasing, we waited a few minutes until the current disappeared; otherwise, we would discharge the electrode and perform conditioning with the tube section vented. After this treatment, all electrodes were able to sustain 18 kV without a measurable leakage current. We then allowed the electrodes to “soak” at 18 kV for 30 to 60 minutes to improve surface quality.

Safety precautions are necessary during the conditioning of the electrodes. When electrons are accelerated across the vacuum gap between two HV electrodes and hit the anode, their kinetic energy is transformed into bremsstrahlung, which can pose a radiation hazard [143]. Although we expected the bremsstrahlung X-ray at the conditioning voltage to be blocked by the stainless steel, a Geiger counter was placed directly in contact with the chamber. As we increased the voltage, we made sure that the click rate of the Geiger counter did not increase. Another safety hazard arises from the HV components. To mitigate this hazard, the tube section was connected to the ground of the

²⁹Borrowed from the Kasevich Group. Ben had a new design but it was not finalized.

³⁰CeramTec 86" HVL 1/2L to SCID cables, CTNA 26179-01-A.

building with a grounding braid. Extra caution must be taken when conditioning in air as some HV components may be exposed.

3.3.3 Bake-Out Equipment and Linear Bearing System

After the vacuum connection of the tube section, we installed permanent bake-out equipment around it to increase the temperature (“baking”) during the pump down to achieve a better vacuum pressure. The bake-out temperature is limited to 125°C by the CeramTec HV cable connectors externally plugged into the feedthroughs. However, due to the lack of thermal insulation locally at the feedthroughs, it is acceptable to bake the tower at above 150°C without overheating the connectors.

To achieve such bake-out temperatures, we wrapped two HTS/Amptek 16.5’ heat tapes around the tube section. These heat tapes are non-magnetic and have a flexible silicone jacket. Each of them is rated as 314 W at 120 V. We arranged them in a double-helix geometry, paying attention not to create any heat tape overlap, which may cause damage due to local overheating. Homemade Type E thermocouples, summarized in Table 3.4, were placed along the length of the tube to monitor the temperature during bake-out³¹. The heat tapes and thermocouples were fixed to the tube section using high temperature cable ties and Kapton tape. See Figure 3.16 for details.

To thermally isolate the tube section from the environment during baking, we wrapped it with a 1” thick fiberglass insulation sheet³². This job requires respiratory, skin, and eye protection, as fibers in the insulation material are harmful to the human respiratory system and can cause allergic reactions upon contact. The appropriate PPE shown in Figure 3.17 was worn throughout the installation procedure.

Due to the protrusion of the flanges in the electrode chamber, the insulation was wrapped in two steps shown in Figure 3.18. First, we wrapped the bottom tube, the top tube, and the tube part of the electrode chamber. Note that for the electrode chamber, insulation was done as two half shells, so that the HV feedthroughs could stick out. Since this layer of insulation increases the tube OD to about the same as the 8” flanges on the electrode chamber, we proceeded to the second step in which we covered all flanges with an additional layer of insulation, with two small holes to bring out the HV connectors and cables. The insulation layers were secured with Kapton tapes and the gaps were patched with additional fiberglass. Finally, we covered the ends of the insulation with aluminum foil to prevent human exposure to the fiberglass material.

The tube section is then enclosed with an 80/20 shield scaffolding, shown in Figure 3.19 (a), which attaches to the base plates at the bottom and spans the length of the section. The shield scaffolding measures 10” × 10”, just enough to accommodate the thermal insulation material. 45° trusses were added to the sides of the shield scaffolding to stiffen it. The function of this shield scaffolding is to provide anchor points to the magnetic shield and bias coil bars, which will be

³¹They are also arranged at different radial locations for better sampling.

³²McMaster-Carr 9333K71 pipe insulation with foil facing.

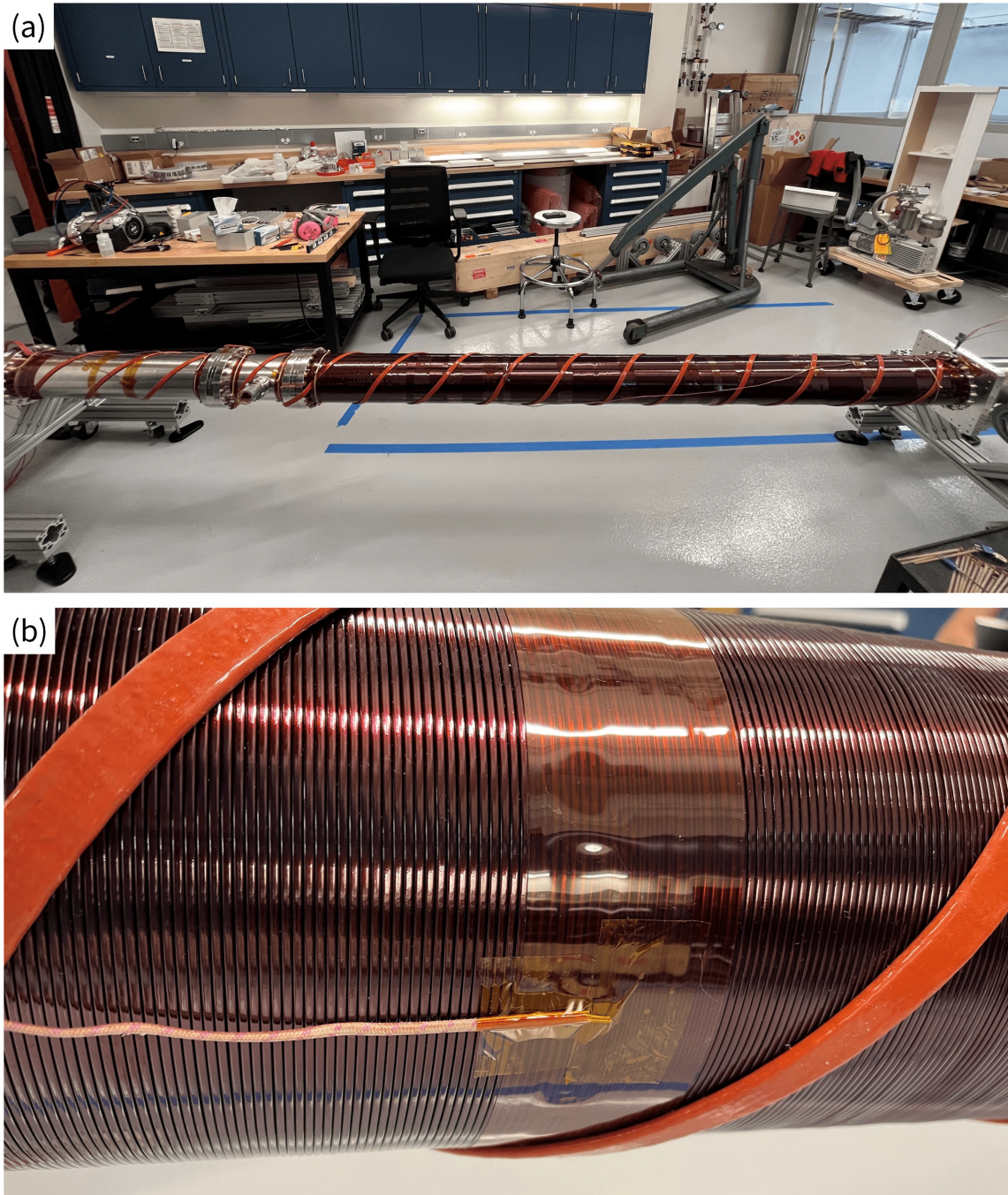


Figure 3.16: (a) The lower tower section with the heat tapes (orange) and thermocouples installed. The solenoid is also shown around the bottom tube to the right. (b) Zoom-in view on the solenoid, the heat tapes, and a thermocouple. The tip of the thermocouple is first wrapped in 0.002" Kapton tape for electrical insulation, then secured to the solenoid by a Kapton tape ring.

Table 3.4: Locations of thermocouples along the upper and lower sections, indicated by their distance with respect to the base plate. The thermocouples placed outside the thermal insulation, whose exact locations are not recorded (entered as N/A), are roughly positioned at the center of the respective tube or chamber.

Location	Distance from the base plate (upper section)	Distance from the base plate (lower section)
Base plate	0"	0"
Bottom tube	21"	18"
Bottom tube	45"	47"
Bottom tube	68"	76"
Bottom tube (outside insulation)	N/A	N/A
Electrode chamber	91"	95"
Electrode chamber (outside insulation)	N/A	N/A
Lower HV feedthrough	92"	92"
Upper HV feedthrough	94"	94"
Top tube	111"	122"
Top tube	125"	153"
Top tube (outside insulation)	N/A	N/A

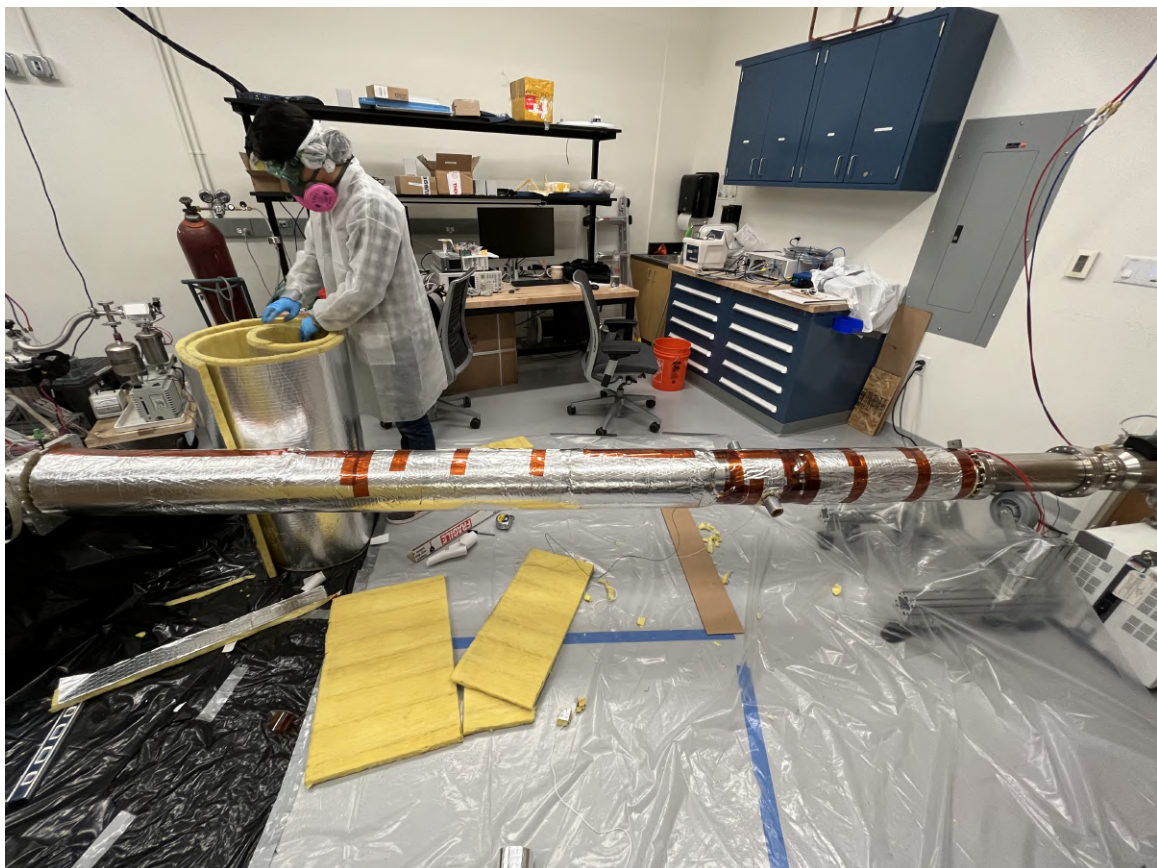


Figure 3.17: A happy graduate student (Mahiro) fully armored with PPE while wrapping the insulation layer. A tarp was used to cover the floor and collect the fiberglass debris.

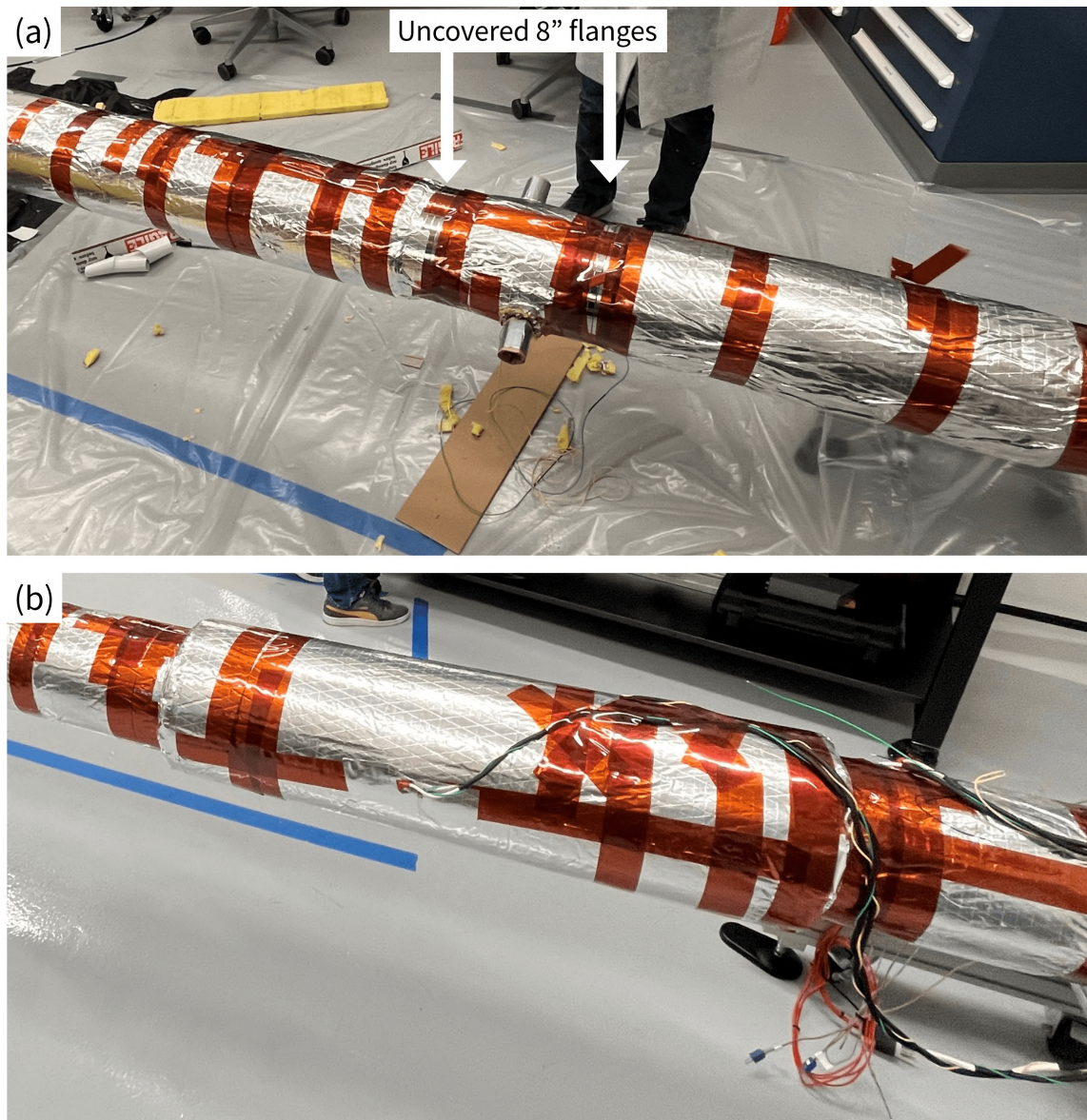


Figure 3.18: Zoom-in view of the thermal insulation around the electrode chamber. (a) In the first step, we wrapped the vacuum tubes and the electrode chamber with fiberglass insulation, while leaving the 8" flanges (white arrows) uncovered. The HV feedthroughs were covered by cardboard caps for protection. (b) In the second step, an additional layer of fiberglass was used to cover the exposed flanges.

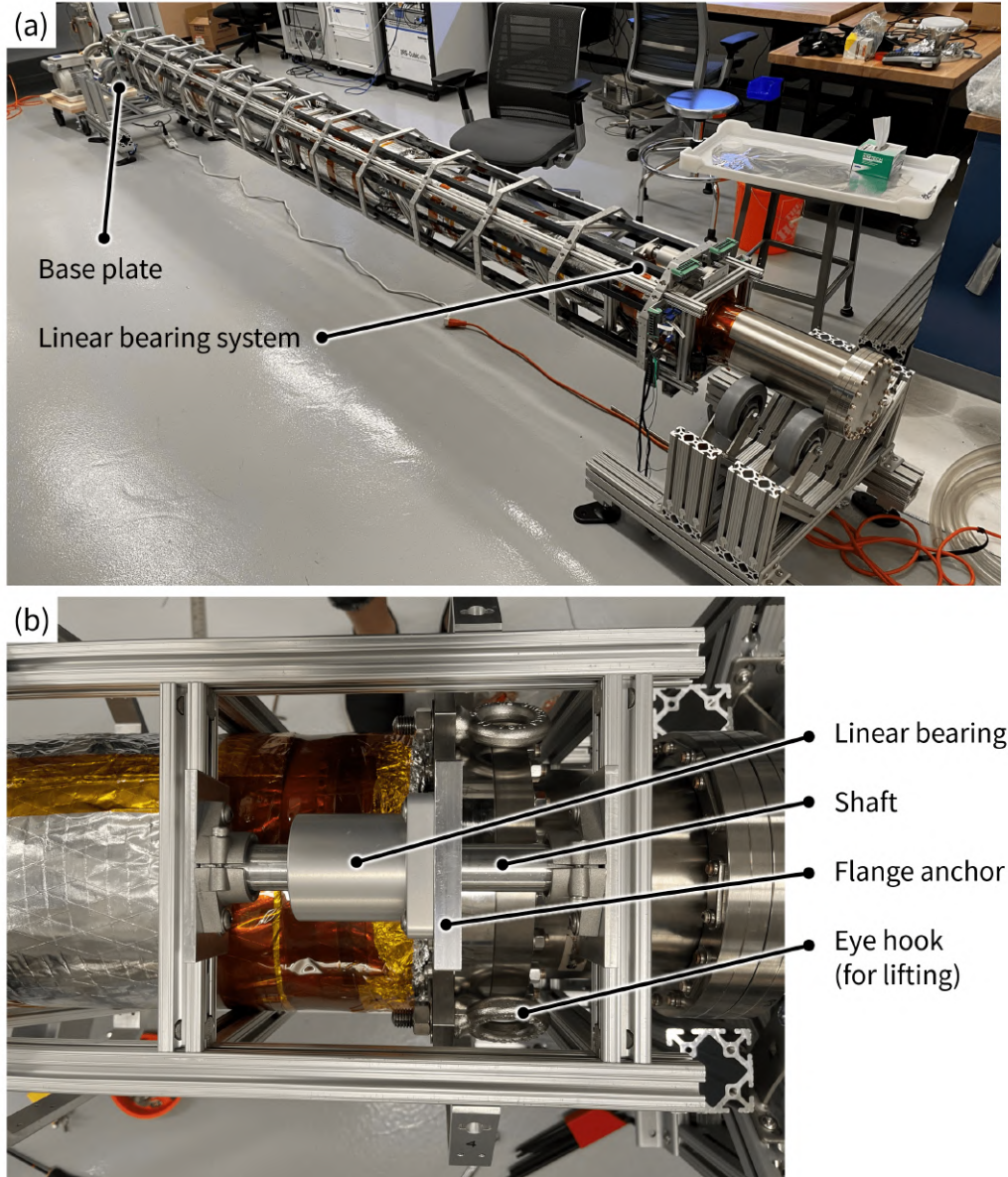


Figure 3.19: (a) The lower tube section enclosed by an 80/20 shield scaffolding. The shield scaffolding is anchored to the base plate at the bottom end of the section, and to a flange on the top end via a linear bearing system, which allows thermal expansion of the tube section with respect to the shield scaffolding during bake-out. We also mounted octagonal rings along the shield scaffolding to support the magnetic shield, which is discussed in Section 4.2.3. (b) The linear bearing system on the top end of the section. Note that the short vacuum tube on the right of this figure is not a part of the tube section. Its purpose is to support against gravity when the tube section in the horizontal “rotisserie” configuration, and is replaced by bellows prior to vertical lifting, when the load is transferred to an 80/20 strongback. A pair of two linear bearings were mounted on opposite sides of the shield scaffolding, but only one is visible from this viewing angle.

discussed in Chapter 4. Due to its structural purpose, an attachment to the tube section at the top is desired. However, a simple attachment that constrains the length of the shield scaffolding with respect to the tube section is not acceptable, as thermal expansion during vacuum bake-out will exert tension on the shield scaffolding and cause structural failure. Therefore, we designed a linear bearing system that only restricts the shield scaffolding radially and azimuthally from the tube but allows axial motion between the two. As Figure 3.19 (b) shows, the same fasteners that make the vacuum connection at the very top of the tube section also connect two linear bearings³³, which can slide on two 1" shafts supported by horizontal 80/20 beams on the top side of the shield scaffolding. We chose the length and location of the shafts to allow around 1" of movement of the top flange. This is larger than the expected thermal expansion of the tube, which is estimated to be 6 mm when the lower section is heated from 25°C to 200°C³⁴. The temperature-dependent growth of length in the vacuum system is absorbed by the bellows on top of both tube sections.

3.3.4 Magnetic Field System Overview

Ambient magnetic field causes an uncontrolled Zeeman splitting and perturbs the quantization axis, leading to population transfer errors and interferometer phase noise. To suppress the magnetic field from Earth and ferromagnetic materials in the building, we built a magnetic shield around the tube section by anchoring mu-metal sheets to periodic octagonal rings attached to the 80/20 shield scaffolding mentioned above. The design and assembly of this magnetic shield is elaborated in Chapter 4. In short, facilitated by the rotisserie, we assembled mu-metal sheets of carefully chosen lengths in a novel pattern that minimizes magnetic field penetration. With a single-layer shield, we have achieved an RMS residual field below 1 mG, which is sufficient given the magnetic insensitivity of strontium.

A uniform bias field is required inside the magnetic shield to define a quantization axis during interferometry. In addition to the solenoid mentioned above that generates a longitudinal bias field, each section incorporates bias coils that generate a transverse bias field. These coils take the form of long magnet wires along the length of the section, guided by Unistrut channels at certain azimuthal locations around the tube axis. As Section 4.3.1 shows, when properly connected end-to-end, these wires generate a uniform transverse magnetic field similar to that of the Helmholtz coils. The same coils can be reconfigured as part of a degaussing circuit to eliminate the remnant field inside the magnetic shield.

³³McMaster-Carr 64825K131 chemical-resistant flange-mount linear sleeve bearing.

³⁴Thermal expansion coefficient is $8.9 \times 10^{-6}/^{\circ}\text{C}$ for SS 316. This calculation is aggressive by assuming that there is no thermal expansion of the shield scaffolding (that is, perfect thermal insulation) and a very high bake-out temperature. In practice, we usually bake up to 150°C.

3.3.5 Mechanical Structure

In the final vertical configuration, the two tower sections and their respective connection nodes are connected and anchored to the two-story lab. Load-bearing 80/20 structures, known as “tables”, are installed on both floors to secure the tower sections and the connection nodes from the bottom end. Each table is designed to include a top part that interfaces with the respective connection node and a bottom part that interfaces with the structural components of the lab. Four precision leveling feet³⁵ are installed between the two parts to fine-tune the height and angle of the tower sections with respect to the lab. These mounts provide 0.25" of travel and are separated by 27" (N-S) and 41.25" (E-W) along the table edges, thus providing angle adjustment of 9.3 mrad and 6.1 mrad, respectively. The maximum angle adjustment corresponds to about 3 mm and 2 mm translation on the top end of the tube sections. However, note that, as discussed in Chapter 5, the upper launch lattice scaffolding does not allow the top of the lower tower section to translate by more than 1 mm. Therefore, care must be taken when adjusting the leveling mounts on the lower table. For each leveling mount, once its height is finalized, a pair of pulling screws are fastened to lock the height and provide side-to-side constraint to the corresponding leg of the top part of the table. To further secure the top part, each of its legs is connected to the bottom part of the table through two diagonal 80/20 beams³⁶. Levelness within 1 mrad is achieved with the help of a precision bubble level³⁷.

As Figure 3.20 shows, the bottom part of the upper table is anchored around the U-shaped opening on the second floor reserved for the tower, through custom brackets to 4" hardened steel beams that are part of the lab infrastructure. These beams were drilled through to allow for 1"-8 fasteners, forming a positive connection that restrains the horizontal motion of the table. The floor on which the table rests was grouted to form four flat and even contact regions to improve the stability and leveling of the table. Additional 80/20 beams allow the upper table to straddle the kick plates on both sides and increase the area of contact to the floor³⁸. The upper table is also clamped against the concrete floor by six 1 1/8"-7 threaded rods³⁹ that extend downward into two additional 80/20 beams, which are anchored to pre-existing I-beams below the second floor. This is shown in Figure 3.21.

The lower table, shown in Figure 3.22, is attached to the first floor through 1/2"-13 concrete anchors⁴⁰. Spherical washers are used to account for angle errors during concrete drilling. The position of the lower table is indicated by the upper table via plumb bobs at key locations.

Each connection node interfaces with the corresponding table through a custom double-sided flange adapter known as the “double crown”. This component is inspired by Kimball Physics

³⁵ McMaster-Carr 3757K15 precision-adjust rigid leveling mounts.

³⁶ With the exception of the southwest leg of the upper table. It has only one diagonal beam due to spatial constraints.

³⁷ McMaster-Carr 21515A21 Starrett precision level. Calibration is needed before use.

³⁸ The kick plates were pre-drilled to allow the insertion of four 3/4"-10 fasteners. Shims were added between the 80/20 beams and the floor.

³⁹ McMaster-Carr 93250A185 SS 316 3' threaded rod.

⁴⁰ Grainger 15W080 female-threaded anchors.

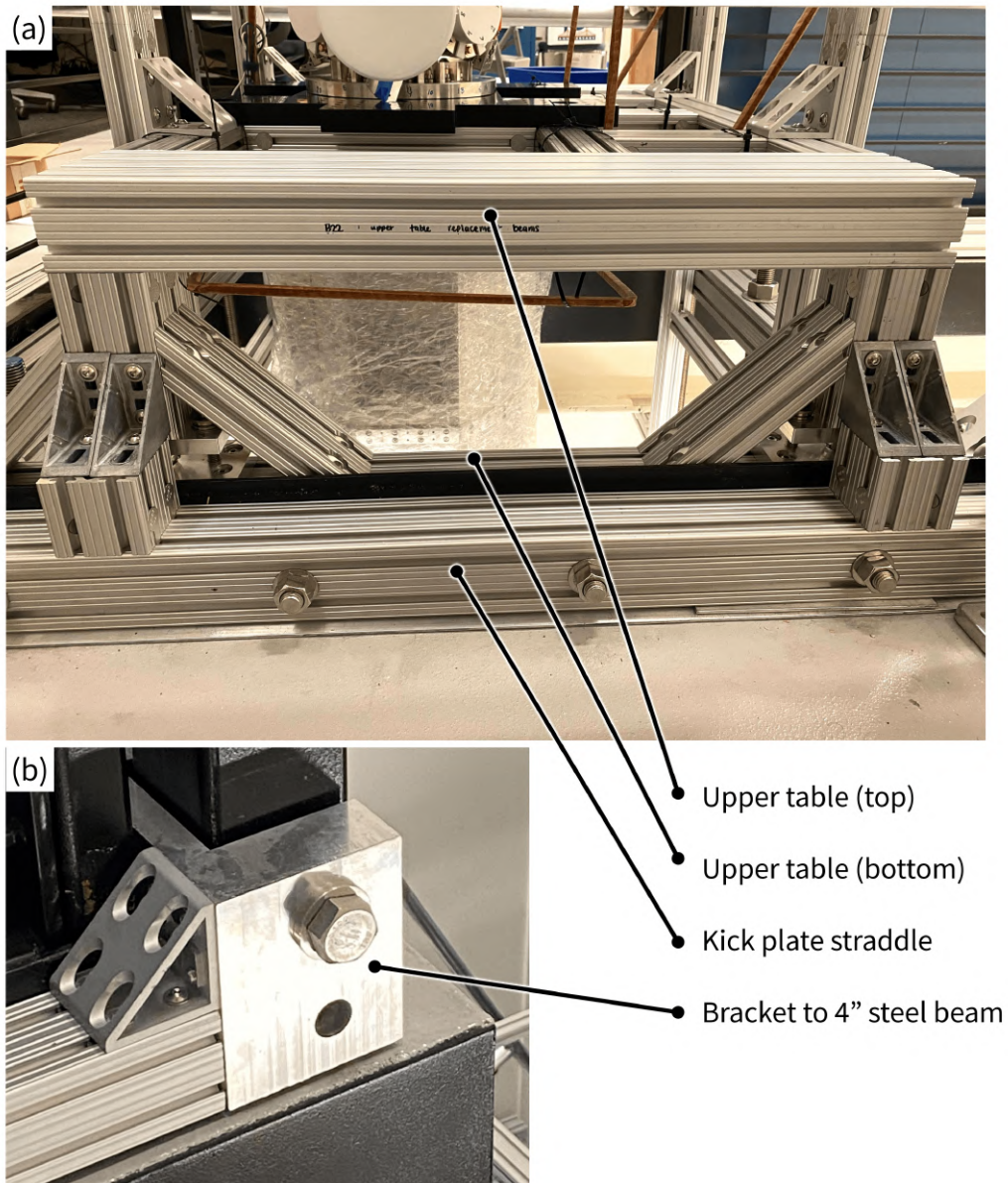


Figure 3.20: The upper table that supports the weight of the upper tube section. (a) The table is positioned in a U-shaped opening on the second floor and straddle the kick plates. The top and bottom parts of the table are separated by precision leveling feet, and connected through pulling screws and diagonal 80/20 beams. (b) The 80/20 beam on each side of bottom part interfaces with a hardened steel beam through a custom bracket.

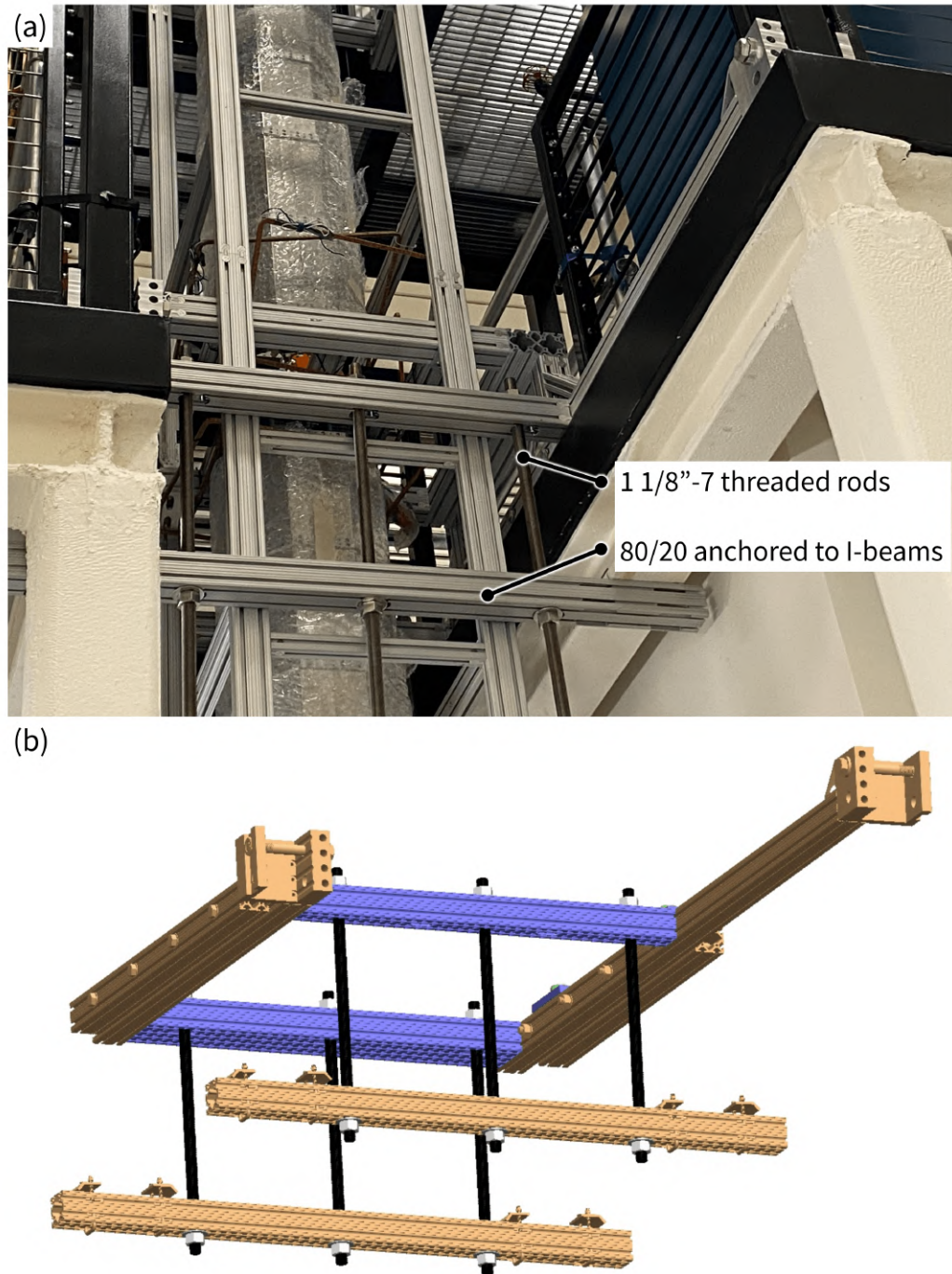


Figure 3.21: (a) The actual structure and (b) the CAD model of the bottom part of the upper table, clamped against the concrete floor by threaded rods that extend into 80/20 beams mounted to the I-beams.

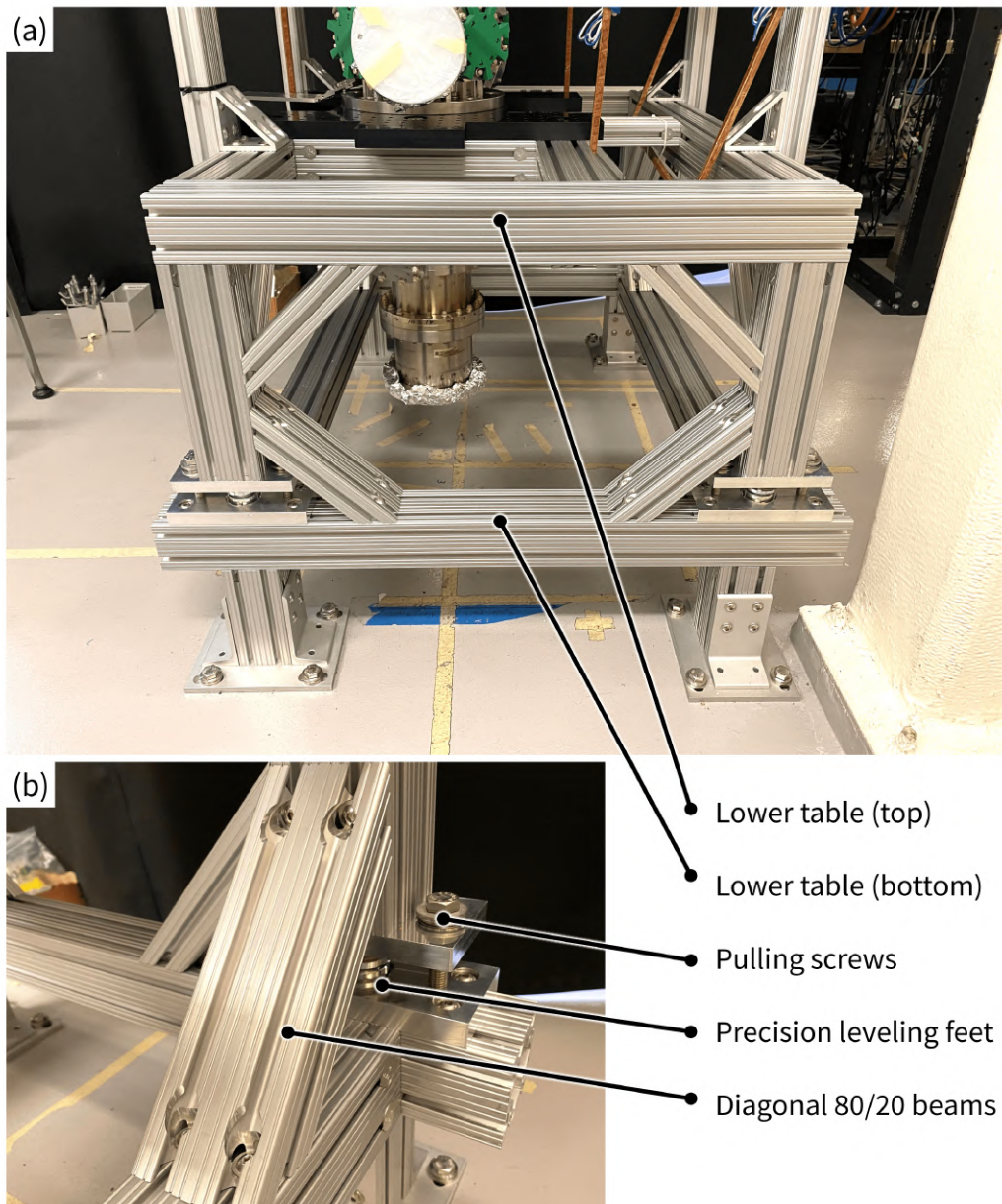


Figure 3.22: The lower table that supports the weight of the lower tube section. (a) Side view of the table, showing the top and the bottom parts. The two parts are separated by precision leveling feet, and connected through pulling screws and diagonal 80/20 beams. Panel (b) shows a zoom-in view of this connection.

MCF800-FlgAdptr-G2⁴¹ and is designed to have a minimal length, which reduces the region around the connection node that is not covered by the magnetic shield. The double crown forms a UHV seal with the bottom of the connection node and spreads the weight of the tower section to a custom 1" thick aluminum bracket, known as the "H-plate" due to its shape, mounted on top of the 80/20 table. Figure 3.23 shows the mechanical simulations to verify the structural rigidity of the double crown and the H-plate under the weight of the tower section. Despite its structural functionality, the H-plate is black anodized⁴² and patterned with a grid of 1/4–20 threaded holes to serve as an optical breadboard.

To decouple the two tower sections from thermal expansion and ease the alignment between them, edge-welded vacuum bellows were installed on top of both tower sections. Since the bellows do not take structural load, their flanges⁴³ cannot provide mechanical support to the top. Instead, we secure the top of the lower shield scaffolding to the upper table and the top of the upper shield scaffolding to additional 80/20 beams anchored to the mezzanine. These joints restrict the tilt of each tower section, significantly reducing the amount of torque exerted on the double crown and the H-plate. The 80/20 structure on the mezzanine also supports the weight of the horizontal interferometry beam delivery tube, as shown in Figure 3.24.

3.3.6 Lifting

The lab is equipped with a 10-ton overhead crane on a remotely movable I-beam. Unfortunately, the headroom of this crane is too large to lift the upper tower section to the desired height. To address this problem, a 1-ton low headroom chain hoist⁴⁴ shown in Figure 3.25 was installed on the same I-beam as the overhead crane and used for the lift. The two tower sections and their connection nodes were first horizontally connected and then vertically lifted as a single piece. To add stiffness to the tower during lift, a load-bearing 80/20 strongback shown in Figure 3.26 was built around each tower section and rigidly connected to the shield scaffolding.

Another purpose of the strongback is to guide the installation of the connection nodes. The in-vacuum optics scaffolding attached to the connection node extrudes out of the chamber by 18" on both sides and needs to be inserted into the tubes of the tower sections. Since the clearance between the mirror mounts on top of the in-vacuum optics scaffolding and the inner wall of the tube is only about 1 mm, during insertion it is crucial to keep the axis of the connection node aligned to the axis of the tower section to avoid accidental shock to the pre-aligned mirror mounts. We mounted the connection node on a separate 80/20 structure that can slide parallel to the strongback with the

⁴¹Namely, both sides has a copy of the feature found in the Kimball Physics adapter, but are offset with each other by 9°.

⁴²By a local service shop, Haro's Anodizing Specialist Inc.

⁴³Only the top flange of each bellows is accessible from outside the magnetic shield, which is the free end and should not be under strain.

⁴⁴CM Hurricane 360 HU1000 1-ton hand chain hoist with customized trolley to fit our thick I-beam.

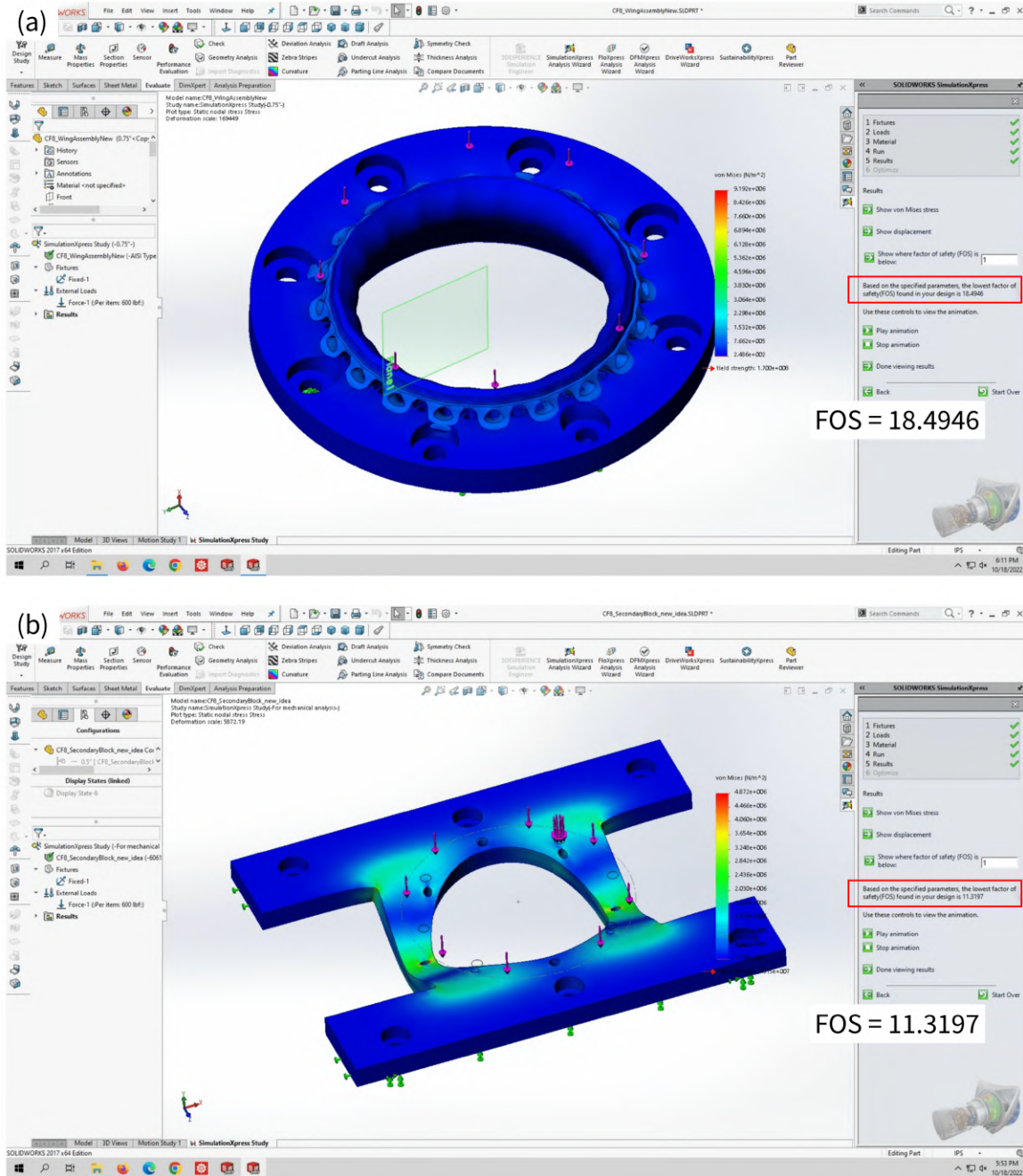


Figure 3.23: Solidworks simulation of the von Mises stress of (a) the double crown and (b) the H-plate under the weight of a tower section. The factors of safety (FOS) for both components exceed 10, allowing large enough safety margins. The maximum displacement of the double crown due to this load is 0.2 μm , and of the H-plate is 10 μm .

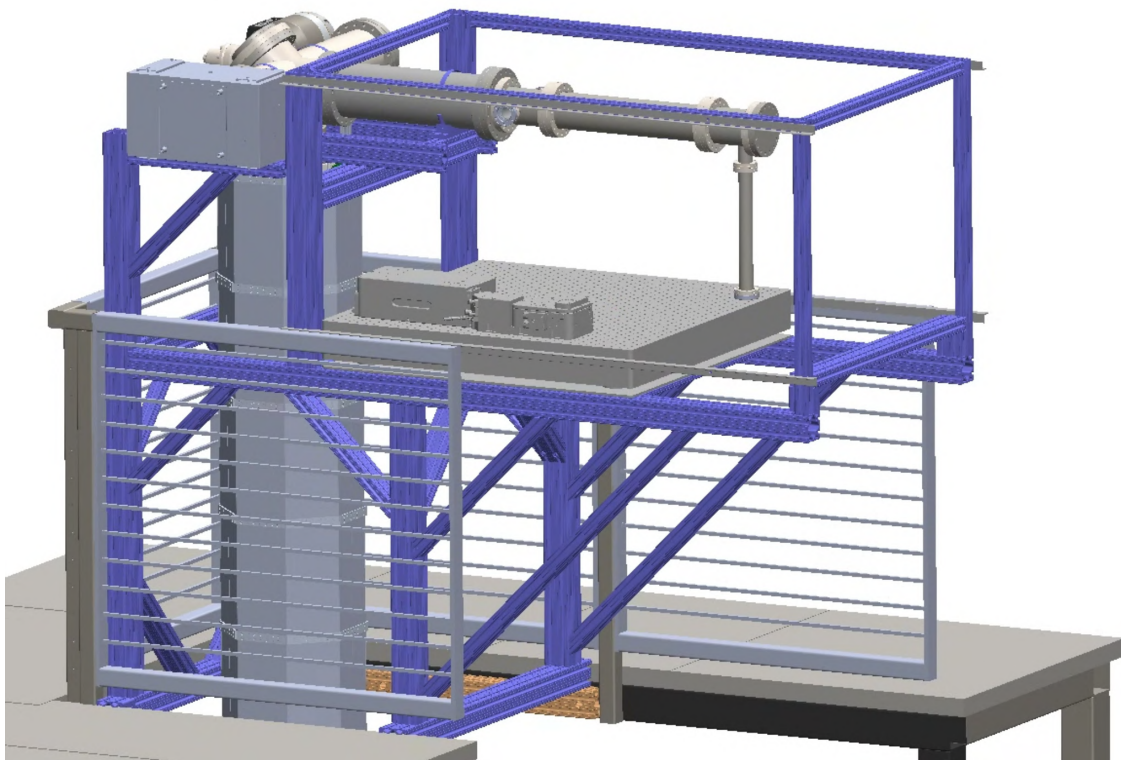


Figure 3.24: The 80/20 structure on the mezzanine, shown in blue, to which the top of the upper tower section is anchored. The horizontal interferometry beam delivery tube, the vacuum pumps, and the interferometry laser breadboard are also supported by this structure. All of the load is then transferred to a pair of two orange 80/20 beams (only one visible), which are fastened to 4" hardened steel beams shown in black color by 3/4"-10 fasteners through both beams. This allows a positive connection between the tower support and the structural components of the lab.

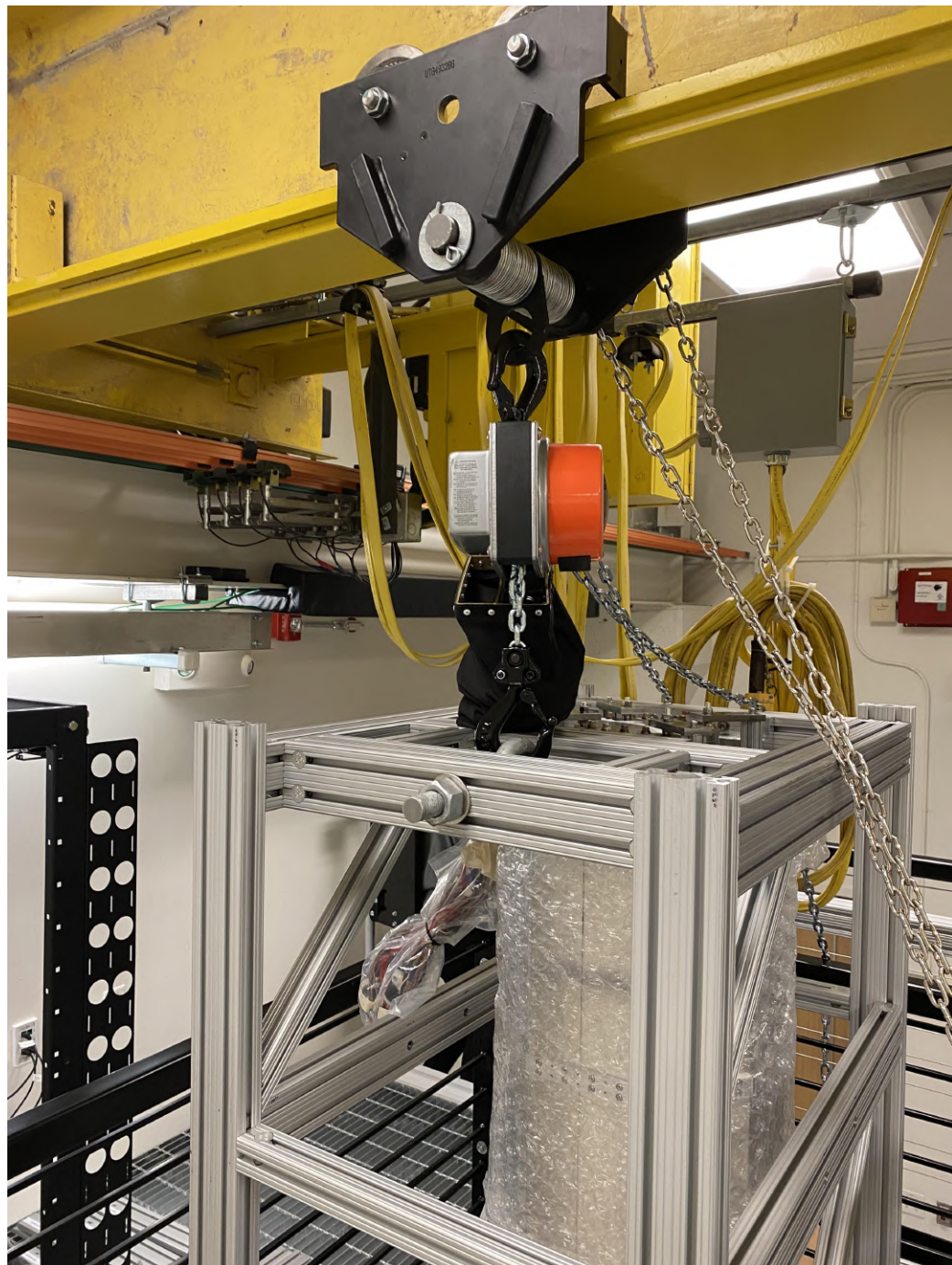


Figure 3.25: The 1-ton low headroom chain hoist that was used to lift the tower. It is mounted on a trolley which translates along the I-beam that the 10-ton crane is on.

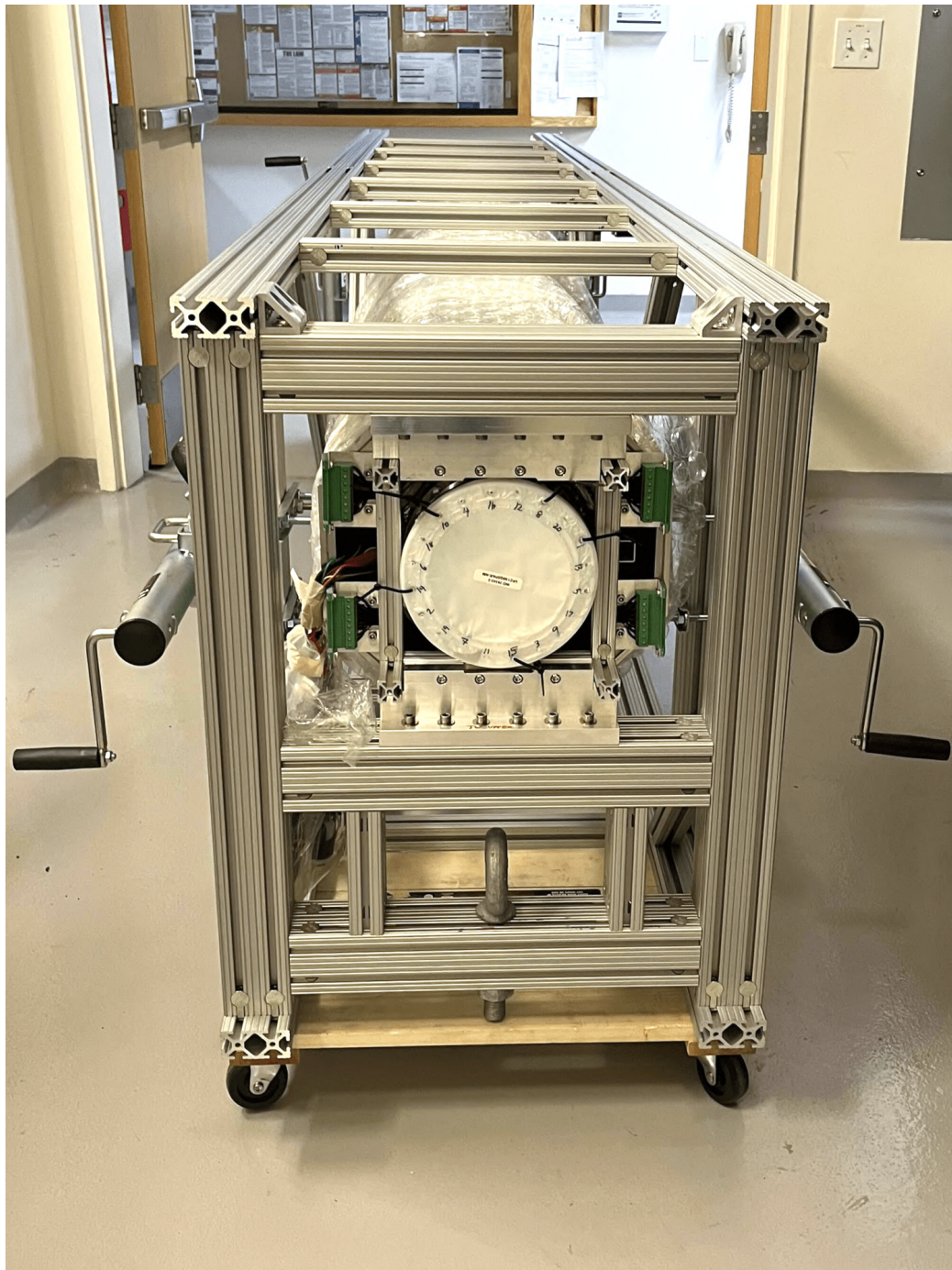


Figure 3.26: The upper tower section and its strongback. The strongback is equipped with four height-adjustable casters for mobility. However, we found that using a dolly to support the front allowed smoother movement.

help of sleeve bearings⁴⁵, which allowed us to vacuum connect each connection node to its respective tower section in the horizontal configuration. The details of this installation procedure are discussed in my labmate Megan Nantel’s dissertation [140].

After vacuum connection between the two tower sections, their strongbacks were connected to form a single rigid structure. This structure contained 80/20 beams that eventually transformed into the tables, and additional beams that provided structural rigidity during the lift, which were removed once the tower became vertical. An eye-hook was installed on the top of the strongback that acted as a lifting point for the vertical installation. Heavy-duty rubber wheels were attached to the bottom of the strongback, so that the tower could translate while being lifted.

Once the tower was lifted to the desired location shown in Figure 3.27, the tables were adjusted to match the height and mounted on pre-installed 80/20 beams anchored to the lab on both floors. With the part of the strongback disassembled, we then built the 80/20 structure on the mezzanine⁴⁶ and transferred the top of the tower from the chain hoist. Other parts of the interferometer, including the interferometry beam delivery tube on the top, the retro chamber on the bottom, and the atom sources on the side, will be added to the tower sections as subsequent assembly steps. The tower will then undergo a final round of bake-out and pump-down to reach the UHV required for interferometry.

3.4 Interferometry Laser Delivery

A clock atom gradiometer requires common laser pulses in alternating directions to address its component interferometers. As a result, interferometry pulses must be delivered vertically both upward and downward. The tower is designed so that the main entrance of the interferometry laser is at the top of the vacuum tube. The laser is then reflected by a mirror at the bottom of the vacuum system, known as the “retro mirror”. For narrowband interferometers, it is possible to utilize the velocity selectivity of the pulses to ensure that the atoms interact only with pulses traveling in one of the two directions. However, for broadband interferometers, upward and downward laser beams should not spatially overlap, in order to avoid light-atom interaction from pulses in the wrong direction. To achieve this, the tower includes a broadband interferometry laser delivery option, which uses a combination of the retro mirror at its extreme tilt angle and a specially designed retractable mirror to achieve spatial separation of interferometry pulses in the two directions.

3.4.1 Specifications for the Interferometry Laser

An ideal interferometer should be driven by laser pulses with frequency fixed on resonance in the rest frame of the atoms, uniform intensity across the atom cloud and at all heights, pure polarization with respect to the quantization axis given by the bias magnetic field, and pointing stability taking

⁴⁵80/20 6892 double-keyed UniBearing™ pads or equivalent products.

⁴⁶Some of this work requires operating in a rental scissor lift.

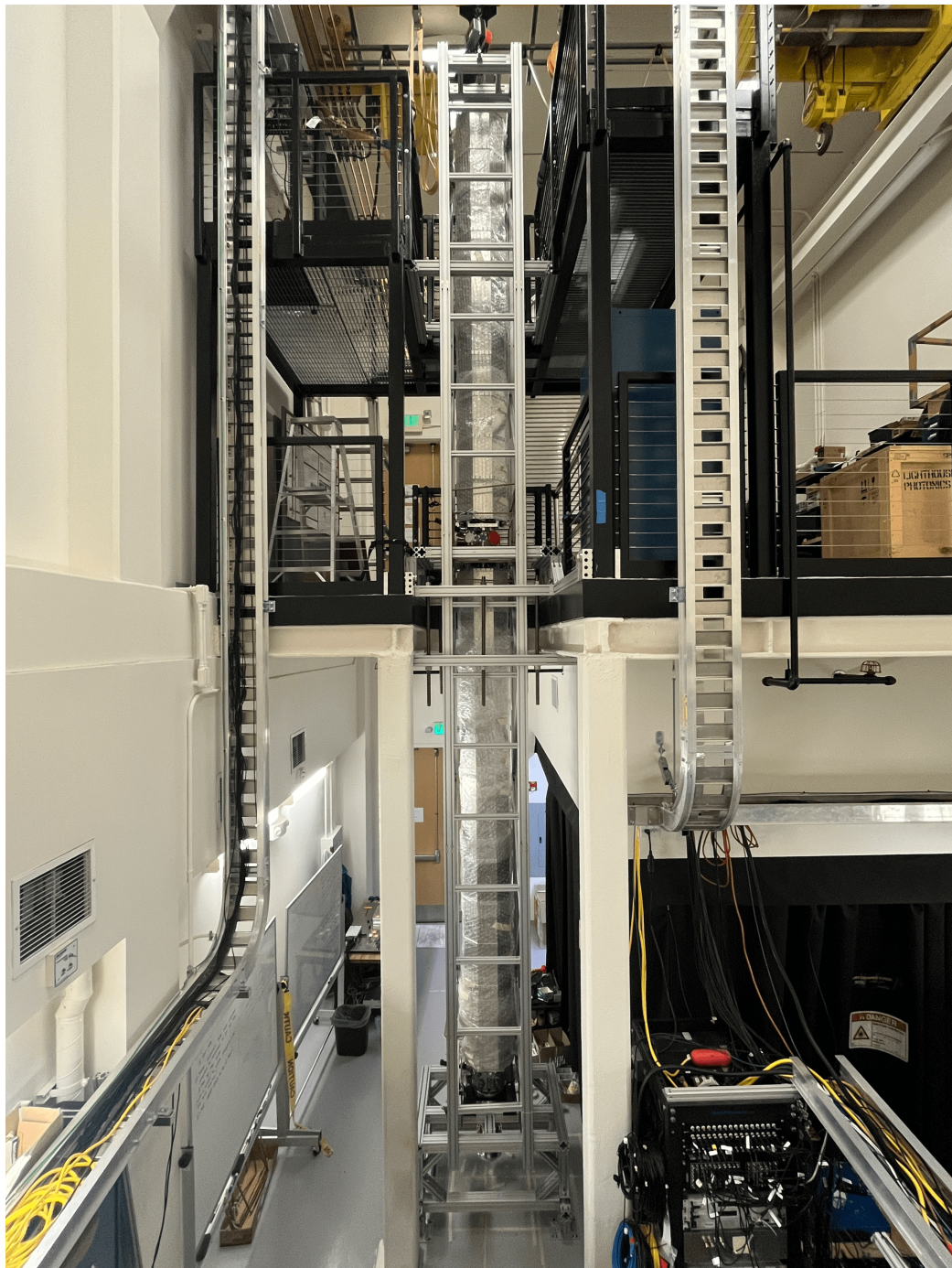


Figure 3.27: The tower lifted vertically and translated to the desired location. It was then attached to the pre-installed 80/20 beams after adjusting the height of the tables.

into account the non-inertial nature of the lab frame due to rotation of the Earth. In reality, none of these criterion can be achieved perfectly, and any associated noise will lead to phase error in the atom interferometer. Despite the fact that many of them can be canceled as common modes in a gradiometer configuration, any differential noise will be picked up along with the signal. Moreover, these noises generally lead to population loss in each interferometer, which constrains our ability to extract phase information from the atoms, thereby limiting the maximum number of pulses that can be applied.

All of the noise sources mentioned above have been studied during the development of the tower. Specifically, the laser frequency stability requirement is discussed in detail in Chapter 6. However, when designing the interferometer laser delivery system, we focus on addressing intensity homogeneity and pointing stability of the pulses.

The spatial mode of the laser beam must be tailored to achieve a uniform intensity across the beam over the entire atom cloud and at all heights along the atom trajectory. The simplest realistic mode that meets this requirement is a Gaussian beam with a properly selected waist radius, whose intensity as a function of radius r and distance z follows

$$I(r, z) = I_0 \left(\frac{w_0}{w(z)} \right)^2 \exp \left(-\frac{2r^2}{w(z)^2} \right) \quad (3.1)$$

where w_0 is the waist radius, and $w(z)$ is the (amplitude) “ $1/e$ -radius” at distance z . Near the axis, the intensity distribution across the beam thus follows

$$I(\delta r, z) \approx I_0 \left(\frac{w_0}{w(z)} \right)^2 \left(1 - \frac{2\delta r^2}{w(z)^2} \right) \quad (3.2)$$

with a small quadratic roll-off based on the ratio between radial position δr and $w(z)$. When δr is small enough that this quadratic term can be ignored, the intensity approximates a uniform distribution. On the other hand, the intensity on the axis depends on the distance through $w(z)$,

$$w(z) = w_0 \sqrt{1 + \left(\frac{z}{z_R} \right)^2} \quad (3.3)$$

where $z_R = \pi w_0^2 / \lambda$ is the Rayleigh range. Near the waist, the intensity distribution along the axis thus follows

$$I(0, \delta z) \approx I_0 \left(1 - \frac{\delta z^2}{z_R^2} \right) \quad (3.4)$$

Similar to the radial dependence, there is a small quadratic roll-off based on the ratio between axial position δz and z_R . When δz is small enough that this quadratic term can be ignored, the intensity again approximates a uniform distribution. The above analysis informs us that a suitable Gaussian mode must satisfy the following two constraints.

Uniformity Over Expanded Cloud

The waist w_0 must be chosen to be much larger than δr , interpreted as the width of the atom cloud. Assuming a cloud that is matter-wave lensed to $T = 10\text{ nK}$, over a launch of $h = 4\text{ m}$, thermal expansion leads to a final cloud size of

$$\delta r = \frac{1}{2} \times \sqrt{\frac{k_B T}{M}} \times 2\sqrt{\frac{2h}{g}} = 0.9\text{ mm} \quad (3.5)$$

where the factor 1/2 corresponds to collimating the cloud at the apogee instead of at launch. In order to fulfill $w_0 \gg \delta r$, a waist radius on the cm scale is necessary.

Uniformity Over the Baseline

Maintaining intensity uniformity along the length of the tower is important to keep the Rabi frequency identical for both interferometers and regardless of their height. This means

$$w_0^2 \gg \frac{L\lambda}{\pi} = 2.2\text{ mm}^2 \quad (3.6)$$

where $L = 10\text{ m}$. A cm-sized beam can easily achieve this requirement.

Although both uniformity constraints favor a large beam, the beam size cannot grow infinitely due to the following two practical reasons.

Practical Rabi Frequency

For the narrowband interferometer on the ${}^1\text{S}_0 - {}^3\text{P}_0$ transition in ${}^{87}\text{Sr}$, the Rabi frequency is

$$\Omega = \Gamma_{698} \sqrt{\frac{I(0,0)}{2I_{s,698}}} \quad (3.7)$$

$$= 2\pi \times 1.0\text{ kHz} \times \left(\frac{P_0}{1\text{ watt}}\right)^{1/2} \left(\frac{1\text{ cm}}{w_0}\right) \quad (3.8)$$

where the peak intensity $I(0,0)$ is used and relates to the total power via $P_0 = \pi w_0^2 I(0,0)/2$. The inverse relationship between w_0 and Ω favors a small beam. In practice, kHz-level Rabi frequency is required to achieve $10^3\hbar k$ in an interferometer whose free-fall time is limited by the tube section length to seconds. Therefore, a beam larger than cm-scale is undesirable unless significantly higher laser power becomes available.

Diffraction From In-Vacuum Components

Edge diffraction can cause interference fringes across the beam and limit the intensity uniformity. Near the axis of a Gaussian beam, in the presence of a sharp-edged circular aperture of radius a ,

the intensity distribution follows a complicated pattern [144],

$$I(\delta r, z) \approx I_0 \left(\frac{w_0}{w(z)} \right)^2 \times \left| 1 - e^{-i\pi N_f \delta_a} J_0 \left(\frac{2\pi N_f \delta r}{a} \right) \right|^2 \quad (3.9)$$

where $\delta_a \equiv e^{-a^2/w(z_a)^2} \approx e^{-a^2/w_0^2}$ and $N_f \equiv \frac{a^2}{(z-z_0)\lambda}$. In Equation (3.9) it is observed that the intensity ripples scale proportionally to δ_a , which decays rapidly as the aperture increases. It is therefore beneficial to design the in-vacuum components to leave as much clear aperture as possible. After taking into account all other geometry constraints, the limiting aperture in the vacuum system is at the mirror mounts on top of the launch lattice scaffolding with a radius of $1.72''$. In principle, Equation (3.9) states that 1% intensity ripple can be achieved by choosing a waist radius that is 43% of the aperture radius, yet we use a more conservative empirical number $w_0 < a/3$ to account for practical effects such as the nonconcentricity of the beam. This limits our maximum waist radius to 1.5 cm.

With all of the factors in mind, if a Gaussian mode is used, the optimal beam radius for the narrowband interferometry laser ranges from 1 cm to 1.5 cm. Beyond simple Gaussian beams, advanced mode engineering techniques can be applied to generate more complex spatial intensity distributions, such as super-Gaussian or top-hat beams [145–148]. Such beams often trade off axial uniformity for transverse uniformity, thus allowing smaller and more intense beams in experiments whose lengths are far from reaching the Rayleigh range of a Gaussian mode.

3.4.2 In-Vacuum Laser Delivery System

Despite of the benefits from intensity uniformity, a cm-sized laser beam requires more free propagation distance to “clean up” high-frequency Fourier components on the wavefront. This is because the intensity variation caused by a small wavefront modulation at spatial period Λ , after propagating for a distance z , scales as [144]

$$\delta I \propto e^{-2\theta^2(z/w_0)^2} \quad (3.10)$$

where $\theta = \lambda/\Lambda$ is the angle that the diffraction order propagates out of the beam. We expect that most of the wavefront distortion comes from air current and the viewport from which the laser enters the vacuum system. Therefore, it is beneficial to keep the beam small in these stages and allow a free propagation distance in vacuum, before using an in-vacuum telescope with high-quality surfaces to expand the beam to the target size. For this purpose, we designed a horizontal vacuum tube for beam delivery at the top of the tower, shown in Figure 3.28, which hosts a telescope of magnification 10, consisting of an off-the-shelf $1'' f_1 = +50$ mm lens⁴⁷ and a custom $4'' f_2 = +500$ mm lens⁴⁸. In addition, we placed a beam sampler in a small chamber with optical access in front of the telescope for diagnostic purposes.

⁴⁷Thorlabs AL2550G-A diffraction-limited N-BK7 aspheric lens.

⁴⁸Machined and coated by Changchun Bena Optical Products Co., Ltd.

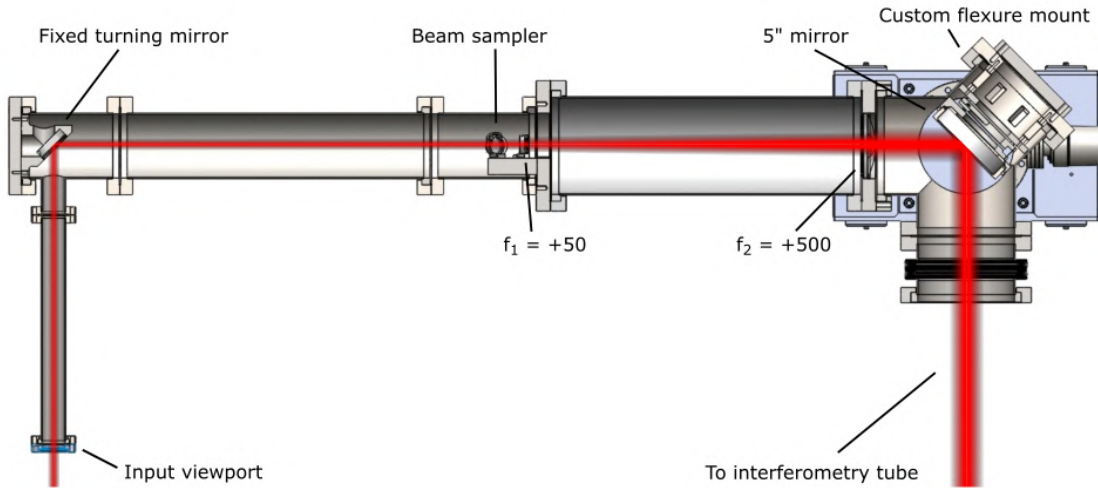


Figure 3.28: Cross section of the beam delivery tube. Laser beam enters the vacuum system through a downward-pointing CF 2.75" viewport, and is directed into a horizontal tube for mode cleaning. The beam is then expanded by a telescope of magnification 10. The second, custom made lens of the telescope is mounted in a flange adapter by a retaining ring on an SM4 threaded hole. The rim of the flange adapter has additional venting holes (not shown here but visible in Figure 3.29) to minimize conductance loss due to the lens. A final 5" mirror at 45° delivers the beam down to the interferometry tube. The flexure mount for this mirror is not accessible out of vacuum. It is designed for coarse alignment during installation and is permanently set fixed prior to the vacuum seal.

The expanded beam is then steered by a custom 5" 45° mirror⁴⁹ downward into the interferometry tube sections. The mirror is housed by a custom flexure-based kinematic mount attached to a five-way cross at the end of the beam delivery tube, as shown in Figure 3.29. The degrees of freedom on this mirror mount can only be adjusted during installation and are kept locked and inaccessible in operation. Any further adjustment to the beam alignment can be achieved by actuating the input light outside the vacuum system.

In addition to housing the 45° mirror, the five-way cross provides connection ports to a variety of vacuum pumps necessary to maintain the UHV environment of the tower. These include a 200 L/s ion pump⁵⁰, a titanium sublimation pump⁵¹, and a temporary turbo molecular pump for initial pump down.

⁴⁹Machined and coated by Changchun Bena Optical Products Co., Ltd.

⁵⁰Gamma Vacuum 200LCV8SSC1N TiTan ion pump.

⁵¹Gamma Vacuum G360819 three-filament TSP, in a tube section that is long enough to prevent sputtering onto the optics.

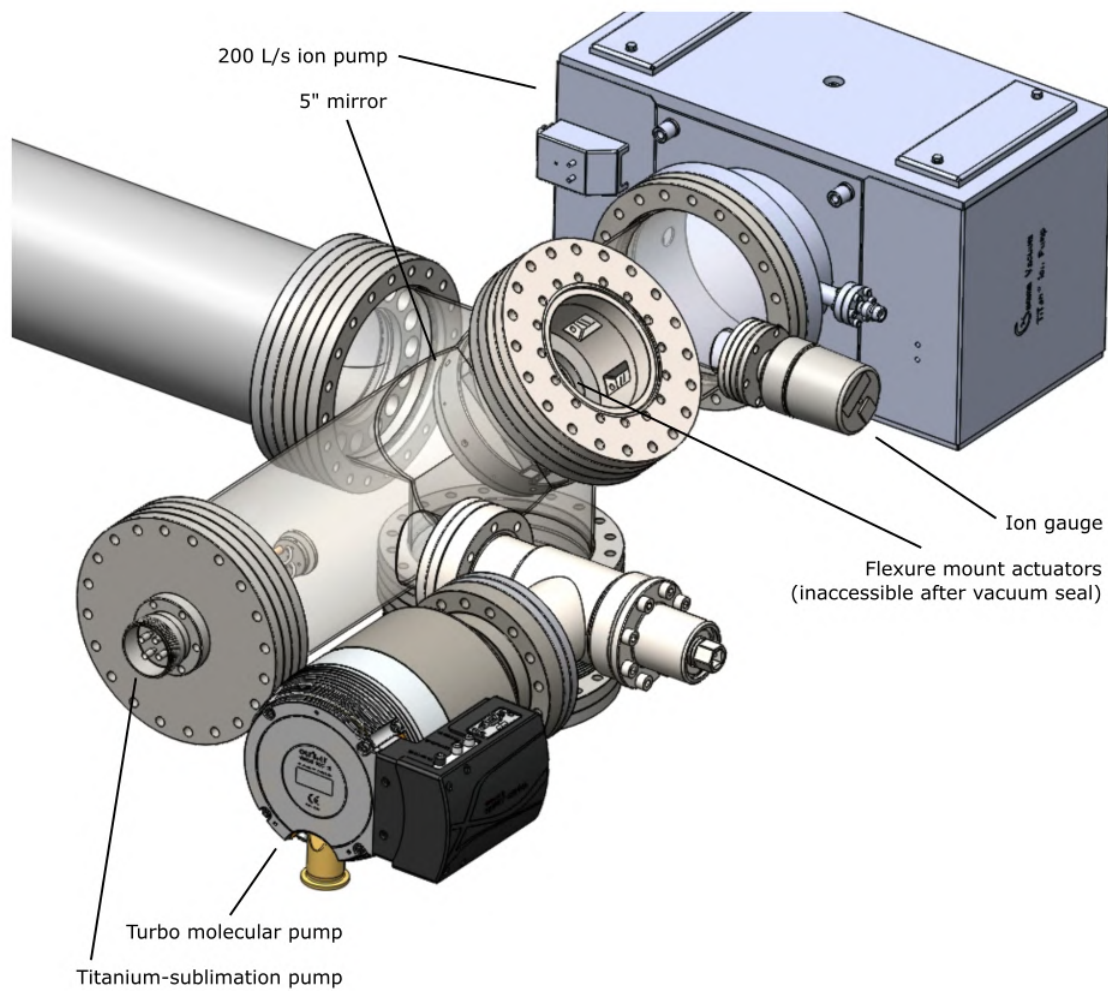


Figure 3.29: CAD model of the five-way cross, whose tube sections are made transparent to reveal the components inside. The main purpose of the five-way cross is to host the 5" 45° mirror as well as the vacuum pumps at the top of the tower.

3.4.3 Rotation Compensation System

In a long-baseline interferometer, the rotation of the Earth must be taken into account. As the non-inertial lab frame, along with the beam delivery optics, rotates with respect to the freely falling atomic frame, the atoms will not only move out of the center of the beam, but also accumulate a Coriolis phase shift [56, 120, 149]. In order to compensate for this effect, a general solution is to rotate one of the mirrors that delivers the interferometry laser in sequence to cancel the rotation of the beam with respect to the atoms by incorporating piezoelectric actuators. In a two-photon interferometer, it is possible to rotate the retro mirror to align k_{eff} of each pulse with gravity [120]. In a clock atom interferometer, however, rotating the retro mirror does not affect the direction of momentum transfer from the downward-propagating pulses, but only changes those of the upward-propagating pulses. In this scenario, the retro mirror must be tilted in a rate that aligns the average momentum transfer with gravity. Additionally, the retro mirror can be used to introduce a transverse phase variation across the atom cloud which enables phase-shear readout [61, 62].

The rotation compensation system in the tower shares the same design as the one planned for MAGIS-100. As shown in Figure 3.30, a custom 4" mirror⁵² is installed inside a stainless steel mirror mount, protected by a dust shutter that will stay closed during assembly and open during operation. This mirror is polished and coated not only on the top but also on the bottom surface, with the intention of performing an optical lever measurement of its angle with an auxiliary laser beam from the bottom. The signal from this measurement can be used to actively stabilize the mirror angle, which is adjusted by three flexure-based piezo actuators⁵³ below the mirror mount. The piezo actuators have a stroke of 82 μm and allow a maximum actuation angle of 1.3 mrad. This is sufficient even for the most extreme full-scale launch in MAGIS-100, which requires a compensation angle of 0.5 mrad. Coarse adjustment of the angle of the mirror with respect to gravity is achieved by three motorized linear actuators⁵⁴ outside the vacuum chamber that encloses the retro mirror. These actuators are mounted on stainless steel tabs welded to the vacuum chamber and push against three corners of a triangular base plate, which is mounted to the floor of the lab by 3/8"-16 concrete anchors⁵⁵. Due to the compressibility of the bellows above the retro chamber, an upward atmospheric load of 2.5 kN at the bottom of the chamber must be compensated. This is done by three spring-loaded fasteners on the same tabs that hold the linear actuators, each spring compressed to an extent that exerts about 1/3 of the force downward. Each tab is then pulled down with an additional fastener to lock the angle of the chamber and provide an extra safety measure in addition to the electromagnetic break in the linear actuators.

The retro chamber also hosts a 100 L/s non-evaporable getter pump⁵⁶ and an optional roughing

⁵²Since MAGIS-100 uses the same mirror, we made a batch procurement from Optimax.

⁵³Cedrat Technologies APA60SM-SG flexure-amplified piezoelectric actuator.

⁵⁴Oriental Motors DRSM60-05A4AZMK 60 mm compact linear actuator with encoder.

⁵⁵Grainger 15W079 female-threaded anchors.

⁵⁶SAES Getters Z100 sintered NEG cartridge.

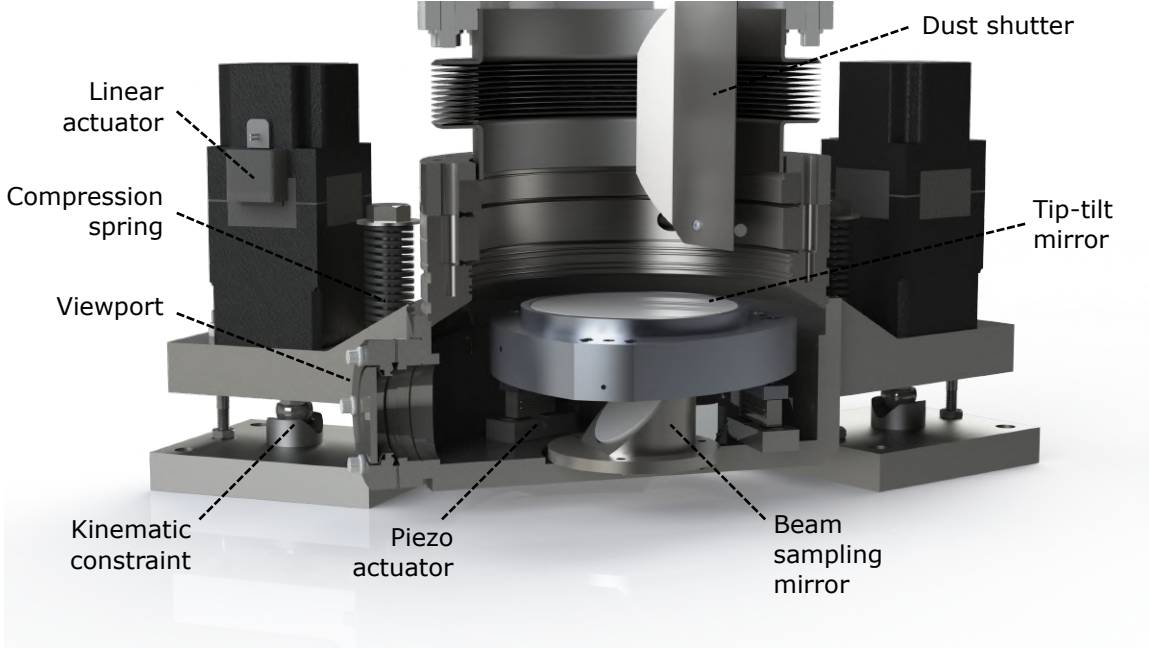


Figure 3.30: (Adapted from Ref. [43]) A cutaway view of the tip-tilt mirror system CAD model at the bottom of the tower. The mirror angle is controlled by three in-vacuum piezoelectric actuators, together allowing 1.3 mrad angle tuning range. The inclination of the vacuum chamber itself can be coarsely adjusted by several degrees using three motorized linear actuators mounted to the outside of the chamber. A set of three compression springs, one near each stepper motor, compensates for the force of atmospheric pressure on the chamber and pre-loads the linear actuators with positive axial force. An in-vacuum shutter flap is situated above the mirror to protect its surface from dust during initial bake-out. The mirror angle can be directly measured from the bottom using light reflected off the back surface of the mirror into a position sensitive detector, enabling closed-loop control.

port for vacuum purposes. Caution must be taken when baking the retro chamber, as its maximum temperature is limited by the piezoelectric stack to only 75°C.

3.4.4 Broadband Interferometry Option

For the broadband interferometry applications, such as operation on the ${}^1\text{S}_0 - {}^3\text{P}_1$ transition [35, 39], the upward and downward-propagating pulses must be spatially separated. To achieve this, we designed a custom four-way cross right above the retro chamber, which allows the entrance of the upward-propagating pulses as well as the exit of the downward-propagating pulses. This is achieved by a mirror on a retractable mount, in conjunction with the retro chamber set at its extreme tilt angle, as shown in Figure 3.31. When the interferometer is operated in broadband mode, the retractable mirror is set at the extended position using the linear actuator. The upward-propagating pulses enter from the viewport on the right side of the custom cross and are redirected downward

by the retractable mirror, slanted at an angle of 5.48° . This beam is then reflected straight upward by the retro mirror. In this way, the retro mirror can still be used to make Coriolis compensation to the upward-propagating pulses. To align the reflected beam with the tube axis, the retro chamber must be tilted by 2.74° , which is done by the external actuators on the three feet of the chamber. The angle and location of the retractable mirror are chosen to make sure that the beam is clear of obstructions along its path, one of them being the tip of the retractable mirror mount and the other imposed by the lower launch lattice scaffolding. The effective aperture is $0.92''$. When reversed, the beam path in Figure 3.31 allows the downward-propagating pulses to exit the vacuum tube.

In the narrowband mode, the linear actuator is fully retracted to move the retractable mirror out of the vertical tube section. This allows for the clearance of a larger interferometry beam. The retro chamber is also set horizontal to use the retro mirror at near 0° incidence.

3.5 Adaptations to MAGIS-100

As a prototype of MAGIS-100, the tower is intentionally designed so that many of its features can be transferred to a 100-meter interferometer, including, but not limited to, the following aspects.

Atom Source

MAGIS-100 will have three atom sources, each with a vacuum system similar to the existing ones for the tower. These atom sources are under design and will be assembled and tested at Stanford. In comparison with the existing ones, the new atom sources will be more compact and protected from the elements by a NEMA-rated enclosure. They will also include two 19" racks for electronics and a selection of lasers for cooling and trapping. The optical path will incorporate more remote diagnostic and adjustment capabilities.

Connection Node

Just like the tower, each atom source in MAGIS-100 will be attached to a connection node chamber. MAGIS-100 is expected to incorporate the atom shuttle, atom launch, state preparation, and atom detection schemes developed for the tower. Adaptations will be made to the MAGIS-100 connection node to enlarge the clear aperture through the launch lattice scaffolding and allow vertical installation to the tube sections.

Modular Tube Section

MAGIS-100 will be modularized into 17 identical sections. Despite the difference in length, each section will implement a bake-out system, an 80/20 shield scaffolding, an octagonal magnetic shield, and transverse bias coils in the same spirit as the tower, with modifications to address the axial

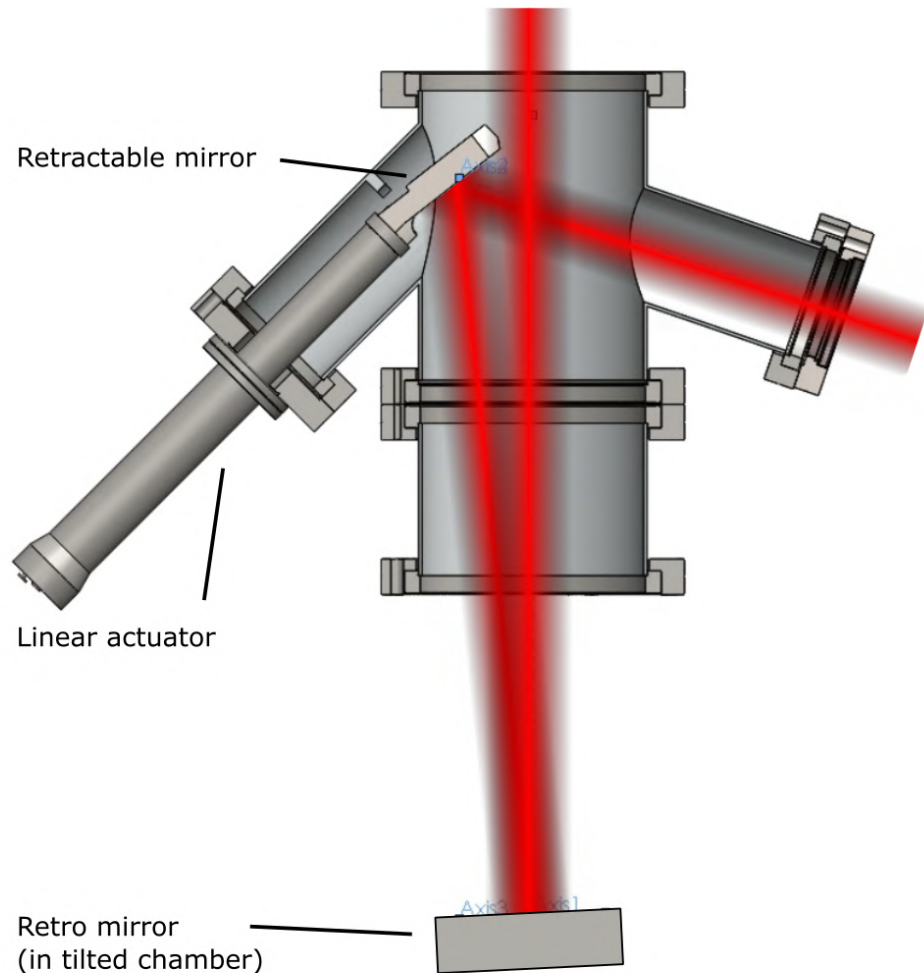


Figure 3.31: Cross section of the broadband bottom beam delivery tube, which is split into a custom four-way cross and a short straight tube, to enable installation around the launch lattice scaffolding that extrudes out of the lower connection node. Laser beam enters the vacuum system from the CF 4.50" viewport on the right and is redirected downwards to the retro mirror, which is set at an extreme angle of 2.74° by the external linear actuators on the retro chamber. The retro mirror then reflects the beam upwards. The beam size is limited by both the tip of the retractable mirror mount and the edge of a launch lattice mirror mount (not shown). We designed the geometry to achieve a balance between these two edges, and the resulting effective aperture is 0.92". When reversed, the beam path shows how the downward-propagating beam exit the vacuum tube.

alignment between the sections and the discontinuity of the magnetic shield at each section joint, where an additional chamber is planned for diagnostics and vacuum pumps. Furthermore, the rotisserie system developed for the tower can be applied directly to the MAGIS-100 sections, which will also be assembled and tested in the horizontal configuration.

Chapter 4

Magnetic Field System

This chapter summarizes the design and fabrication of the magnetic field system for the tower, which has been one of the biggest projects in my Ph.D. training. This system includes an octagonal mu-metal shield covering most of the interferometry tube to suppress ambient magnetic field, active coils configured in both transverse and longitudinal directions inside the magnetic shield to apply a uniform DC bias field, as well as compensation coil boxes at each end of the magnetic shield to suppress edge effects. The design parameters of the shield as well as the coils have been optimized by extensive finite element simulation, and are expected to meet the specifications for magnetic field noise in the 10-meter interferometer.

After the design has matured, we put in a lot of effort in the lab to build and characterize the magnetic field system. In this chapter, I will elaborate on the assembly of the magnetic shield and the bias coils. I will discuss not only the order of operation but also the lessons we learned the hard way during construction, which unfortunately forced us to assemble and disassemble the mu-metal shield multiple times. Through these iterations, we have developed several characterization techniques, which I will also discuss here. Since the magnetic field system for the tower is largely inherited by MAGIS-100, I hope that this chapter can also serve as a design and fabrication guidebook for the 100-meter interferometer. For this reason, towards the end of the chapter, I will describe a few adaptations of the magnetic field system to meet the requirements for MAGIS-100.

4.1 Magnetic Field Requirements

Ambient magnetic field leads to uncontrolled Zeeman energy shifts that reduce the performance of the interferometer. This problem is more severe in alkali interferometers, where the atom possesses a single valence electron [150, 151]. Such instruments must use magnetically insensitive $m = 0$ states to minimize the effect of magnetic forces on the atoms. However, even the second-order Zeeman energy shift in alkali atoms, on the order of kHz/G, requires magnetic field control below mG level

for optimal performance. The magnetic susceptibility of the transitions used in a strontium clock interferometer, on the other hand, is approximately 1000 times smaller, easing the requirements for magnetic shielding. To determine how well the magnetic field needs to be controlled inside the interferometer region, we consider the following magnetic effects:

Phase Shifts

To suppress the phase shift from linear Zeeman effect due to magnetic field noise, a clock atom interferometer operated on the ${}^1\text{S}_0 - {}^3\text{P}_0$ transition of ${}^{87}\text{Sr}$ can be arranged in the co-magnetometer configuration such that spin-polarized atoms in an equal mixture of $m_F = \pm 9/2$ are used [66]. The residual phase comes from the quadratic Zeeman effect, with a coefficient of $\delta_2 = -0.223 \text{ Hz/G}^2$ [76]. With a power spectral density δB for the time-varying magnetic field noise and a DC bias magnetic field B_0 , the interferometer accumulates a phase shift over an interrogation time T

$$\Delta\phi = 2\pi\delta_2 B_0 \delta B T \quad (4.1)$$

which we would like to control below $10^{-3} \text{ rad}/\sqrt{\text{Hz}}$. This poses a magnetic field noise specification

$$\delta B = 0.7 \text{ mG}/\sqrt{\text{Hz}} \times \left(\frac{\Delta\phi}{10^{-3} \text{ rad}/\sqrt{\text{Hz}}} \right) \left(\frac{1 \text{ G}}{B_0} \right) \left(\frac{1 \text{ s}}{T} \right) \quad (4.2)$$

thus an RMS amplitude on mG level assuming an integration time of 1 s. Similarly, in the presence of a magnetic field gradient along the vertical axis \hat{z} , the phase shift of an $n\hbar k$ interferometer is

$$\Delta\phi = 2\pi\delta_2 B_0 \frac{\partial B}{\partial z} \frac{n\hbar k}{m} T^2 \quad (4.3)$$

The magnetic field gradient requirement is

$$\frac{\partial B}{\partial z} = 1 \text{ mG/m} \times \left(\frac{\Delta\phi}{10^{-3} \text{ rad}/\sqrt{\text{Hz}}} \right) \left(\frac{100}{n} \right) \left(\frac{1 \text{ G}}{B_0} \right) \left(\frac{1 \text{ s}}{T} \right)^2 \quad (4.4)$$

Energy Shifts

Although linear Zeeman effect does not cause a phase shift in the co-magnetometer configuration, it can reduce pulse efficiency by making the hyperfine states out of resonance. The differential linear Zeeman coefficient for the ${}^1\text{S}_0 - {}^3\text{P}_0$ transition of ${}^{87}\text{Sr}$ is $\delta_1 = 109 \text{ Hz/G}$, causing an energy shift

$$\delta\nu = m_F \delta_1 \langle \delta B \rangle \quad (4.5)$$

where $\langle \delta B \rangle$ denotes the RMS amplitude of magnetic field noise. This energy shift needs to be controlled below the laser linewidth $\Delta\nu$, which we assume to be about 10 Hz as is justified in

Chapter 6. Taking $m_F = 9/2$,

$$\langle \delta B \rangle = 20 \text{ mG} \times \left(\frac{\Delta\nu}{10 \text{ Hz}} \right) \quad (4.6)$$

Assuming this magnetic field noise comes from a linear gradient along the entire 10-meter interferometer, this sets a gradient specification of 2 mG/m.

Atom Loss

The magnetic field noise also perturbs the quantization axis of the atoms set by the DC bias field. This leads to a projection error that degrades the pulse efficiency. The leading order of population loss in a π -pulse is given by

$$\delta P = \frac{3\pi^2}{32} \frac{\langle \delta B \rangle}{B_0} \quad (4.7)$$

which sets a magnetic field specification

$$\langle \delta B \rangle = 1 \text{ mG} \times \left(\frac{B_0}{1 \text{ G}} \right) \left(\frac{\delta P}{10^{-3}} \right) \quad (4.8)$$

In conclusion, the magnetic field system is expected to suppress spurious magnetic field to mG, and the gradient to mG/m level. This requires the mu-metal shield to suppress the ambient magnetic field by a few hundred fold. The bias coils should be capable of producing gauss-level DC magnetic field at the same level of homogeneity.

4.2 Magnetic Shield

The magnetic shield specifications mentioned above are undemanding compared to an interferometer with alkali atoms, where multiple layers of magnetic shield are usually required [150–152]. For our experiment, a single-layer mu-metal shield with proper geometry can provide the necessary ambient field suppression. However, the large aspect ratio of the interferometry region poses challenges to shield performance. To address these issues, I was inspired by the Hanover group [152] and designed a novel magnetic shield with an octagonal cross section consisting of multiple mu-metal pieces, which are fastened together in an arrangement that maximally reduces field penetration. In this section, I will discuss the design choices and the assembly procedure of this magnetic shield.

4.2.1 Mu-Metal Properties

Our mu-metal shield components were ordered from Magnetic Shield Corporation¹. This material is a soft nickel-iron unoriented ferromagnetic alloy with very high permeability in low-intensity magnetizing fields, shown in Figure 4.1, with an effective shielding bandwidth of 100 kHz [153]. To

¹MuMETAL magnetic shielding alloy (mu-metal grade ASTM A753 Alloy 4, UNS N14080, 80NiFe).

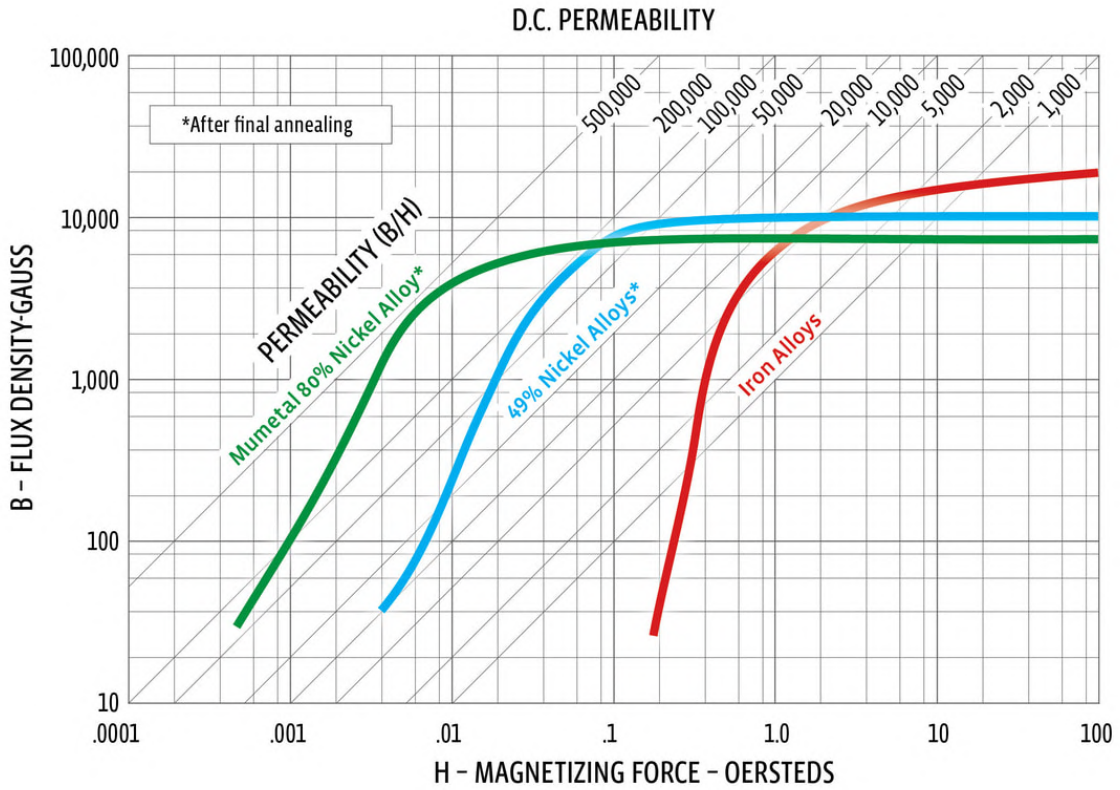


Figure 4.1: (Adapted from Ref. [154]) B - H curve of the mu-metal alloy from Magnetic Shield Corporation. This material saturates at a low magnetic flux density of around 8000 G.

reach maximum permeability, the alloy went through dry hydrogen annealing as the last step of treatment, and it must be treated carefully as any shock or deformation may affect its shielding performance. As required by the manufacturer, all shield components have 0.5" holes at one end to interface with jigs in the annealing furnace. These holes are designed to be at the ends of the magnetic shield after assembly to minimize the effect of lack of material.

4.2.2 Challenges from a Large Aspect Ratio

In the tower, the interferometry tube is segmented into two modular sections, whose lengths measure 129.4" and 155.8" (from flange to flange, not including the bellows), respectively. The lengths of the magnetic shield sections are $L_{\text{upper}} = 127.5"$ and $L_{\text{lower}} = 153"$, slightly less than those of the modular sections to allow tool access to the flanges. As mentioned in Section 3.3.3, each section is enclosed in an aluminum frame with a 10" \times 10" cross section. The diagonal of this frame sets the diameter of the magnetic shield to $D \approx 15"$. The length-to-diameter ratios of the magnetic shield sections are thus much larger than one.

This large aspect ratio poses challenges to the performance of longitudinal shielding, as indicated by the simulation of a capless cylindrical shield in the presence of a longitudinal background field in Figure 4.2, where the residual flux density B_{res} increases with the length of the shield L beyond the meter scale (that is, aspect ratio $L/D > 3$). The simulation is done with FEMM, an open-source electromagnetic simulation software², interfaced with Mathematica.

It is helpful to understand the problem by considering the limit of an infinitely long cylindrical shield along the \hat{z} direction, subject to a uniform incident magnetic field $\mathbf{H} = H_0 \hat{z}$. Mirror, translational, and rotational symmetry require that the field intensity everywhere does not have a $\hat{\phi}$ component or a gradient along the \hat{z} and $\hat{\phi}$ directions, namely

$$H_\phi(z, \rho, \phi) = 0 \quad (4.9)$$

$$\partial_z H_z = \partial_z H_\rho = 0 \quad (4.10)$$

$$\partial_\phi H_z = \partial_\phi H_\rho = 0 \quad (4.11)$$

In combination with the Maxwell's equations, we further obtain

$$\partial_\rho H_z = 0 \quad (4.12)$$

$$\partial_\rho(\rho H_\rho) = 0 \quad (4.13)$$

Therefore, the field intensity in or out of the shield, or inside the mu-metal itself, can only have a \hat{z} component³, which is independent of the position, and must equal H_0 due to the magnetic boundary condition for parallel field components. This means that an infinitely long mu-metal tube does not provide any shielding along the longitudinal direction. The longitudinal shielding performance of a finite shield deteriorates towards this infinite limit as the length increases. In contrast, shielding in the transverse direction is easily achieved at mG level, as shown in Figure 4.3.

We also notice from Figure 4.2 that the maximal magnetic flux intensity inside mu-metal increases with the length of the shield. Above a certain length $L_{\text{sat}} \sim 15$ m, the shield becomes saturated and the permeability quickly drops from the optimal value. Although not taken into account in the simulation, it is expected that saturation further decreases shielding performance in both longitudinal and transverse directions. Fortunately, the shielded region of the tower is shorter than L_{sat} , and the mu-metal is expected to stay in the linear regime of the B - H curve. However, this statement is not true for MAGIS-100, where the interaction between multiple sections concentrates flux intensity inside the shield, especially when “couplers” are introduced to bridge the gaps between neighboring sections, as discussed in detail in Section 4.5.2. This shield saturation problem, which is intrinsic

²Finite Element Method Magnetics: <https://www.femm.info/wiki/HomePage>. FEMM can be interfaced with Mathematica through a package called MathFEMM. See <https://www.femm.info/wiki/mathfemm>. It only supports 2D simulation, so the problem must have a certain symmetry.

³Although the general solution to Equation (4.13) is $H_\rho = C/\rho$, the field must not diverge at $\rho = 0$, therefore $C = 0$.

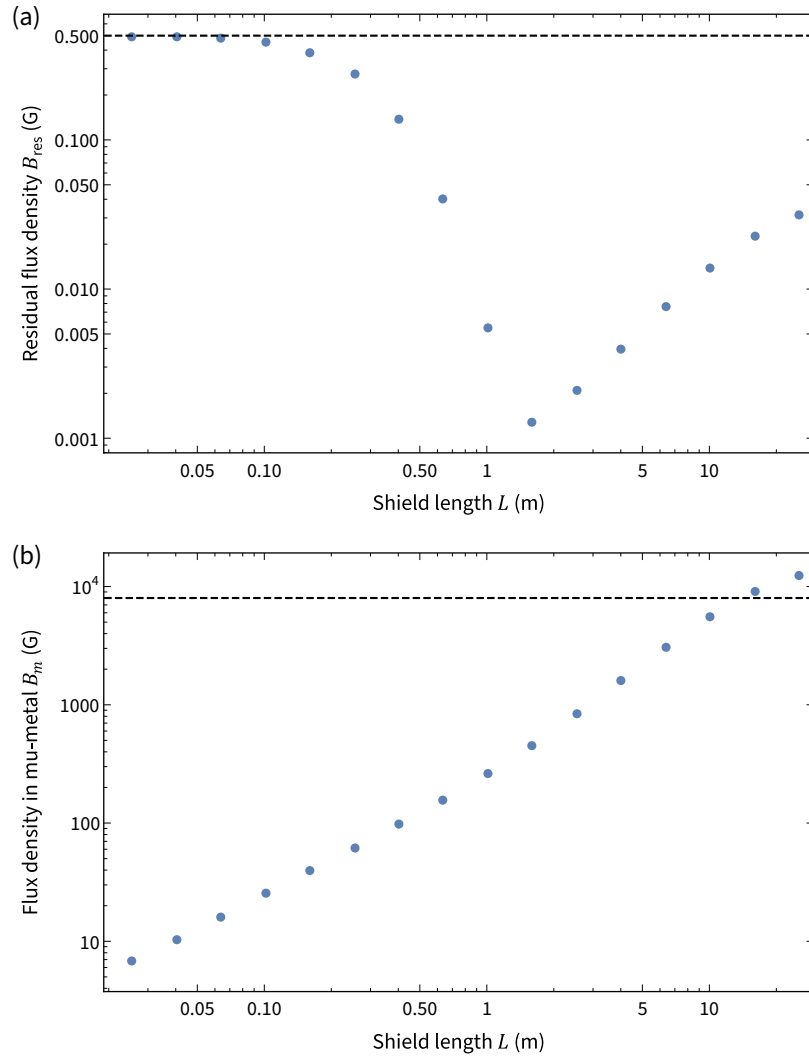


Figure 4.2: Simulation of a capless cylindrical shield in the presence of a longitudinal external magnetic field $B_0 = 0.5$ G. The radius of the shield is fixed at 7.5'', and the thickness is 0.080'', both matching the values used for the tower. The length of the shield L is varied to analyze the shielding performance as the aspect ratio is increased. The permeability of mu-metal is taken to be 4×10^5 according to Figure 4.1. For simplicity, a linear B - H relationship is used, which will break down when the magnetic flux density inside mu-metal exceeds the saturation threshold of around 8000 G. (a) Residual flux density B_{res} at the center of the shield as a function of L . The longitudinal shielding is not effective when $L \ll D$ or $L \gg D$. In the first scenario, there is significant field penetration from the two opening ends. In the second scenario, the shield approaches the infinite-length limit and cannot shield well longitudinally. The black dashed line refers to the background field. (b) The flux density inside mu-metal. Beyond the saturation threshold indicated by the black dashed line at 8000 G, the linear B - H relationship is no longer valid and the simulation assumption breaks down. For the parameters used here, this happens at $L_{\text{sat}} \sim 15$ m. Further increasing the length deteriorates shielding performance due to a decrease of permeability.

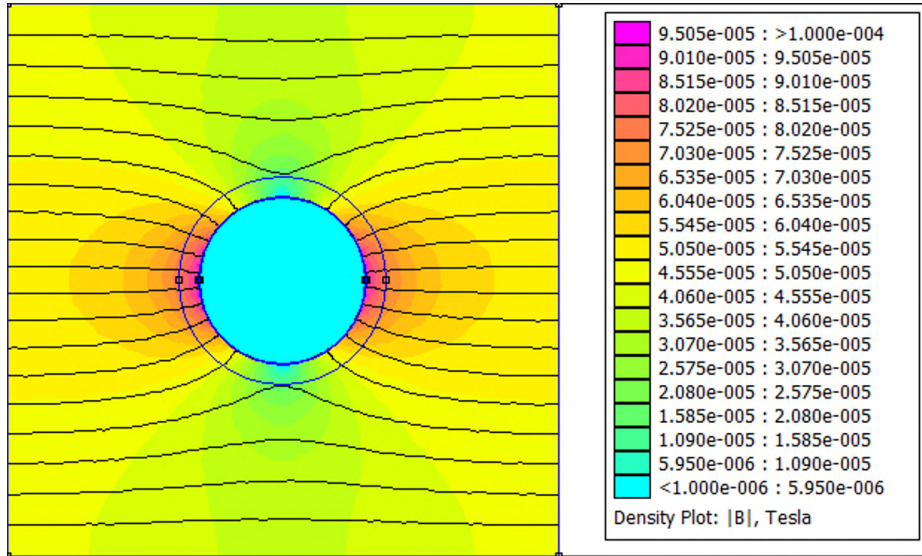


Figure 4.3: Simulation of an infinitely long cylindrical shield in the presence of a transverse external magnetic field $B_0 = 0.5$ G. The radius of the shield is 7.5" and the thickness is 0.080", both matching the values used for the tower. The permeability of mu-metal is taken to be 4×10^5 according to Figure 4.1. A residual field of 0.2 mG is achieved at the center of the shield, with a variation of 10^{-5} within a radius of 0.5". The outer blue circle is the boundary of a fine-meshed region in the simulation domain and does not correspond to any physical object.

to the extreme aspect ratio of MAGIS-100, is resolved by placing active coils periodically along the length. Details of this active coil system are also discussed in the same section.

Another difficulty of a long shield section arises due to the constraint of the available furnaces. Typical mu-metal manufacturers' annealing furnaces are limited to ~ 3 m tall, so it is impossible to cover the entire shield section with a monolithic mu-metal tube. Therefore, the magnetic shield has to be concatenated by multiple shorter mu-metal pieces. This leaves inevitable gaps at the joints, where field leakage can occur. From previous experience [151], it is challenging to control field leakage to below mG levels, especially without an inner layer of the shield. Therefore, we performed a careful analysis of the joints and engineered a method to stack the mu-metal pieces that minimized the effects of the joints, as discussed in Section 4.2.3.

4.2.3 Magnetic Shield Geometry

The gaps between mu-metal pieces are known to cause field leakage in a cylindrical cross-sectional shield due to the imperfect match in local curvature between two adjacent curved surfaces [151]. To avoid this problem, people have attempted shield geometry with flat faces, such as octagonal cross section, and achieved nT-level shielding with two layers of mu-metal separated by a macroscopic

radial distance [152]. This geometry has the additional advantage of easy interfacing with an underlying support structure. This knowledge from the community motivates us to pursue an octagonal cross-sectional shield. With the reduced magnetic sensitivity of our choice of atomic species, we determined that a single-layer magnetic shield with a wall thickness of $0.080"$ is sufficient to achieve the shielding specifications described in Section 4.1.

Since the length of the mu-metal pieces provided by the manufacturer is limited to $120"$, on each side of the octagon there have to be at least two mu-metal pieces connected end-to-end along the longitudinal direction. To minimize the number of joints, it is optimal to span each side by exactly two pieces, which creates one seam per side, where a gap inevitably appears due to machining tolerance. To reduce field leakage, the seams on neighboring sides are offset from each other by alternating the direction of the two mu-metal pieces with different lengths. Furthermore, additional mu-metal pieces are stacked on top to cover these seams. In fact, it is beneficial to stack multiple sheets of mu-metal to ensure sufficient coverage of all the joints. Following this spirit, we invented a novel way to construct an octagonal shield section with 64 mu-metal pieces of $0.020"$ thickness, arranged in four radially stacked sheets to form an effective single-layer shield of $0.080"$ thickness. The lengths of these pieces are carefully chosen so that

- Neighboring seams in the same octagonal sheet are offset by a macroscopic amount.
- Each seam in any sheet joint is always covered by the other three sheets stacked above or below it.
- The shield pieces only have a limited number of length variations to reduce the types of parts.
- The lengths are commensurate to allow periodic fastening to a support structure.

which when assembled creates a “staggered” structure in the longitudinal direction illustrated by Figure 4.4. Additionally, note that we allow the shield pieces to be flat or bent at 135° so that they can be placed along a face or an edge. We choose bent pieces for the innermost and outermost sheets and flat pieces for the two center sheets for the following considerations. First, by doing so, each radial gap is covered by two mu-metal sheets, which can be viewed as an analogy of the staggered geometry in the transverse direction, as shown in Figure 4.5. Second, having the bent pieces on the inner and outer surfaces increases the structural rigidity of the entire shield assembly. Table 4.1 enumerates all mu-metal pieces for the upper and lower shield sections.

We performed extensive finite element simulations to validate this shield geometry and study how the implementation of the staggered geometry affects the shielding performance in both longitudinal and transverse directions. For the longitudinal simulation in Figure 4.6, we have assumed a gap size of $0.025"$ in the joints and a sheet-to-sheet spacing of $0.010"$ due to ripples along the mu-metal surface. These are pessimistic estimates of the actual shield and are set so that the meshing is

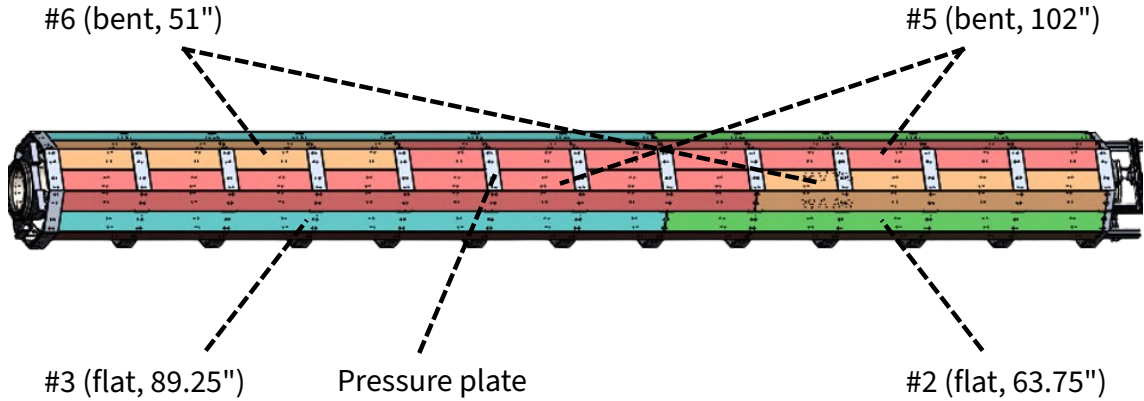


Figure 4.4: Longitudinal structure of the magnetic shield, showing the staggered pattern of the lower shield section. Although four sheets of mu-metal are clamped together on each side of the octagon, this figure only exposes the outermost sheet and the sheet below it. The outermost sheet contains two types of bent pieces with alternating directions on each side, indicated by red and orange. The next sheet contains two types of flat pieces with alternating directions on each side, indicated by blue and green. Underneath these two sheets, there is another sheet of flat pieces and then a sheet of bent pieces. This arrangement reduces the magnetic field leakage at the mu-metal joints [152], and the choice of lengths allows the four sheets to be periodically clamped to each other and to an underlying support structure. The labels of the mu-metal pieces match those in Table 4.1.

Table 4.1: All mu-metal pieces in the upper and lower shield sections to enable the staggered geometry.

No.	Matching No.	Length	Type	Section	Qty
1	3	38.25"	Flat	Upper only	16
2	3	63.75"	Flat	Lower only	16
3	1 and 2	89.25"	Flat	Upper and Lower	32
4	6	76.5"	Bent	Upper only	16
5	6	102"	Bent	Lower only	16
6	4 and 5	51"	Bent	Upper and Lower	32

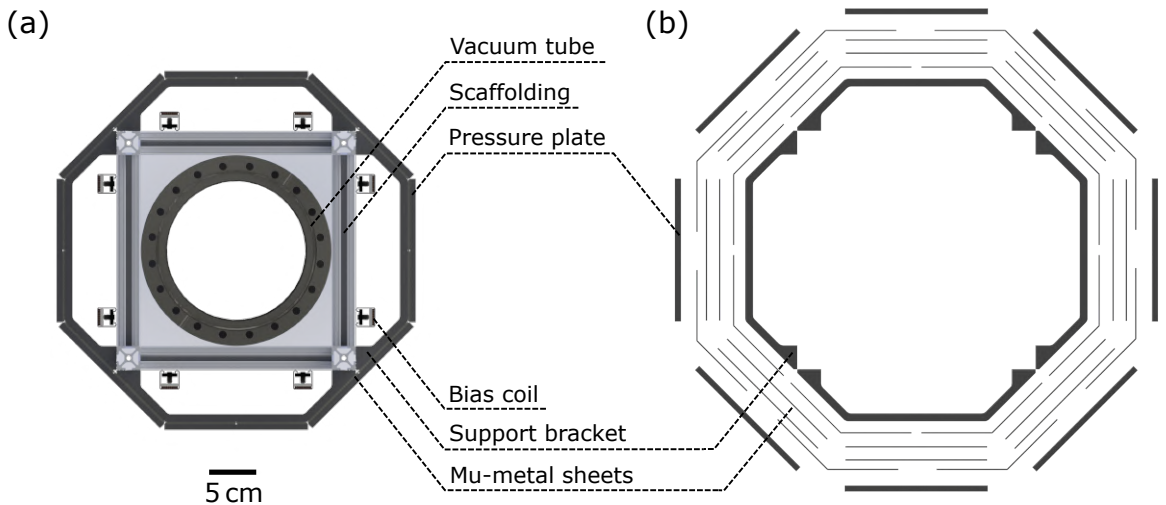


Figure 4.5: (Adapted from Ref. [43]) Transverse cross section of the magnetic shield and its support structure. (a) Cross-sectional view of the interferometer vacuum pipe and surrounding magnetic shield. The octagonal magnetic shield is supported internally by a square cross-section aluminum shield scaffolding that surrounds the vacuum pipe. A set of support brackets are attached periodically to this shield scaffolding, serving as octagonal ribs for the shield. The shield sheet metal plates attach to these ribs, and pressure plates are applied from the outside to clamp the multiple sheet metal layers together. Eight vertical bias coil bars, elaborated in Section 4.3.1, provide a uniform transverse magnetic field in the center of the vacuum pipe. (b) Exploded view of the magnetic shield assembly. On each face of the octagon, four sheets of mu-metal are clamped together, with sheets on the corners and on the faces arranged to cover all radial gaps.

affordable on a regular laptop computer. For the transverse simulation in Figure 4.7, the sheet-to-sheet spacing is still 0.010", but the gap size is increased to 0.1" to match the realistic errors⁴. With these assumptions, we have observed a reduction of field leakage of 100× in the longitudinally staggered shield and around 60× in the radially staggered shield.

To mechanically support the staggered shield pieces, we have designed an octagonal shield scaffolding that connects to the vacuum tube through an 80/20 frame with square cross section⁵. This shield scaffolding contains periodic “ribs” shown in Figure 4.8, which are batch-machined custom aluminum brackets that form a quarter of an octagon. Each rib contains 16 threaded holes (8-32) arranged in two rows, which are used to fasten the shield pieces. The longitudinal spacing between two ribs is 12.75"⁶, which is consistent with the typical fastener spacing in mu-rooms according to the manufacturer⁷. The exact distance between the ribs is determined so that the lengths of both the upper and the lower shield contain an integer number of rib spacings. We stack four mu-metal sheets as a single layer of the shield and clamp them against the ribs by custom aluminum plates known as the “pressure plates”. The choice of length for each mu-metal sheet summarized in Table 4.1 ensures that each seam between two adjacent sheets is always covered by a pressure plate to secure the joint.

4.2.4 Magnetic Shield Assembly

Due to the unexpected magnetization of the stainless steel chambers discussed in Section 4.4.2, the magnetic shield was put together and taken apart multiple times. Although this unfortunately delayed the construction of the tower, during the > 5 iterations of the magnetic shield assembly, we developed an efficient procedure which can easily be transferred to MAGIS-100.

1. With the vacuum tube on the rotisserie, build the 80/20 shield scaffolding and attach the ribs. A tape measure or equivalent measurement tool is used to coarsely separate the ribs by appropriate spacing. Make sure that the ribs on the same octagonal ring are aligned with each other.
2. Place long set screws in a subset of the threaded holes in the ribs. It is usually sufficient to populate only half of the holes. Use the set screws as indicators to try and fit a flat shield piece⁸ to the ribs. If the ribs are perfectly aligned, then a flat shield piece should easily fit. If this does not happen, check which set screw is binding and adjust the position of the corresponding

⁴The errors come from alignment as well as the thickness of mu-metal, which forces a gap on the outer sheets.

⁵Unlike other places in the tower support structure that uses 15 Series, the shield scaffolding uses 10 Series 80/20 due to its smaller profile.

⁶With the exception of the ribs at both ends, which are separated from their neighbors by 12.25", because only one of the two rows of threaded holes is used on these ribs.

⁷We are advised to have at least one fastener per foot in the longitudinal direction to reduce bulging of the mu-metal pieces given the thickness we ordered.

⁸It is better to have a jig that shares the same hole pattern as the shield pieces, so we do not have to use the fragile shield piece for alignment.

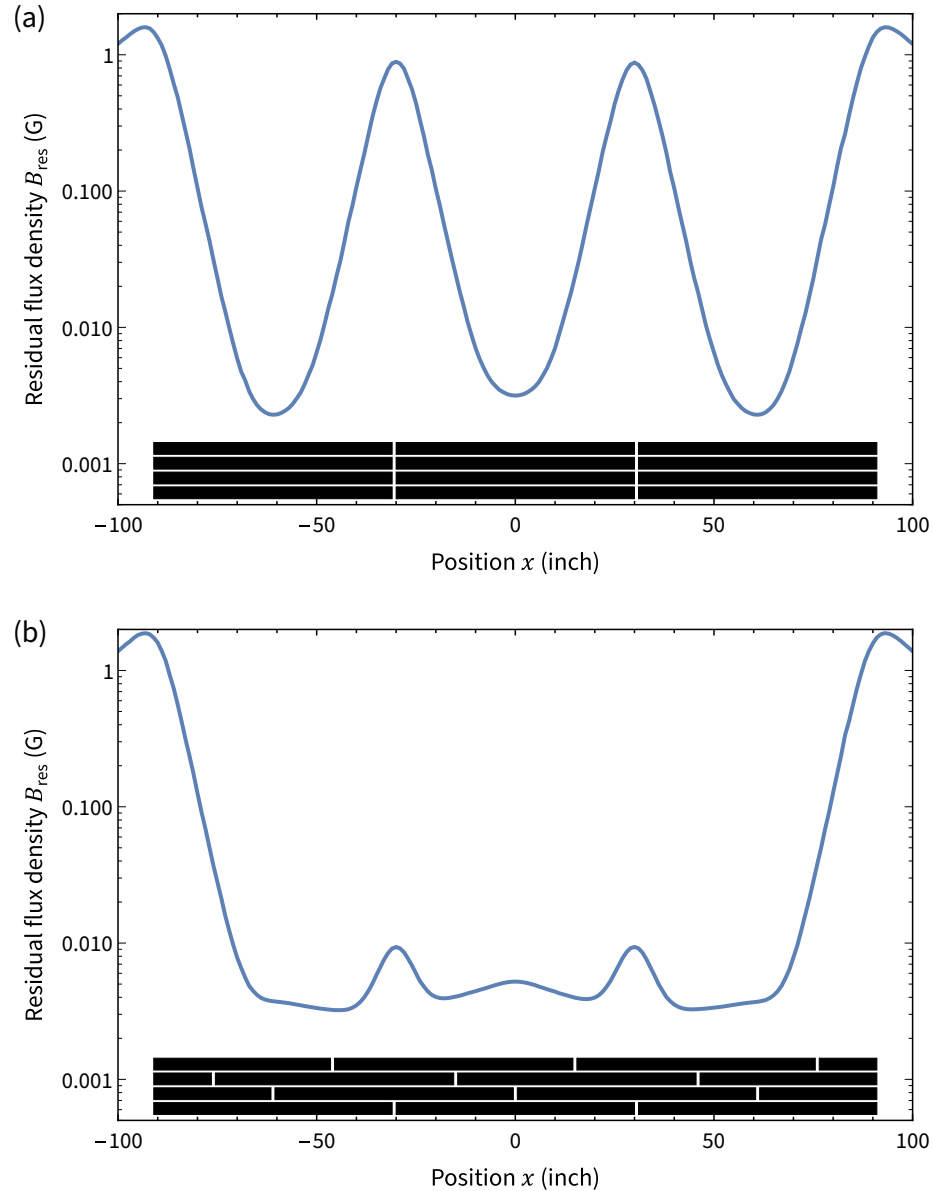


Figure 4.6: Simulation of a cylindrical shield stacked by mu-metal sheets in the presence of a longitudinal external magnetic field $B_0 = 0.5$ G. The shield diameter, thickness, and permeability are set to the same realistic values as in previous simulations, while the gap size and sheet-to-sheet spacing are set to be pessimistic values of 0.025" and 0.010", respectively, so that meshing can run smoothly. The length of the shield is arbitrarily chosen as 180" and broken up into pieces with a maximum length of 60". (a) The mu-metal sheets are not staggered. The common gaps cause significant magnetic field penetration. (b) The sheets are staggered to avoid common gaps indicated by the black bars (innermost at the bottom). This is in the same spirit as the actual shield, whose geometry is illustrated by Figure 4.4. The magnetic field penetration is suppressed by about 100 \times .

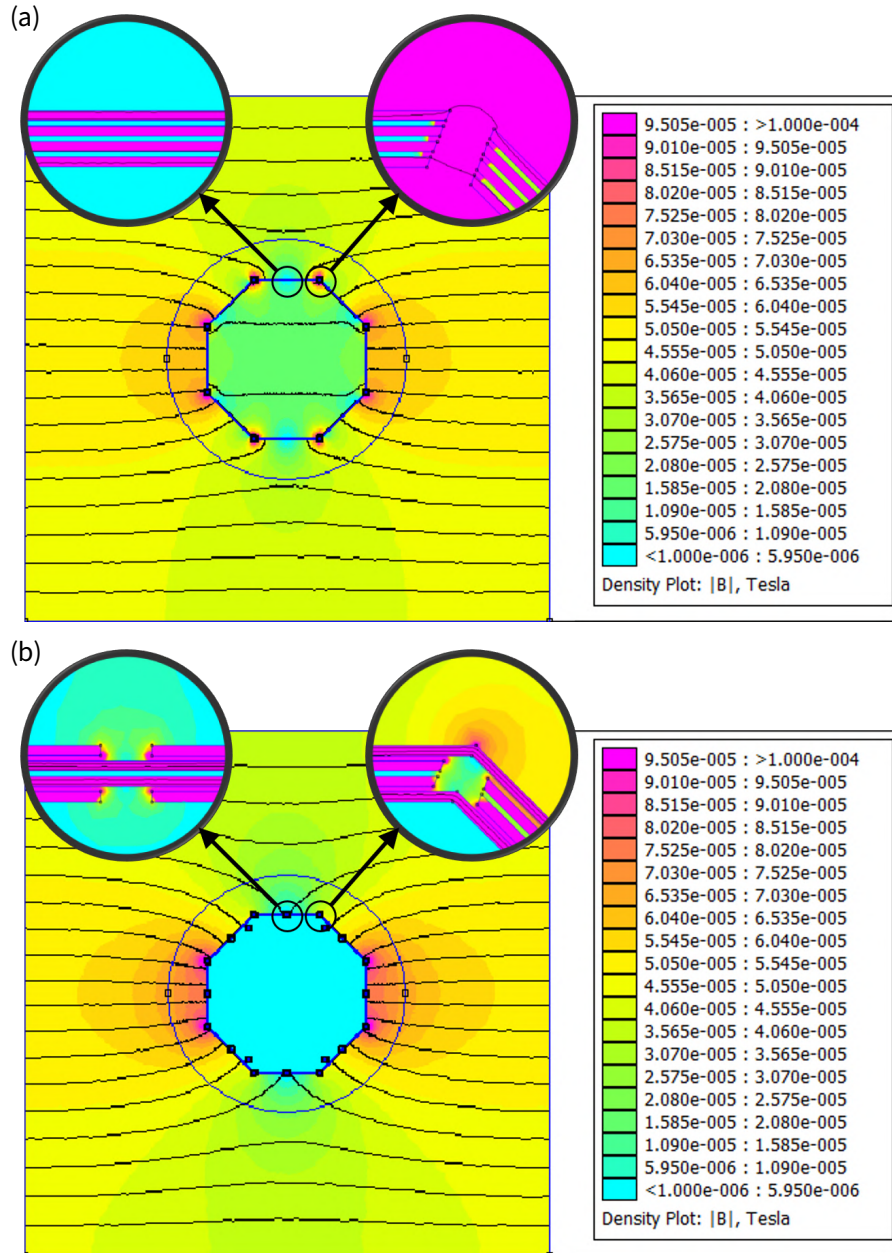


Figure 4.7: Simulation of an octagonal shield stacked by mu-metal sheets in the presence of a transverse external magnetic field $B_0 = 0.5$ G. The shield diameter, thickness, and permeability are set to the same realistic values as in previous simulations, while the gap size and sheet-to-sheet spacing are set to be 0.1" and 0.010", respectively. The length of the shield is infinite. (a) The mu-metal sheets are not staggered. The gaps are common at eight corners and cause significant magnetic field penetration. (b) The sheets are staggered to distribute the gaps at corners and edges. This is the strategy taken by the actual shield, whose geometry is illustrated by Figure 4.5. The magnetic field penetration is suppressed by about 60×.

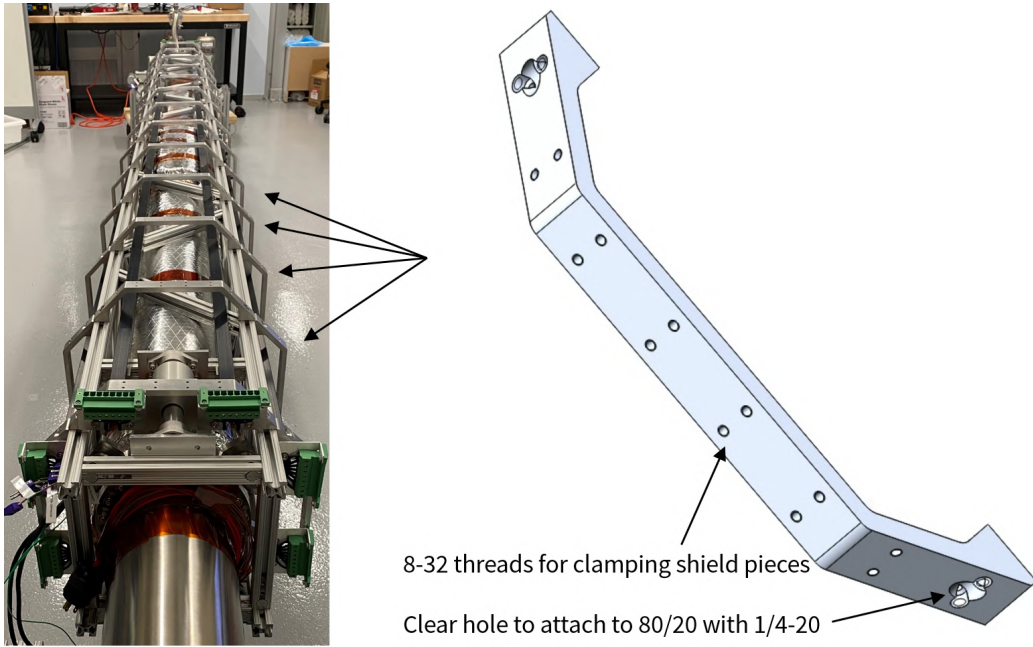


Figure 4.8: Shield scaffolding ribs that form the periodic octagonal rings to structurally support the mu-metal sheets.

rib. Use this method to fine-tune the rib positions on all faces. Iterate this procedure several rounds until the alignment is satisfactory everywhere along the scaffolding.

3. Rotate the rotisserie so that one of the eight sides of the octagon faces up. Cover each long edge of this face with two bent mu-metal sheets whose lengths add up to the total length of the shield but arrange them in an alternated way so that their seams do not line up. For each mu-metal sheet, make sure that the end with annealing jig holes faces outward.
4. Use some pressure plates and fasteners along this face to secure the two sheets. Alternatively, since the ribs still have set screws installed, it is possible to use some nuts on the set screws to hold the sheets.
5. Rotate the rotisserie by 45° and add bent mu-metal sheets to the new edge that is brought to the top, making sure that the neighboring seams do not line up. Clamp these sheets as in the previous step. If the rotisserie becomes imbalanced and spontaneously rotates due to the extra weight of the sheets, use some doorstops on the rotisserie wheels to stop its motion or lock the rotisserie with additional 80/20 beams. Repeat this process until the rotisserie is turned by a full revolution and all eight faces are covered with bent sheets.
6. Remove the clamps on the top face and place the second and third layer of mu-metal, both of which are flat sheets. The seams in these two layers must also be arranged in an alternated

way. Then put the clamps back.

7. Rotate the rotisserie by 45° and clamp down two layers of flat mu-metal sheets to the new face that is brought to the top, making sure that the neighboring seams do not line up for each layer. Repeat this process until the rotisserie is turned by a full revolution and all eight faces are covered with flat sheets.
8. Repeat steps 3 – 5 to add the fourth layer of mu-metal, which consists of bent sheets. Arrange the sheets so that the seams in the fourth layer do not line up with those in the first layer. Some previous sheets may need to be temporarily unclamped in this step.
9. Replace all set screws and fill in the empty holes with 8-32 button head fasteners. With a torque wrench, tighten all of them to 30 in-lbs⁹. Note that the ribs require longer fasteners near the mounting holes to the shield scaffolding.

This installation procedure takes about one day for an experienced team of two people. To disassemble the shield, simply reverse the process, but be aware of loose mu-metal sheets falling off from the scaffolding.

4.3 Active Field Control

This section introduces the coils we integrated to the tower for active control of the magnetic field. Each tower section is equipped with three different types of coil: two sets of long bias coil bars (four bars per set) to create a transverse bias field in the interferometry region, a solenoid to create a longitudinal bias field in the lower portion of the interferometry region, and a rectangular coil box to compensate the Earth field and the edge effect of the magnetic shield at the connection node chamber, where no passive shielding is available.

4.3.1 Transverse Bias Coil Bars

Clock atom interferometry in the tower uses the magnetic field insensitive $m_J = 0$ states. In the case of a co-magnetometer configuration with the clock transition in the fermionic isotope ^{87}Sr , both the ground and the excited states have $m_F = \pm 9/2$ so the transition still introduces no change in the angular quantum momentum number. This means a π -transition and requires the laser polarization to align with the quantization axis defined by the bias magnetic field. Since the interferometry laser propagates in the vertical direction, the bias field must be implemented in the transverse direction. The magnitude of the bias field must dominate the residual ambient field, which is at the level of 1 mG. Taking into account the practical limitations, we set the maximum achievable bias field

⁹There were some fasteners with more resistance. In this case, we tightened them so that their head was just flush with the counterbores in the pressure plates.

to be of order 10 G. This magnetic field is also useful for suppressing undesired excitation to the neighboring magnetic substates due to polarization impurities, given a linear Zeeman coefficient of 109 Hz/G in the clock transition.

The simplest way to create a near-uniform transverse bias field over a large longitudinal span is by using two parallel coil loops that are no shorter than the region of interest. This can be viewed as an elongated version of the Helmholtz coils, where each coil loop extends significantly more in one direction than in the other. To simplify construction in the presence of a magnetic shield, each coil loop can be broken down into two long straight wires that extend inside the shield and two short wires outside the shield to connect the ends of the long ones. The two connector wires can be arranged so that their magnetic field is mostly shielded, and the main contribution to the magnetic field in the interferometry region comes from the four long wires, two in each coil loop.

Just like the Helmholtz coils, there is an optimal coil-to-coil spacing in the four-wire configuration that maximizes the magnetic field homogeneity, which is measured by the lowest non-trivial term in the series expansion of the magnetic field at the geometric center. Moreover, it is possible to add more coil loops to this configuration to achieve cancellation of higher orders, forming a discrete cosine coil. Here, a simple mathematical treatment is first given to determine the optimal location of the wires in the presence of a perfect circular shield with infinite permeability. Next, the resulting geometry is put into numerical simulations to verify its feasibility with practical shield parameters and an octagonal cross section. Then I discuss the practical technicalities to achieve this coil configuration in a realistic tower section.

Mathematical Model

Consider the following coil geometry. A set of four wires is configured on the vertices of a rectangle centered around the origin, perpendicular to the xy plane. The wires in the first and second quadrants carry current in the \hat{z} direction, while the wires in the third and fourth quadrants carry current in the $-\hat{z}$ direction. We want this set of wires, to the lowest order, to resemble the first-order cosine coil $\mathbf{J}_{\cos}^1(\theta) = J_0 \sin \theta \hat{z}$ that creates a uniform magnetic field in the \hat{x} direction. More sets of wires can be added to further approximate the cosine coil.

The distance from each wire to the origin is denoted as r , which is less than the radius of the magnetic shield R . The angular position of the wire in the first quadrant of the i -th set is θ_i . In other words, the Cartesian coordinates of the i -th set of wires are $(\pm r \cos \theta_i, \pm r \sin \theta_i)$. We use (x, y) or (ρ, ϕ) to denote the point where the field is evaluated. Here, $x, y, \rho \ll r, R$, so that we can expand the field at the origin to low orders of x, y or ρ .

To calculate the interaction between a perfect cylindrical shield and a general odd azimuthal current distribution $\mathbf{J}(\theta)$ (that is, $\mathbf{J}(\theta) = \mathbf{J}(\theta + 2\pi) = -\mathbf{J}(-\theta)$), we consider an order- k cosine coil whose current density is $\mathbf{J}_{\cos}^k(\theta) = J_0 \sin k\theta \hat{z}$. An arbitrary odd $\mathbf{J}(\theta)$ can be expanded in the order- k cosine coil basis due to the completeness of $\sin k\theta$ over the space of odd functions of θ . The

magnetic field from an order- k cosine coil is derived as [155]

$$\mathbf{B}_{\cos}^k(\rho, \phi) = C_k J_0 \rho^{k-1} (\cos k\phi \hat{\rho} - \sin k\phi \hat{\phi}) \quad (4.14)$$

$$= C_k J_0 \rho^{k-1} (\cos(k-1)\phi \hat{x} - \sin(k-1)\phi \hat{y}) \quad (4.15)$$

where C_k is the “reaction factor” between the shield and the coil. This can be viewed as the collective contribution of the coil and its “image coil” generated by the shield with the same azimuthal distribution, and takes a simple form

$$C_k = 1 + (r/R)^{2k} \quad (4.16)$$

The geometry of a four-wire set mentioned above has an additional symmetry of $\mathbf{J}(\theta) = \mathbf{J}(\pi - \theta)$, which leads to

$$B_\rho(\rho, \phi) = -B_\rho(\rho, \pi - \phi) \quad (4.17)$$

$$B_\phi(\rho, \phi) = B_\phi(\rho, \pi - \phi) \quad (4.18)$$

so only the odd order cosine coil terms survive. Therefore, the magnetic field generated by n sets of wires at $\{(\pm r \cos \theta_i, \pm r \sin \theta_i)\}$, where $i = 1, 2, \dots, n$, takes the form

$$\mathbf{B}(\rho, \phi; r, \theta_1, \theta_2, \dots, \theta_n) = \sum_{k=0}^{\infty} A_k(r, \theta_1, \theta_2, \dots, \theta_n) C_{2k+1} \rho^{2k} (\cos 2k\phi \hat{x} - \sin 2k\phi \hat{y}) \quad (4.19)$$

where A_k is the expansion coefficient that depends on the geometric parameters and the summation indices have been rearranged. One can show with Biot–Savart law that¹⁰

$$A_k(r, \theta_1, \theta_2, \dots, \theta_n) = \frac{2\mu_0 I}{\pi} \frac{\sum_{i=1}^n \sin(2k+1)\theta_i}{r^{2k+1}} \quad (4.20)$$

The zeroth order in Equation (4.19) is the homogeneous magnetic field, given by

$$\mathbf{B}_0 = A_0(r, \theta_1, \theta_2, \dots, \theta_n) C_1 \hat{x} \quad (4.21)$$

$$= \frac{2\mu_0 I}{\pi r} \left(\sum_{i=1}^n \sin \theta_i \right) \left(1 + \left(\frac{r}{R} \right)^2 \right) \hat{x} \quad (4.22)$$

and the higher order terms are the residuals. In general, we have the degree of freedom to choose θ_i , where $i = 1, 2, \dots, n$, to cancel the lowest n terms in the residual field to optimize homogeneity.

¹⁰It is easy to discover this pattern with Mathematica without proving it.

This means solving the following n equations

$$\sum_{i=1}^n \sin(2k+1)\theta_i = 0 \quad \text{for } k = 1, 2, \dots, n \quad (4.23)$$

For example, with one set of wires ($n = 1$), the solution $\theta_1 = \pi/3$ suppresses the field inhomogeneity to the $(\rho/r)^4$ level, similar to the Helmholtz coils. Normalized by $|\mathbf{B}_0|$, the leading order of the residual field is

$$\mathbf{B}_{\text{res,norm}} = \frac{C_5}{C_1} \left(\frac{\rho}{r}\right)^4 \frac{\sin 5\theta_1}{\sin \theta_1} (\cos 4\phi \hat{\mathbf{x}} - \sin 4\phi \hat{\mathbf{y}}) \quad (4.24)$$

$$= \frac{1 + \alpha^5}{\alpha^2(1 + \alpha)} \left(\frac{\rho}{R}\right)^4 (-\cos 4\phi \hat{\mathbf{x}} + \sin 4\phi \hat{\mathbf{y}}) \quad (4.25)$$

where $\alpha \equiv (r/R)^2 < 1$. Since the α -dependent prefactor monotonically decreases as α increases, we conclude that the wires should be positioned as close to the shield as possible¹¹.

With two sets of wires ($n = 2$), the solution to Equation (4.23) is $\theta_1 = 11\pi/30, \theta_2 = \pi/30$. The field inhomogeneity is suppressed to the $(\rho/r)^6$ level, and the leading order of the normalized residual field is

$$\mathbf{B}_{\text{res,norm}} = \frac{C_7}{C_1} \left(\frac{\rho}{r}\right)^6 \frac{\sin 7\theta_1 + \sin 7\theta_2}{\sin \theta_1 + \sin \theta_2} (\cos 6\phi \hat{\mathbf{x}} - \sin 6\phi \hat{\mathbf{y}}) \quad (4.26)$$

$$= \frac{1 + \sqrt{5}}{2} \frac{1 + \alpha^7}{\alpha^3(1 + \alpha)} \left(\frac{\rho}{R}\right)^6 (\cos 6\phi \hat{\mathbf{x}} - \sin 6\phi \hat{\mathbf{y}}) \quad (4.27)$$

However, in practice, $\theta_2 = \pi/30$ (6°) is a very small angle and may cause mechanical conflicts. A possible workaround is to have different currents in the two sets of wires. For example, one can show that if the second set has half the current compared to the first set, then $\theta_1 = 1.15951$ and $\theta_2 = 0.240814$ (66.4° and 13.8°) is a viable solution.

Although using two or more sets can improve the homogeneity of the transverse bias field, we conclude that the marginal gain is not worth the extra effort. In practice, we implement a single set of four wires to create a bias field in one transverse direction, and a second set rotated by 90° for field in the orthogonal direction. The ideal mathematical model states that the field variation can be controlled to $(\rho/R)^4 \approx 2 \times 10^{-5}$ assuming $\rho = 0.5''$ and $R = 7.5''$.

Numerical Simulation

The mathematical model assumes a circular shield with infinite permeability. The reaction factor between the coil and a realistic shield is more complicated due to the finite permeability of mu-metal [155] and the octagonal cross section that we chose for practical reasons discussed in Section 4.2.3.

¹¹This is different from the conclusion in Ref. [155]. They only minimized for C_5/C_1 , but did not include the additional r^{-4} dependence in the residual field, which I do not agree with.

Finite element simulations were performed to understand the field homogeneity in this scenario, as well as to identify any saturation regions inside the mu-metal.

As shown in Figure 4.9, in a gapless octagonal shield, the simulated magnetic field is 0.073 G/A, with a variation of about 7×10^{-5} within a radius of 0.5". Therefore, to obtain a uniform bias field around 10 G, a total current of 140 A·turns is driven through the coil. To understand whether the mu-metal is still in the linear regime, we also include a background field of 0.5 G, in the direction that is the worst case for the field B_m inside the mu-metal. This results in a maximum B_m of 1197 G at the corners close to the wires, which is still far below the saturation threshold. A staggered gap with the same parameters as in Figure 4.7 does not significantly affect the bias field obtained and its homogeneity. However, the change in geometry leads to a local field concentration inside the mu-metal, which almost doubles B_m . Despite this, the magnetic shield still operates below the saturation limit with a large margin.

Practical Technicalities

The 140 A·turns current needed to achieve a 10 G bias field is too large for a single wire. Therefore, in reality, a coil with multiple turns is implemented. The current load, and thus the gauge of the wires, reduces with increasing number of turns. However, keeping the number of turns relatively low eases the construction procedure and reduces the possibility of failure in the connection or the insulation of the wires. In addition, the impedance of the coil must be considered to ensure that it matches a commercial power supply. Taking into account all these factors, we designed a transverse bias coil so that each of the four "wires" mentioned above consists of eight parallel conductors. These conductors are AWG 12 square magnet wires with enamel coating¹², arranged in an anodized aluminum Unistrut channel¹³, forming a "bias coil bar". With this choice of gauge and number of turns, a complete set of four bars measures 0.83Ω and 2.1 mH in the lower section. Unistrut compatible nuts¹⁵ are used to clamp the wires periodically under Teflon pads to ensure that the wires are straight and parallel. We homemade eight bias coil bars for each tower section to form two sets of coils, one for each transverse direction. The procedure for winding a bias coil bar is summarized below.

1. Figure 4.10 (a): Join two Unistrut channels together to achieve the required length for a bias coil bar. The joint is done with 80/20 flat joining plates¹⁶.
2. Figure 4.10 (b): Coat the Unistrut channel with two layers of 0.005" Kapton tape. The purpose of this step is to add extra insulation on top of the aluminum anodization. It is helpful to

¹²MWS Wire 12 SQ HAPT NEMA MW36-C magnet wires.

¹³We first ordered aluminum Unistrut channels P6000, cut them to length¹⁴ and drilled fastener holes at the ends, then sent them to Haro's Anodizing Specialist Inc. for anodization.

¹⁵Unistrut does not sell non-magnetic nuts so we ordered custom nuts from Hubs (now Protolabs Network) based on the same drawing.

¹⁶We drilled holes at the ends of the Unistrut channels to match 20 Series 80/20.

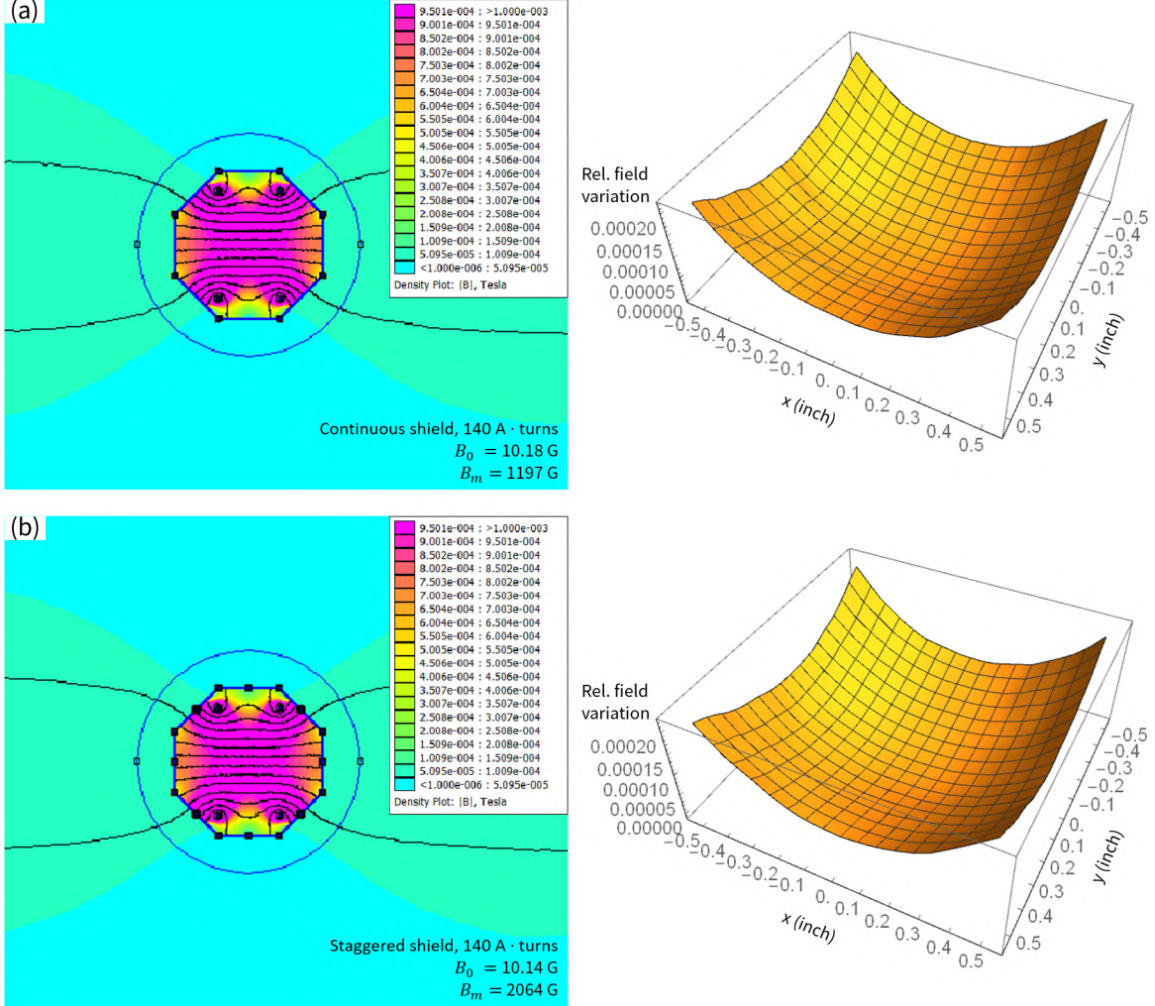


Figure 4.9: Simulation of the bias field generated by a set of four wires placed in the optimal azimuthal location. The radial coordinate of the wires is $r = 6.34''$, set by practical geometry constraints in the tower sections. The wires are positioned in an octagonal shield whose diameter, thickness, and permeability are set to the same realistic values as in previous simulations. We compare the following two scenarios in the presence of a background field of 0.5 G in the direction that is the worst for mu-metal saturation: (a) an ideal continuous shield with no gaps and (b) a staggered shield with gap parameters identical to Figure 4.7. The staggering strategy does not affect the amplitude and homogeneity of the bias field but concentrates the field locally inside the mu-metal more than the ideal scenario. However, the shield is still far from being saturated. This four-wire design achieves a bias field of 0.073 G/A, thus around 140 A·turns is required to reach a magnetic field of 10 G. The field variation is 7×10^{-5} within a radius of 0.5'', which is a few times worse than the ideal mathematical model.

use a small hex key to ensure good contact between the tape and the channel and to remove bubbles in between. Since the width of the Kapton tape is 1" and larger than the inner width of the Unistrut, it also covers the part of the side walls. Having two layers of Kapton allows us to cover both walls on the side.

3. Figure 4.10 (c–f): Arrange the eight parallel wires using the shield scaffolding and two custom machined screw terminals as a jig. (c) The wire is supplied by a spool on a cart that moves from one end of the scaffolding to the other. (d) The screw terminals hold the ends of the wires across a distance larger than the length of the bars. (e) Tension the wires and then (f) tape them periodically to form a “wire sheet” that is one wire thick and eight wires wide. The width of this wire sheet is just smaller than the width of a Unistrut channel (this is why eight wires are used).
4. Figure 4.10 (g): Put the wire sheet inside the channel. The channel needs to be rotated to allow the wire sheet to pass its lips.
5. Figure 4.10 (h): Fix the wires in the channel by periodically clamping them under Teflon pads with set screws extending from aluminum nuts that are compatible with Unistrut. The density of the clamp is about two per foot.
6. Figure 4.10 (i–j): Release the bias coil bar from the jig. (i) Remove the insulation at the ends and install the terminal connectors¹⁷. The wires are first bent, measured, and trimmed to ensure that they all reach the terminal connector. Then remove the enamel insulation at the tip of each wire with a small file. Apply heat shrink to ensure that roughly the same amount of copper is exposed on each wire. Finally, connect each wire to the terminal connector. The connector is then mounted to the Unistrut by a custom sheet metal piece and two brackets. Panel (j) is the corresponding CAD model.

According to the mathematical model, it is desirable to make the bias coil bars as close to the shield as possible. However, in practice, the ribs pose a constraint on the location of these bars. Since the bars must be inside the ribs, the most convenient location to mount them is the 80/20 shield scaffolding. The opening of the Unistrut channels is faced towards the shield scaffolding, and the same type Unistrut nuts that clamp the wires are used to connect the channels to horizontal 80/20 beams through angle brackets. The bias coil bars are then fastened in positions that avoid conflicts with the linear bearings and the HV feedthroughs of the electrode chamber, while allowing hex key access to the necessary fasteners. As a result, the realistic azimuthal angle is 63°, which is larger than the optimal angle by 5%. Finite element simulation shows that the resulting magnetic field inhomogeneity is worse by an order of magnitude, but still below 10^{-3} in the region of interest.

¹⁷Phoenix Contact DFK-PC 4/8-GF-7,62 - female feedthrough plug. Many of them are modified to remove some plastic material that causes conflicts with the 80/20 structure or blocks the reach of the screw connectors from certain angles, as shown in Panel (j). The corresponding male connector is PC 4/8-STF-7,62.

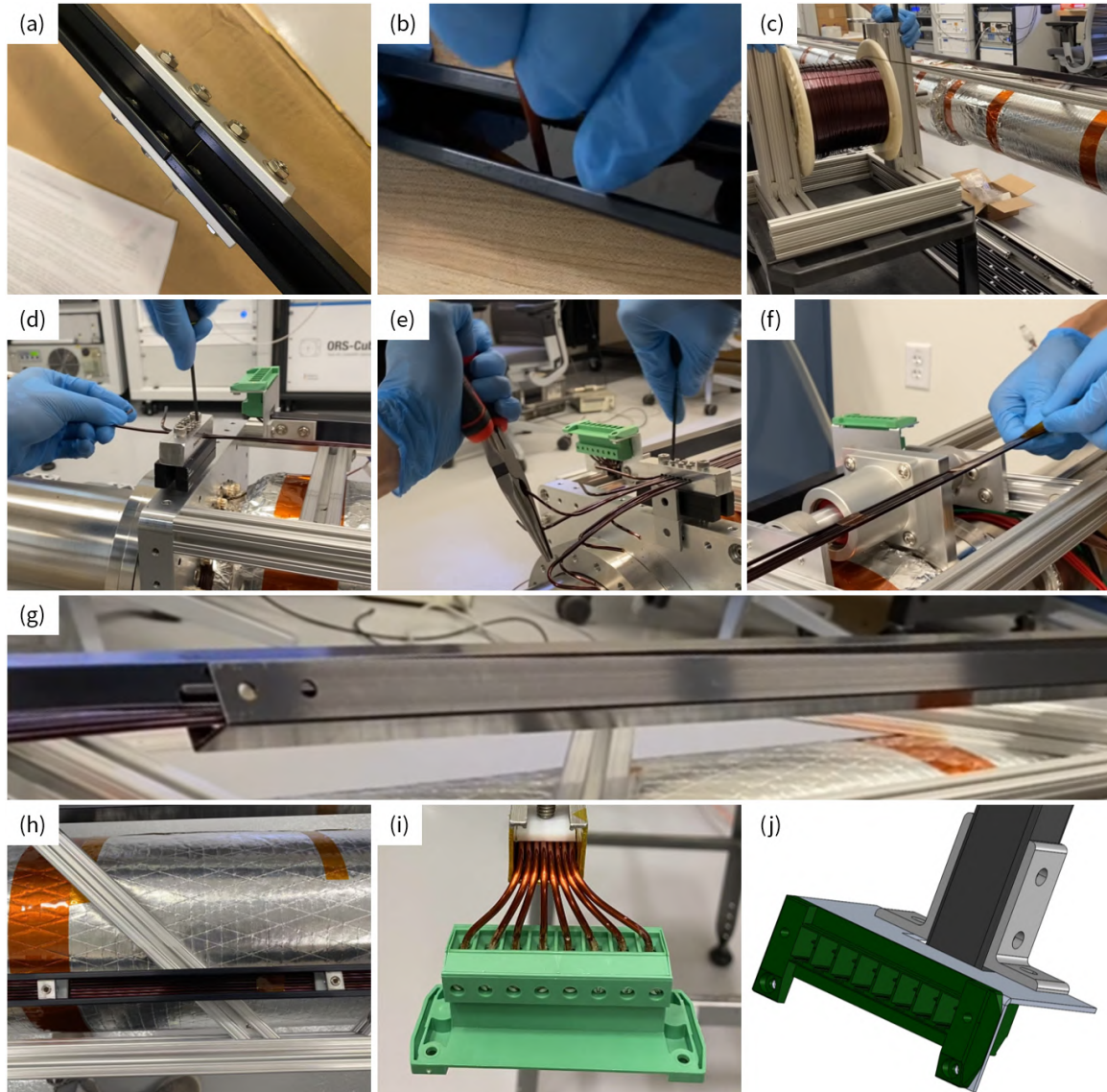


Figure 4.10: The procedure for winding the bias coil bar. Note that Panel (i) is a from a test run and does not include the black anodization and the heat shrink. Panel (j) is a screenshot of the CAD model showing the connection between the terminal connector and the Unistrut channel.

4.3.2 Longitudinal Bias Solenoid

In some cases, such as certain state preparation procedures, σ^\pm transitions that do not preserve the angular momentum quantum number may be used. In this case, the ability to generate a bias field along the longitudinal direction is desired.

As mentioned in Section 3.3.1, we added a solenoid to the bottom tube of each tower section to generate a longitudinal bias field. Figure 4.11 (a) shows the tube without the solenoid. To ensure electrical isolation, a 0.005" layer of Kapton tape is coated around the tube. The solenoid is made of 12 AWG square magnet wire¹⁸ with enamel insulation. We mounted the spool on an 80/20 frame secured to a cart, allowing it to spin and translate. Solenoid winding requires teamwork of at least three people: the first person needs to move the cart and control the spin of the spool; the second person needs to guide the wire when it is about to wind on the tube and periodically push the magnet wire loops close to each other to avoid gaps¹⁹; the third person needs to slowly but steadily rotate the rotisserie. The solenoid starts from the base plate at the bottom flange and makes its way to the top flange of the tube. Kapton tape loops are used to periodically secure the magnetic wires. At the top flange, the magnet wires are wounded back in the same helicity, forming a second layer of the solenoid. Finally, the magnet wire exits the solenoid at where it starts. The two ends of the solenoid are clamped against the base plate and electrically connected to a terminal plug. Figure 4.11 (b) shows the bottom tube after winding the solenoid.

It is worth mentioning that a single spool is not long enough to cover the round trip of the solenoid. Therefore, a splice is made at the top flange where two magnet wires are soldered together. The solder joint had an oblique cut to increase the contact area. We used high-temperature solder and wrapped the joint with additional Kapton tape. Electric connectivity was checked with a multimeter.

The solenoid is expected to generate a magnetic field of 11.4 G/A, assuming the turn density is given by the inverse of the maximal wire thickness 0.0868" from the manufacturer. The resistance of the solenoid measures $4.6\ \Omega$ in room temperature, and the inductance is 45.5 mH.

During the design of the tower sections, there have been discussions on whether we would extend this solenoid to the electrode chamber and beyond, while suppressing the fluctuation of the bias field to below 1 mG. We then realized that maintaining such a field homogeneity requires additional compensation coils around the flanges, which are larger in diameter and disrupt the continuous winding of the solenoid. Mounting these coils and driving them at the exact current that compensates for the field anomalies is extremely difficult, as the entire section has to be wrapped with bake-out equipment and enclosed in an 80/20 shield scaffolding. Considering that the solenoid is likely only used in certain state preparation scenarios in which the atoms never reach the height of the electrodes, we decided to keep the solenoid just around the bottom tube.

¹⁸Same MWS Wire product as the wires for the bias coil bars. We ordered three 12" spools, each carrying 1,800" of wire. It is undesirable to pursue larger spools due to weight.

¹⁹Work gloves are required to avoid injury.



Figure 4.11: (a) The bottom tube resting on the rotisserie before the solenoid is wound. The tube is covered with Kapton and the magnet wire is on a cart by its side. (b) The bottom tube with a double-layer solenoid. The Kapton tape loops used to secure the solenoid are visible.

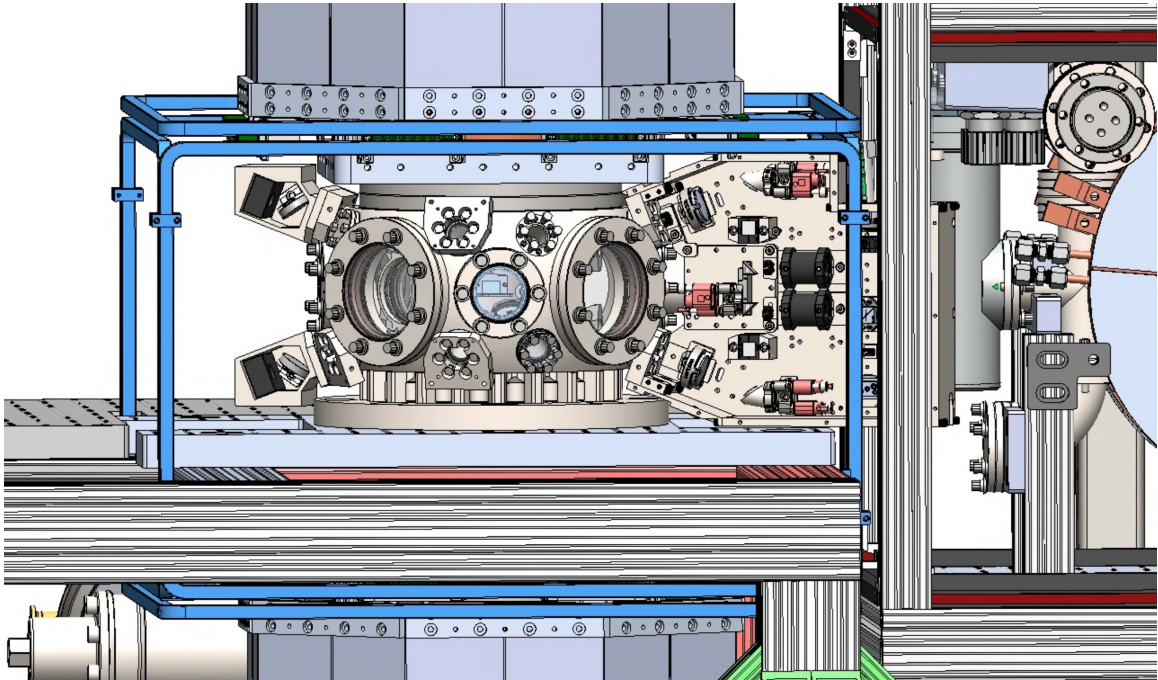


Figure 4.12: CAD model of the compensation coil box (highlighted) at the connection node. Clamps between the coils and fixture to the table are not finalized.

4.3.3 Compensation Coils

The two sections of the magnetic shield are separated at the upper connection node by a distance of $14.66''$, over which no passive shielding is implemented due to the conflict with the optical components around the connection node chamber. Although this shield gap has been minimized in the tower design, it is still large enough to cause significant magnetic field inhomogeneity along the tube axis. This can be thought of as the edge effect of both shield sections, where the magnetic field lines concentrated in the mu-metal are released and expanded at the metal-air interface. In practice, magnetic field leakage affects not only the connection node chamber but also a region inside the magnetic shield with a depth up to the diameter of the shield $D \approx 15''$. The same phenomenon is expected at the bottom connection node, where the edge effect of only the lower shield section plays a role. Similarly, the very top of the tower experiences the edge effect of the upper shield section.

To compensate for the magnetic field inhomogeneity while minimally impacting the optics around the connection node chamber, we have designed a compensation coil box consisting of three pairs of active coils. The transverse footprint of this coil box is mostly determined to avoid conflicts with the 80/20 table and the atom source frame, whereas the height is informed by finite element simulations to be slightly larger than the shield gap. The final dimensions are measured as $21.3''$ (N-S) \times

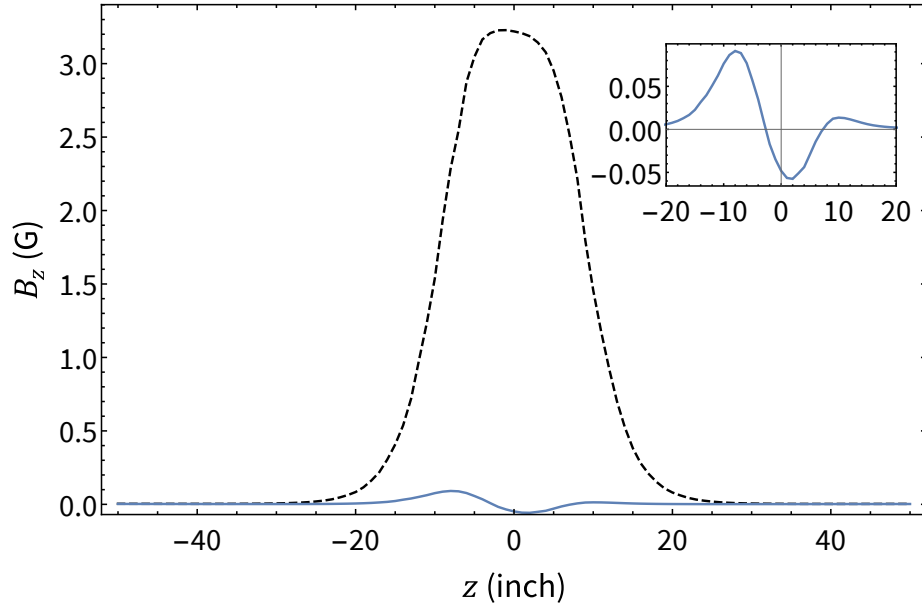


Figure 4.13: Simulation of edge effect suppression at the upper connection node with realistic tower dimensions. The longitudinal coils are simplified to axial symmetric with a radius of 15''. The magnetic field in the shield gap is reduced from 3.2 G (black dashed) to few-10 mG (blue) when DC currents of 78.1 A·turns and 77.4 A·turns are driven through the two longitudinal coils. The inset is a zoomed-in view of the residual magnetic field.

22.4'' (E-W) \times 15.1'' (H)²⁰. For the convenience of manufacturing and assembly, the coils on four sides are designed to be identical, which are referred to as the “transverse coils”. The top and bottom coils are larger in size and are referred to as the “longitudinal coils”. All six coils contain 25 turns of AWG 14 square magnet wires arranged in a 5×5 configuration. The coils were manufactured by TechniCoil, LLC. They were wound on a mandrel that was later removed and then wrapped with a fiberglass protective layer²¹. Epoxy was applied to form a hard surface and strain relieve the two terminals that exit the coil at a corner. The thicknesses of the coils vary due to the fiberglass and epoxy layers, but are generally within 0.5''. Since the coils are interleaved with the 80/20 beams of the table, they need to be pre-installed with the tower and then assembled to each other via custom clamps.

From a finite element simulation in Figure 4.13, it is observed that with about 80 A·turns in the longitudinal coils, the edge effect of the shield is suppressed from 3.2 G to few-10 mG. Furthermore, the compensation coil box can be used to trim the magnetic field and gradient from Earth and establish a uniform bias field in any direction up to an amplitude of about 10 G.

In addition to two compensation coil boxes for the connection nodes, we also ordered two extra

²⁰N-S is the shuttle direction and E-W is the transverse direction perpendicular to the shuttle.

²¹This allows a frameless coil which is cheaper and faster to manufacture, unlike the coils in the atom source frame.

longitudinal coils to place on the top of the upper section. By reducing the edge effect that is most significant in the longitudinal direction, we can extend the usable length of the upper tower section.

4.4 Magnetic Field Characterization

This section discusses methods for characterizing the residual magnetic field, both inside and outside the vacuum system. All measurements were performed with a three-axis fluxgate magnetometer²² that can measure up to 1 G with a precision of sub-100 μ G. Through a combination of various characterization techniques, we identified several sources of magnetic field anomalies and developed methods to alleviate them. After several rounds of iteration, the residual magnetic field inside the tube section was able to meet the specifications introduced in Section 4.1.

4.4.1 External Magnetometry

External magnetometry refers to the measurement of field anomalies outside the vacuum tube, which can be performed on the component level or on the system level, and with or without the magnetic shield. In our experience, external magnetometry on the component level is necessary and can inform about magnetized parts. This measurement can be performed quickly without building the shield to save time and effort. The tube section should only be put together once all components have passed this magnetometry test. Even after that, a means of performing a system-level measurement of the residual magnetic field outside the vacuum tube is useful and can be periodically revisited after the interferometer has been fully assembled.

Component-level measurement of the magnetic field anomaly is performed by slowly moving the part to be examined close to or away from the magnetometer whose position is fixed. The magnetometer reading is recorded as a function of time. Since low-frequency magnetic field noise is rare in the lab, it is safe to attribute all the time variation in the measurement to the change of position of the part. The magnetic field signal caused by the part at the same nominal distance to the atoms is then compared to our specifications.

System-level measurement is made possible by the integration of a magnetometer channel that is inside the magnetic shield but outside the vacuum tube. This channel is a long 80/20 Quick Frame tube²³ mounted on the shield scaffolding, which allows the magnetometer to be dragged from one end to the other with a fish tape. Since vacuum cleanliness is no longer a concern, the magnetometer is operated with data and power wires, so electronics can stay out of the channel. The inhomogeneity of the magnetic field along the magnetometer channel can be used to indicate the residual field noise inside the vacuum tube.

²²Applied Physics Systems Model 534D 16-bit 3-axis fluxgate magnetometer.

²³Due to length constraints we had two tubes connected end-to-end.



Figure 4.14: Vacuum annealing of the stainless steel components. The parts were placed on heat-resistant spacers on a grid and then sent into a vacuum oven. The oven was heated to 1066°C and kept for over three hours. This procedure significantly reduced the magnetization in the parts. We did not notice any degradation in the knife edges after annealing.

4.4.2 Annealing the Vacuum Components

Stainless steel exhibits an austenite form and remains so when cooled, due to the presence of nickel which stabilizes this non-magnetic phase. In particular, 316/316L stainless steel, the material for our vacuum chambers and in-shield fasteners, outperforms 304 stainless steel in magnetic field susceptibility and can achieve a permeability of as low as 1.002 to 1.005. However, many factors such as cold work, welding, or impurities can locally convert the austenite back to the martensite form, which is ferromagnetic. In practice, we have found through external magnetometry that some of the vacuum components, especially the double crown and the flange adapters on the electrode chamber, exhibited higher-than-usual magnetization and led to few-mG magnetic field anomalies at the nominal distance to the atoms.

Our initial attempts to degauss away this magnetization were unsuccessful even with homemade

coils that could produce an AC magnetic field larger than 6 kA/m . We believe that even with our best effort, the degaussing field that we could apply was insufficient to saturate the stainless steel parts.

We then turned to vacuum annealing²⁴ shown in Figure 4.14, which is a common demagnetization method, as the austenite form is preferred at high temperatures [156]. The parts were heated to 1066°C for more than three hours and cooled in a controlled manner. A second round of external magnetometry on the annealed components showed that the magnetization has been significantly reduced to 1 mG or less.

4.4.3 Degaussing the Magnetic Shield

Although mu-metal has been annealed in a dry hydrogen environment to achieve optimal permeability, the magnetic shield needs to go through a second procedure referred to as “degaussing” after being assembled to eliminate the remnant magnetization. This usually means exposing the ferromagnetic material to an oscillating magnetic field of decreasing intensity, which causes a progressive reduction of the hysteresis loop, resulting in a residual magnetization tending to zero. The mu-metal manufacturer suggested a maximum magnetic field intensity of $100 \sim 150\text{ A/m}$, at a low frequency of around 10 Hz with a decreasing envelope of 1% every cycle. It is also possible to degauss with 60 Hz wall power by slowly decreasing the output of a Variac autotransformer.

To drive the magnetic field, a coil loop needs to be established that encloses the entire magnetic shield. We make use of the bias coil bars inside the magnetic shield as half of the circuit and connect the two ends outside the magnetic shield to close the loop as shown in Figure 4.15. In practice, using two bias coil bars connected in series is sufficient to generate the necessary degaussing field at a current of 10 A . To better match the impedance to the Variac, we added a 5Ω power resistor in series. The total impedance is estimated to be 7.0Ω . During degaussing, the Variac was slowly ramped up from 0 to 70 V over the course of a minute, kept steady for about a minute, and then ramped down at the same rate. This procedure was repeated two to three times. It is important to note that during the degaussing process the magnetometer should stay away from the magnetic shield, as the large degaussing field may void the sensor calibration.

4.4.4 Internal Magnetometry

To better evaluate shielding performance, it is important to measure the residual magnetic field in the region of interest, that is, along the center axis of the tube section. Additionally, this measurement informs us about potential magnetic anomalies in the stainless steel vacuum system that are too small to be resolved by external magnetometry. This information is useful in estimating the deflection of the atoms and the transfer efficiency of π -pulses during an interferometry sequence.

²⁴By a local service shop, BodyCote Heat Treatment.

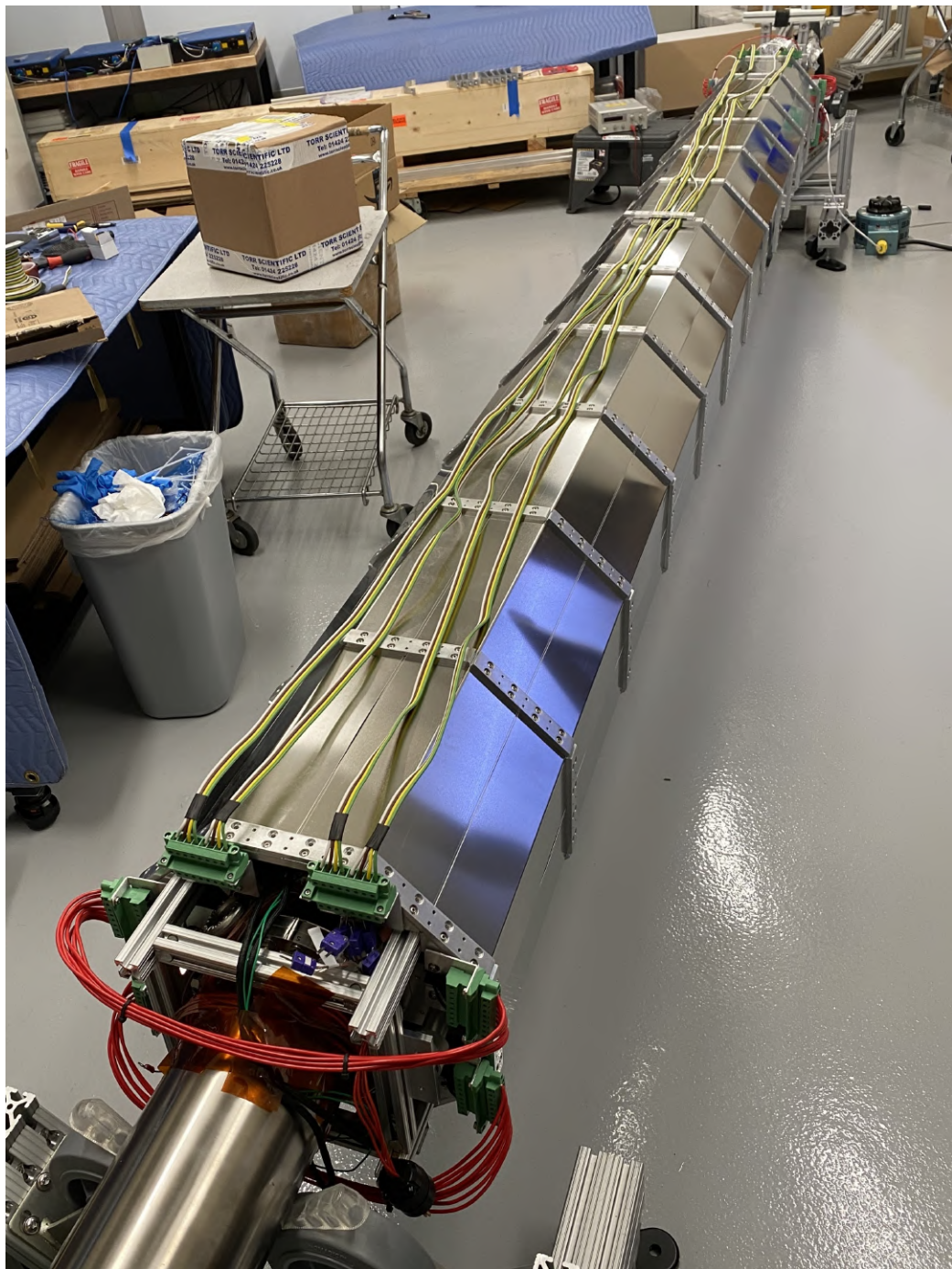


Figure 4.15: Degaussing of the magnetic shield is achieved by connecting the bias coil bars outside the shield to form a coil loop (with the ribbon wires on the top face), then driving an oscillating magnetic field with a Variac autotransformer (in the upper-left corner) with a minute-scale ramp time.

The main challenge of this measurement is to prevent the magnetometry system from contaminating the UHV vacuum tube in which it is measuring. Any shuttle system that sends a magnetometer down the length of the vacuum tube needs to be sufficiently cleaned, at least on the surfaces that may contact the inner wall. For the tower, additional complexity arises because of the smaller aperture of the QMATCH electrodes. Since the electrodes require a polished surface to suppress high-voltage discharge, to avoid any scratching, it is preferred that the magnetometer shuttle does not touch the electrodes during operation. Our design features a cable-car-like system on a cable loop, which is tensioned over pulleys that interface with the vacuum system on both ends. The two sides of the loop move in opposite directions inside the vacuum tube when a hand wheel is turned. The magnetometer is mounted in an aluminum box that is secured to one side of the loop but slides freely on the other side. Turning the hand wheel thus moves the magnetometer from one end of the vacuum system to the other. The magnetometry system consists of the following parts.

- The cable loop and the tools that help thread the cable through the vacuum system.
- The cart holding the magnetometer and electronics, which moves on the cable loop and takes data.
- The active pulley side with a hand-wheel-turned pulley, also serves as the access port of the magnetometer cart.
- The passive pulley side with a pulley on a ratchet strap, used to tension the cable loop.
- The laser distance sensor on the passive pulley side, used to measure the position of the cart and communicate with it.

For the rest of this subsection, I will discuss each of these parts in detail, as well as our magnetometer calibration and data analysis procedures. All codes, PCB schematics, and Gerber files for internal magnetometry can be found in my GitHub [134].

The Cable Loop

In order to suspend the magnetometer cart with a small sag (ideally less than 5 mm change in height from the end to the middle), the cart must be light and the wire must be under high tension. For UHV cleanliness, we prefer a surface that can be wiped down. The best high-tension flexible cable available is a metal wire rope, which is usually steel and therefore too magnetic to be used for magnetometry. It is also often lubricated and has a risk of hydrocarbon contamination. PVC-coated 316 stainless steel wire rope has an oil-free smooth surface and is relatively non-magnetic. However, we found that the magnetization of this wire rope still limited the sensitivity of our magnetic field measurements as it moved with respect to the cart. This is especially problematic when we degaussed the vacuum system, as the wire segments at the end of the shield were simultaneously exposed to an

AC degaussing field and a large edge-effect DC field, leading to remnant magnetization afterwards. Another option for a high-tension cable is a woven polymer rope, often used for climbing. However, it is a multi-stranded polymer and cannot be wiped down, making it undesirable for our purpose.

We eventually turned to a 1.5 mm thick monofilament nylon fishing line²⁵, which is completely non-magnetic and can hold 400 lbs of tension. However, this choice has its own drawbacks. First, the monofilament nature of the wire gives it a poor bending radius. Second, and more importantly, plastics are susceptible to plastic deformation, which causes them to stretch under sustained load and increases the sag²⁶. We typically tensioned the cable loop to 50 lbs with the help of a spring scale²⁷ and noticed that the tension reading would drop over the course of a few hours. As a result, periodic further tensioning was necessary between measurements. When we needed to leave the setup overnight, we released the tension on the nylon cable to prevent overstretching. This inevitably caused the nylon cable to touch the floor of the vacuum system, which emphasizes the importance of cleaning the surface of the cable to UHV standards.

Cleaning was performed before the cable was fed into the vacuum tube, where isopropyl alcohol was used instead of acetone to avoid damaging the nylon, and cleanroom gloves were required. During feeding, to prevent the cable from coiling inside the vacuum tube, we first passed through the vacuum tube a stiffer “guiding cable”, which was a spool of 1/4” PVC pipe with clean foil wrapped around it. The wrapped pipe was cleaned and handled the same way as the wire to ensure vacuum cleanliness. Once the wrapped pipe passed through the entire vacuum system, we doubly folded the clean nylon cable and connected it to the end of the pipe, then pulled the nylon across the vacuum tube. The ends of the cable were then threaded through the pulleys and the cart, and finally crimped together to form a loop. In our experience, both PVC feeding and nylon wiping require three people, whose tasks are summarized in Table 4.2.

Table 4.2: Labor split between a team of three to prepare a cable loop for internal magnetometry.

	Person 1	Person 2	Person 3
PVC feeding	Hold spool	Wrap sections of PVC pipe in foil and wipe the surface	Feed wrapped pipe section into vacuum tube
Nylon wiping	Hold one end	Hold the other end and stand far away from Person 1, keeping nylon cable stretched	Wipe between Person 1 and Person 2

The cable loop was out of contact with the vacuum system after tensioning. Before its tension was released, the cable should be wiped again with isopropyl alcohol. The cable sections inside the

²⁵Available on Amazon.

²⁶It may even break after prolonged time under stress. We had a data collection run when the fishing line broke catastrophically, leaving plastic debris inside the vacuum system, which took us a while to clean up.

²⁷This refers to the tension inside the cable. The spring scale reading is twice this value because the gauge is pulled by both sides of the loop.

tube were accessed and cleaned by turning the hand wheel on the active pulley side.

The Cart

To avoid vacuum contamination, the magnetometer must work autonomously inside the vacuum tube without power or data cables. Therefore, we designed an enclosed cart shown in Figure 4.16 to house a battery-powered magnetometry system, where an Arduino Nano is used to read the output of a flux-gate magnetometer and store it on a MicroSD card. This design also includes an accelerometer to read the tilt of the cart and allow angle correction in data analysis, but we have rarely used this feature in reality. All of these components are either plugged in or soldered to a custom PCB inside the cart. The Arduino also receives data from a laser distance sensor, which measures the position of the cart by sending a modulated red laser beam and recording the time of arrival of the reflected light. Since the laser distance sensor is placed outside the vacuum tube, data transmission is done with infrared transceivers.

Table 4.3 contains the part numbers of the electronics, including those used in the cart and with the laser distance sensor. The cart itself is made of 5052 aluminum alloy sheet metal in two parts: a top-open box with riveted corners (also aluminum) and a lid that can be opened to access the components inside. Two pulleys are mounted on the sliding side to guide the cable. The cart measures 5.5" (L) × 1.875" (W) × 1.625" (H) and weighs around 300 g, including its components.

Table 4.3: List of electronics used in the internal magnetometry measurement.

Name	Part number	Notes
Magnetometer	Applied Physics 534D 150-7117	Digital fluxgate, range 1 G
Arduino	Nano	One for each PCB (cart and laser distance sensor)
MicroSD card board	Adafruit 254	≤16 G card only
Battery		Lithium ion polymer 3.7 V
Battery board	Adafruit 2465	
Accelerometer	Adafruit 163	Not necessary
IR transceiver	Vishay TFBS4652-TR1	Need lens on transmitting side
IR encoder/decoder	Microchip MCP2120-I/P	
Laser distance sensor	DFRobot SEN0366	

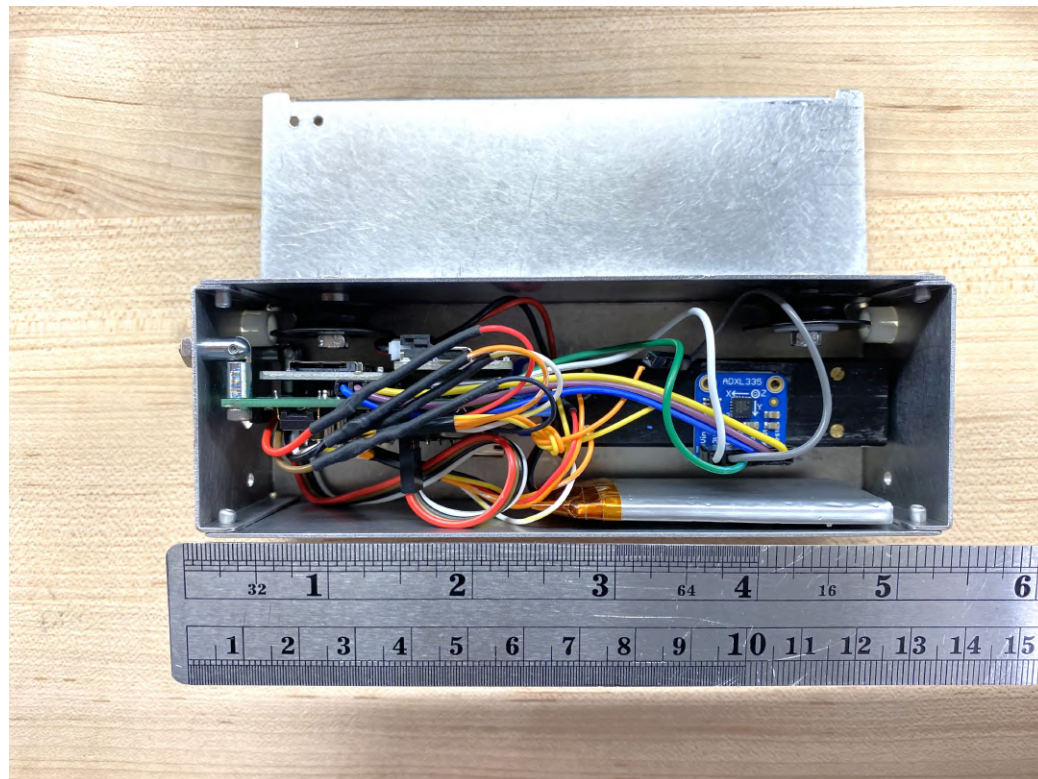


Figure 4.16: The magnetometry cart and its enclosed electronics, which includes a flux-gate magnetometer, an Arduino Nano, a data-logger, an accelerometer, and a battery. The cart has two internal pulleys that allow sliding on the cable loop. The lid is the actually same size as the cart. It looks smaller because it is farther away from the camera.

Active Pulley Side

The cable loop is held in tension by two pulleys with vertical shafts: a fixed position “active pulley” with a hand wheel to turn the loop and a sliding “passive pulley” on a carriage to tension the loop. Both pulleys are mounted to 80/20 structures, which are attached to the 8” ConFlat flanges at both ends of the vacuum tube. Each connection is made through an aluminum adapter plate of 8” × 8” × 0.25” with two or four mounting holes for 5/16”–24 fasteners. The adapter plate contains a rectangular cut in the center for the cart to travel through and fastener holes to attach to the 80/20 beams. A guard such as a clean used copper gasket should be positioned between the adapter plate and the flange to protect the knife edge.

As shown in Figure 4.17 (a), the 80/20 frame on the active pulley side is just long enough to allow easy access to the magnetometer cart. This is handy since the lid needs to be opened at the start and the end of each measurement.

The preparation for a measurement is done on this side. This includes plugging in the MicroSD card, turning on the electronics, closing the lid, and wiping the cart with isopropyl alcohol. The cart is then sent into the vacuum tube by turning the hand wheel. Once it hits a stop on the other end, the hand wheel is turned backward to retrieve the cart. Thus, the magnetometer measures along the length of the tube twice. The measurement ends when the cart returns to the active pulley side. The MicroSD card is collected and the system is ready for the next measurement.

Passive Pulley Side

As shown in Figure 4.17 (b), the pulley on the passive side is mounted on a T-slot slider, which can move on a pair of long 80/20 rails and modify the tension of the cable loop. The slider is pulled by a spring scale and then a ratchet strap. The stretchiness of the cable loop requires 2.5’ ~ 3’ extra length on the 80/20 rail, hence the extra length of the rails. Cable tensioning is done with the ratchet strap. We usually targeted around 100 lbs on the gauge, which translates to 50 lbs tension on the cable.

Although we were generally satisfied with the mechanical structure, we recognized that the longer length of the 80/20 structure on the passive pulley side led to deflections and uncertainty in the position of the magnetometer. It is better to split the length between the active and the passive pulley side, possibly by moving the laser distance sensor to the active pulley side.

Laser Distance Sensor

The laser distance sensor shown in Figure 4.17 (c) is controlled by a second Arduino Nano and periodically measures the location of the cart using a laser beam. The Arduino then encodes this information and sends it to the cart via an IR transceiver. All electronics, except for the laser distance sensor itself, are mounted on a custom PCB. The laser distance sensor has a larger profile

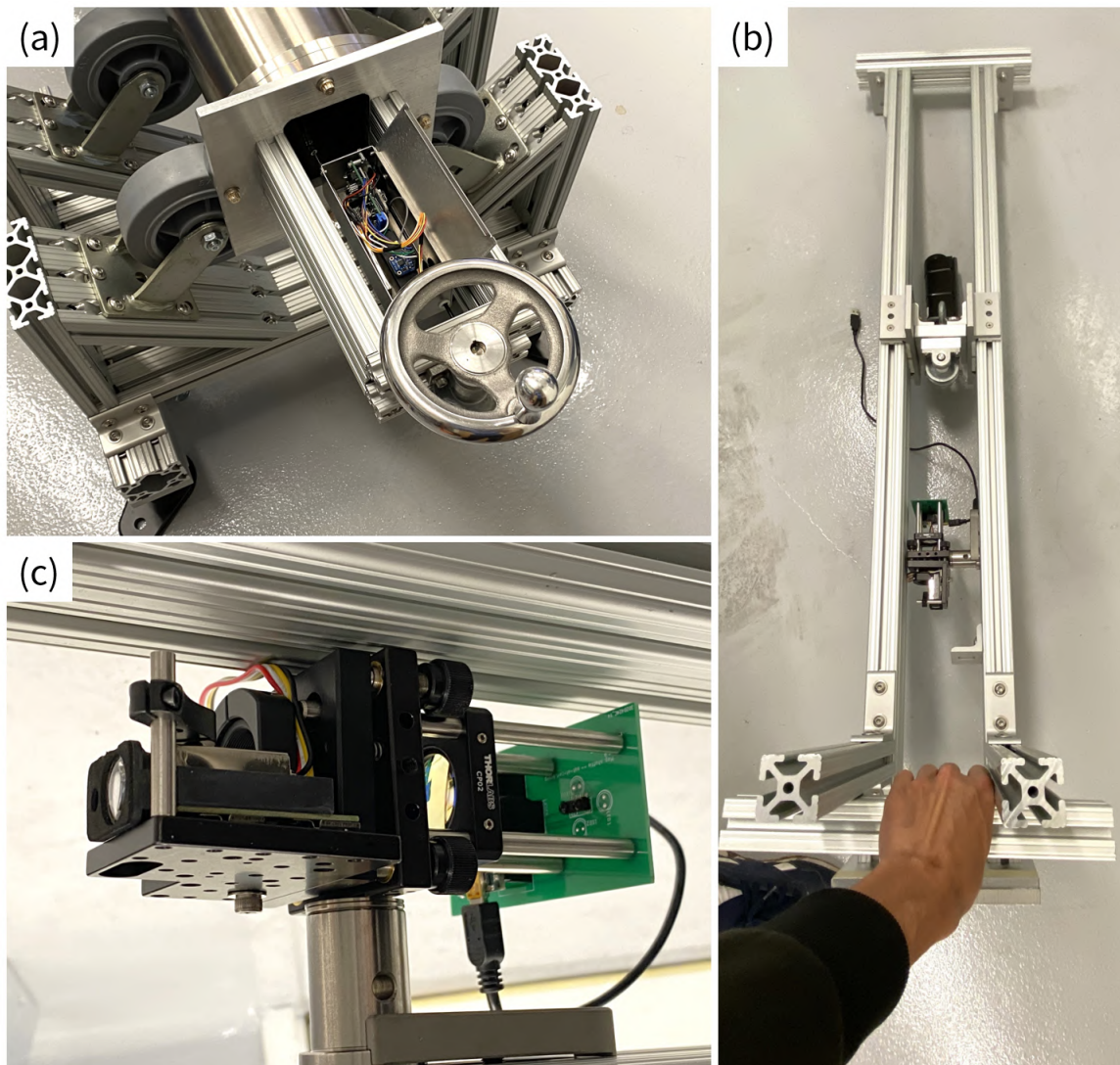


Figure 4.17: The internal magnetometry setup, including (a) the active pulley side with a hand wheel, (b) the passive pulley side with the spring scale and the laser distance sensor, and (c) the laser distance sensor on a kinematic mount.

and connects to the PCB via ribbon wires.

To enhance the range of IR transmission, an $f = +50$ mm lens is placed in front of the IR transceiver. The lens is supported by a Thorlabs 30 mm cage. The PCB design has incorporated mounting holes for the cage system. A kinematic mount fixed to the 80/20 on the passive pulley side supports the laser distance sensor. It also supports the lens mount mentioned above. The setup is arranged so that the laser and IR transceiver are facing the same direction, which can be adjusted via the kinematic mount knobs. We used these knobs to align the laser beam into the vacuum system, so that it would not hit the walls of the vacuum tube and always landed on the front surface of the cart.

Magnetometer Calibration

Bias in the magnetometer reading comes from two sources: the internal offset of the sensor chip, and the magnetization from the electronics inside the cart. Each of them can contribute to a background of a few to tens of mG. Keep in mind that this bias is not a function of position, and thus is not relevant if we only care about field variation. It matters when we need to measure the absolute field inside the shield.

To remove the first source of sensor bias, we fixed the magnetometer inside a small mumetal container²⁸, while leaving all the electronics out, sufficiently far away from the container. We then closed the lid as much as we could, leaving only a small space for the wires to exit the container. We then flipped or rotated the container 180°. For both orientations, the magnetic field readings were recorded and compared. For the axes of the magnetometer that are flipped, the readings should nominally be equal and opposite, yet the bias would have the same sign. We therefore deduced the bias by averaging the readings. We used this method to calibrate all three axes. To remove the second source of sensor bias, we secured the magnetometer to the cart and set the cart at a fixed position. We then moved the electronics into and out of the cart and measured the differential field. After calibration, the bias was subtracted from the measured field. We believed that the bias could be measured up to mG level, which set the error bar of our absolute field measurement.

Data Analysis and Results

In a typical measurement, as we turn the hand wheel and send the cart down the tube, the Arduino queries the IR receiver about its position data. Once the data are received, the Arduino sends a serial command to the magnetometer asking for the field components. It also reads the output voltages of the accelerometer and converts them into units of g ²⁹. Once the magnetometer has received the feedback, it writes the position, acceleration, and field values to the MicroSD card. To analyze the

²⁸A cylindrical 3.4" × 1.73" can from [Magnetic Shield Corporation](#).

²⁹The acceleration data can be used to correct for the tilt of the cart. This correction is not always necessary.

data, the file on the MicroSD card is cleaned (somehow the first data point is always corrupted) and read by a Mathematica script.

Magnetic field measurements of both shield sections are summarized as Figure 4.18 and Figure 4.19. In both measurements, a single coil was looped around the shield section at each end and driven by a DC power supply in constant current mode to suppress the edge effect from the shield. The current was set to roughly cancel the magnetic field reading in the longitudinal direction when the cart was parked at a specific location near the coil³⁰. The measurement was taken in two passes when the cart made a round trip through the vacuum tube. The good agreement between the two passes indicates the reproducibility of the position of the cart and the smoothness of the drive by the active pulley.

The measured magnetic field achieves an RMS amplitude below 1 mG and meets our design specifications. The residual magnetic field features are concentrated in a few regions in the long vacuum tube and the electrode chamber, which we attribute to the small magnetization of the stainless steel vacuum system despite all the annealing steps we have performed. Since all of these field anomalies are within 2 mG in amplitude, we decide that they should not significantly affect the performance of the interferometer. We are also pleased to find that the shield joints do not contribute to noticeable magnetic field spikes, which validates the staggered shield design.

4.5 Adaptations to MAGIS-100

The lessons learned and procedures developed during the design and construction of the tower magnetic system can be applied to MAGIS-100 with some adjustments tailored to the much longer shielded region. Some of these modifications are summarized here.

4.5.1 Sectional Shield and Bias Coil Bars

Since the MAGIS-100 sections are about 5.8 m and 40% longer than the lower section of the tower, the lengths of the mu-metal pieces that make up the magnetic shield need to be redesigned. Taking into account the length constraint set by annealing furnaces, along the length of the shield section, three pieces of mu-metal are likely required. Despite this difference, the shield design should still follow the principles summarized in Section 4.2.3. The assembly procedures described in Section 4.2.4 can be easily applied to MAGIS-100 and allow fast construction of many identical shield sections.

The bias coil bars, on the other hand, may require major modifications, as the current strategy with eight magnet wires in a Unistrut channel is not scalable to a total of 17 shield sections and requires too many connector cables between them. Ongoing work has been performed to simplify

³⁰A single coil only cancels the magnetic field at a single location. In the actual tower, we use two coils to achieve cancellation of both the field and its gradient, allowing better suppression of the edge effect of the shield. Also note that the current setting of the coil on one end will affect the magnetic field reading on the other end due to the magnetic conductivity of the shield.

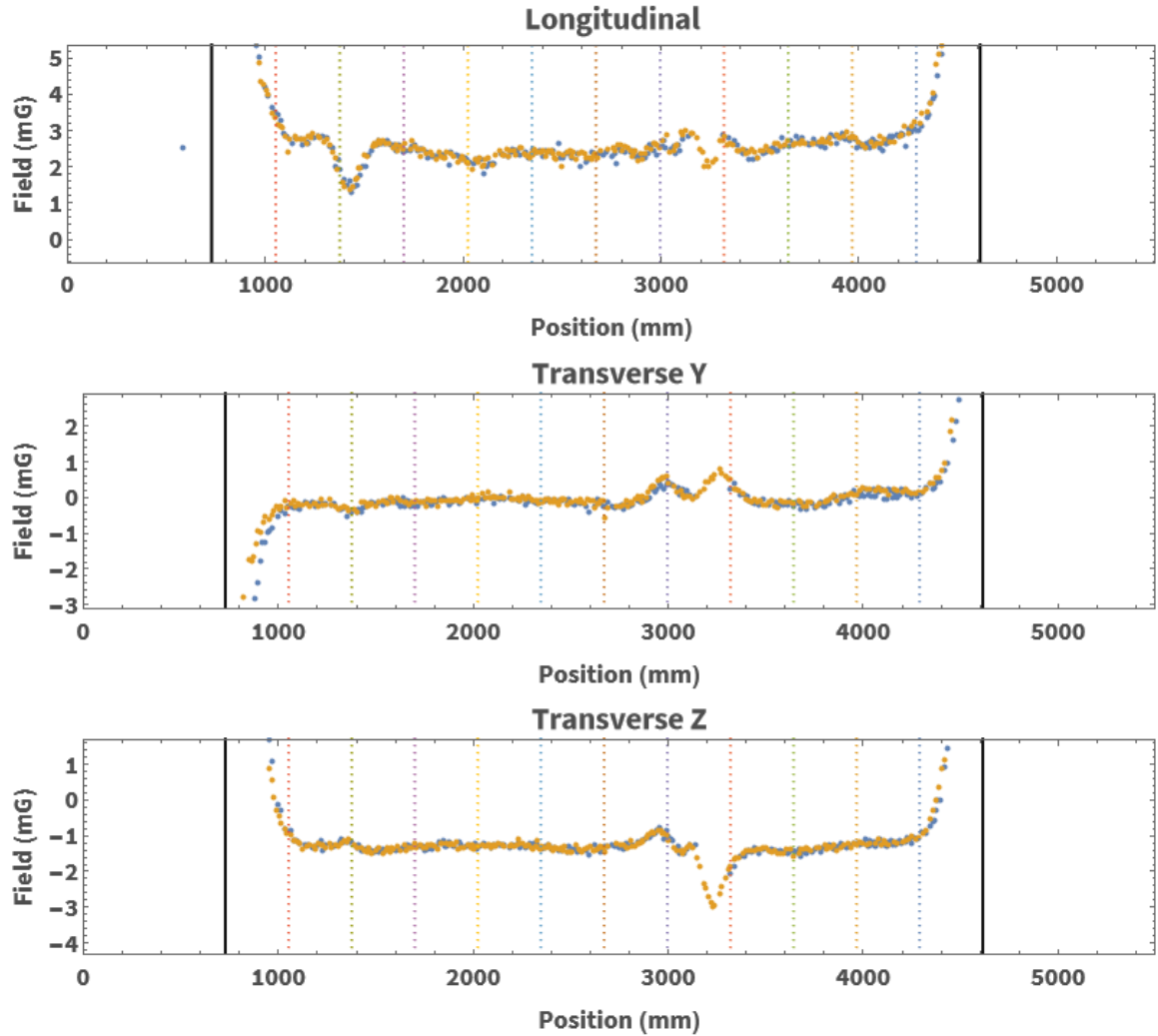


Figure 4.18: Internal magnetometry result of the lower shield section. The magnetometer was calibrated with the procedure described above and the edge effect of the shield along the longitudinal direction was roughly canceled by a single coil at each end of the section indicated by the black lines. The dotted lines indicate the rib locations. Blue and yellow data points are magnetic field measurements in two passes of a round trip. The good agreement between the two passes show the reliability of our internal magnetometry method.

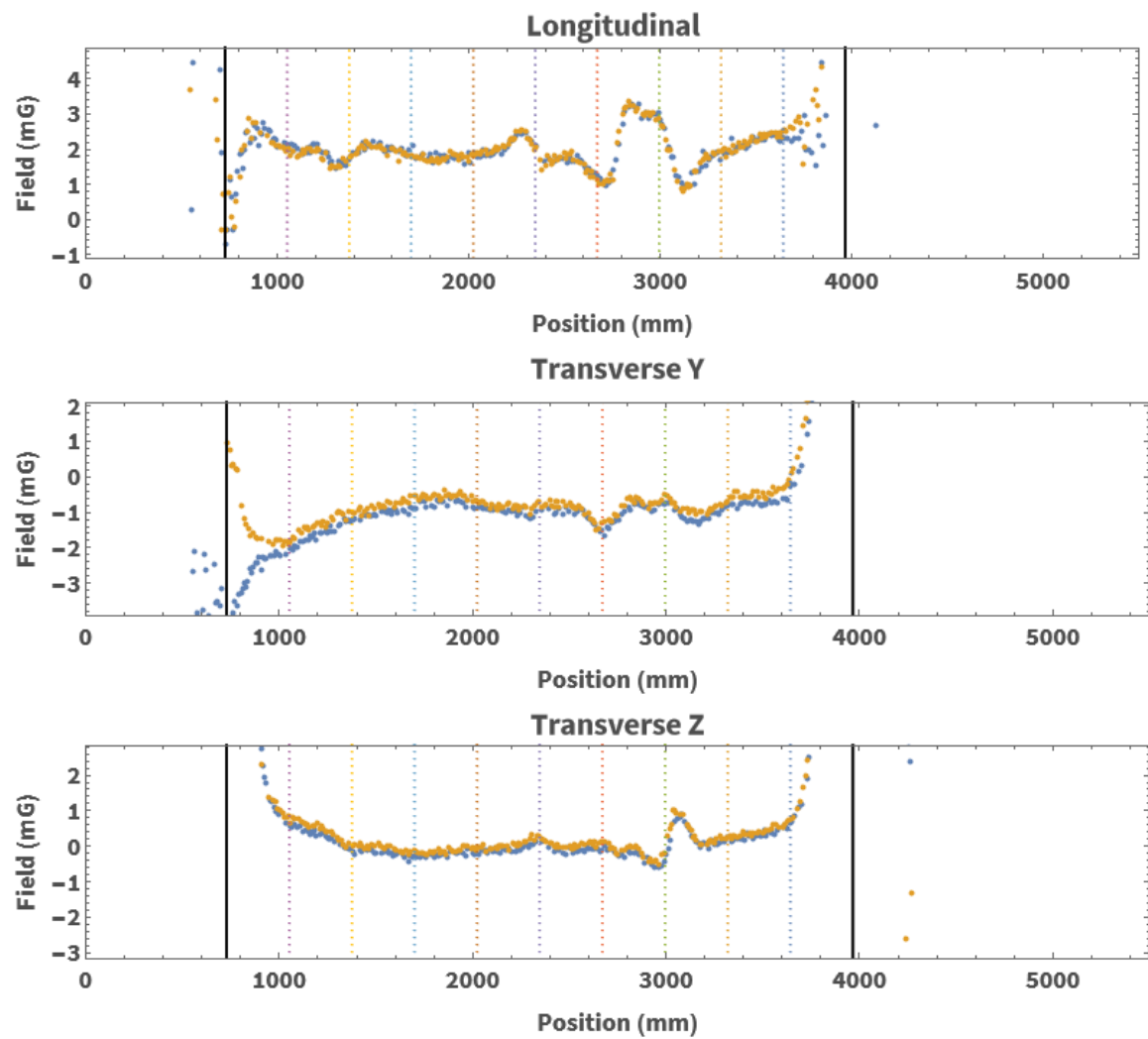


Figure 4.19: Internal magnetometry result of the upper shield section. This section is shorter than the lower shield section by two rib spacings.

the bias coil bar into a single conductor. Permanent out-of-shield conductors are also planned to complete a degaussing loop that encloses multiple shield sections at the same time.

4.5.2 Couplers and Longitudinal Compensation Coils

The vacuum design of MAGIS-100 requires an ion pump between each 5.8 m-long modular section. Therefore, a modular connection node referred to as the “non-atom-source connection node” is planned between each tube section, except for at each of the three atom sources, where a tower-like “atom-source connection node” is installed. These non-atom-source connection nodes also provide optical access for diagnostic cameras. They are much smaller than the atom-source connection nodes, but still require a macroscopic gap in the magnetic shield to allow equipment access and to create a vacuum extension for the ion pump so its magnet can be far away from the shielded region. Although compensation coil boxes similar to the one discussed in Section 4.3.3 can be used to maintain the homogeneity of the magnetic field at the shield gaps, this strategy requires more than 40 coil pairs and power supplies, which are difficult to deploy in the shaft.

Instead, a magnetic shield joint referred to as the “coupler” was proposed, which is illustrated in Figure 4.20 without the mechanical details. Each coupler consists of two separate pieces of octagonal mu-metal sleeves that slide up and down along the neighboring shield sections. They can be opened for equipment access at the non-atom-source connection node, or closed to bridge the magnetic shield gap during interferometry operations. Although the coupler has a radial gap with respect to the shield sections, simulation shows that the homogeneity of the magnetic field is minimally impacted in the transverse direction. To address the field leakage in the longitudinal direction, a pair of coils is positioned outside the coupler. This design effectively reduces a three-dimensional coil compensation problem to one-dimensional, significantly reducing the number of power supplies per connection node.

Furthermore, although the couplers effectively couple the neighboring shield sections to form a 50 m-long continuous shield, simulation shows that the existence of these longitudinal compensation coils avoids the saturation of mu-metal in the large aspect ratio limit discussed in Section 4.2.2. This can be viewed as the coils acting as a sparse solenoid that partially cancels the background field experienced by the mu-metal, which in turn low-pass filters the spatial discreteness of the coils. Inspired by this fact, we have found that an additional compensation coil at the middle of each shield section can achieve better magnetic field homogeneity and further alleviation of mu-metal saturation.

4.5.3 Magnetometry

Due to the possibility of fracturing, I do not recommend the use of a monofilament fishing line for internal magnetometry in MAGIS-100. After we performed our magnetometry measurements, we found suppliers for titanium wire ropes. For example, Spectore sells a 1/8" diameter wire rope by

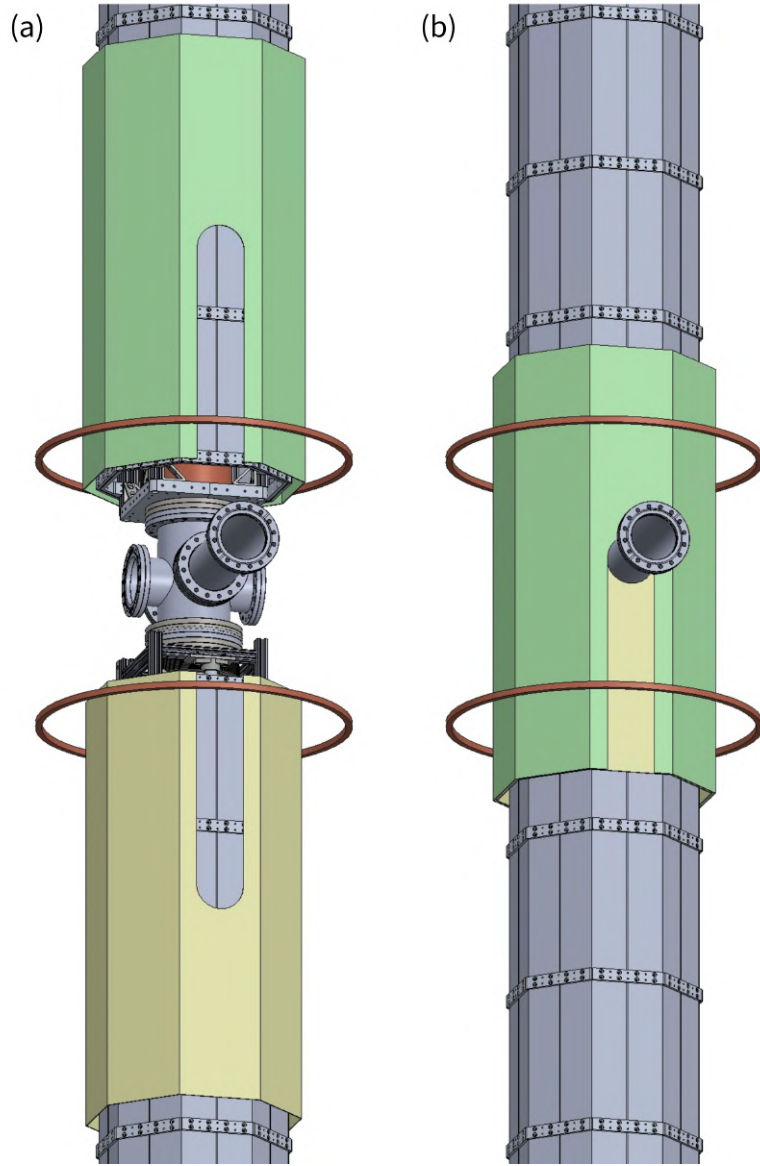


Figure 4.20: Magnetic shield coupler at the shield gap of a non-atom-source connection node. Since the connection node has an ion pump port that extends out of the shield, the coupler is split into two slotted parts, shown as green and yellow. They are able to slide along the shield sections to switch between (a) open and (b) closed configurations. In the open configuration, the connection node is fully accessible for equipment installation and maintenance. In the closed configuration, the connection node is magnetically shielded for the experiment. Magnetic field leakage through the coupler gaps is mostly in the longitudinal direction, and can be compensated by a pair of coils, which also serves the purpose of reducing the magnetic field concentration inside mu-metal. Additional longitudinal coils can be placed at the middle of the shield sections to further suppress mu-metal saturation.

foot³¹. Titanex claims that theirs are medical grade and can offer ultrasonic cleaning and alcohol rinse, which can ensure that there are no contaminants³². Carl Stahl Sava Industries claims to be able to produce a titanium or tungsten wire rope with a plastic coating for wipe-down, but it would be a custom item³³. These non-magnetic metal wire rope should allow high tension without the risk of mechanical failure. For MAGIS-100 sections, a distance of 6 m between the pulleys requires 100 lbs tension to reduce the sag to 5 mm.

Alternatively, since the modular tube sections in MAGIS-100 do not contain in-vacuum components and have a uniform aperture, an automated cart with clean wheels can also be considered as a magnetometer carrier [151].

³¹Spectore grade 5 titanium cable.

³²Titanex titanium strands, cables, and ropes.

³³Carl Stahl Sava Industries custom wire ropes.

Chapter 5

Optical Lattice Transport

Optical lattices are periodic trapping potentials generated by standing-wave laser fields. A stationary 1D lattice is usually formed by interfering two counterpropagating laser beams of identical polarization and frequency detuned from the atomic transition. The periodicity is defined by half of the laser wavelength. Higher-dimensional lattices can be created with more than two laser beams. The spatially dependent light intensity induces a proportional potential landscape in atoms interacting with an optical lattice, via a phenomenon known as the AC stark shift [54, 55]. The atoms are trapped in the nodes or anti-nodes of the lattice depending on the sign of the shift and exhibit the same periodic spatial distribution as the interference fringes of light.

Optical lattices of various dimensions have been widely used in the trapping and cooling of ultracold atoms due to their merits such as simplicity of construction and large span over space [157–166]. Moreover, one can move a 1D optical lattice in space simply by setting the frequencies of the two counterpropagating beams different. The velocity of the moving lattice is proportional to the frequency difference. A time-dependent motion is achieved if the differential light frequency is a function of time. Atoms loaded in such a lattice will efficiently follow its motion as long as the acceleration is small compared to some critical value determined by the band structure. Since the frequency of the lattice beams can be precisely controlled by optical modulation devices, it is possible to impart a well-defined velocity to an atom cloud at rest. When the process is later reversed, the atoms can be brought back to rest but shuttled over a macroscopic distance [136, 167, 168].

The prototype tower and MAGIS-100 use moving optical lattices in two scenarios. After sufficient cooling in the atom source chamber, the atoms are loaded into a shuttle lattice, which transports them horizontally over a macroscopic distance to the connection node chamber. Then, the atoms are loaded into a vertical launch lattice, which accelerates them to an initial velocity that is necessary to achieve long free-fall times under gravity. This chapter introduces the design and realization of both optical lattices in the tower.

5.1 Optical Lattice Basics

5.1.1 Periodic Optical Potential

As discussed in Section 2.1, when atoms in the ground state are exposed to an off-resonant electromagnetic field, they experience an AC Stark shift that changes the energy level in a direction determined by the sign of detuning Δ . In the limit where $|\Delta|$ is much larger than the Rabi frequency Ω , this light shift approximates to

$$\Delta E = \frac{\hbar\Omega^2}{4\Delta} = \frac{I}{I_{\text{sat}}} \frac{\hbar\Gamma^2}{8\Delta} \quad (5.1)$$

where I is the laser intensity, I_{sat} and Γ are the saturation intensity and linewidth of the specific transition. Therefore, when the laser intensity changes as a function of position, the atoms experience a position-dependent potential, which can be used to trap the atoms to where $I(\mathbf{x}) \text{sgn}(\Delta)$ is minimized. In a red-detuned optical potential, $\Delta < 0$ and the atoms are trapped in regions of high intensity. In contrast, in a blue-detuned optical potential, $\Delta > 0$ and the atoms are trapped in regions of low intensity.

The optical potential does not necessarily have one single minima. For example, a 1D optical lattice is a periodic potential with multiple peaks and troughs that span a long distance, engineered by overlapping two laser beams of identical intensities and polarizations and similar frequencies. Although an optical lattice can occur with any non-zero angle between the wave vectors, it is often desirable to arrange the two beams in a (near) counterpropagating configuration to maximize their overlap and reduce the lattice spacing. However, for general discussion, we assume that the two laser beams have wave vectors \mathbf{k}_1 and \mathbf{k}_2 of almost the same magnitudes, and corresponding angular frequencies $\omega_1 = ck_1$ and $\omega_2 = ck_2$, so that $\delta\omega = \omega_1 - \omega_2$ is small compared to ω_1 or ω_2 . The electric fields of the two beams are

$$\mathbf{E}_1(\mathbf{x}, t) = E_0 \hat{\epsilon} \cos(\mathbf{k}_1 \cdot \mathbf{x} + \omega_1 t + \phi_1) \quad (5.2)$$

$$\mathbf{E}_2(\mathbf{x}, t) = E_0 \hat{\epsilon} \cos(\mathbf{k}_2 \cdot \mathbf{x} + \omega_2 t + \phi_2) \quad (5.3)$$

where the two beams have the same electric field amplitude E_0 and polarization $\hat{\epsilon}$. Their phases are denoted as ϕ_1 and ϕ_2 . The total electric field is

$$\mathbf{E}(\mathbf{x}, t) = \mathbf{E}_1(\mathbf{x}, t) + \mathbf{E}_2(\mathbf{x}, t) \quad (5.4)$$

$$= 2E_0 \hat{\epsilon} \cos(\mathbf{k}_{\text{avg}} \cdot \mathbf{x} + \omega_{\text{avg}} t + \phi_{\text{avg}}) \cos(\mathbf{k}_{\text{half-diff}} \cdot \mathbf{x} + \omega_{\text{half-diff}} t + \phi_{\text{half-diff}}) \quad (5.5)$$

where the subscripts “avg” and “half-diff” refer to the average and half-difference between the two beams. The total intensity is proportional to the time-averaged energy density of the electromagnetic

wave, given by

$$I(\mathbf{x}, t) = c \varepsilon_0 \langle \mathbf{E}(\mathbf{x}, t)^2 \rangle \quad (5.6)$$

$$= 4c \varepsilon_0 E_0^2 \langle \cos^2(\mathbf{k}_{\text{avg}} \cdot \mathbf{x} + \omega_{\text{avg}} t + \phi_{\text{avg}}) \rangle \cos^2(\mathbf{k}_{\text{half-diff}} \cdot \mathbf{x} + \omega_{\text{half-diff}} t + \phi_{\text{half-diff}}) \quad (5.7)$$

$$= 2c \varepsilon_0 E_0^2 \cos^2(\mathbf{k}_{\text{half-diff}} \cdot \mathbf{x} + \omega_{\text{half-diff}} t + \phi_{\text{half-diff}}) \quad (5.8)$$

where the fast oscillating term averages to 1/2. Notice that $I_0 = c \varepsilon_0 E_0^2 / 2$ is the intensity of a single beam. Therefore,

$$I(\mathbf{x}, t) = 4I_0 \cos^2(\mathbf{k}_{\text{half-diff}} \cdot \mathbf{x} + \omega_{\text{half-diff}} t + \phi_{\text{half-diff}}) \quad (5.9)$$

$$= 2I_0 (1 + \cos((\mathbf{k}_1 - \mathbf{k}_2) \cdot \mathbf{x} + \delta\omega t + (\phi_1 - \phi_2))) \quad (5.10)$$

In the scenario of near counterpropagating beams, we denote the small angle between \mathbf{k}_1 and $-\mathbf{k}_2$ as $\delta\theta$, and arrange the coordinate system so that

$$\mathbf{k}_1 = \frac{1}{c} \left(\omega + \frac{\delta\omega}{2} \right) \left(\cos \frac{\delta\theta}{2} \hat{\mathbf{x}} + \sin \frac{\delta\theta}{2} \hat{\mathbf{y}} \right) \quad (5.11)$$

$$\mathbf{k}_2 = -\frac{1}{c} \left(\omega - \frac{\delta\omega}{2} \right) \left(\cos \frac{\delta\theta}{2} \hat{\mathbf{x}} - \sin \frac{\delta\theta}{2} \hat{\mathbf{y}} \right) \quad (5.12)$$

where ω is used as a shorthand for ω_{avg} . Then the wave vector difference is

$$\mathbf{k}_1 - \mathbf{k}_2 = \frac{2\omega}{c} \left(1 - \frac{1}{8} \delta\theta^2 + \mathcal{O}(\delta\theta^4) \right) \hat{\mathbf{x}} + \frac{\delta\omega}{2c} (\delta\theta + \mathcal{O}(\delta\theta^3)) \hat{\mathbf{y}} \quad (5.13)$$

Since $\omega \sim 10^{15}$ rad/s is many orders of magnitude larger than typical $d\omega$, it is safe to drop the $\hat{\mathbf{y}}$ component. Keeping the lowest non-trivial order in $\delta\theta$, we have

$$I(x, t) = 2I_0 \left(1 + \cos \left(\frac{2\omega}{c} (1 - \delta\theta^2/8) x + \delta\omega t + (\phi_1 - \phi_2) \right) \right) \quad (5.14)$$

which is a 1D spatial intensity modulation moving along $-\hat{\mathbf{x}}$, whose effective wave vector and velocity are given by

$$k_{\text{eff}} = \frac{2\omega}{c} (1 - \delta\theta^2/8) \quad (5.15)$$

$$v = \frac{c \delta\omega}{2 \omega} (1 + \delta\theta^2/8) \quad (5.16)$$

The velocity can be a function of time by chirping $\delta\omega$, allowing acceleration and deceleration of the optical lattice. This intensity modulation leads to a periodic potential experienced by the atoms, whose depth is obtained by applying the intensity difference between the peak and the trough to

Equation (5.1). This can be written in terms of single beam Rabi frequency Ω_0 as

$$U = \frac{\hbar\Omega_0^2}{\Delta} \quad (5.17)$$

5.1.2 Bloch States and Band Structure

Atoms in a stationary 1D optical lattice can be described by the following Hamiltonian

$$\hat{H} = -\frac{\hbar^2}{2m}\partial_x^2 + \frac{U}{2} \cos(k_{\text{eff}}x) \quad (5.18)$$

whose general eigenstates take the form of the Bloch states, which, up to a phase e^{iqx} , have the same periodicity as the potential. The wave vector q is referred to as the quasimomentum and is defined up to the lattice reciprocal vector k_{eff} , thus usually taking values in the first Brillouin zone where $q \in (-k_{\text{eff}}/2, k_{\text{eff}}/2]$. The eigenvalues form discrete energy bands, and the eigenstates are labeled by the band index n and the quasimomentum q .

Here we drop the $\delta\theta^2$ terms in k_{eff} and use the simplified expression $k_{\text{eff}} = 2k$, where $k = \omega/c$. Since the periodic potential takes the form of a simple cosine, it is straightforward to decompose the Bloch states in the plane-wave basis. Let $\psi_{q+jk} = e^{i(q+jk)x}$ where $j \in \mathbb{Z}$, then¹

$$\hat{H}\psi_{q+jk} = -\frac{\hbar^2}{2m}(-i(q+jk))^2\psi_{q+jk} + \frac{U}{4}(e^{ikx} + e^{-ikx})\psi_{q+jk} \quad (5.19)$$

$$= \frac{\hbar^2(q+jk)^2}{2m}\psi_{q+jk} + \frac{U}{4}\psi_{q+(j-2)k} + \frac{U}{4}\psi_{q+(j+2)k} \quad (5.20)$$

which states that the Hamiltonian couples a plane wave to other plane wave states whose wave vectors are separated by $2k$. We introduce the dimensionless quasimomentum $\tilde{q} = q/k$, as well as the recoil energy $E_r = \hbar^2k^2/2m$ and the dimensionless trap depth $u = U/E_r$. The Bloch states as a superposition of plane waves correspond to the eigenvectors of the following tri-diagonal matrix

$$\mathcal{H}_q = E_r \begin{pmatrix} \ddots & \ddots & & & & & \\ \ddots & (\tilde{q}-4)^2 & u/4 & & & & \\ & u/4 & (\tilde{q}-2)^2 & u/4 & & & \\ & & u/4 & \tilde{q}^2 & u/4 & & \\ & & & u/4 & (\tilde{q}+2)^2 & u/4 & \\ & & & & u/4 & (\tilde{q}+4)^2 & \ddots \\ & & & & & \ddots & \ddots \end{pmatrix} \quad (5.21)$$

¹This notation is a bit weird, but I cannot find a better symbol than j for integers. Among the other common integer labels, n is reserved for the band index, m is already used as the mass, i is the imaginary unit, and k is the wave vector. Readers should be able to figure out that jk means j units of the wave vector k .

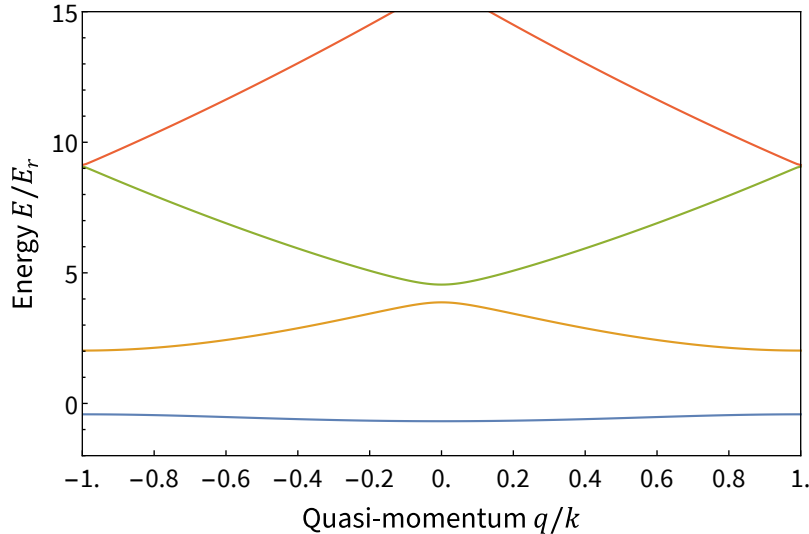


Figure 5.1: The band structure of an optical lattice when $u = 5$.

where the basis consists of plane waves ψ_{q+jk} with $j = \dots, -4, -2, 0, 2, 4, \dots$. The coupling between plane waves separated by $2k$ can be understood as a coherent two-photon process, where the atoms absorb a photon from one beam and stimulated emit a second photon into the other.

The Hamiltonian in Equation (5.21) can be numerically diagonalized by truncating to a certain momentum order. The resulting eigenvalues $E_{q,n}$ form a band structure like Figure 5.1, where the first band gap occurs at the edge of the first Brillouin zone and increases with the depth of the trap shown in Figure 5.2. In the limit of a shallow trap, the band gap approximates to

$$E_{\text{BG}}^{(1)} \approx U/2 = \frac{\hbar\Omega_0^2}{2\Delta} \quad (5.22)$$

which matches the Rabi frequency of the two-photon process mentioned above, detuned from the virtual excited state by Δ .

Generally speaking, it is preferable that the atoms stay in the lowest band. Excitation to higher-order Bloch states leads to momentum sidebands after transport [169], which may or may not be resolved from the desired momentum state depending on the temperature of the cloud. Although a momentum filter can be later applied, there is an inevitable reduction of the atom number in the correct velocity class. Therefore, it is important to load, accelerate, and unload the atoms in an adiabatic way, so that the atomic wave function always stays in the instantaneous eigenstate of the Hamiltonian according to the adiabatic theorem. Alternatively, the dynamics can be driven in a controlled manner to achieve “shortcut to adiabaticity”, so that the interband excitations can be suppressed by destructive interference [170].

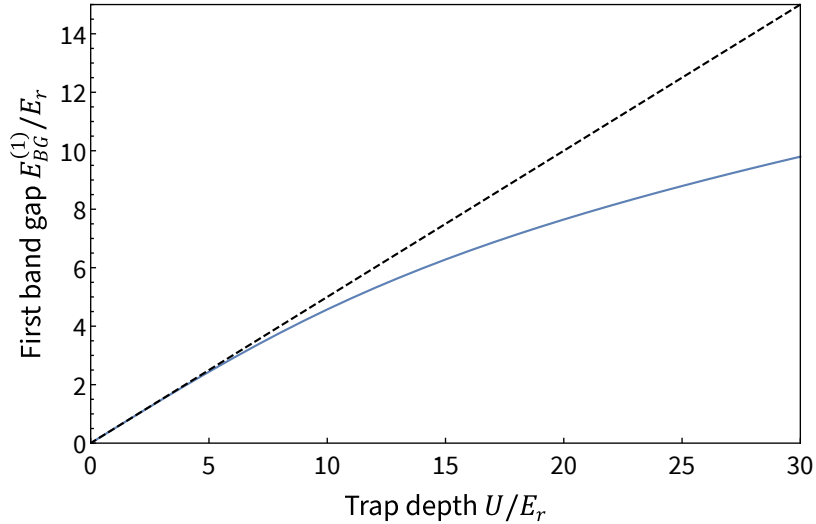


Figure 5.2: The first band gap as a function of the trap depth u . The black dotted line is the shallow trap approximation, where the band gap equals half the trap depth.

5.1.3 Atoms in an Accelerating Lattice

When the two arms (that is, counterpropagating beams) of the lattice are chirped relative to each other, the lattice acquires an acceleration

$$a = \frac{c}{2\omega} \frac{d(\delta\omega)}{dt} \quad (5.23)$$

which exerts a non-inertial force on the atoms in the lattice frame. Assuming a constant acceleration, the lattice Hamiltonian becomes

$$\hat{H} = -\frac{\hbar^2}{2m} \partial_x^2 + \frac{U}{2} \cos(2kx) - ma \cdot x \quad (5.24)$$

when this force is small enough to not cause interband excitations, the quasimomentum of the instantaneous eigenstate increases linearly with time as $q(t) = q(0) + ma/\hbar \cdot t$. The group velocity $v_g = (dE/dq)/\hbar$ changes sign at the center and the edge of the first Brillouin zone, making the atoms oscillate in real space, hence the name “Bloch oscillation”.

In momentum space, every time the quasimomentum crosses the edge of the first Brillouin zone, the momentum of the atoms increases by $2\hbar k$ when observed in the lab frame. Since the period of the oscillation is

$$T_{BO} = \frac{2k}{ma/\hbar} \quad (5.25)$$

over a time $T = n_{BO} T_{BO}$, where n_{BO} is the number of Bloch oscillations, the atoms accumulate a

real momentum

$$p = \frac{T}{T_{\text{BO}}} \times 2\hbar k = maT \quad (5.26)$$

which is equivalent to the classical picture where the atoms are dragged by the accelerating lattice without slipping for a duration T .

The above analysis is performed in the small a limit and ignores the interband excitation. In reality, there is a non-zero transition rate when crossing the edge of the first Brillouin zone, where the band gap is finite. This phenomenon is known as “Landau-Zener tunneling”, with an excitation probability [171, 172]

$$P_{LZ} = e^{-a_c/a} \quad (5.27)$$

where a_c is the critical acceleration given by

$$a_c = \frac{\pi \left(E_{\text{BG}}^{(1)} \right)^2}{4\hbar^2 k} \quad (5.28)$$

In the shallow trap limit, $E_{\text{BG}}^{(1)} = U/2$, thus

$$a_c \approx \frac{\pi U^2}{16\hbar^2 k} \quad (5.29)$$

Note that this approximation underestimates Landau-Zener tunneling by using a larger approximated band gap.

5.2 Shuttle Lattice Design

Horizontal shuttling of atoms is an important procedure for both the tower and MAGIS-100. The necessity of this step originates from the requirement to maximally reduce the interference between atom cooling and atom interferometry, with regard to scattered light, magnetic field, optical access, vacuum system, etc. The vacuum and magnetic field components set the span from the cooling chamber in each atom source to the corresponding connection node in the vertical interferometer to be 62.5 cm, measured from the center of both chambers. This is the distance that the atoms need to travel across.

In this section, I present the concept of a pair of optical lattices that shuttles ultracold atoms horizontally by tossing them from one lattice into the other. By choosing the velocity and acceleration of both lattices, we expect ballistic transport of the atoms over the desired macroscopic distance in a total time of few-10 ms. Gravitational sag during transport is canceled by a small tilt angle of both lattices.

5.2.1 Long-Distance Transport Strategies

Traditional methods of horizontal transport are based on a trapping potential that moves throughout the distance of the shuttle. Because strontium is not magnetically trappable in its ground state, an optical trap is required.

Two types of optical potential are often used as ingredients to achieve long-distance horizontal transport: optical dipole traps (ODTs) and optical lattices, both of which are one-dimensional along the shuttle direction. An ODT is a red-detuned laser beam tightly focused to a small waist, whose axial confinement is often used to counteract gravity [173–175]. Since the region of strong confinement is limited by the typically cm-scale Rayleigh range, movement of the trap must be achieved by shifting the focus of the beam, with devices such as translational stages or varifocal lenses [176, 177]. However, the trapping potential is soft in the axial direction, which limits the maximal acceleration to prevent excitation to higher motional states. An optical lattice, on the other hand, is a periodic potential from the interference of two counterpropagating laser beams. It can provide a tight axial confinement over a long distance, which is movable by introducing a frequency difference between the two beams. However, the Rayleigh range has to be comparable to or greater than the transport distance, which compromises the trap depth against gravity.

To simultaneously achieve fast transport, large movement range, and strong confinement against gravity, one can overlap a lattice with a co-moving ODT. Recently, there has been work [176] that uses focused light in one of the lattice beams to act like an ODT in the axial direction. The focus is shifted by a varifocal lens and is synchronized with the movement of the lattice fringes. Our shuttle system, however, does not benefit from the strategies mentioned above, due to the following reasons:

- Mechanically movable components are not preferred in the system, to reduce heating during transport and minimize maintenance once the interferometer is deployed.
- The shuttle distance is even longer than that in typical works on long-distance atom transport. Confinement against gravity over 62.5 cm is challenging.
- Compatibility with a large atom number of $> 10^6$, thus high efficiency is desired over a large cloud. The beam should be larger than the cloud to reduce loss during loading and shuttling. For our experiment, the size of the cloud is $\sim 100 \mu\text{m}$ assuming loading from a red MOT and $\sim 1 \text{ mm}$ assuming loading from a cloud lensed to $\sim 10 \text{nK}$ temperature.

To address these challenges, we avoid ODTs and design a system that only uses optical lattices formed by mm-sized beams. If arranged horizontally, such a lattice would provide negligible support against gravity. A transport time of 50 ms, which requires a practical acceleration of $\sim 100 g$ for an optical lattice over the shuttle distance, leads to a sag under gravity of 12 mm, much larger than the beam. However, notice that the sag scales quadratically with time. Therefore, if the atom-light interaction time is shortened to $\sim 10 \text{ ms}$, the sag will be only 0.5 mm, which is acceptable for our

chosen beam size. This short amount of time is not sufficient to move the atoms over the required distance with practical acceleration, so we release them at the terminal velocity and allow a free flight of the atoms before they are captured and decelerated by a second lattice. This scheme requires tilting both lattices at opposite angles specifically chosen such that the atoms follow a trajectory that starts and ends at the same height, as shown in Figure 5.3.

By introducing a period of time when the atoms do not interact with the laser beams, we not only alleviate the constraint on the beam size from gravitational sag, but also reduce spontaneous emission loss. However, this benefit does not come for free as we need a more complicated geometry to tilt both lattices and fulfill kinematic requirements.

5.2.2 Double Lattice Geometry

We define the lattice tilt angle θ as the acute angle between the lattice moving direction and the shuttle axis². It is an important parameter that couples to acceleration and atom-light interaction time via kinematics equations, and thus impacts lattice detuning and loss numbers. The tilt angle is chosen such that

- The atoms catapulted from the accelerating lattice are caught by the decelerating lattice and come to a stop at the desired position. In the vertical direction, the atoms must return to the initial height, so they reach apogee half way during free flight. In the horizontal direction, the atoms travel across the full shuttle distance.

$$(a_l \theta - g) t_l = g t_f / 2 \quad (5.30)$$

$$2 \times a_l t_l^2 / 2 + a_l t_l t_f = d \quad (5.31)$$

where t_l, a_l are the time and acceleration the atoms experience inside each lattice, t_f is the free-flight time between the lattices, and $d = 62.5$ cm is the shuttle distance.

- During lattice acceleration, the atoms do not fall out of the laser beam.

$$w = c_1 \times g t_l^2 / 2 \quad (\text{with } c_1 > 1) \quad (5.32)$$

where $w = 2$ mm is the $1/e$ radius of the beams, chosen to be larger than the gravitational sag of ~ 0.5 mm over $t_l \sim 10$ ms time scale, while not too large for considerations of lattice depth. We introduce a dimensionless safety factor c_1 to quantify the overlap between the atoms and the lattice light.

- When the atoms are in one lattice, they are far away from the other lattice.

$$(d/2 - a_l t_l^2 / 2) \times 2\theta = c_2 w \quad (\text{with } c_2 > 1) \quad (5.33)$$

²I use the convention that θ is unsigned. The two lattices should always tilt opposite each other.

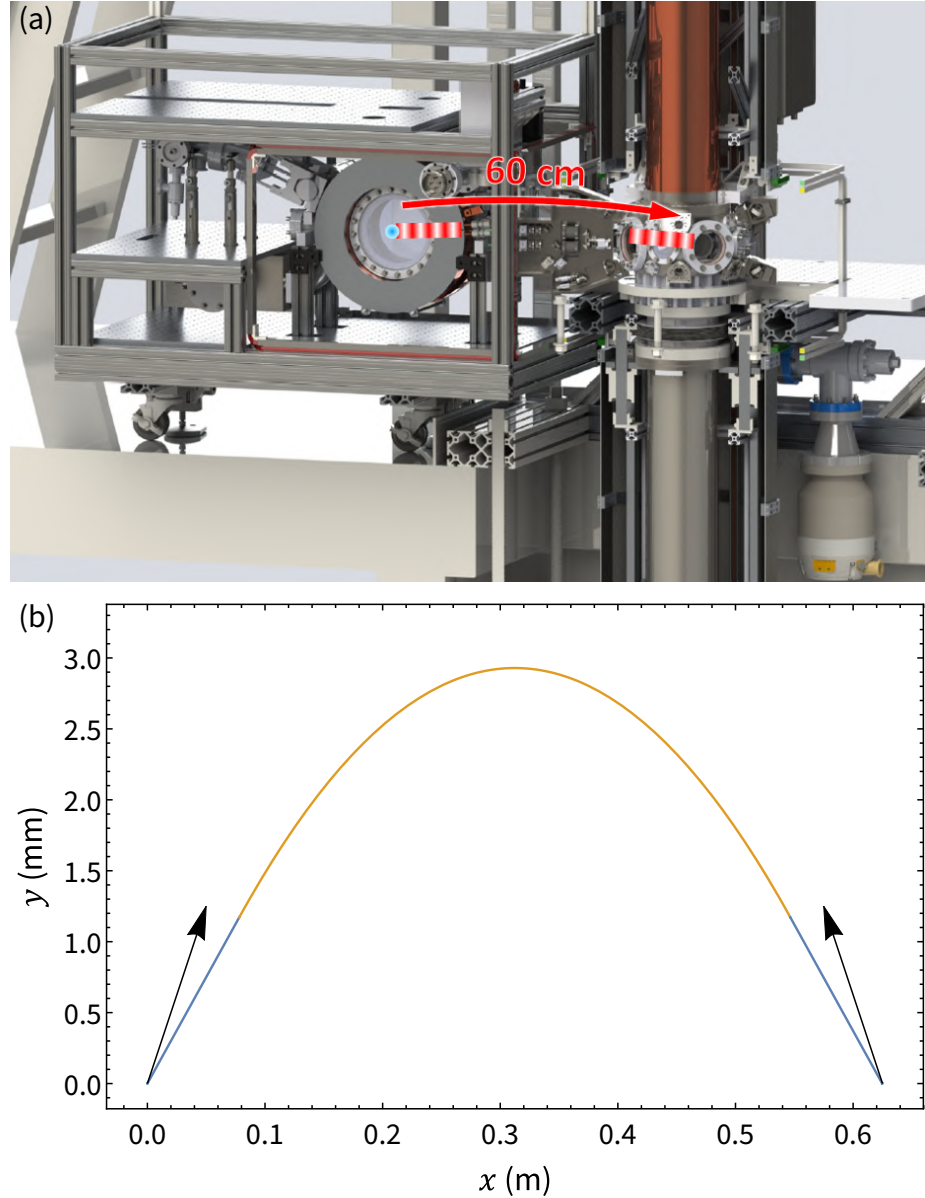


Figure 5.3: Trajectory of the atoms in the toss-and-catch double lattice. (a) An illustration of the double lattice shuttle of the atoms from the atom source to the connection node. (b) The calculated atom trajectory when the lattices are tilted by $\theta = 25$ mrad. The black arrows represent the directions of lattice acceleration. In the presence of gravity, the atoms deviate from the arrows and follow the blue trajectory in the lattice region. In between the two lattices, the atoms trace a parabolic trajectory indicated by the yellow curve.

This is done to make sure that the atoms in one lattice are not affected by the other lattice, with a safety factor c_2 .

- The separation between the two beams at both 2.75" viewports (atom source and connection node) is small enough to clear an aperture of radius $r = 18$ mm.

$$r - d_{v-v}\theta/2 = c_3 w \quad (\text{with } c_3 > 1) \quad (5.34)$$

where $d_{v-v} = 1$ m is the viewport-to-viewport distance. This is the length of the vacuum system along the shuttle axis. The safety factor for beam clipping is c_3 .

We aim for an acceleration of $a_l = 100$ g, which has been demonstrated [29] and is much less than the Laudau-Zener critical acceleration given our lattice specifications. Using Equations (5.30) to (5.34) with the known numbers, we get

$$c_1 = -0.64 + 128\theta > 1 \quad (5.35)$$

$$c_2 = 312.5 \times \frac{\theta(\theta - 0.01)}{\theta - 0.005} > 1 \quad (5.36)$$

$$c_3 = 9 - 250\theta > 1 \quad (5.37)$$

which is illustrated in Figure 5.4. We choose to operate the double lattice at $\theta = 25$ mrad. The corresponding acceleration in each lattice takes $t_l = 12.6$ ms up to a velocity $v_l = 6.2$ m/s, and the time spent in free flight is $t_f = 37.9$ ms. According to Equation (5.16), to achieve this trajectory, the lattice arms needs to be chirped relative to each other over a frequency of

$$\delta f = \frac{2f}{c} v_l = 18 \text{ MHz} \quad (5.38)$$

5.2.3 Orthogonal Degrees of Freedom

To achieve the lattice shuttle geometry described in Figure 5.3, while maximally recycling the light between the lattice arms, we have designed an optical layout shown in Figure 5.5. The two lattice arms, colored red and purple, are delivered by two polarization-maintaining fibers. The lattice light is mainly P-polarized, but contains a small amount of S-polarized mixture for the purpose of fiber noise cancellation that is retro-reflected back into the fiber by a combination of a polarizing beamsplitter (PBS) and a mirror. The details of fiber noise cancellation are discussed in Section 5.3.3. Then both lattice arms are polarization filtered and directed by Picomotor³-actuated mirrors to a common prism mirror. This prism mirror is mounted on a two-axis translational stage, which is also driven by Picomotor actuators. The reflected beams are sent through a lens system where a

³Picomotor™ is the brand name for Newport piezo linear actuators.

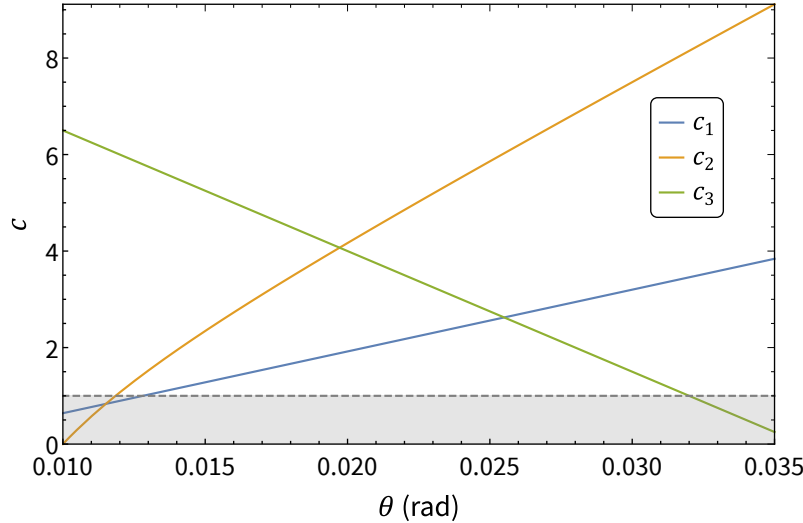


Figure 5.4: Safety factors c_1 , c_2 , and c_3 as functions of θ . The shadowed region is forbidden, where at least one safety factor is less than one. We operate at $\theta = 25$ mrad, where all safety factors are greater than 2.5.

$f = +75$ mm lens and a $f = +250$ mm lens are placed on the atom source side, a $f = +200$ mm lens and a $f = +75$ mm concave mirror (also with Picomotor actuators) on the connection node side. The distances between optics are set so that the first lattice arm on its return path maintains collimation in vacuum and overlaps with the second arm, and vice versa, forming two lattice regions in a cross-geometry. The two returned lattice arms are monitored by lateral position sensors⁴, whose readings can feedback to the Picomotors to stabilize the double lattice.

The tilt of the two lattices, or equivalently, the opening angle and the pointing of the cross, can be adjusted by the two Picomotor-actuated mirrors. However, this adjustment usually leads to a parasitic translation of the cross. To avoid this phenomenon, the lens system is designed so that when the mirrors are tuned, both lattice arms pivot about the center of the cross, placed at the midpoint between the atom source and the connection node. This is achieved by choosing the lens locations to make each of the two mirror surfaces conjugate with the center of the cross, and is verified by a homemade ray tracer shown in Figure 5.6. As a result, changing the lattice tilt angle θ does not induce any translation. The location of the cross, on the other hand, can be independently adjusted by translating the prism mirror. The orthogonality of the degrees of freedom in the double lattice is a highlight of this design and can significantly simplify the alignment procedure.

⁴Thorlabs PDP90A lateral effect position sensor, 320 to 1100 nm.

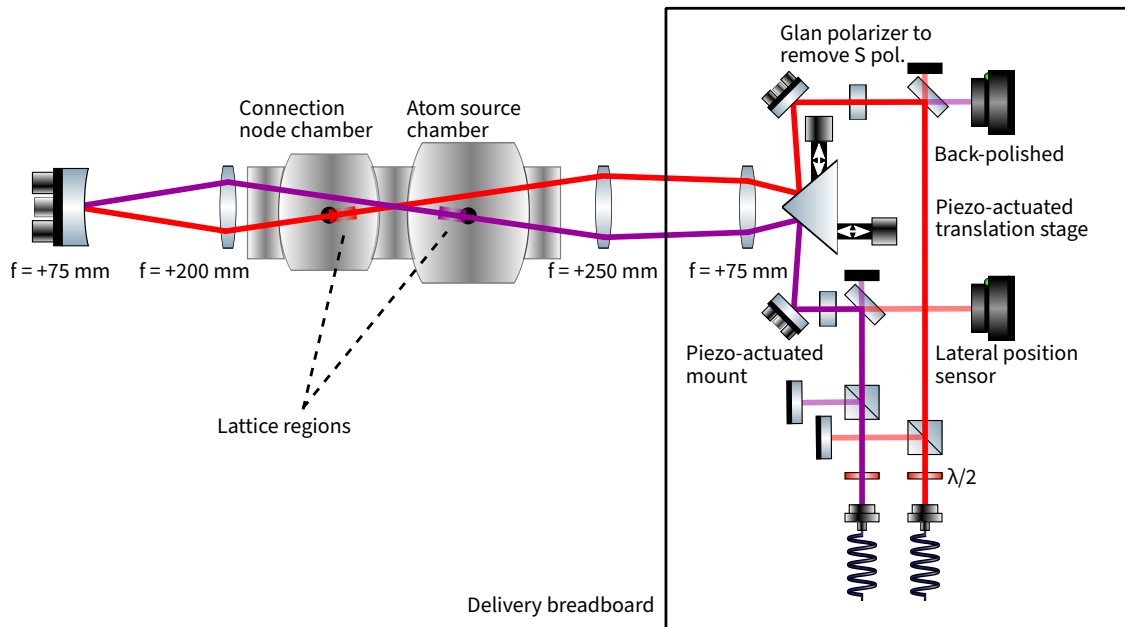


Figure 5.5: Optical diagram of the shuttle lattice. The two lattice arms, colored red and purple, overlap with each other on the return path and form two lattice regions. The lens system is designed to decouple the angle and position adjustment of the lattice cross illustrated in Figure 5.6. The black box contains parts placed on the shuttle lattice delivery breadboard, which is arranged in 3D but shown in 2D for clarity. Note that unlike Figure 5.3, here the shuttle direction is from right to left.

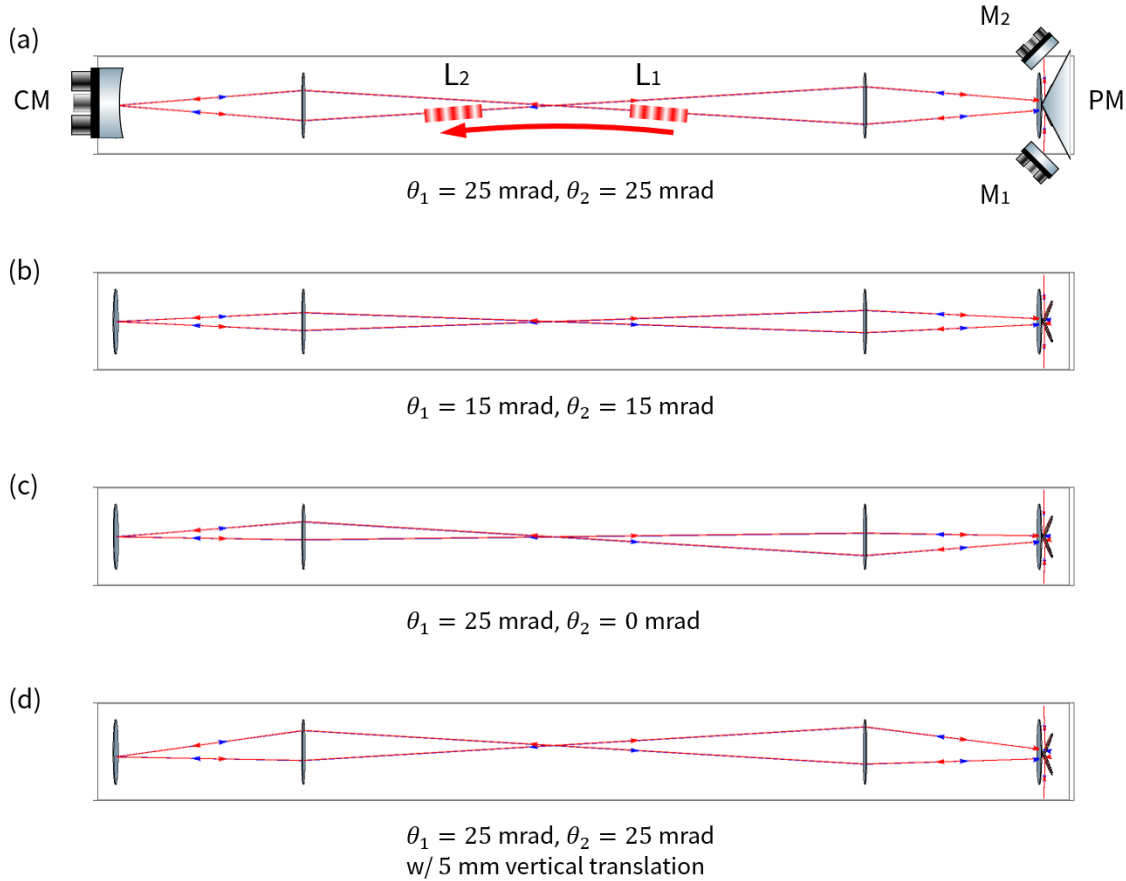


Figure 5.6: Ray tracing of the shuttle lattice delivery setup. (a) The nominal ray diagram where the two lattice regions L_1 and L_2 are tilted by (unsigned) angles $\theta_1 = \theta_2 = 25 \text{ mrad}$. This common angle is tuned by two Picomotor-actuated mirrors M_1 and M_2 by the same amount in opposite directions, whereas an angle difference between L_1 and L_2 can be introduced by adjusting M_1 and M_2 differentially, while compensating with the concave mirror CM on the left. Both types of angle adjustments keep the location of the cross fixed, a result of the conjugate point arrangement in the optical system. The lattice cross can be moved by translating the prism mirror PM on the right and does not affect the lattice angle in the paraxial limit. Examples of these adjustments are shown in the subsequent panels. (b) Turning M_1 and M_2 by 16.7 mrad in opposite directions reduces both θ_1 and θ_2 symmetrically to 15 mrad. (c) Turning M_2 by 66.8 mrad and CM by 13.4 mrad reduces θ_2 to zero while keeping θ_1 unchanged. (d) Translating PM by 1.7 mm raises the lattice cross by 5 mm while keeping both θ_1 and θ_2 unchanged.

5.2.4 Loss Calculation

During optical lattice transport, heating can be induced by several mechanisms and lead to loss of atoms. Specifically, in this subsection, I analyze the effects from non-adiabatic loading and unloading, scattering in the lattice, and Landau-Zener tunneling introduced in Section 5.1.3. We choose 689 nm as the lattice wavelength, so that we can use the same red MOT laser for the lattice. Using the lattice geometry parameters discussed in Section 5.2.2, we can achieve a lattice depth

$$U = 41.5E_r \times \left(\frac{P_{\text{per-beam}}}{200 \text{ mW}} \right) \left(\frac{150 \text{ MHz}}{|\Delta|/(2\pi)} \right) \quad (5.39)$$

from the AC Stark shift of the $^1\text{S}_0 - ^3\text{P}_1$ transition. When each beam is 150 MHz detuned from resonance and has a power of 200 mW, the critical acceleration given by Equation (5.28) evaluates to $1100 g$.

Non-adiabatic Loading

According to the adiabatic theorem, when the lattice is ramped up, the atoms will remain in the instantaneous eigenstate and will not be excited across the band gap if the lattice Hamiltonian increases slowly enough. In the regime of adiabatic loading, the population is completely transferred to the ground band. Similarly, adiabatically ramping down the lattice unloads the atoms into the $p = 0$ plane wave state. However, non-adiabaticity during loading and unloading leads to loss of atoms to the excited bands when loaded and to the $p = \pm 2\hbar k, \pm 4\hbar k, \dots$ plane wave states when released [169]. This can be observed in Figure 5.7.

In addition, optimal control strategies can be used to design lattice pulsing sequences that achieve “shortcut to adiabaticity”, which shortens the loading and unloading times while maintaining low excitation of the atoms [170]. These sequences can be applied in the experiment to improve the performance of the shuttle lattice.

Landau-Zener Tunneling

The critical acceleration calculated above is 11 times higher than the actual acceleration of the lattice. Landau-Zener tunneling is therefore exponentially suppressed to be negligible. This suggests that it is possible to attempt a more aggressive acceleration, which shortens the lattice duration and reduces spontaneous emission loss.

Spontaneous Emission

Scattering of photons leads to heating in an optical lattice. For a deep lattice and atoms initially in the ground band, the total heating rate, measured by the change in energy per unit time of the atoms, is independent of the sign of detuning [137]. However, the origin of this heating is different between a

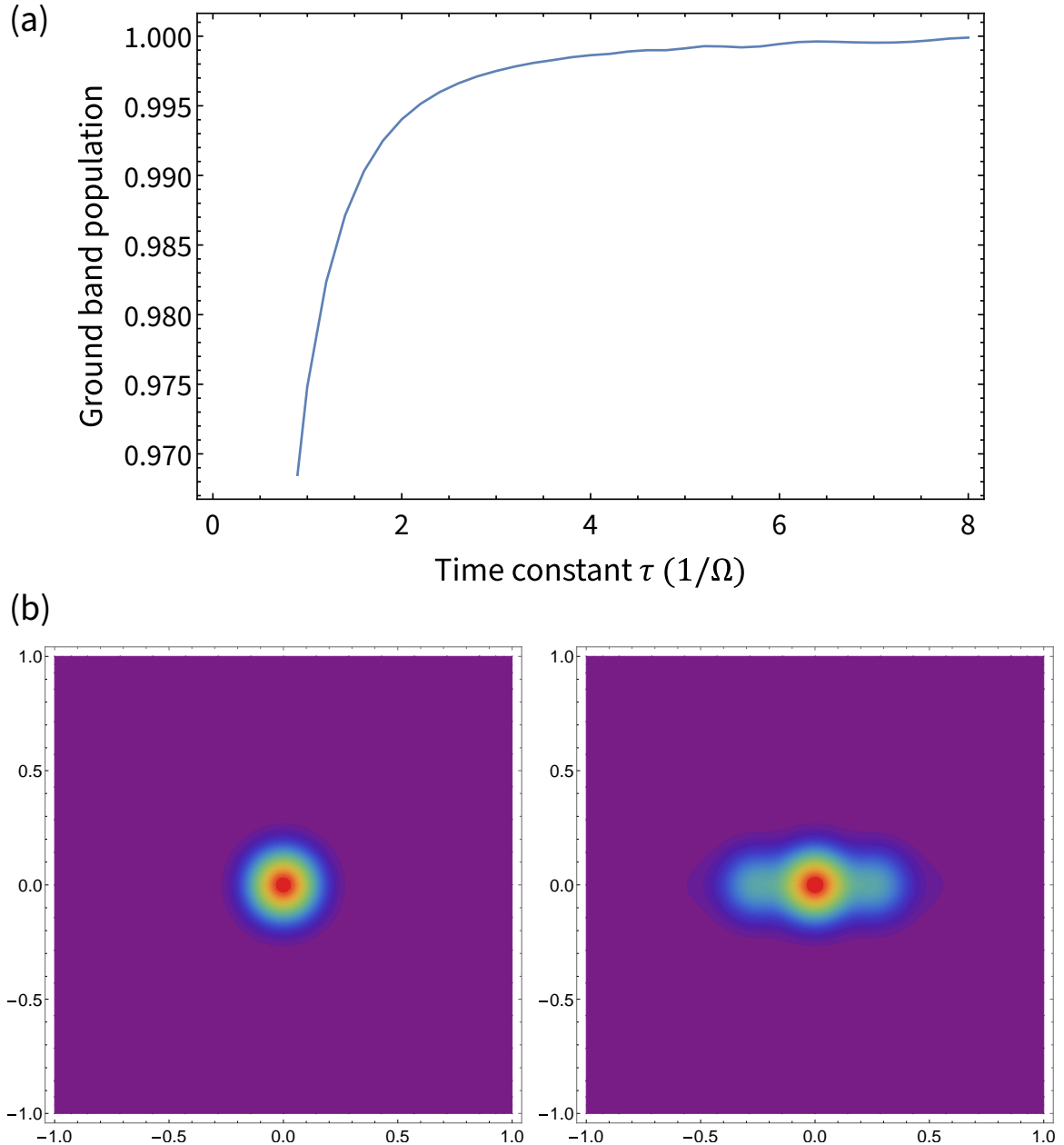


Figure 5.7: Effects of non-adiabatic loading and unloading. (a) Ground band population as a function of the time constant τ when the lattice is ramped up as $U(t) = U(1 - e^{-t/\tau})$. In practice a spline shaped ramp can be applied, but the diabatic behavior is qualitatively the same. (b) Comparison of atoms released from the lattice after a time-of-flight period of $t = 20$ ms. The lattice is ramped down adiabatically on the left and abruptly on the right. Diabatic unloading leads to population loss to the higher order momentum states. Here, the cloud is assumed to have a diameter of $100 \mu\text{m}$ and a temperature of 10nK .

red-detuned and a blue-detuned lattice. In a red-detuned lattice, heating is dominated by intraband scattering which returns the atoms to the ground band. The rate of this event is determined by the transition linewidth Γ . In contrast, in a blue-detuned lattice, heating is dominated by interband scattering, which excites the atoms to the first excited band. The rate of this event is suppressed by $E_r/(\hbar\omega_{\text{osc}})$, where $\hbar\omega_{\text{osc}} \sim E_{\text{BG}}^{(1)}$ is the energy quanta of an oscillator in the trap, but the energy change in a single event is much larger. The heating rate of the ground band in a blue-detuned lattice, on the other hand, is suppressed by $E_r^2/(\hbar\omega_{\text{osc}})^2$.

For our application, the atoms in higher bands can be filtered away if the cloud is sufficiently cold, and it is more important to reduce the heating in the ground band. Therefore, the lattice is designed to be blue-detuned. Assuming 150 MHz detuning and 200 mW power per beam, spontaneous emission leads to a population loss of 3.4% in the ground band when the two lattice arms are intensity balanced. The introduction of a 5% intensity mismatch between the arms leads to an additional loss of 1%.

5.3 Shuttle Lattice Realization

This section discusses practical considerations when we realize the shuttle lattice, including the choices of optics and optomechanics, the RF system that drives the acousto-optic modulators (AOMs), the fiber noise cancellation functionality, and the alignment procedures we have developed to overlap the two lattice arms.

5.3.1 Optical System

The optical components of the shuttle lattice can be roughly divided into two parts: those on the main optical table that chirps the frequency and stabilizes the phase of the laser, as well as those on the atom source frame and connection node that delivers the beams in the configuration discussed in Section 5.2.3.

The optical diagram on the main table is shown in Figure 5.8. The laser for the shuttle lattice is the zeroth-order output of an upstream AOM used for the red MOT, whose frequency is set to 190 MHz red detuned from the ${}^1\text{S}_0 - {}^3\text{P}_1$ resonance. This light is first divided equally into two paths on a PBS, one for each lattice arm, then each path is frequency modulated by a double-pass AOM⁵ to create a symmetric chirp between the two lattice arms. By chirping both arms at equal and opposite frequencies, we can reduce the RF tuning range on each AOM by half, which alleviates the efficiency roll-off during chirping. The lattice light exiting each double-pass AOM is P-polarized, which is then mixed with a small amount of S-polarized light. The combined light is sent through a 40 MHz single-pass AOM⁶ to cancel the fiber noise based on the beatnote of the S polarization before and

⁵Gooch & Housego AOMO 3200-125 200 MHz AOM.

⁶Isomet M1201-SF40-1.7VE 40 MHz AOM. The frequency is chosen to match the desired lattice detuning. This is a low-frequency AOM and requires a long propagation distance ($> 10''$) to separate the orders.

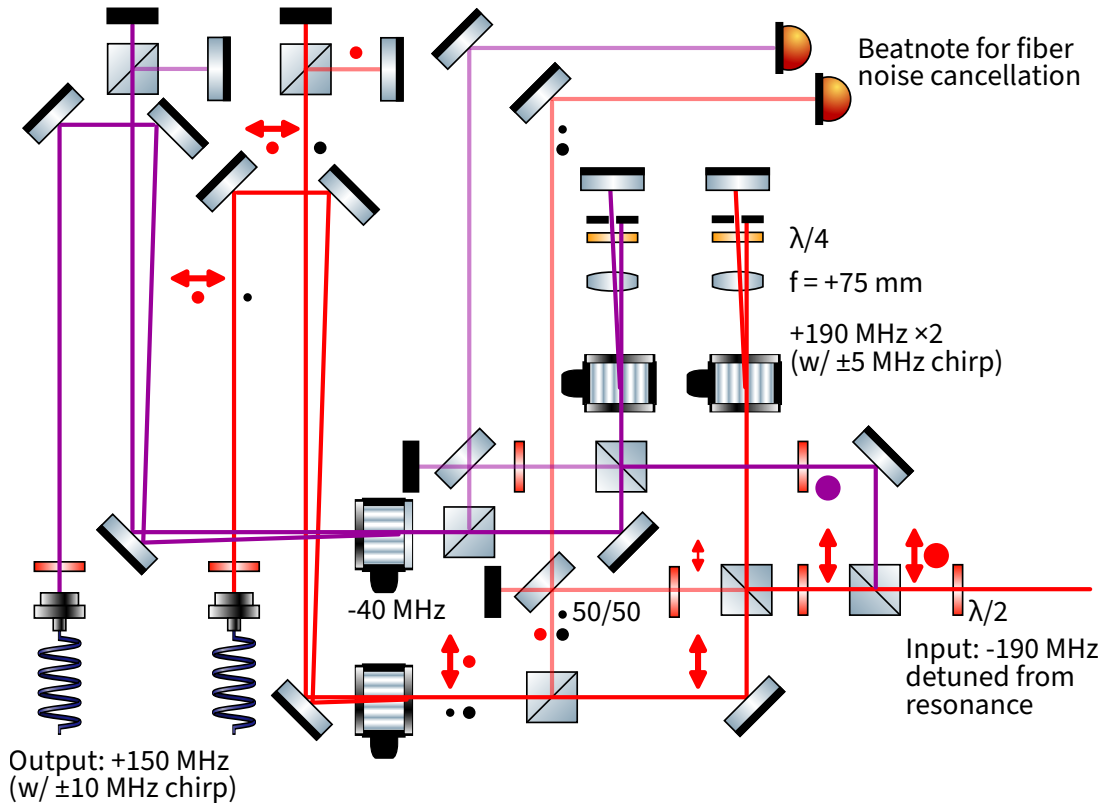


Figure 5.8: Optical diagram of the double-pass chirping AOMs and the fiber noise cancellation scheme on the main optical table. The two arms are colored red and purple, with polarizations marked as • (S) and ♦ (P) in the same color. Black markers represent retro-reflected beams that create a beatnote for fiber noise cancellation. The sizes of the polarization markers qualitatively represent the corresponding laser intensity. Note that some beam shaping optics are not shown.

after a 15 m optical fiber, which delivers each of the two beams to the shuttle lattice breadboard on the atom source frame. The output lattice arms have a center frequency blue detuned by 150 MHz and a chirp range of ± 10 MHz.

Due to spatial constraints and temperature stability considerations, we mostly used half-inch optics and their corresponding stainless steel optomechanics on the optical table. On the atom source side, most of the shuttle lattice delivery optics are mounted on a custom stainless steel breadboard shown in Figure 5.9. Unlike the 2D optical diagram in Figure 5.5, in reality a stainless steel block extends perpendicularly from the breadboard and holds part of the optics outside the plane of the breadboard, forming a 3D geometry which reduces the footprint of the module.

As mentioned in Section 5.2.3, the two-axis translation stage that holds the prism mirror and the two 45° mirrors above and below are integrated with Picomotor actuators to allow remote adjustment

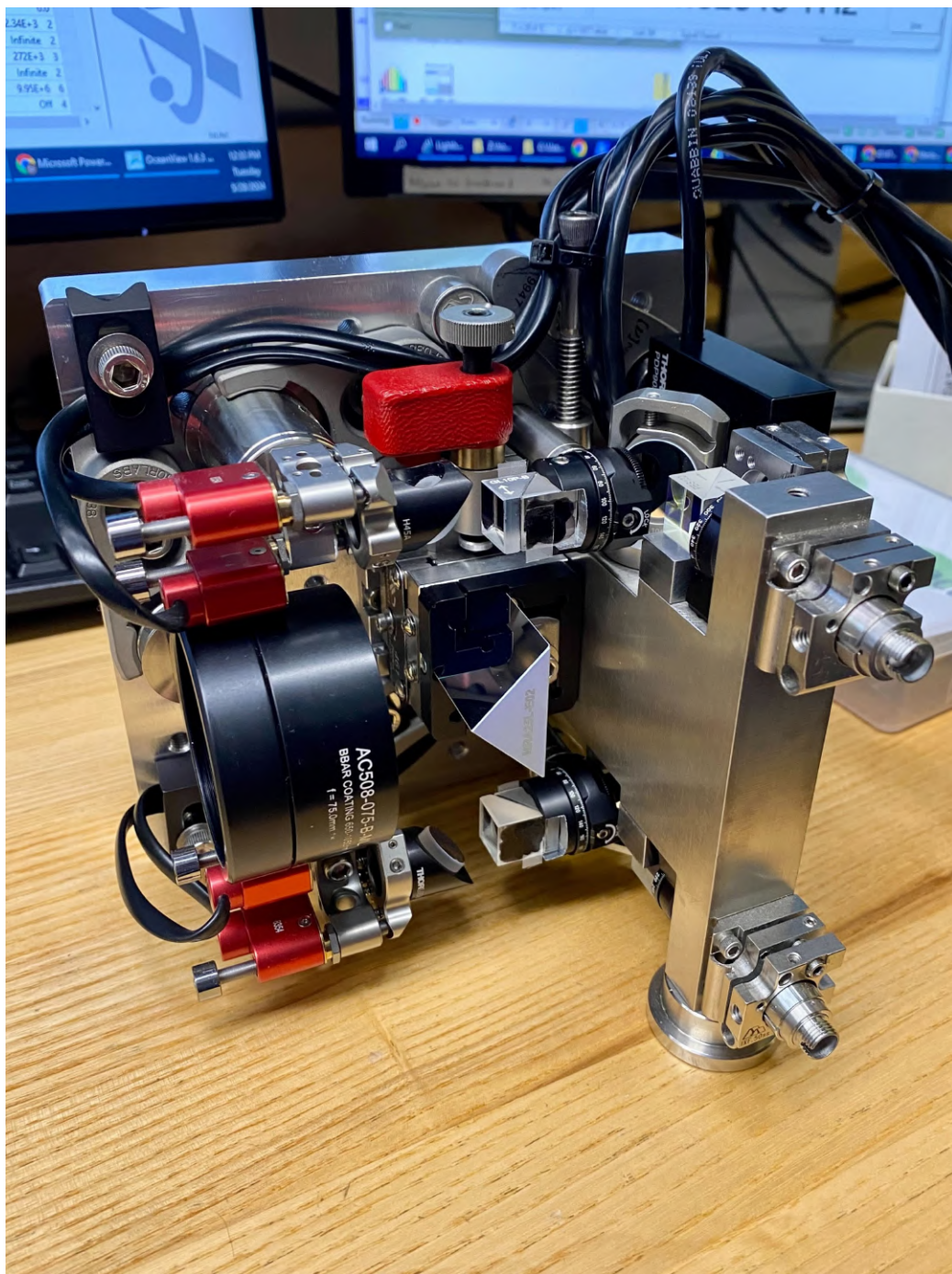


Figure 5.9: The shuttle lattice delivery module, whose diagram is shown in the black box in Figure 5.5, mounted on a custom stainless steel breadboard. The lattice arms input from the two fiber ports on the right and output to the atom source chamber through a 2" $f = +75$ mm lens on the left.

in a spatially confined region. Although actuators in the translation stage⁷ can be easily replaced by the corresponding Picomotors⁸, we were unable to find any half-inch stainless steel mirror mount compatible with Picomotor or similar products. Therefore, we turned to our local machine shop and modified the actuator mounting holes in the backplates of Thorlabs half-inch Polaris mounts⁹. The holes were enlarged from $3/16''$ –130 to $1/4''$ –40 to accept tiny Picomotors with a threaded shank¹⁰. This custom-modified mirror mount can be seen in Figure 5.9.

The $f = +250$ mm and $f = +200$ mm lenses in Figure 5.5 are mounted to CF 2.75" viewports on the atom source and the connection node through a custom flange adapter. Both lenses, as well as the $f = +75$ mm lens on the shuttle lattice breadboard, are chosen to be 2" in diameter so as not to clip the two lattice beams. The $f = +75$ mm concave mirror can be folded to reduce the footprint on the connection node side.

5.3.2 RF System

According to Equation (5.38), when the two lattice arms chirp symmetrically, each of them must cover a frequency range of $\delta f/2 \approx 10$ MHz, thus each double-pass AOM must be able to chirp by at least $\delta f_{\text{AOM}} = \delta f/4 \approx 5$ MHz in opposite directions. To drive these two AOMs, we have designed an RF system that allows independent adjustment of the center frequency f_{AOM} and the sideband frequency δf_{AOM} . The diagram of this system is shown in Figure 5.10.

A center frequency $f_1 = 190$ MHz, close to the nominal frequency of the AOMs, is generated on a DDS channel. This frequency is mixed with the output of a 50 MHz crystal oscillator¹¹, and after filtering, we obtain two arms at $f_1^{\text{low}} = 140$ MHz and $f_1^{\text{high}} = 240$ MHz, respectively. A second DDS channel is swept from $f_2 = 50$ MHz downward by $\delta f_2 = -5$ MHz and the output is sent to a 90° hybrid, generating two signals of the same frequency, but with a relative phase shift of $\pi/2$. These two signals are used as the I and Q sidebands of an IQ mixer, with f_1^{low} or f_1^{high} as the local oscillator. In this configuration, the IQ mixers act as a single-sideband mixer, resulting in $f_1^{\text{low}} + f_2$ and $f_1^{\text{high}} - f_2$ as the frequencies of the two arms. We identify $f_{\text{AOM}} = f_1$ and $\delta f_{\text{AOM}} = |\delta f_2|$, then the two arms have the desired frequencies $f_{\text{AOM}} \pm \delta f_{\text{AOM}}$.

This design uses a frequency offset followed by single-sideband mixers. It has the advantage of achieving more suppression of the unwanted sideband compared to the regular strategy, where a double-sideband mixer is used to create the positive and negative chirping sidebands. This is specifically true when $\delta f_{\text{AOM}} \approx 0$, where the two sidebands in a double-sideband mixer become nearly degenerate and it is difficult to isolate them. Our current RF system, with the addition of a small number of filters at the output, achieves more than 30 dB sideband attenuation for all δf_{AOM}

⁷Newport 461-XY-M XY linear stage with 9.5 mm shank actuators.

⁸Newport 8301NF piezo linear actuator.

⁹Thorlabs POLARIS-K05S1 1/2" mirror mount.

¹⁰Newport 8354 tiny piezo linear actuator.

¹¹Crystek CRBSCS-01-50.000 RF clock source sine wave oscillator.

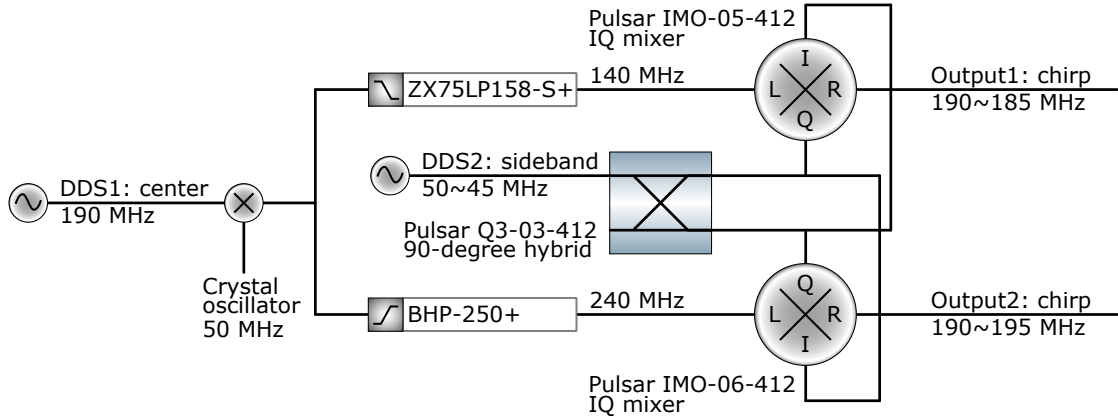


Figure 5.10: A simplified diagram of the shuttle lattice RF system. Some filters and amplifiers are omitted.

values in the range of interest. The center frequency f_{AOM} can also be tuned over a bandwidth of about 20 MHz in case a different lattice detuning is desired.

5.3.3 Fiber Noise Cancellation

Since the lattice beams are delivered from the main optical table to the atom source frame through two independent optical fibers, the associated mechanical vibration is not necessarily common between them. This leads to a differential phase noise between the two lattice arms, which results in jittering of the lattice and heating of the atoms. To address this issue, it is important to stabilize the phase of the lattice with a PID loop. Although it is sufficient to lock the relative phase between the two lattice arms, we chose a more straightforward strategy of locking the absolute phase of each individual arm by modulating it with a single-pass AOM to compensate for the phase noise from the fiber, a technique known as “fiber noise cancellation” [178–180].

In the conventional fiber noise cancellation scheme, a small portion of the light sent through the fiber is retro-reflected to sample the fiber noise twice, assuming that the time scale of the noise is much slower than the few-10 ns light propagation time, which is true for vibrations. The backward-propagating light is then compared with the light before entering the fiber through a beatnote. The beatnote thus contains information about the fiber noise and can be used to modulate the light in an equal and opposite way to the noise. However, since the light used to sample fiber noise is picked off from the same light used for the experiment, any intensity modulation before the fiber changes the magnitude of the beatnote signal. In the extreme scenario where the experiment requires the light to be turned on and off regularly in sequence, the phase lock needs to be re-obtained frequently, unless switching occurs after the fiber.

For the shuttle lattice, the double-pass chirping AOMs also serve as a mechanism of intensity

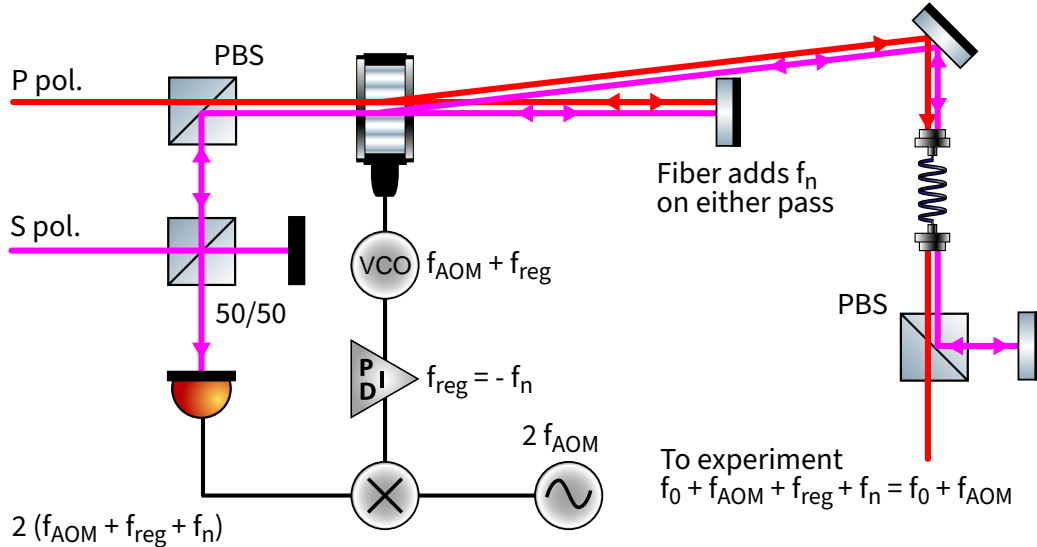


Figure 5.11: Fiber noise cancellation scheme with an auxiliary polarization (S, in magenta) that is orthogonal to the polarization being used for the lattice (P, in red). The auxiliary light is merged with the main light on a PBS and two beams experience the same AOM modulation and fiber noise. On the output end of the fiber, the auxiliary polarization is separated by another PBS and sent back through the fiber, and samples the same fiber noise for a second time. A beatnote is created between the auxiliary light before and after the fiber to extract the noise and feedback into the AOM. This setup allows suppression of the fiber noise even when the main polarization is turned off.

modulation during lattice loading and unloading, as well as shortcut-to-adiabaticity sequences. The footprint of the double-pass setup does not allow it to be installed on the atom source side after the fiber. To avoid frequent acquisition of the lock signal in the conventional fiber noise cancellation scheme, we follow previous work [180] and implement a phase stabilization loop shown in Figure 5.11, where an auxiliary noise-sampling light is used with a polarization orthogonal to the light intended for the shuttle lattice. The auxiliary beam (S-polarized) and the main beam (P-polarized) are merged on a PBS and then experience the same modulation from the fiber noise cancellation AOM and the same phase noise in the fiber¹². On the output side, the auxiliary beam is separated and retro-reflected. The returned auxiliary beam is then interfered with the zeroth AOM order of itself (but without going through the fiber) on a photodiode, whose output is then demodulated as the error signal to the PID.

¹²According to [180], noise along the fast axis can be a good proxy of the slow axis, and vice versa.

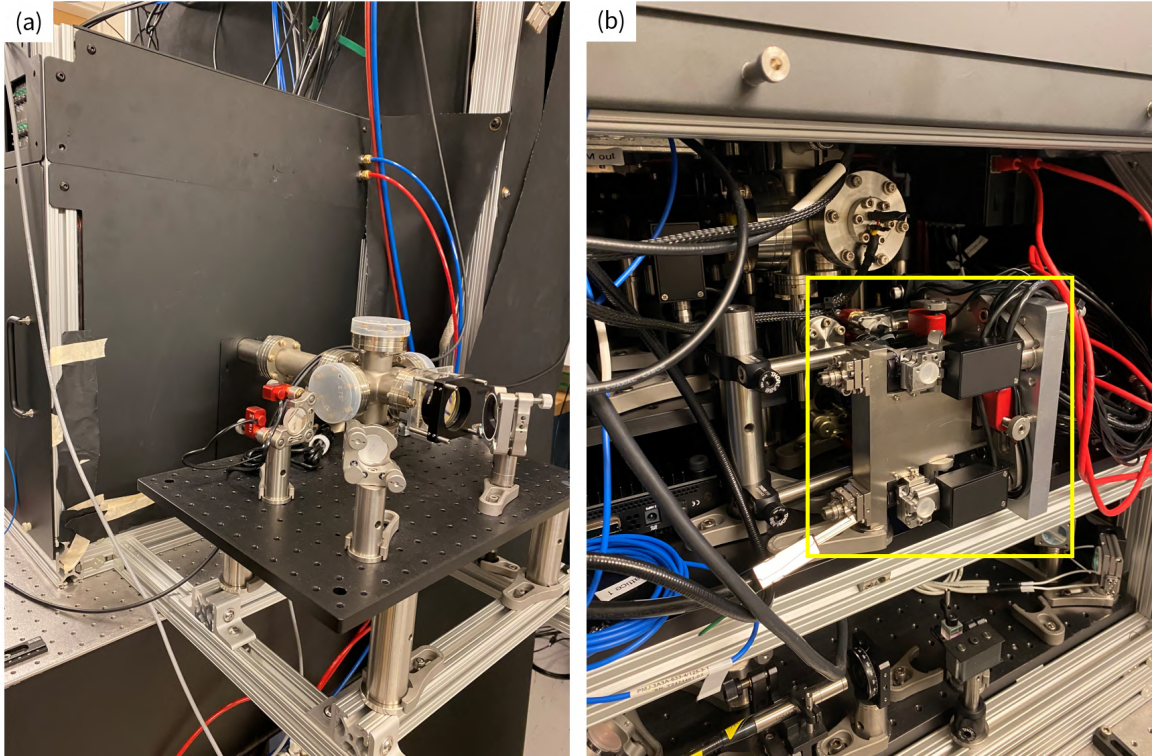


Figure 5.12: The shuttle lattice test setup. (a) The six-way cross at the nominal position of the connection node chamber and the optics on the connection node side. (b) The shuttle lattice delivery breadboard in the atom source frame below the oven, highlighted by the yellow box.

5.3.4 Shuttle Lattice Test

To test the shuttle lattice before connecting the atom source to the tower, we have installed a mock-up chamber on one of the two atom source frames (Frame Two) at the same location as the connection node, shown in Figure 5.12. This chamber is a six-way cross with CF 2.75" flanges, connected to the gate valve of the atom source through a standard nipple and a tee. The distance between the center of the cross and the center of the MOT chamber is 61.6 cm, very close to the target shuttle distance of 62.5 cm.

All five free ports on the six-way cross are covered with viewports¹³. With the gate valve open, the front viewport on the cross has a line of sight through the long axis of the vacuum system to the rear viewport on the atom source. The shuttle lattice delivery breadboard shown in Figure 5.9 is mounted in the rear of the atom source frame below the oven. The optics on the connection node

¹³Except the front one, four viewports were purchased from Torr Scientific and had coating issues. Some regions in these viewports are blurred after normal bake-out. We returned most of their viewports for re-coating, but had to keep these four mounted. It is not worth the effort to fix these viewports given the test nature of this setup. Fortunately, the front viewport, through which the shuttle lattice light enters and exits the vacuum system, is from MPF and remains clear.

side are mounted on a solid aluminum breadboard supported by 80/20 beams.

The alignment of the lattice arms is performed with Picomotor degrees of freedom using a commercial controller from Newport¹⁴. To facilitate alignment, we laser cut pairs of alignment targets with two holes in each, indicating the locations of the two arms when they enter and exit the vacuum system on both sides. Based on where the two beams hit the alignment targets, we can tell whether a common or differential mode of adjustment is needed. Then the corresponding degrees of freedom, summarized in Figure 5.6, are tuned. After iterating between different adjustment modes, the optical system can converge to a satisfactory overlap between the two lattice arms. A shuttle test with atoms loaded from the red MOT is planned in the near future.

5.4 Launch Lattice

Once the atoms are shuttled to the center of the connection node chamber, they are transferred to a vertical launch lattice and accelerated upward to initiate a strontium fountain. This leads to a prolonged free-fall time under gravity, allowing more photon recoils to accumulate between the interferometer arms and/or a longer interrogation time within the interferometer sequence.

The trap depth, laser detuning, and acceleration specifications of the launch lattice are similar to those of the shuttle lattice. Therefore, it is convenient to let both lattices share the same light source. This can be achieved via, for example, an in-line fiber switch that delivers the lattice arms to the appropriate lattice based on the experimental sequence. Moreover, the RF system that chirps the laser frequency can be reused. The launch lattice also incorporates the fiber noise cancellation scheme discussed in Section 5.3.3.

The remainder of this section discusses the optical configuration of the launch lattice. Although I will include some basic content regarding the installation and alignment of lattice optics, interested readers should refer to my labmate Megan Nantel's dissertation [140] to learn the details.

5.4.1 Launch Lattice Geometry

Both the tower and MAGIS-100 contain multiple connection nodes that are designed to be operated independently. In order to perform a vertical launch in one of the connection nodes without affecting the rest, it is undesirable to use a launch lattice formed by two vertical counterpropagating beams along the entire interferometry region. Moreover, a global launch lattice may affect the implementation of interleaving interferometers, where a new batch of atoms is launched while the previous batch is still in free fall. Therefore, we keep the launch lattice local to the corresponding connection node. This is achieved by introducing a small nonzero angle $\delta\theta$ between \mathbf{k}_1 and $-\mathbf{k}_2$, where \mathbf{k}_1 and

¹⁴Newport 8742 4-channel open-loop Picomotor motion controller.

\mathbf{k}_2 are the wave vectors of the two lattice arms. The length of the overlap region is reduced to

$$L \approx \frac{4w_0}{\delta\theta} \quad (5.40)$$

where w_0 is the waist radius of the beam, which in practice is large enough (a few mm) so that the Rayleigh range is much larger than the optical length.

The overlap region must be long enough to satisfy the launch specifications. To achieve an apogee of 10 m, the launch lattice must reach a terminal velocity of 14.1 m/s. Assuming an acceleration of 100 g as planned in the shuttle lattice, the length of the launch lattice must be at least 10 cm. In practice, our launch lattice achieves an overlap of $L = 11.2$ cm shown as the diamond-shaped region in Figure 5.13 (b). In this configuration, the lattice beams are delivered from a compact, stainless steel module containing beam-shaping optics and piezo-actuated mirrors. The two beams are directed to a pair of concave mirrors supported by the in-vacuum scaffoldings mounted on the top and bottom of the connection node by custom groove grabbers, which collimate and reflect the light towards the center of the chamber at $\delta\theta = 12.6^\circ$ with respect to each other (6.3° with respect to gravity). According to Equation (5.15), this angle will only reduce the effective wave vector by 0.6%. At this point, the size of the lattice beam measures 12.5 mm \times 5 mm in diameter, with the long dimension ($w_0 = 6.25$ mm) in the plane of the lattice cross to expand the overlap region. The two lattice beams exit the connection node and are then incident on a pair of lateral position sensors, which provide feedback to the piezo-actuated delivery mirrors to stabilize the lattice.

5.4.2 Adjustment of Launch Angle

For simplicity, all in-vacuum optics are placed on fixed mounts. The adjustment of the launch lattice is achieved through optomechanics in the launch lattice module shown in Figure 5.14, which is attached to the connection node from the side. After elliptical beam shaping, the two lattice beams are reflected by a pair of prism mirrors in opposite directions, then directed by mirrors at 55.5° towards two CF 1.33" viewports on the connection node chamber¹⁵. Both the prism pair and the 55.5° mirrors can be adjusted remotely by Picomotor actuators, and serve as the major degrees of freedom to align the lattice. A telescope consisting of a $f = +100$ mm lens outside vacuum and a $f = +500$ mm concave mirror inside vacuum expands each beam to the desired size for the launch lattice.

Similarly to the shuttle lattice, the telescope is positioned not only to maintain collimation of the lattice beams but also to form a conjugate relation between the prism mirrors and the center of the lattice cross. We have designed a custom mount for the prism mirrors shown in Figure 5.15, which allows the two mirrors to pivot symmetrically about $\hat{\mathbf{z}}$ and $\hat{\mathbf{y}}$ as a common mode¹⁶. The

¹⁵The 55.5° adapter is custom machined, similar to Thorlabs H45A 45° adapter.

¹⁶Similar to a gimbal mount, but the pivot is not exactly at the geometric center of the pair. Instead, the pivot axis passes through the symmetry plane between the pair.

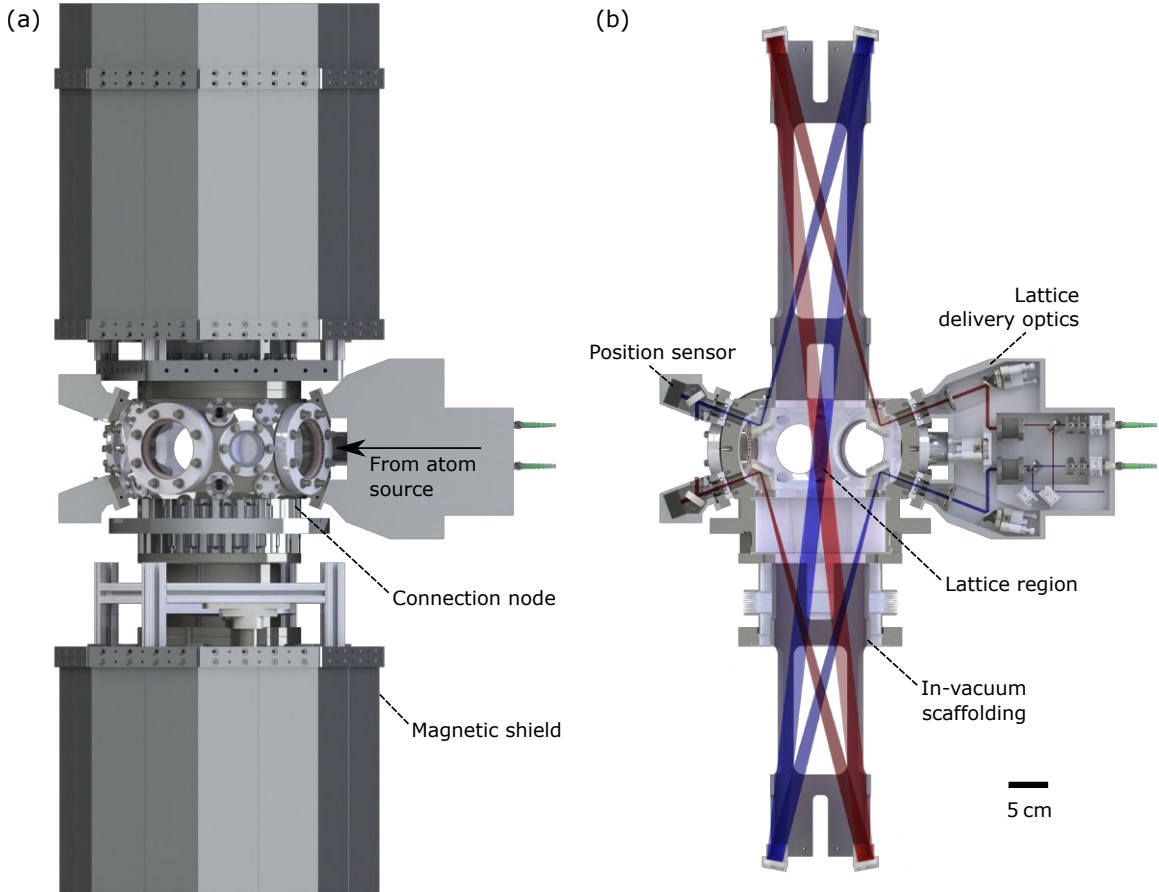


Figure 5.13: (Adapted from Ref.[43]) CAD model of the launch lattice in the connection node. (a) The launch lattice module mounted on the connection node from the side. Note that a recent modification made to the launch lattice breadboard moves the fiber ports to the vertical direction. (b) Cutaway view showing the in-vacuum lattice scaffolding and delivery optics, as well as the two lattice beam paths (red and blue) which intersect in the center of the chamber to form the diamond-shaped launch lattice region. Although here the lower scaffolding is shown on the flange of the bellows, during construction, we moved it to the bottom of the connection node chamber, symmetric to the top scaffolding (the length was made the same as top, too). This avoids potential lattice misalignment when the bellow flange is installed as the last vacuum connection.

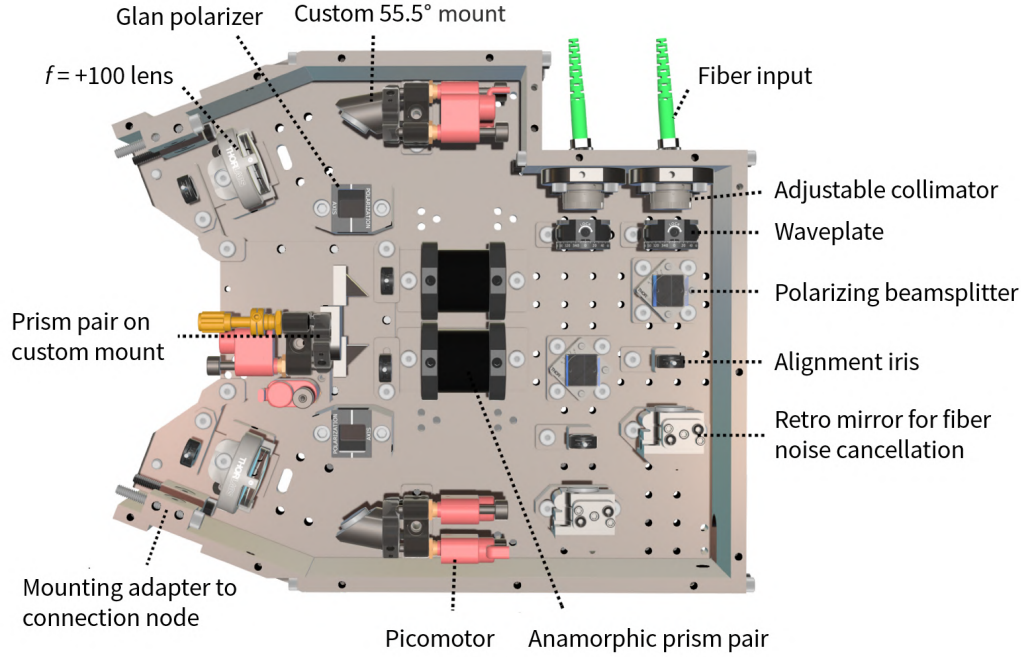


Figure 5.14: CAD model of the launch lattice module. This figure incorporates some updates that are not shown in Figure 5.13.

angle adjustment of the prism mirrors by the two Picomotors leads to the in-plane and out-of-plane rotations of the lattice cross about its center. Like in the shuttle lattice, these rotations maintain the location of the lattice cross. This allows us to fine-tune the lattice launch angle with respect to gravity without affecting the loading height of the atoms.

The decoupling between the angle and position of the lattice cross is verified by a homemade ray tracer shown in Figure 5.16. From the ray tracer, we can deduce that the maximum adjustment range of the lattice launch angle is about 4 mrad, before the concave mirror clips the beam as an effective aperture with diameter $a = \pi w_0$. This is a commonly used clipping threshold that allows the transmission of about 99% of the optical power [144]. In practice, the tuning range may be lower due to imperfect alignment, but is still sufficient to correct for the small angular error of the connection node during tower construction, which we estimate to be within 1 mrad.

Moreover, the lattice launch angle can be used to compensate for the trajectory deviation due to the Coriolis effect. Considering the rotation of the Earth, the transverse equation of motion of a freely falling atom in the lab frame is given by

$$\ddot{x}(t) = 2\Omega_E v_z(t) \cos \theta_{\text{lat}} \quad (5.41)$$

where $\Omega_E = 72.7 \mu\text{rad/s}$ is the rotation rate of the Earth and θ_{lat} is the latitude of the detector,

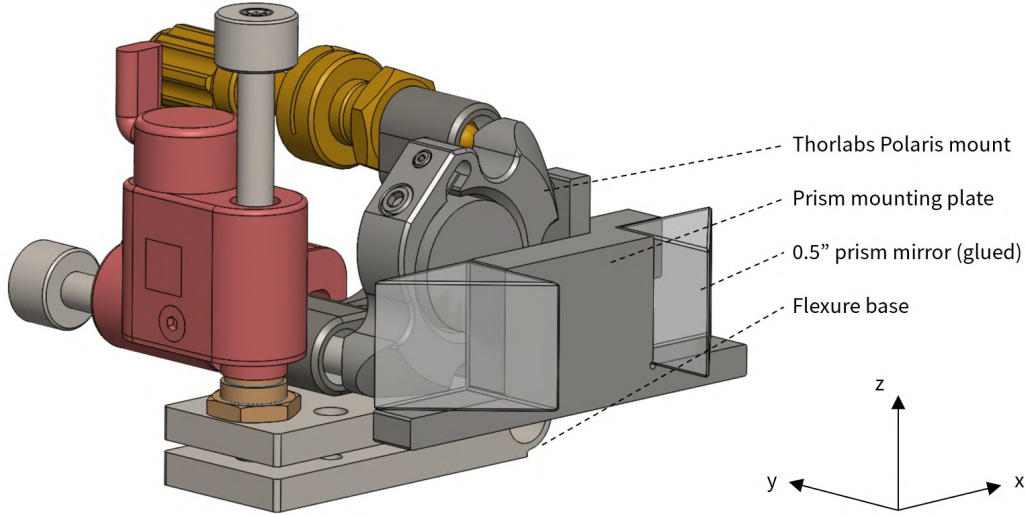


Figure 5.15: The custom optomechanics for the pair of prism mirrors. Two Picomotor actuators rotate the pair about \hat{z} and \hat{y} , respectively, corresponding to the in-plane and out-of-plane rotation of the lattice cross.

which is 37.4° for the tower and 41.8° for MAGIS-100. Using $v_z(t) = v_z(0) - gt$, we can integrate Equation (5.41) twice and obtain

$$x(t) = \Omega_E \cos \theta_{\text{lat}} \left(v_z(0) t^2 - \frac{1}{3} g t^3 \right) + v_x(0) t \quad (5.42)$$

where the initial conditions $x(0) = 0$ and $\dot{x}(0) = v_x(0)$ are used. Assuming the atoms fall back to the same location after an interferometer time $2T$, the initial transverse velocity must be

$$v_x(0) = \Omega_E \cos \theta_{\text{lat}} \left(\frac{4}{3} g T^2 - 2T v_z(0) \right) \quad (5.43)$$

$$= -\frac{4}{3} h \Omega_E \cos \theta_{\text{lat}} \quad (5.44)$$

where $v_z(0) = \sqrt{2gh}$ and $T = \sqrt{2h/g}$ are used for a target launch height h . This corresponds to a lattice launch angle

$$\theta = \left| \frac{v_x(0)}{v_z(0)} \right| = \frac{2\sqrt{2}}{3} \sqrt{\frac{h}{g}} \Omega_E \cos \theta_{\text{lat}} \quad (5.45)$$

$$= 0.017 \text{ mrad} \times \left(\frac{h}{1 \text{ meter}} \right)^{1/2} \quad (\text{using Fermilab latitude}) \quad (5.46)$$

Therefore, even for an extreme 100-meter launch in MAGIS-100, the required angle is still an order

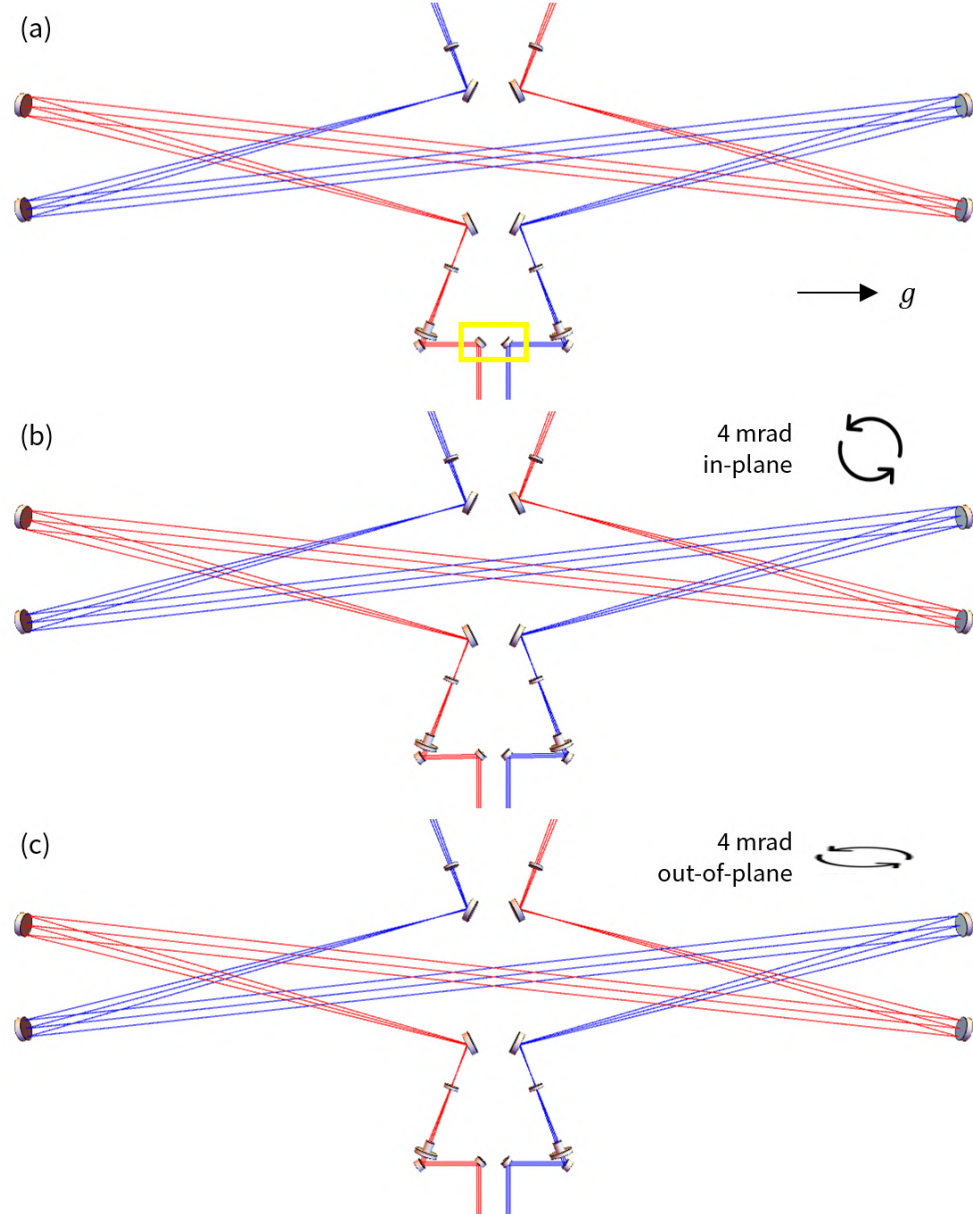


Figure 5.16: Ray tracing of the launch lattice delivery setup. (a) The nominal ray diagram where the two beams (red and blue) overlap to form a lattice region of 11.2 cm along the gravity direction. The beam thickness represents a clipping threshold of diameter $a = \pi w_0$, where $w_0 = 6.25$ mm. The pair of prism mirrors is highlighted by the yellow box. (b) A common adjustment of the pair of prism mirrors by 10 mrad parallel to the page leads to a 4 mrad in-plane rotation of the lattice launch angle. The beams reach the edge of the concave mirrors on both sides. (c) A common adjustment of the pair of prism mirrors by 20 mrad in the orthogonal direction leads to a 4 mrad out-of-plane rotation of the lattice launch angle.

of magnitude smaller than the adjustment range of the launch lattice.

5.4.3 Alignment of Lattice Beams

The installation and initial alignment of the optics were performed in a cleanroom environment. The setup is shown in Figure 5.17. After the assembly of the groove grabbers, the connection node was fixed to an 80/20 jig, then the in-vacuum scaffoldings were installed. The in-vacuum mirrors were mounted with the help of a guiding laser beam along the nominal optical path to ensure that they were in the correct locations. Since the in-vacuum optics are not tunable, to correct for the angular errors due to machining and installation tolerances, shims were added below certain mirror mounts. My labmates Megan Nantel and Mahiro Abe have developed an effective procedure to align and characterize the in-vacuum optics with the help of customized tools, which is documented in Megan’s dissertation [140]. Thanks to their hard work, satisfactory alignment was achieved inside the connection node chamber.

After the integration of the launch lattice delivery breadboard, fine-tuning of the lens position is required to ensure the conjugate relation between the pair of prism mirrors and the center of the lattice cross. This is a complicated process and is also discussed in detail in Megan’s dissertation. In particular, as shown in Figure 5.18, a custom machined alignment target, normally in the retracted configuration to avoid blocking the lasers, can be moved to the center of the connection node by a linear actuator installed on one of the unused CF 1.33” flanges to help align the launch lattice. This target also contains a resolution chart to adjust and characterize the imaging system.

After alignment of the launch lattice, we performed a bake test on each of the two connection node chambers. The optical system was verified to maintain alignment after the thermal cycle, demonstrating the robustness of this launch lattice design.

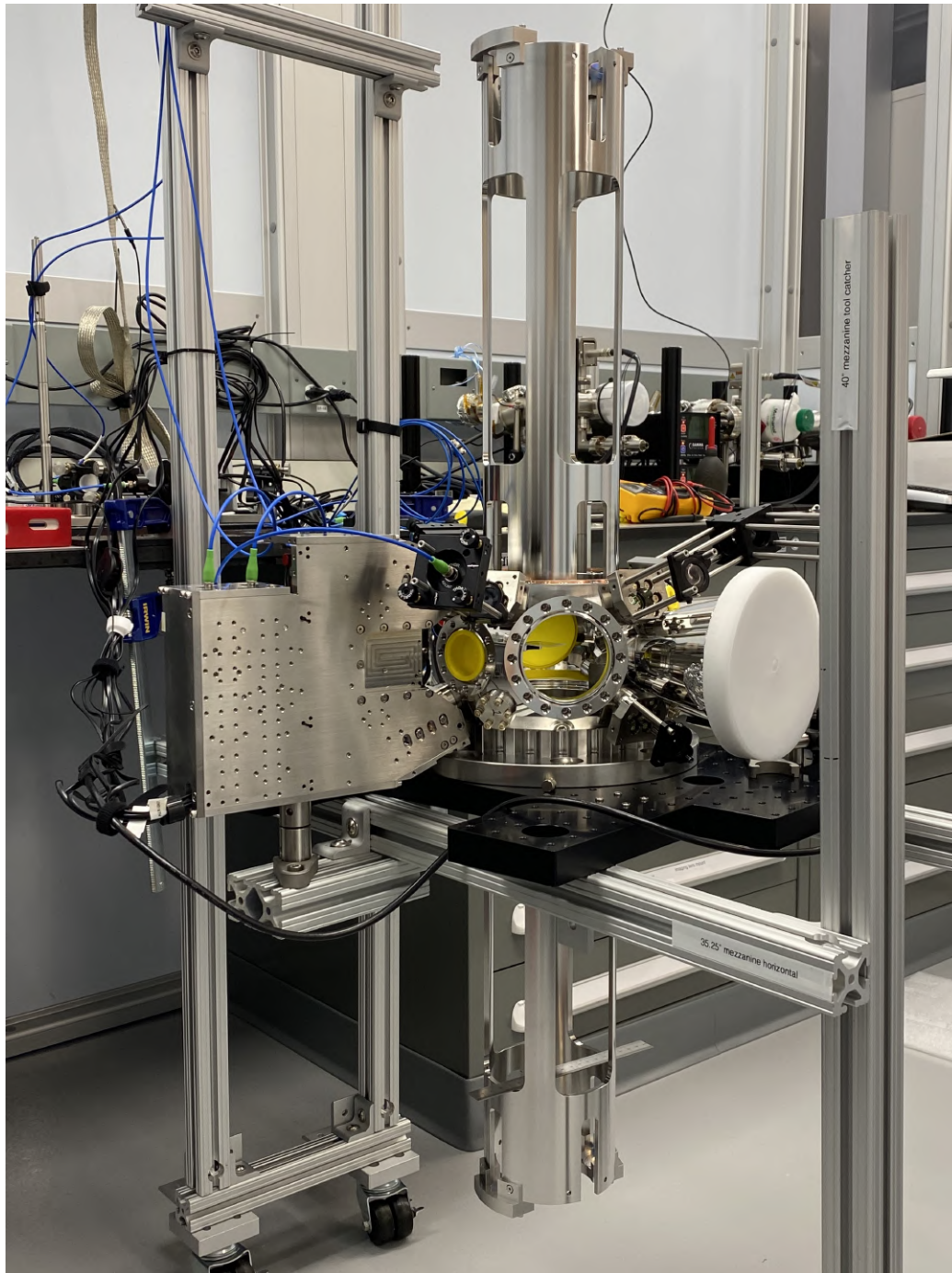


Figure 5.17: The connection node on an 80/20 jig, with the launch lattice optics and alignment tools installed. This setup is assembled in our cleanroom for vacuum cleanliness considerations.

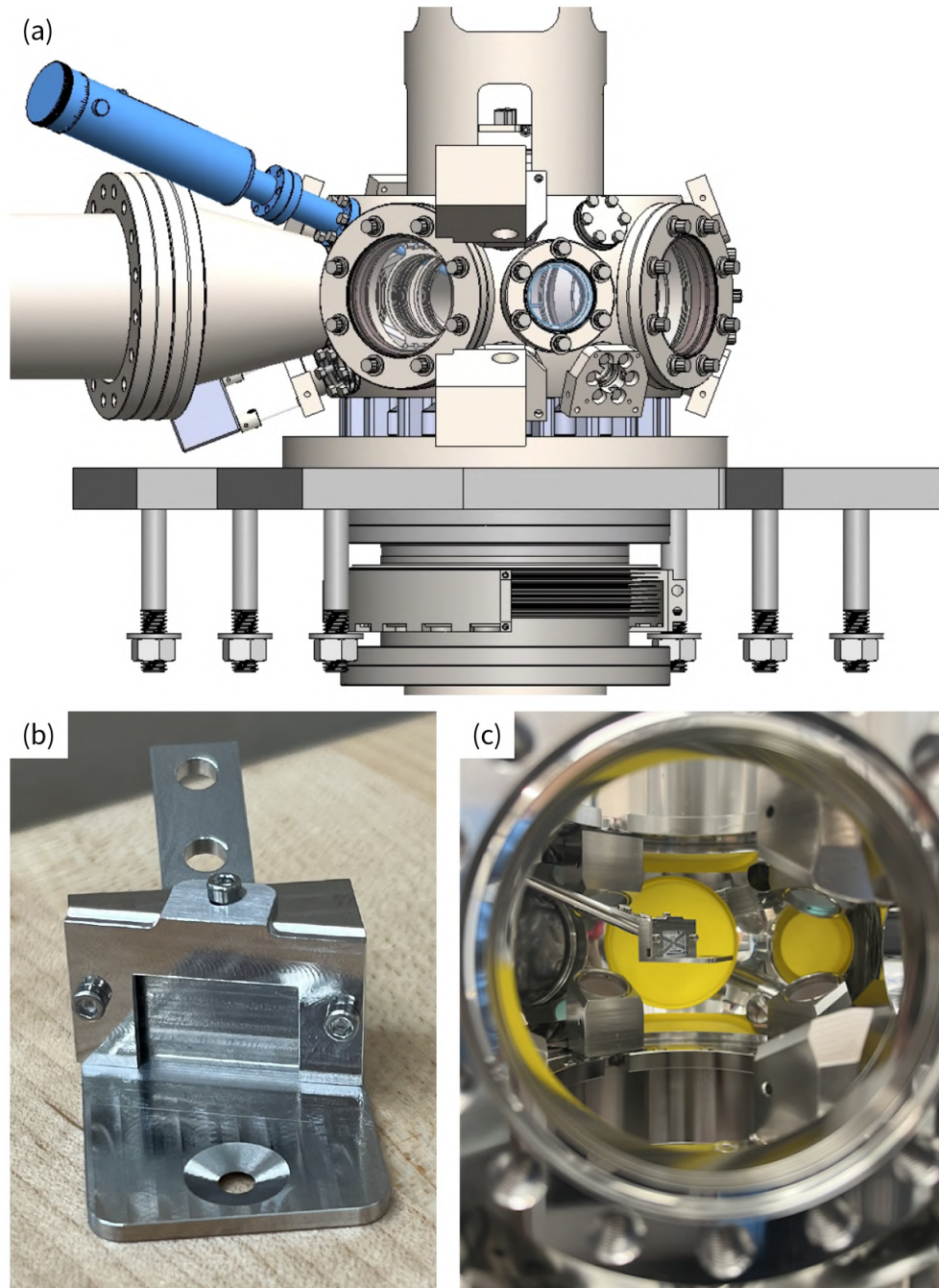


Figure 5.18: The alignment target on a linear actuator. (a) CAD model of the linear actuator (highlighted) connected to the connection node chamber on a CF 1.33" flange. (b) A picture of the alignment target. It contains an iris to align the launch lattice and a plate to mount a resolution chart for the imaging system. (c) The alignment target moved to the center of the connection node.

Chapter 6

Cumulative Fidelity in LMT Interferometers

This chapter presents my theoretical work on how pulse errors in an LMT interferometer sequence accumulate and reduce interferometer fidelity and contrast. My discussion focuses on single-photon atom interferometers¹, where the ground and excited states are directly coupled by an optical transition. For multi-photon atom interferometers, the same analysis can be applied to the effective two-level transition.

Most of the content is from our manuscript in preparation for publication. We initiated this project due to recent criticism by M. Chiarotti *et al.* [44] on the ~ 10 Hz laser frequency stability requirement for MAGIS-100 [43]. This paper assumes that the wave function amplitude error induced by each imperfect π -pulse adds up coherently, leading to a total fidelity loss that scales quadratically with the LMT order n . This paper thus concludes that a more stringent requirement on laser linewidth has to be placed, and the LMT order for optimal phase sensitivity enhancement is limited to below 10^3 for practical laser specifications.

However, this statement is not true. The coherent accumulation of pulse error originates from probing a two-level system n times with a noisy laser from the same direction, where the external momentum states are not of significance. In an LMT interferometer, however, these momentum states are crucial to the space-time separation of the two arms, and they significantly expand the Hilbert space. In this theory project, we consider a realistic narrowband clock atom interferometer, where the atoms are interrogated by pulses from alternating directions. As I will discuss in this chapter, the wave function error induced by each π -pulse is momentum separated from majority of the wave function in the correct state, and is suppressed from interacting with subsequent pulses in a narrowband interferometer due to strong velocity selectivity. Summing over errors from n sequential

¹I will use the more common terminology “clock atom interferometer”, since there is unlikely any confusion about collinear multi-photon clock atom interferometers [86, 87] in this dissertation.

π -pulses leads to a fidelity loss proportional to n .

Such linear scaling is not hampered by the parasitic paths that arise from the pulse errors. To prove this, we study the wave function when parasitic paths interfere with the main interferometer at the output ports. Using a mathematical formalism that groups the parasitic paths by the number of errors, we bound their contribution to the fidelity and contrast of the interferometer to the level of 10^{-2} for practical narrowband pulse parameters regardless of n .

Furthermore, we put this analysis in the context of a noisy laser and obtain an analytic expression of the frequency noise transfer function for n sequential π -pulses. Using practical parameters, we calculate the fidelity of the pulse sequence and derive the LMT enhancement of a full interferometer. With a Rabi frequency of $2\pi \times 1$ kHz and a moderate laser stability requirement of 10 Hz RMS noise amplitude, a narrowband clock atom interferometer can support LMT order greater than 10^4 . These numbers agree with the MAGIS-100 specifications on laser frequency stability [43], and contradict the claims made by the recent paper [44].

Finally, this chapter briefly introduces several other error sources that can be incorporated in this analysis framework, as well as experimental techniques to mitigate these errors in the first place. These techniques can be implemented in both the tower and MAGIS-100 to improve the interferometer fidelity and contrast.

6.1 Sequence Structure of LMT Interferometers

6.1.1 Narrowband Interferometers

The structure of a clock atom interferometer depends on the velocity selectivity of the pulses. In a narrowband interferometer, each pulse is customized so that its frequency offset compensates for the Doppler shift of only one momentum state. All other momentum states are detuned with respect to the pulse by $|\Delta| \gg \Omega$ so that they are essentially transparent. An example is the atom interferometer operated on the ${}^1S_0 - {}^3P_0$ transition in ${}^{87}\text{Sr}$, where the Doppler shift from a single photon recoil

$$\Delta_{698} = \frac{\hbar k_{698}^2}{m} = 2\pi \times 9.4 \text{ kHz}. \quad (6.1)$$

is much larger than the typical Rabi frequency of around $2\pi \times 1$ kHz.

In the narrowband regime, the upper and lower arms of the interferometer must be addressed by different photons. A conventional way to structure a narrowband clock interferometer is to have the first half of the sequence address the upper arm and the second half address the lower arm, with a single pulse in the middle shared between the two arms. This can be viewed as inserting acceleration and deceleration subsequences into a Mach-Zehnder interferometer, which I will refer to as “augmentation zones”. To formally describe this interferometer sequence, I introduce the following notation.

A generic state in the interferometer is denoted as $|\psi\rangle = |s, p\rangle$, where s is the internal level with values $s = 1$ for the ground state and $s = -1$ for the excited state, and p is the external momentum in units of photon recoils. A π -pulse is denoted as a dimensionless tuple (d, f) and a $\pi/2$ -pulse is denoted with an additional subscript as $(d, f)_{\frac{\pi}{2}}$. In this notation, $d = \pm 1$ represents the direction of the pulse, and $f = \tilde{f}d$, where \tilde{f} is the laser detuning in the freely falling frame in units of $\hbar k^2/m$. The state $|s, p\rangle$ is coupled to the state $|s', p'\rangle$ where $s' = -s$ and $p' = p + sd$, if and only if the laser detuning compensates for the Doppler effect of the moving atoms. This resonance condition can be derived from the detuning expression in Equation (27) of Ref. [56], which is copied here

$$\Delta(\mathbf{p}) = \omega_0 - \omega + \mathbf{k} \cdot \dot{\mathbf{x}}_c + \frac{\mathbf{k} \cdot \mathbf{p}}{m} + \frac{\mathbf{k}^2}{2m} \quad (\text{for } |\text{g}, \mathbf{p}\rangle \leftrightarrow |\text{e}, \mathbf{p} + \mathbf{k}\rangle) \quad (6.2)$$

$$\Delta(\mathbf{p}) = \omega_0 - \omega + \mathbf{k} \cdot \dot{\mathbf{x}}_c + \frac{\mathbf{k} \cdot \mathbf{p}}{m} - \frac{\mathbf{k}^2}{2m} \quad (\text{for } |\text{e}, \mathbf{p}\rangle \leftrightarrow |\text{g}, \mathbf{p} - \mathbf{k}\rangle) \quad (6.3)$$

We identify $\omega_0 - \omega + \mathbf{k} \cdot \dot{\mathbf{x}}_c = -fd \frac{k^2}{m}$, $\mathbf{k} = kd \hat{\mathbf{x}}$, and $\mathbf{p} = pk \hat{\mathbf{x}}$, where $\hat{\mathbf{x}}$ is the unit vector along the interferometry axis. The sign of the last term is determined by the internal level s . Then $\Delta(\mathbf{p}) = 0$ can be equivalently written as

$$-fd \frac{k^2}{m} + pd \frac{k^2}{m} + s \frac{k^2}{2m} = 0 \quad (6.4)$$

which implies the dimensionless resonance condition

$$f = p + \frac{1}{2}sd = \frac{p + p'}{2} \quad (6.5)$$

We denote a pulse sequence as a chain L , with arrows between its constituent pulses or subsequences to indicate time ordering. For example, a Mach-Zehnder interferometer made of an opening $\pi/2$ -pulse, a mirror π -pulse and a closing $\pi/2$ -pulse, whose momentum-time and space-time diagrams are shown in Figure 6.1, can be expressed as

$$L_{\text{MZ}} = \left(1, \frac{1}{2}\right)_{\frac{\pi}{2}} \xrightarrow{T} \left(1, \frac{1}{2}\right) \xrightarrow{T} \left(1, \frac{1}{2}\right)_{\frac{\pi}{2}} \quad (6.6)$$

where T represents a finite interrogation time. A narrowband $n\hbar k$ interferometer shown in Figure 6.2 is structured by inserting the augmentation sequence

$$L_{\text{aug}} = \left(-1, \frac{3}{2}\right) \rightarrow \left(1, \frac{5}{2}\right) \rightarrow \cdots \rightarrow \left((-1)^{n-1}, n - \frac{1}{2}\right) \quad (6.7)$$

and its reversed sequence, denoted as L_{aug}^{-1}

$$L_{\text{aug}}^{-1} = \left((-1)^{n-1}, n - \frac{1}{2}\right) \rightarrow \left((-1)^{n-2}, n - \frac{3}{2}\right) \rightarrow \cdots \rightarrow \left(-1, \frac{3}{2}\right) \quad (6.8)$$

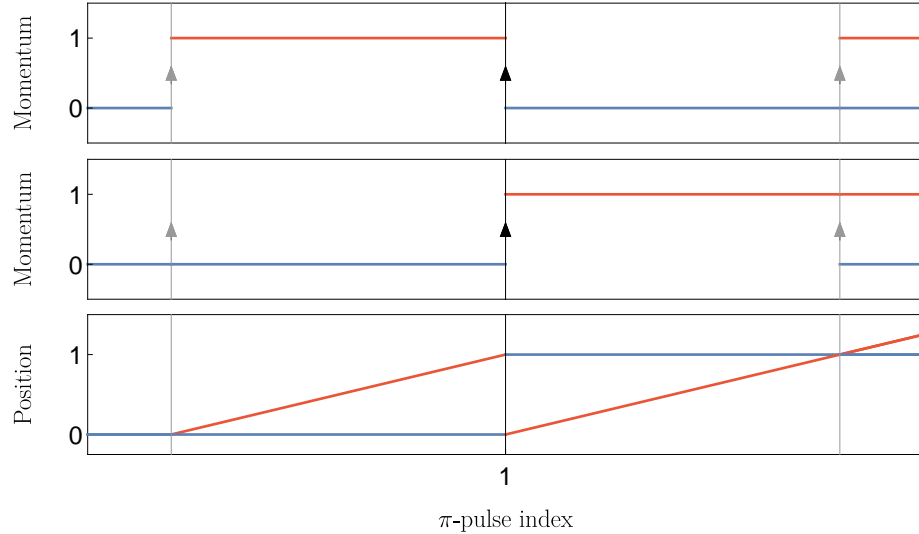


Figure 6.1: A Mach-Zehnder atom interferometer. From top to bottom, the panels show the momentum-time diagram of the upper arm, the momentum-time diagram of the lower arm, and the space-time diagram of both arms. The internal atomic levels are indicated as blue (ground) and red (excited). The vertical lines represent π -pulses (black) and $\pi/2$ -pulses (gray). The vertical axes are dimensionless, with momentum in units of $\hbar k$ and position in units of $v_r T$, where v_r is the recoil velocity and T is the interrogation time.

into a Mach-Zehnder interferometer. The resulting sequence has the form

$$L_{\text{nb}} = \left(1, \frac{1}{2}\right)_{\frac{\pi}{2}} \rightarrow L_{\text{aug}} \xrightarrow{T} L_{\text{aug}}^{-1} \rightarrow \left(1, \frac{1}{2}\right) \rightarrow L_{\text{aug}} \xrightarrow{T} L_{\text{aug}}^{-1} \rightarrow \left(1, \frac{1}{2}\right)_{\frac{\pi}{2}} \quad (6.9)$$

Each augmentation zone L_{aug} or L_{aug}^{-1} contains $n - 1$ π -pulses. The complete interferometer has four augmentation zones and a center mirror pulse, which totals to $4n - 3$ π -pulses.

Note that this is not the only way to arrange a narrowband interferometer sequence. In fact, since all π -pulses but the center one interact with only a single arm, pulses for the upper arm can be interleaved with pulses for the lower arm. Figure 6.2 shows a different sequence with the same space-time separation between the two arms. However, for the rest of this chapter, I will use the more common narrowband interferometer sequence described by Equation (6.9). This choice will not affect the pulse error analysis in the rest of this chapter.

6.1.2 Broadband Interferometers

A broadband clock atom interferometer operates in the opposite regime where $|\Delta| \ll \Omega$, such that even when the two arms are separated by a significant number of photon recoils, they can still couple efficiently to a common laser pulse. In this regime, it is possible to keep the pulse nominally

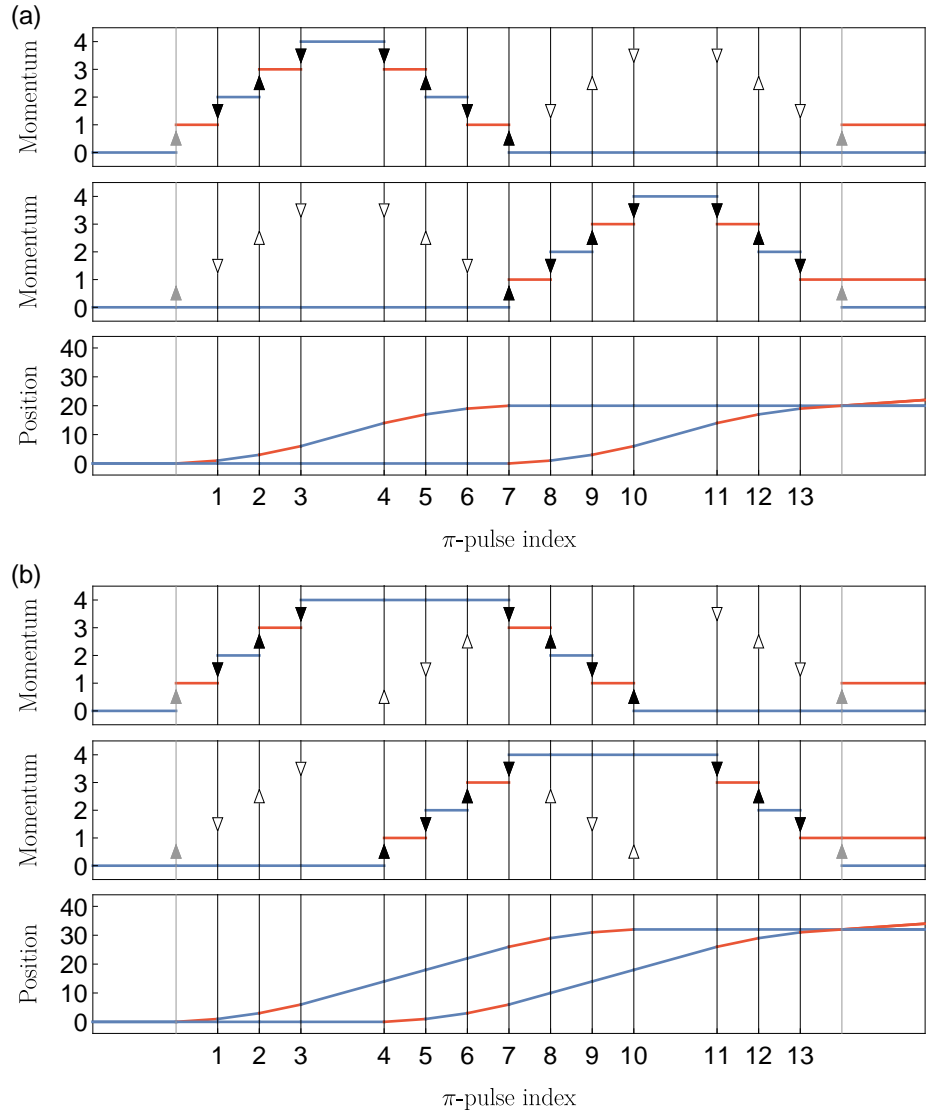


Figure 6.2: (a) A narrowband $4\hbar k$ clock atom interferometer arranged in the sequence described by Equation (6.9). From top to bottom, the panels show the momentum-time diagram of the upper arm, the momentum-time diagram of the lower arm, and the space-time diagram of both arms, similar to Figure 6.1. The arrows on the pulse lines indicate their directions and detunings. Note that the first half of the sequence is off-resonant with the upper path, and the second half is off-resonant with the lower path, represented by the open arrows. We assume equal pulse spacing δt and a non-zero interrogation time T (between pulse 3 and 4, as well as pulse 10 and 11). The vertical axes are dimensionless, with momentum in units of $\hbar k$ and position in units of $v_r \delta t$, where v_r is the recoil velocity. (b) A narrowband $4\hbar k$ clock atom interferometer with a different sequence. The upper-arm augmentation zones are interleaved with the lower-arm augmentation zones. This changes the final location of the output ports but keeps the space-time area enclosed by the interferometer identical as (a).

on resonance with the center of mass until the LMT order is too large such that $n\Delta$ is no longer negligible. For the ${}^1S_0 - {}^3P_1$ transition in strontium, we have

$$\Delta_{689} = \frac{\hbar k_{689}^2}{m} = 2\pi \times 9.5 \text{ kHz}. \quad (6.10)$$

which is about $100\times$ smaller than the typical Rabi frequency of $2\pi \times 1 \text{ MHz}$, so the broadband assumption breaks down beyond $n \sim 100$. We have experimentally observed the reduction of pulse efficiency and thus interferometer contrast in a broadband interferometer at large n . To solve this problem, we have developed a Floquet modulation technique that allows pulses to simultaneously compensate for Doppler shifts in the upper and lower arms even when $|n\Delta| \sim \Omega$ [39].

Whether or not Floquet atom optics are used, a broadband interferometer differs from a narrowband interferometer in the amount of momentum difference accrued per pulse between the two arms. Each π -pulse always imparts a photon recoil in the opposite direction to the upper and lower arms, leading to a momentum separation that is twice that of a narrowband interferometer. Taking into account the additional photon recoil from the first $\pi/2$ -pulse, which only applies to the upper arm, a broadband interferometer always has an odd LMT order n as shown in Figure 6.3 (a). Its sequence structure is similar to Equation (6.9),

$$L_{\text{bb}} = (1, \cdot)_{\frac{\pi}{2}} \rightarrow L_{\text{aug}} \xrightarrow{T} L_{\text{aug}}^{-1} \rightarrow (1, \cdot) \rightarrow L_{\text{aug}} \xrightarrow{T} L_{\text{aug}}^{-1} \rightarrow (1, \cdot)_{\frac{\pi}{2}} \quad (6.11)$$

where the frequency is irrelevant and denoted as placeholder (\cdot) . The augmentation sequence $L_{\text{aug}} = (-1, \cdot) \rightarrow (1, \cdot) \rightarrow \dots$ contains $\frac{n-1}{2}$ π -pulses. The total number of π -pulses required to close this interferometer is $2n - 1$, approximately half the amount in a narrowband interferometer.

6.1.3 Double-Diffraction Narrowband Interferometers

The double number of pulses required in a narrowband interferometer is not ideal to fully utilize the finite time of the experiment, often limited by the free-fall duration under gravity instead of the typically 10–100 s lifetime of the transition. To relieve the time constraint, a technique known as “double-diffraction” can be implemented to impart photon recoil to both arms simultaneously with a single pulse, just like what a broadband interferometer naturally does. To achieve this, a pulse must contain two tones that are tailored to the Doppler shifts of each individual arm. The laser power is evenly divided between the two tones, making the Rabi frequency in each arm lower by $1/\sqrt{2}$. However, since the total number of pulses required to reach a certain LMT order is reduced by half, overall there is a factor of $\sqrt{2}$ gain in the rate of momentum accumulation, or equivalently in the maximal LMT order obtainable within a limited duration.

Figure 6.3 (b) shows the structure of a double-diffraction narrowband interferometer, whose

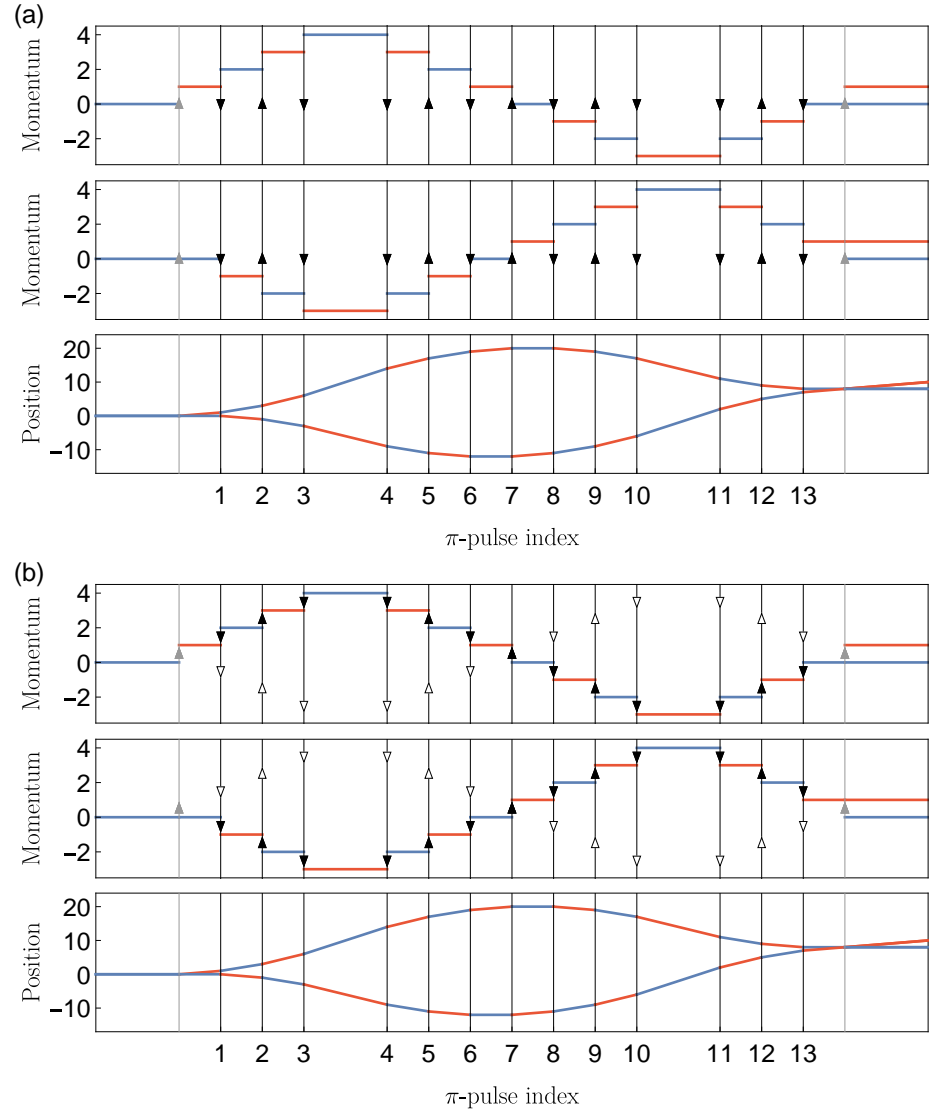


Figure 6.3: (a) A broadband $7\hbar k$ clock atom interferometer arranged in the sequence described by Equation (6.11), where the pulse arrows no longer indicate detuning. (b) A double diffraction narrowband clock atom interferometer, whose momentum-time and space-time diagrams are identical to the broadband interferometer shown in (a). With the exception of the center mirror pulse, each π -pulse contains two tones, indicated by the double arrows on each vertical line.

augmentation sequence has the form

$$L_{\text{aug}} = (-1, \{\frac{3}{2}, -\frac{1}{2}\}) \rightarrow (1, \{\frac{5}{2}, -\frac{3}{2}\}) \rightarrow \cdots \rightarrow ((-1)^{n-1}, \{n - \frac{1}{2}, -n + \frac{3}{2}\}) \quad (6.12)$$

where $f = \{f_{\text{upper}}, f_{\text{lower}}\}$ is a set of two tones.

6.2 Interferometer Fidelity and Contrast

Regardless of the type of interferometer, pulses can induce transfer error at each atom-laser interaction due to various noise sources. The effect of such errors is two-fold. First, the reduction of wave function amplitude in the correct state builds up over the sequence, resulting in a population loss in the output ports and a decrease of interferometer fidelity and contrast. Second, the error wave function will propagate with its own momentum and interact with subsequent pulses depending on its Doppler shift. As a result, in the classical limit, the upper or the lower arm does not stay as a single trajectory in the space-time diagram but branches into a family of trajectories like a binary tree, leading to unwanted interference at the output ports.

We use the terminology “main paths” to denote the two desired trajectories of the upper and the lower arms, which lead to the interferometer phase of interest at the end of the sequence. These are the only two paths existent in an error-free interferometer. The terminology “parasitic paths” refers to all other trajectories induced by transfer errors.

For the rest of this chapter, I will focus on single-diffraction narrowband interferometers for the following reasons. First, a narrowband interferometer, with an example shown in Figure 6.4 (b), has a cleaner parasitic path structure. Unlike the broadband interferometer in Figure 6.5, where a path always branches into two at each pulse due to velocity insensitivity, in a narrowband interferometer a path only branches when its velocity class is on resonance with the pulse. This leads to a reduction of the total number of parasitic paths and simplifies the analysis. Moreover, as the LMT order n increases, an interferometer that starts broadband will eventually be out of the broadband regime. In this case, parasitic paths that are many photon recoils apart from the main paths are sufficiently Doppler-detuned to be treated similarly as the narrowband scenario.

To analyze the consequence of pulse errors, we consider a narrowband LMT clock atom interferometer depicted in Figure 6.4 (b), where besides two beamsplitter $\pi/2$ -pulses at each end and a mirror π -pulse in the center, additional augmentation zones of π -pulses are inserted to increase or decrease the momentum difference between the interferometer arms. To close an $n\hbar k$ interferometer, $4n-3$ π -pulses are required, among which the first $2n-2$ are nominally on resonance with only the upper arm, the last $2n-2$ are nominally on resonance with only the lower arm, and the center pulse is shared between the two arms. For convenience, we assume perfect beamsplitter $\pi/2$ -pulses and focus on the effects of imperfect π -pulses on the upper arm.

During the acceleration of the upper arm, π -pulses are applied from alternating directions, with

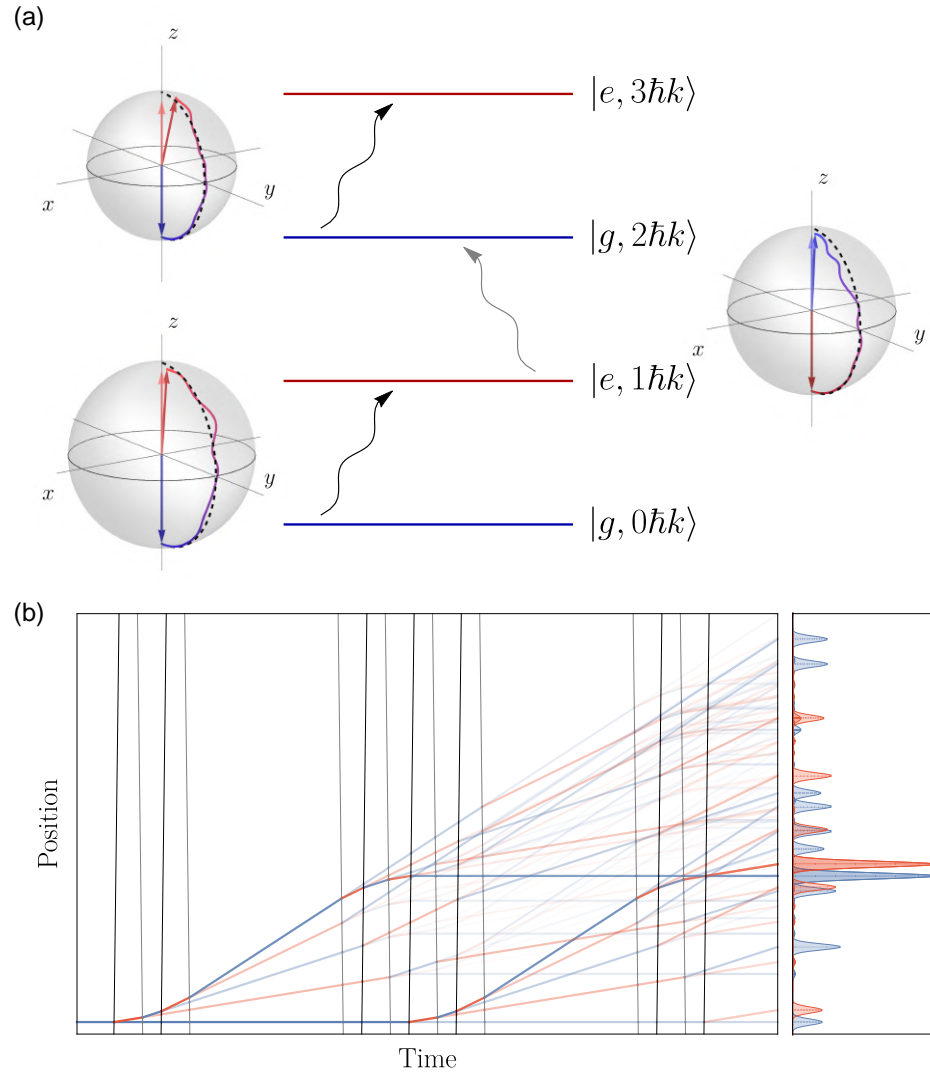


Figure 6.4: (a) Bloch sphere representation of an LMT clock atom interferometer operated on a narrowline transition. Each π -pulse couples two states with opposite internal levels and an external momentum difference of $\hbar k$. The alternation of pulse direction (black slanted arrows) builds up momentum in the wave function, moving it to a new Bloch sphere after each pulse. Laser frequency noise leads to untransferred population that is not carried over to the next Bloch sphere but merely decreases its size, resulting in a reduction in the radius as shown. (b) Space-time diagram of a narrowband clock atom interferometer with exaggerated pulse infidelities. The vertical lines represent light pulses traveling in opposite directions (black vs gray), with the speed of light exaggerated. The first and last pulses are $\pi/2$ -pulses while all others are π -pulses. The internal levels are color-coded in blue (ground) and red (excited), with opacity representing the path amplitudes. The position distribution of all paths after a finite drift time is also shown.

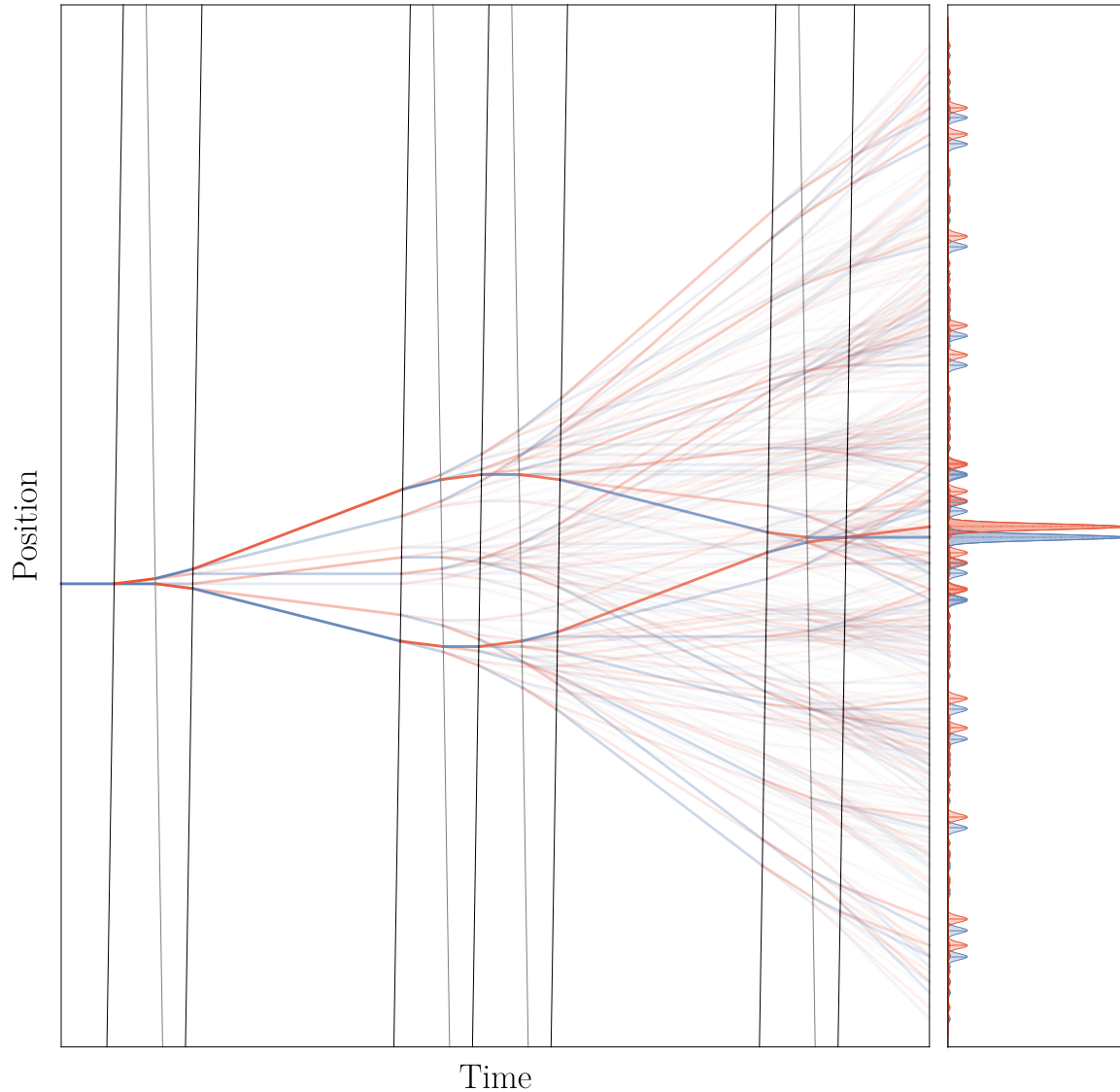


Figure 6.5: A broadband interferometer to be compared with Figure 6.4 (b). The velocity insensitivity of the pulses leads to a more complicated parasitic path structure. Due to the resemblance to a betta fish, we nickname such space-time trajectories “fish diagrams”.

their nominal frequencies adjusted to compensate for the Doppler shift of the atoms. As Figure 6.4 (a) shows, each pulse in this sequence changes the current state by flipping its internal level and increasing its momentum by a photon recoil, while leaving a small fraction of the wave function untransferred due to noise sources such as laser frequency instability. Since the next pulse comes from the opposite direction and is frequency-tuned to the new momentum, it is Doppler suppressed from interacting with the wave function error induced by the previous pulse, assuming a practical kHz-level Rabi frequency on a narrowband transition such as ${}^1\text{S}_0 - {}^3\text{P}_0$ in alkaline-earth(-like) elements. In fact, this wave function error will not accumulate momentum for the rest of the acceleration sequence and will drift away from the main upper path. However, it can interact with certain future pulses after the peak velocity has been reached in the main upper path, branching into parasitic paths which may drift back and interfere with the main paths at the output ports.

Without loss of generality, we can express the population loss in the main paths separately from loss arising from interference due to parasitic paths. Upon interaction, each π -pulse imprints a phase ϕ_j^u , and the pulse imperfection reduces the amplitude of the wave function by $\sqrt{1 - \delta P_j^u}$, where δP_j^u is the population loss from the j -th pulse nominally on resonance, and the superscripts here refer to the upper path. For a full $n\hbar k$ interferometer, the final state of the upper arm right before the closing beamsplitter can be written as

$$|\Psi^u\rangle = c^u |g, 0\rangle + \varepsilon_{g,0}^u |g, 0\rangle + \varepsilon_{e,1}^u |e, 1\rangle + \sum_{\substack{s=g,e \\ 2 \leq p \leq n}} \varepsilon_{s,p}^u |s, p\rangle \quad (6.13)$$

$$= c^u |g, 0\rangle + \varepsilon_{g,0}^u |g, 0\rangle + \varepsilon_{e,1}^u |e, 1\rangle + \{p \geq 2 \text{ states}\} \quad (6.14)$$

where the states are labeled by their internal levels $s = g, e$ and external momentum $p \in \mathbb{Z}$ measured in units of $\hbar k$. The first term is the final state of main upper path, with amplitude

$$c^u \equiv \prod_{j=1}^{2n-1} e^{i\phi_j^u} \sqrt{1 - \delta P_j^u} \quad (6.15)$$

and the subsequent terms describe the parasitic states. Among all possible parasitic paths, we explicitly group those terminating in $|g, 0\rangle$ and $|e, 1\rangle$, and denote their total amplitudes as $\varepsilon_{g,0}^u$ and $\varepsilon_{e,1}^u$. These states will affect the readout after the closing beamsplitter, while all other parasitic states do not have the relevant momentum and are gathered in the last term. Similarly, the lower arm before the closing beamsplitter is

$$|\Psi^\ell\rangle = c^\ell |e, 1\rangle + \varepsilon_{g,0}^\ell |g, 0\rangle + \varepsilon_{e,1}^\ell |e, 1\rangle + \sum_{\substack{s=g,e \\ 2 \leq p \leq n}} \varepsilon_{s,p}^\ell |s, p\rangle \quad (6.16)$$

$$= c^\ell |e, 1\rangle + \varepsilon_{g,0}^\ell |g, 0\rangle + \varepsilon_{e,1}^\ell |e, 1\rangle + \{p \geq 2 \text{ states}\} \quad (6.17)$$

where

$$c^\ell \equiv \prod_{j=2n-1}^{4n-3} e^{i\phi_j^\ell} \sqrt{1 - \delta P_j^\ell} \quad (6.18)$$

We define the fidelity of the interferometer sequence with respect to the two arms as $F^u \equiv |\langle g, 0 | \Psi^u \rangle|^2$ and $F^\ell \equiv |\langle e, 1 | \Psi^\ell \rangle|^2$. From Equations (6.14) and (6.17) we obtain

$$F^u = |c^u + \varepsilon_{g,0}^u|^2 \quad (6.19)$$

$$\approx |c^u|^2 + 2 \operatorname{Re}(\varepsilon_{g,0}^u c^{u*}) \quad (6.20)$$

$$F^\ell = |c^\ell + \varepsilon_{e,1}^\ell|^2 \quad (6.21)$$

$$\approx |c^\ell|^2 + 2 \operatorname{Re}(\varepsilon_{e,1}^\ell c^{\ell*}) \quad (6.22)$$

up to first order in $\varepsilon_{g,0}^u$ and $\varepsilon_{e,1}^\ell$. Using Equations (6.15) and (6.18), with $\delta P_j^{u,\ell} = \delta P$, the average per-pulse population loss, we have

$$F^{u,\ell} \approx \left| \left(\sqrt{1 - \delta P} \right)^{2n-1} \right|^2 + \delta F_{\text{para}}^{u,\ell} \quad (6.23)$$

$$\approx 1 - 2n \delta P + \delta F_{\text{para}}^{u,\ell} \quad (6.24)$$

where we have assumed $2n \delta P \ll 1$ and defined the fidelity loss from parasitic paths in the upper and lower arms

$$\delta F_{\text{para}}^u \equiv 2 \operatorname{Re}(\varepsilon_{g,0}^u c^{u*}) \quad (6.25)$$

$$\delta F_{\text{para}}^\ell \equiv 2 \operatorname{Re}(\varepsilon_{e,1}^\ell c^{\ell*}) \quad (6.26)$$

Note that since both c^u and c^ℓ has norm no greater than unity, we have the following bound for each arm

$$\delta F_{\text{para}}^u \leq 2 |\varepsilon_{g,0}^u| \quad (6.27)$$

$$\delta F_{\text{para}}^\ell \leq 2 |\varepsilon_{e,1}^\ell| \quad (6.28)$$

For the parasitic path analysis in Section 6.3, it is convenient to use a weaker bound that is common for both arms. With the superscripts omitted,

$$\delta F_{\text{para}} \leq 2(|\varepsilon_{g,0}| + |\varepsilon_{e,1}|) \quad (6.29)$$

Now we derive the contrast of the interferometer, whose state before the closing beamsplitter is

$$|\Psi^{\text{AI}}\rangle = \frac{1}{\sqrt{2}}(|\Psi^u\rangle + |\Psi^\ell\rangle) \quad (6.30)$$

$$\approx \frac{1}{\sqrt{2}} \left((c^u + \varepsilon_{g,0}^u + \varepsilon_{g,0}^\ell) |g, 0\rangle + (c^\ell + \varepsilon_{e,1}^u + \varepsilon_{e,1}^\ell) |e, 1\rangle \right) \quad (6.31)$$

where the $p \geq 2$ states are ignored. Assuming the interferometer closes on a lossless beamsplitter with an arbitrary phase θ

$$\hat{U}_{\text{BS}} = \frac{1}{\sqrt{2}} (|g, 0\rangle\langle g, 0| + |e, 1\rangle\langle e, 1| + e^{i\theta} |g, 0\rangle\langle e, 1| + h.c.) \quad (6.32)$$

the $|e, 1\rangle$ population after the beamsplitter is

$$P_e(\theta) = \left| \langle e, 1 | \hat{U}_{\text{BS}} |\Psi^{\text{AI}}\rangle \right|^2 \quad (6.33)$$

$$= \frac{1}{4} \left(|\chi_{g,0}|^2 + |\chi_{e,1}|^2 + 2 \cos(\theta - \theta_0) |\chi_{g,0} \chi_{e,1}| \right) \quad (6.34)$$

where we have defined

$$\chi_{g,0} \equiv c^u + \varepsilon_{g,0}^u + \varepsilon_{g,0}^\ell \quad (6.35)$$

$$\chi_{e,1} \equiv c^\ell + \varepsilon_{e,1}^u + \varepsilon_{e,1}^\ell \quad (6.36)$$

$$\theta_0 \equiv \arg(\chi_{g,0}) - \arg(\chi_{e,1}) \quad (6.37)$$

The interferometer contrast is then

$$C = |\chi_{g,0} \chi_{e,1}| \quad (6.38)$$

$$= \left| \left(\left(\sqrt{1 - \delta P} \right)^{2n-1} + \varepsilon_{g,0}^u + \varepsilon_{g,0}^\ell \right) \left(\left(\sqrt{1 - \delta P} \right)^{2n-1} + \varepsilon_{g,0}^u + \varepsilon_{g,0}^\ell \right) \right| \quad (6.39)$$

$$\approx 1 - 2n \delta P + \delta C_{\text{para}} \quad (6.40)$$

where the contrast reduction due to interference from parasitic paths is defined up to the first order of $\varepsilon_{s,p}^u$ and $\varepsilon_{s,p}^\ell$ as

$$\delta C_{\text{para}} \equiv |\varepsilon_{g,0}^u + \varepsilon_{g,0}^\ell + \varepsilon_{e,1}^u + \varepsilon_{e,1}^\ell| \quad (6.41)$$

$$\leq 2(|\varepsilon_{g,0}| + |\varepsilon_{e,1}|) \quad (6.42)$$

where we obtained a bound assuming $\varepsilon_{g,0}^u \approx \varepsilon_{g,0}^\ell$ and $\varepsilon_{e,1}^u \approx \varepsilon_{e,1}^\ell$, hence the omission of the superscripts. Note that this bound takes the same form as Inequality (6.29).

As we discuss in Section 6.3, the parasitic amplitudes $\varepsilon_{s,p}^u$ and $\varepsilon_{s,p}^\ell$ are weak perturbations

compared to the population loss in the main paths. Keeping only the latter contribution, Equations (6.24) and (6.40) reduce to the same expression

$$C \approx \frac{F^u + F^\ell}{2} = 1 - 2n \delta P \quad (6.43)$$

which exhibits linear dependence on LMT order n , as expected. The linear scaling of the interferometer fidelity and contrast loss with respect to n in Equation (6.43) is a manifestation of the extended Hilbert space, which is spanned not only by the internal atomic levels but also by the external momentum states from alternating pulse directions, an essential feature of LMT clock atom interferometry.

6.3 Parasitic Interferometer Paths

6.3.1 Parasitic Amplitude Bound

Here we analyze the fidelity loss induced by the parasitic paths and show that it is indeed a small correction for practical LMT clock atom interferometers. As depicted in Figure 6.4, a parasitic path arises when a pulse error occurs, causing a small untransferred amplitude to deviate from the main path. For a mathematical treatment of the parasitic paths, we write the final state of a generic parasitic path as $|\psi^{(m)}(j_1, j_2, \dots, j_m)\rangle$, where m is the number of pulse errors and j_1, j_2, \dots, j_m are the indices of all nominally resonant pulses where errors occur. Take the upper arm as an example, with superscripts omitted for convenience, Equation (6.14) can be rewritten by grouping the parasitic terms according to the number of errors,

$$|\Psi\rangle = c|g, 0\rangle + \sum_{j_1=1}^{4n-3} \alpha_{j_1} |\psi^{(1)}(j_1)\rangle + \sum_{j_1=1}^{4n-3} \sum_{j_2=j_1+1}^{4n-3} \alpha_{j_1} \alpha_{j_2} |\psi^{(2)}(j_1, j_2)\rangle + \dots \quad (6.44)$$

$$= c|g, 0\rangle + \sum_{m \geq 1} \left(\sum_{j_1=1}^{4n-3} \dots \sum_{j_m=j_{m-1}+1}^{4n-3} \alpha_{j_1} \dots \alpha_{j_m} |\psi^{(m)}(j_1, \dots, j_m)\rangle \right) \quad (6.45)$$

where α_j represents the complex amplitude of the projection error at the j -th pulse, and relates to the population loss by $|\alpha_j|^2 = \delta P_j$. For ease of analysis, we drop the phase and use a universal $\alpha \in \mathbb{R}$ as the error amplitude. This simplification treats all parasitic paths in phase and thus leads to an upper bound of their interference at the output ports. To maintain contrast in the main interferometer, we consider the case where $n\alpha^2 \ll 1$.

For a narrowband interferometer, example parasitic paths with various m in the freely falling frame are shown in Figures 6.6 to 6.8. As m increases, the corresponding term in Equation (6.45) is suppressed by α^m , while there are more paths with different combinations of pulse error indices. Counting the number of paths in each m -term of Equation (6.45) is required to bound its contribution

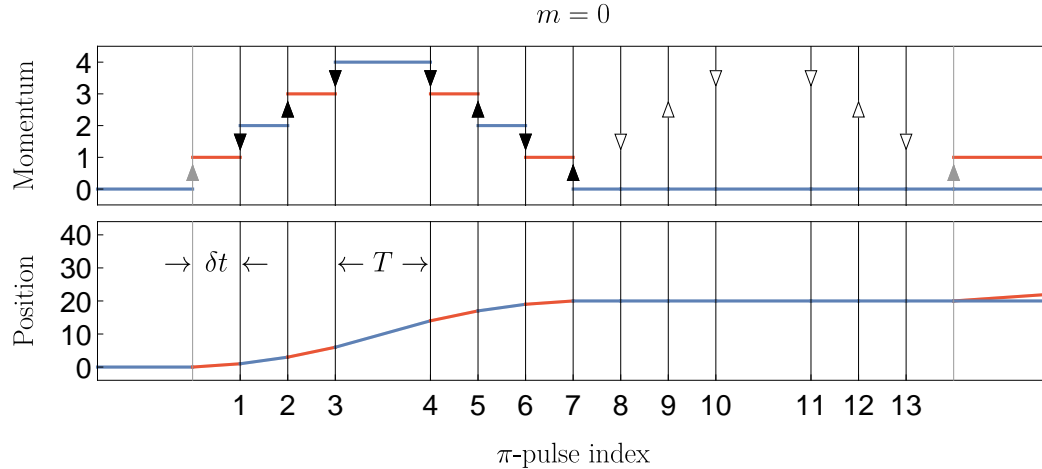


Figure 6.6: Momentum-time and space-time diagrams of the upper arm of a narrowband $4\hbar k$ clock atom interferometer. The internal atomic levels are indicated as blue (ground) and red (excited). The vertical lines represent π -pulses (black) and $\pi/2$ -pulses (gray), with arrows indicating their directions and detunings. We assume equal pulse spacing δt and a non-zero interrogation time T . The vertical axes are dimensionless, with momentum in units of $\hbar k$ and position in units of $v_r\delta t$, where v_r is the recoil velocity. This figure shows the main upper path, where no pulse error occurs and hence $m = 0$. Note that the second half of the sequence is addressed to the lower arm, thus off-resonant with the main upper path, indicated by the open arrows.

to the series. Note that only parasitic paths that lead to the same final momentum states as the main paths cause interference since the other velocity classes have different de Broglie wavelengths. We therefore restrict the counting to those $|\psi^{(m)}(j_1, \dots, j_m)\rangle$ that project onto $|g, 0\rangle$ or $|e, 1\rangle$, leading to a total number of $N_p(m, n)$ paths, where the subscript indicates the momentum constraint. We also exclude paths with final positions far away from the detection region, as they can be separately resolved and excluded by an appropriate choice of region of interest for imaging. This further reduces the number of paths to $N_{p,x}(m, n)$, where the subscripts indicate the constraints from both momentum and position.

The path counting method is elaborated in Section 6.3.2. In summary, the final momentum constraint poses a strong bound to the number of paths. For this condition to be fulfilled, the error pulses must be grouped into pairs that have the same detuning, as shown in Figure 6.7, or occur at the center mirror pulse, as shown in Figure 6.8. The nominal frequency structure of a narrowband LMT clock interferometer sequence shown in Figures 6.6 to 6.8 truncates the series in Equation (6.45) up to terms with $m \leq 6$. For a specific m , only $N_p(m, n) = \mathcal{O}(n^{\lfloor m/2 \rfloor})$ combinations of pulse error indices are allowed. As shown in Figure 6.9 (a), this scaling is numerically validated up to $n = 15$ by enumerating all possible paths for LMT interferometers.

The final position constraint further reduces the number of possible pulse error combinations, because only a small fraction of the $N_p(m, n)$ paths lie within a distance of w from the main paths,

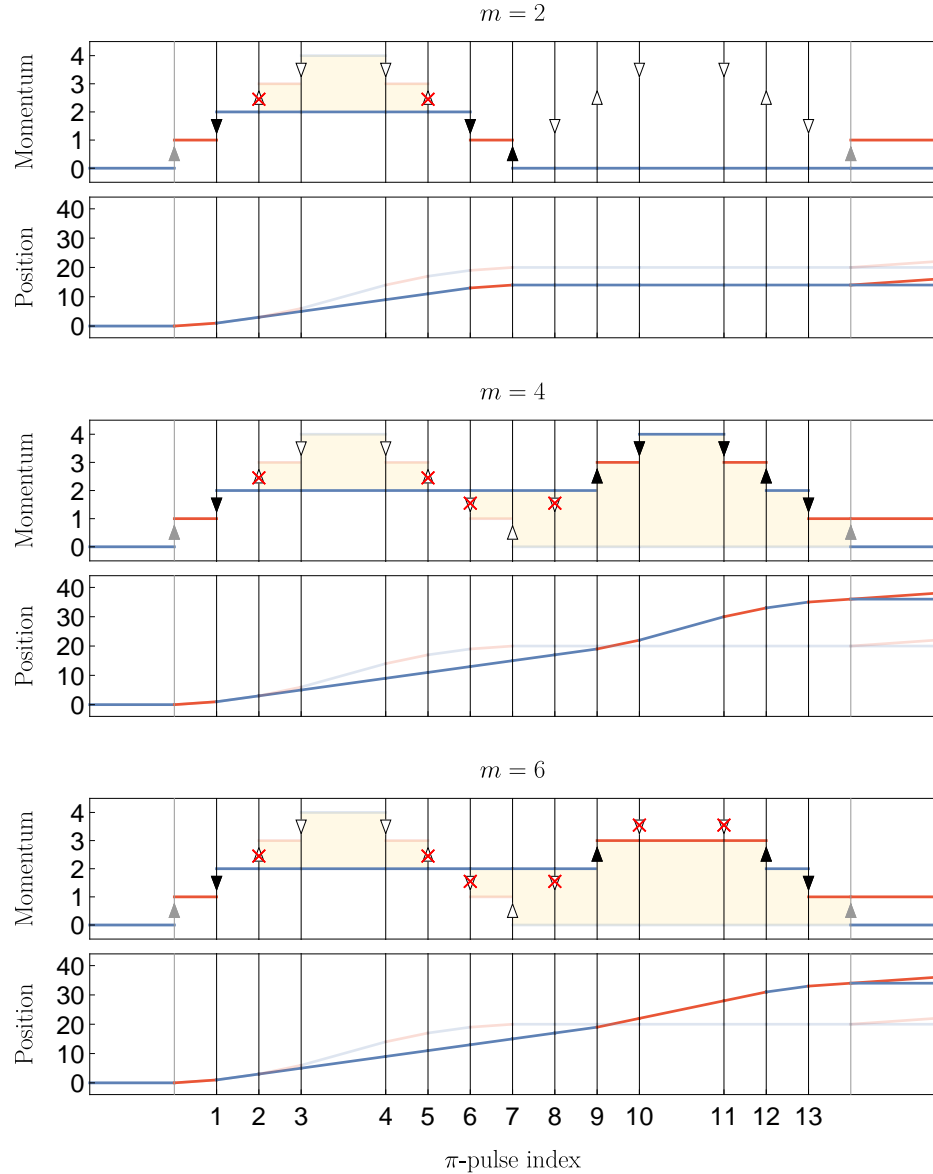


Figure 6.7: Momentum-time and space-time diagrams similar to Figure 6.6 but with non-zero even m values. In the example parasitic paths, the cross marks indicate pulses with transition errors. Due to these errors, the parasitic paths fail to follow the main path (show for reference in lower opacity). The yellow shaded area indicates the relative position error of the parasitic path with respect to the main path, which is also shown explicitly in the space-time diagram. From top to bottom, the number increases as $m = 2, 4, 6$. We have selected an $m = 4$ example such that the first two errors are the same as the $m = 2$ example, and the subsequent errors lead to additional integrated relative position error (indicated by additional yellow shading). A similar choice is made for the $m = 6$ example.

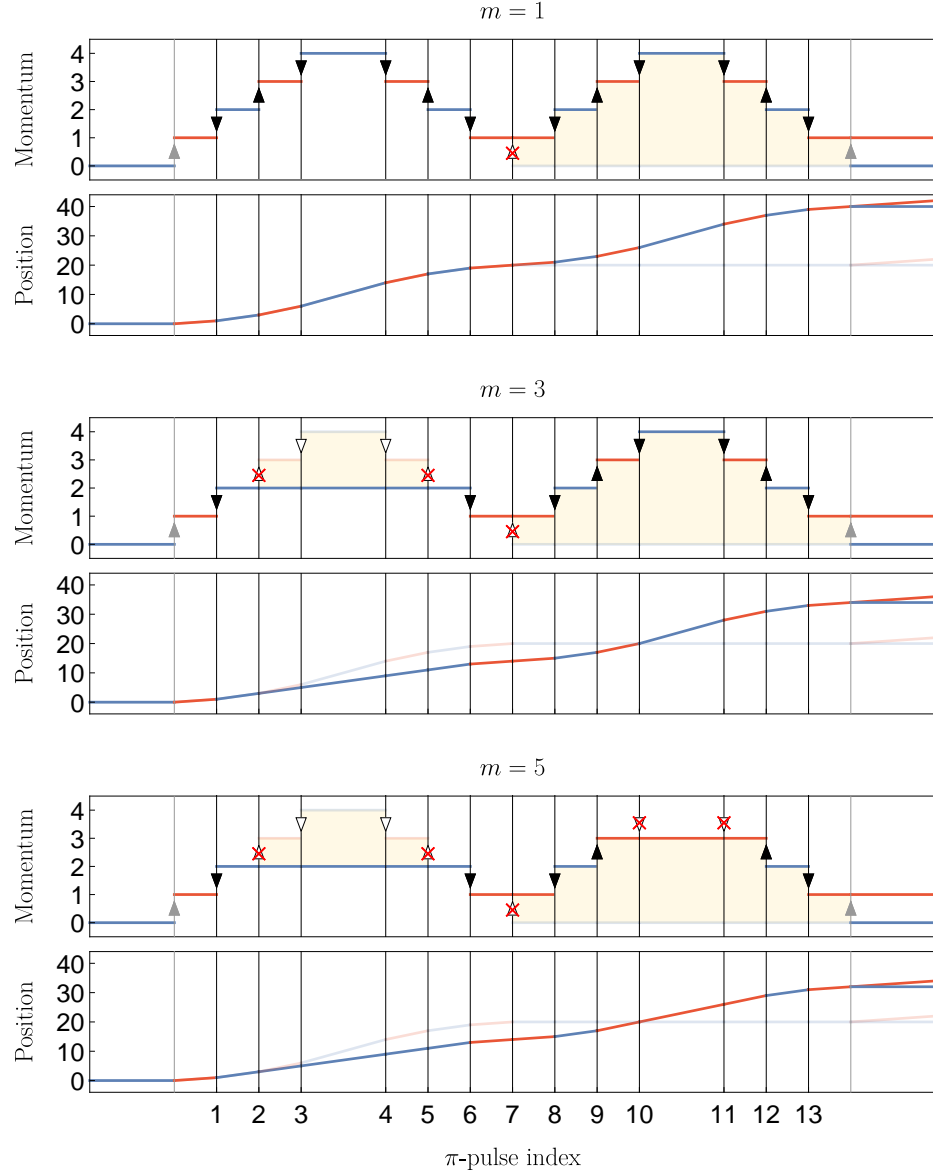


Figure 6.8: Momentum-time and space-time diagrams similar to Figures 6.6 and 6.7 but with odd numbers of errors $m = 1, 3, 5$. To satisfy the momentum constraint with an odd m , an error must occur at the center mirror pulse. Note that the examples here and in Figure 6.7 are only illustrative, and many other parasitic paths are possible.

where w is the radius of the detection region. Here we assume all paths outside of w do not contribute to interference, which is true as long as the wavepackets are localized². The relative position of the example parasitic paths with respect to the main upper path is visualized in Figures 6.7 and 6.8 by the shaded area in the momentum-time diagram. For the sake of generality, in these figures we have included an interrogation time T between the acceleration and deceleration sequences. However, to obtain a worse case bound, we analyze the case with zero interrogation time, as detailed in Section 6.3.2. As shown in Figure 6.8, a parasitic path that satisfies the momentum constraint with $m = 1$ will never terminate in the vicinity of the main path. For parasitic paths with $2 \leq m \leq 6$, we prove in Section 6.3.2 that the number of possible combinations of pulse errors is reduced from $N_p(m, n)$ to $N_{p,x}(m, n)$ with expression

$$N_{p,x}(m, n) = \frac{w}{v_r \delta t} \cdot \mathcal{O}\left(n^{\lfloor m/2 \rfloor - 1}\right) \quad (6.46)$$

where v_r is the recoil velocity and δt is the pulse spacing. At Rabi frequency Ω , we have $\delta t \geq \pi/\Omega$.

We determine an upper bound of the wave function error ε induced by parasitic paths by adding the amplitudes of all relevant paths in phase, namely those that terminate in $|g, 0\rangle$ and $|e, 1\rangle$ with the correct final position. This is equivalent to summing the number of paths $N_{p,x}(m, n)$ over the number of errors m , weighted by the amplitude suppression α^m ,

$$\varepsilon \equiv |\varepsilon_{g,0}| + |\varepsilon_{e,1}| \quad (6.47)$$

$$= \sum_{m=2}^6 \alpha^m N_{p,x}(m, n) \quad (6.48)$$

This expression can be simplified by taking the leading order in the summation,

$$\varepsilon = \sum_{m=2}^6 \alpha^m \frac{w}{v_r \delta t} \cdot \mathcal{O}\left(n^{\lfloor m/2 \rfloor - 1}\right) \quad (6.49)$$

$$\approx \frac{w}{v_r \delta t} \cdot \mathcal{O}(\alpha^2) \quad (6.50)$$

where $n\alpha^2 \ll 1$ is assumed to preserve the interferometer contrast, consistent with the assumption that the contrast in Equation (6.43) is approximately one. Although Equation (6.50) is derived in the context of the upper arm, the same argument holds for the lower arm as well. According to Inequalities (6.29) and (6.42), the loss of fidelity in a single arm δF_{para} and the reduction of contrast of the interferometer δC_{para} due to parasitic paths are both bounded by 2ε .

Note that unlike population loss in the main path, Equation (6.50) suggests that the error induced by the parasitic path is bounded by a constant at large LMT order n . To explain this, we note that the suppression from the transition error amplitudes α^m is more significant than the growth of

²We assume $w \sim 1\text{mm}$, which is about $100\times$ larger than the de Broglie wavelength of a nK cloud.

$N_{p,x}(m, n)$ with respect to m . Equation (6.48) is thus dominated by $m = 2$ paths that satisfy both momentum and position constraints, whose total number $N_{p,x}(2, n) = \frac{w}{v_r \delta t} \mathcal{O}(1)$ is independent of n .

We numerically calculate the amplitude error induced by parasitic paths for LMT interferometers up to $n = 15$ in the case of densely packed pulses such that $\delta t = \pi/\Omega$. Figure 6.9 (b) confirms that the error has a constant upper bound for an interferometer operated at Rabi frequency $\Omega = 2\pi \times 1$ kHz, recoil velocity $v_r = 6.6$ mm/s, and detection region radius $w = 1$ mm. With pulse inefficiency $\alpha^2 = 10^{-4}$ and zero interrogation time, the wave function error at large n is $\varepsilon = 5 \times 10^{-3}$, which causes a small degradation of the fidelity and contrast of the interferometer by at most $2\varepsilon = 1 \times 10^{-2}$. A finite interrogation time T further reduces the loss by posing a stronger position constraint on the parasitic paths.

6.3.2 Parasitic Path Counting

To obtain the functional form of $N_p(m, n)$ and $N_{p,x}(m, n)$, we analyze the narrowband pulse sequence in Equation (6.9). For convenience, we assume perfect beamsplitters and focus on the π -pulse section of L_{nb} , which contains $4n - 3$ pulses whose directions and detunings are indicated by the arrows in Figure 6.6, with the following analytic forms

$$d_j = \begin{cases} (-1)^j & 1 \leq j < n \\ (-1)^{2n-j+1} & n \leq j < 2n - 1 \\ 1 & j = 2n - 1 \\ (-1)^{j-2n-1} & 2n - 1 < j \leq 3n - 2 \\ (-1)^{4n-j} & 3n - 2 < j \leq 4n - 3 \end{cases} \quad (6.51)$$

$$f_j = \begin{cases} j + \frac{1}{2} & 1 \leq j < n \\ 2n - j - \frac{1}{2} & n \leq j < 2n - 1 \\ \frac{1}{2} & j = 2n - 1 \\ j - 2n + \frac{3}{2} & 2n - 1 < j \leq 3n - 2 \\ 4n - j - \frac{3}{2} & 3n - 2 < j \leq 4n - 3 \end{cases} \quad (6.52)$$

where we show the four augmentation zones as piecewise functions, along with the center mirror pulse. Note that each augmentation zone has a monotonic frequency dependence with respect to the pulse index j .

Here we use the examples in Figure 6.7 to show how multiple pulse errors can generate a parasitic path with the same final momentum as one of the main paths in order to contribute to the interference background. In the examples, a pulse error occurs at $j = 2$, and the error state becomes off-resonance with subsequent pulses in the same augmentation zone. The resulting parasitic path drifts at a constant momentum until a pulse $j' = 5$ occurs in the next augmentation zone. This pulse is on resonance since $d_5 = d_2$ and $f_5 = f_2$. From this point on, the parasitic path will undergo a transition

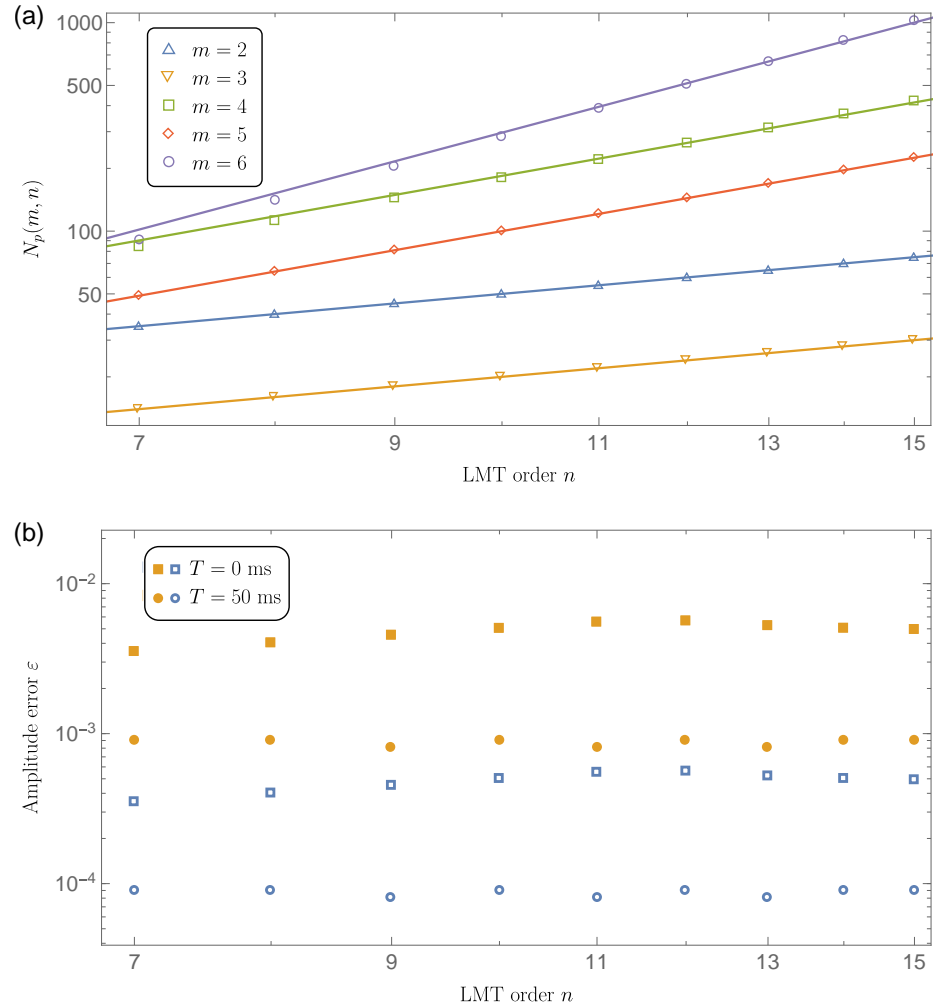


Figure 6.9: (a) Number of parasitic paths that satisfy the momentum constraint $N_p(m, n)$ as a function of LMT order n , obtained by numerically enumerating all paths with a fixed number of pulse errors m , and filtering out those with final momentum $p = 0$ or $p = 1$. The lines are monomial fits at the power of $\lfloor m/2 \rfloor$, showing good agreement with the predicted $\mathcal{O}(n^{\lfloor m/2 \rfloor})$ growth for $n \geq 7$, before further restriction is applied on the final position of the parasitic paths. Note that $\mathcal{O}(n^{\lfloor m/2 \rfloor})$ only describes the limiting behavior of $N_p(m, n)$ at large enough n , hence the fits do not extend to $n < 7$ region. (b) Parasitic-path-induced error ε as a function of LMT order n for densely-packed pulses at $\Omega = 2\pi \times 1 \text{ kHz}$, obtained by constructively summing over amplitudes of all parasitic paths that satisfy both the momentum constraint and the position constraint. We have assumed $w = 1 \text{ mm}$ and $v_r = 6.6 \text{ mm/s}$. We show two pulse inefficiency values $\alpha^2 = 10^{-4}$ (filled orange markers) and $\alpha^2 = 10^{-5}$ (open blue markers), with interrogation time $T = 0 \text{ ms}$ (squares) or $T = 50 \text{ ms}$ (circles).

or not. If an additional error occurs here and it does not make the transition at $j' = 5$, then the rest of the parasitic path overlaps with the main path, either to the end of the interferometer or until another pulse error occurs. The former results in the $m = 2$ path in Figure 6.7, and examples of the latter are given by $m = 4, 6$ in Figure 6.7. However, if the transition at $j' = 5$ is successful, then the parasitic path is again off-resonance with subsequent pulses until it reaches another resonant pulse $j'' = 9$ in the next augmentation zone. Then the process repeats.

Note that when $f_j = f_{j'}$, Equations (6.51) and (6.52) guarantees $d_j = d_{j'}$. We thus conclude that a parasitic path terminates at the same momentum as one of the main paths if two pulse errors occur with the same detuning. As shown in Figure 6.7, this can be generalized to an even number of pulse errors arranged in pairs of equal detuning. In addition, the center mirror pulse at $j_c = 2n - 1$ does not have an equal detuning counterpart, but an error is allowed to occur on this pulse, with examples shown in Figure 6.8. Consequently, if a parasitic path that fulfills the momentum constraint contains m pulse errors, they must be grouped into $\lfloor m/2 \rfloor$ pairs. Since there are $\mathcal{O}(n)$ ways to arrange each pair in an LMT sequence of $4n - 3$ pulses, the total number of parasitic paths is bounded by $N_p(m, n) = \mathcal{O}(n^{\lfloor m/2 \rfloor})$. Finally, the narrowband interferometer structure in Equation (6.9) contains four augmentation zones, limiting the pulse errors to be no more than 3 pairs, or equivalently, $m \leq 6$.

To account for the final position of the parasitic paths, we make the worst-case assumption of zero interrogation time T , and consider a path that terminates with the correct momentum but not necessarily the correct position. Note that $m = 1$ is only possible when the upper arm encounters an error at the center mirror pulse, resulting in a parasitic path that is nominally on resonance with all subsequent pulses, even though they are frequency-tuned to the lower arm. As shown in Figure 6.8, this parasitic path experiences twice the displacement as the main paths in the freely falling frame, and does not terminate at the detection region for large enough n .

We thus focus on paths with $m > 1$ where at least one pair of pulse errors occurs. We denote pulse indices in a pair as j and \bar{j} . Note that up to the choice of which augmentation zone, \bar{j} is completely determined by j based on the constraint $f_j = f_{\bar{j}}$. Then we can express the relative position of a parasitic path with respect to the main path as a function of the integer-valued free variables $j_1, \dots, j_{\lfloor m/2 \rfloor}$, the first indices of the $\lfloor m/2 \rfloor$ pairs of errors,

$$x_{\text{para}} - x_{\text{main}} = \delta x(j_1, \dots, j_{\lfloor m/2 \rfloor}) \quad (6.53)$$

which is also true for odd m since the center mirror pulse j_c is not a free variable. Geometrically, this represents the signed area of the shaded regions in the momentum-time diagrams in Figures 6.7 and 6.8, which must be a quadratic function of the free variables. Moreover, the relative position δx is proportional to the recoil velocity v_r and the pulse spacing δt . We thus define the quadratic form

$$Q(j_1, \dots, j_{\lfloor m/2 \rfloor}) \equiv \frac{1}{v_r \delta t} \delta x(j_1, \dots, j_{\lfloor m/2 \rfloor}) \quad (6.54)$$

as the dimensionless relative position. A parasitic path will interfere with the main paths if

$$|Q(j_1, \dots, j_{\lfloor m/2 \rfloor})| \leq \frac{w}{v_r \delta t} \quad (6.55)$$

where w is the radius of the detection region. We assume $w \sim \text{mm}$, so the wavepacket spread is small in comparison and the paths can be treated classically. Inequality (6.55) poses additional constraints on the $\lfloor m/2 \rfloor$ free parameters, leading to a reduction of feasible parasitic paths from $N_p(m, n)$ to $N_{p,x}(m, n)$.

To deduce $N_{p,x}(m, n)$, we calculate the available choices of j_1 that satisfies the position constraint, while keeping the other indices free. Assuming some $j_1^* \in \mathbb{R}$ exists that satisfies $Q(j_1^*, \dots, j_{\lfloor m/2 \rfloor}) = 0$, we expand Q about j_1^* and obtain

$$Q(j_1, \dots, j_{\lfloor m/2 \rfloor}) = B \delta j_1 + A \delta j_1^2 \quad (6.56)$$

where $\delta j_1 = j_1 - j_1^*$, and we have defined

$$A \equiv \left. \frac{\partial^2 Q}{\partial j_1^2} \right|_{j_1=j_1^*} \quad (6.57)$$

$$B \equiv \left. \frac{\partial Q}{\partial j_1} \right|_{j_1=j_1^*} \quad (6.58)$$

Note that the expansion is exact since Q is quadratic with respect to j_1 . In fact, depending on which augmentation zones j_1 and \bar{j}_1 belong to, we can explicitly write down how Q depends on j_1 by calculating the area of the shaded regions in Figures 6.7 and 6.8. We summarize the results in Table 6.1, and note that $|A| = 0$ or $|A| = 2$ in all scenarios.

Table 6.1: Dependence of the dimensionless relative position Q on the first error index j_1 . Augmentation zones 1,2 refer to the L_{aug} and L_{aug}^{-1} before the center mirror pulse in Equation (6.9), and 3,4 refer to those after the center mirror pulse. The j_1 -independent terms are omitted.

Aug. section of j_1	Aug. section of \bar{j}_1	Q
1	2	$-j_1^2 + 2nj_1 + \dots$
1	3	$2nj_1 + \dots$
1	4	$-j_1^2 + 4nj_1 + \dots$
2	3	$j_1^2 - 4nj_1 + \dots$
2	4	$-2nj_1 + \dots$
3	4	$-j_1^2 + 6nj_1 + \dots$

Inequality (6.55) can be rewritten in terms of δj_1 as

$$|A \delta j_1^2 + B \delta j_1| \leq W \quad (6.59)$$

where $W \equiv \frac{w}{v_r \delta t}$ is the dimensionless width of the detection region. We first consider the $|A| = 2$ scenario, where we define $\Delta j_1 \equiv \frac{|A|}{W}(\delta j_1 + \frac{B}{2A})$ and $X \equiv \frac{B^2}{4|A|W}$. When $X \leq 1$, Inequality (6.59) simplifies to

$$\Delta j_1 \in \left[-\sqrt{X+1}, \sqrt{X+1} \right] \quad (6.60)$$

and when $X > 1$,

$$\Delta j_1 \in \left[-\sqrt{X+1}, -\sqrt{X-1} \right] \cup \left[\sqrt{X-1}, \sqrt{X+1} \right] \quad (6.61)$$

In either case, the total length of the interval does not exceed $2\sqrt{2}$. We thus conclude that δj_1 is confined within an interval of length

$$D \leq 2\sqrt{2} \frac{W}{|A|} \leq \frac{\sqrt{2}w}{v_r \delta t} \quad (6.62)$$

In the $|A| = 0$ scenario, notice from Table 6.1 that $|B| = 2n$, then Inequality (6.59) reduces to a simple form

$$|\delta j_1| \leq \frac{W}{2n} \quad (6.63)$$

and the interval length still satisfies $D \leq \frac{\sqrt{2}w}{v_r \delta t}$ for $n \geq 1$.

With the position constraint imposed, j_1 can only take integer values in an interval of length D around j_1^* , as opposed to $\mathcal{O}(n)$ choices in the interferometer sequence. As a result, although $N_p(m, n)$ parasitic paths terminate with the correct momentum, only $N_{p,x}(m, n) = \frac{D}{n}N_p(m, n) = \frac{w}{v_r \delta t}\mathcal{O}(n^{\lfloor m/2 \rfloor - 1})$ of them can enter the detection region and affect the contrast of the interferometer. Note that the choice of j_1 as the constrained index is arbitrary and is equivalent to constraining any index among $j_1, \dots, j_{\lfloor m/2 \rfloor}$. This concludes the combinatorial treatment of the relevant parasitic paths and proves Equation (6.46).

We incorporate this form of $N_{p,x}(m, n)$ into the weighted sum of the wave function amplitudes in Equation (6.48) assuming constructive interference among all relevant paths. The total contribution of parasitic paths to the relevant states $|g, 0\rangle$ and $|e, 1\rangle$ is then bounded by Equation (6.50), which is a constant independent of the LMT order n .

6.4 Laser Frequency Noise

6.4.1 Frequency Noise Transfer Function

Since interference of the parasitic paths only weakly degrades the sequence fidelity and does not scale with the number of pulses, the dominant effect of laser frequency noise on interferometer contrast is the loss of amplitude in the main paths. To study the practical laser stability requirement, we ignore the parasitic paths and derive the amplitude response of the interferometer wave function when addressed by a π -pulse with frequency noise. To achieve this, we perturbatively expand the time evolution operator and obtain the single-pulse frequency noise transfer function. We then put our results in the context of a narrowband clock atom interferometer and extend the analysis to a sequence of n pulses from alternating directions.

We consider a single π -pulse with time-dependent coupling $\Omega(t)$ driving the transition between two states $|1\rangle$ and $|2\rangle$ split by an energy difference of $\hbar\omega_0$. The light field is assumed to have nominal angular frequency ω and a small noise term $\delta\omega(t)$, where $\delta\omega(t)$ is an arbitrary function. The Hamiltonian after the rotating wave approximation can be written as

$$\hat{H} = \frac{1}{2}\hbar\Omega(t)e^{i((\omega-\omega_0)t+\varphi(t))}|1\rangle\langle 2| + h.c. \quad (6.64)$$

where the phase φ is related to the angular frequency noise as

$$\varphi(t) = \int_{t_0}^t \delta\omega(t') dt' + \varphi_0 \quad (6.65)$$

and t_0 marks the beginning of the atom-light interaction. We begin by transforming the Hamiltonian into a rotating frame using the unitary transformation $\hat{R}(t) = e^{-\frac{i}{2}\hat{\sigma}_z\varphi(t)}$, where $\hat{\sigma}_x, \hat{\sigma}_y, \hat{\sigma}_z$ are the Pauli matrices. Assuming the laser is nominally on resonance, the transformed Hamiltonian can be expressed as

$$\hat{H}_R = \hat{R}\hat{H}\hat{R}^\dagger + i\hbar\partial_t\hat{R}\hat{R}^\dagger \quad (6.66)$$

$$= \hat{H}_0 + \hat{\delta}H \quad (6.67)$$

where the noise-free Hamiltonian \hat{H}_0 and the perturbation $\hat{\delta}H$ are expressed as

$$\hat{H}_0 = \frac{1}{2}\hbar\Omega(t)\hat{\sigma}_x \quad (6.68)$$

$$\hat{\delta}H = \frac{1}{2}\hbar\delta\omega(t)\hat{\sigma}_z \quad (6.69)$$

The interaction picture Hamiltonian is obtained using the time evolution operator $\hat{U}_0(t, t_0) =$

$e^{-\frac{i}{\hbar} \int_{t_0}^t \hat{H}_0(t') dt'}$ as

$$\hat{H}_{\text{int}} = \hat{U}_0^\dagger \delta\hat{H} \hat{U}_0 \quad (6.70)$$

$$= \frac{1}{2} \hbar \delta\omega(t) (\hat{\sigma}_y \sin A(t) + \hat{\sigma}_z \cos A(t)) \quad (6.71)$$

where $A(t) = \int_{t_0}^t \Omega(t') dt'$ is the pulse area. For a π -pulse with duration τ , $A(t_0 + \tau) = \pi$. We expand the interaction picture time evolution operator with a Dyson series truncated at second order of the perturbation and obtain

$$\hat{U}_{\text{int}} \approx 1 - \frac{i}{\hbar} \int_{t_0}^t \hat{H}_{\text{int}}(t') dt' + \left(-\frac{i}{\hbar}\right)^2 \int_{t_0}^t \int_{t_0}^{t'} \hat{H}_{\text{int}}(t') \hat{H}_{\text{int}}(t'') dt'' dt' \quad (6.72)$$

where the approximation is valid as long as $|\delta\omega(t)| \ll \Omega(t)$. The state of the atom at any given time t is $|\psi(t)\rangle = \hat{U}(t, t_0) |\psi(t_0)\rangle$, where $\hat{U}(t, t_0)$ is the complete time evolution operator given by

$$\hat{U}(t, t_0) = \hat{R}^\dagger(t) \hat{U}_0 \hat{U}_{\text{int}} \hat{R}(t_0) \quad (6.73)$$

Assuming the initial state to be $|\psi(t_0)\rangle = |1\rangle$, we can write the amplitude in the target state $|2\rangle$ after the π -pulse of duration τ as

$$\langle 2 | \psi(t_0 + \tau) \rangle = \langle 2 | \hat{U}(t, t_0) | 1 \rangle \quad (6.74)$$

$$= -ie^{-i\bar{\varphi}} (1 - iu_1 - u_2) \quad (6.75)$$

where we have defined

$$\bar{\varphi} \equiv \frac{1}{2} (\varphi(t_0 + \tau) + \varphi(t_0)) \quad (6.76)$$

$$u_1 \equiv \frac{1}{2} \int_{t_0}^{t_0 + \tau} \cos A(t') \delta\omega(t') dt' \quad (6.77)$$

$$u_2 \equiv \frac{1}{4} \int_{t_0}^{t_0 + \tau} \int_{t_0}^{t'} \cos(A(t') - A(t'')) \delta\omega(t') \delta\omega(t'') dt'' dt' \quad (6.78)$$

The population transfer error up to second order of $\delta\omega(t)$ can be written as

$$\delta P = 1 - |\langle 2 | \psi(t_0 + \tau) \rangle|^2 \quad (6.79)$$

$$= 2u_2 - u_1^2 + \mathcal{O}(\delta\omega^3) \quad (6.80)$$

We only keep the first two terms that are of leading order $\mathcal{O}(\delta\omega^2)$. After plugging in the expressions

for u_1 and u_2 , we get

$$\delta P = \left(\frac{1}{2} \int_{t_0}^{t_0+\tau} \sin A(t) \delta\omega(t) dt \right)^2 \quad (6.81)$$

$$= \left(\int_{-\infty}^{+\infty} h_1(t) \delta\nu(t) dt \right)^2 \quad (6.82)$$

where $\delta\nu(t) = \frac{\delta\omega(t)}{2\pi}$. In Equation (6.82), we have introduced the second-order time response function

$$h_1(t) \equiv \pi \sin \left(\int_{t_0}^t \Omega(t') dt' \right) (\Theta(t - t_0) - \Theta(t - (t_0 + \tau))) \quad (6.83)$$

with $\Theta(t)$ being the unit step function. Equation (6.82) can be evaluated in the frequency domain. Using Fourier transforms

$$\widehat{h}_1(f) = \int_{-\infty}^{+\infty} h_1(t) e^{-i \cdot 2\pi f t} dt \quad (6.84)$$

$$\widehat{\delta\nu}(f) = \int_{-\infty}^{+\infty} \delta\nu(t) e^{-i \cdot 2\pi f t} dt \quad (6.85)$$

we write the population error in Equation (6.82) as

$$\delta P = \int_{-\infty}^{+\infty} \int_{-\infty}^{+\infty} \widehat{h}_1(f) \widehat{h}_1^*(f') \widehat{\delta\nu}^*(f) \widehat{\delta\nu}(f') df' df \quad (6.86)$$

The frequency response function $\widehat{h}_1(f)$ can be analytically calculated assuming a π -pulse with $\Omega(t) = \Omega = \pi/\tau$,

$$\widehat{h}_1(f) = \pi\Omega \left(\frac{1 + e^{-i \cdot 2\pi f \frac{\pi}{\Omega}}}{\Omega^2 - (2\pi f)^2} \right) e^{-i \cdot 2\pi f t_0} \quad (6.87)$$

To obtain the transfer function with respect to the frequency noise power spectral density, we assume $\delta\nu(t)$ to be a stationary process and calculate the ensemble average of $\widehat{\delta\nu}^*(f) \widehat{\delta\nu}(f')$,

$$\langle \widehat{\delta\nu}^*(f) \widehat{\delta\nu}(f') \rangle = \int_{-\infty}^{+\infty} \int_{-\infty}^{+\infty} \langle \delta\nu^*(t) \delta\nu(t') \rangle e^{i \cdot 2\pi f t} e^{-i \cdot 2\pi f' t'} dt dt' \quad (6.88)$$

$$= \int_{-\infty}^{+\infty} e^{i \cdot 2\pi (f - f') t} dt \int_{-\infty}^{+\infty} \langle \delta\nu^*(t - \tau) \delta\nu(t) \rangle e^{-i \cdot 2\pi f \tau} d\tau \quad (6.89)$$

$$= \tilde{S}_\nu(f) \delta(f - f') \quad (6.90)$$

where the last step uses the Wiener-Khinchin theorem and identifies the Fourier transform of the autocorrelation function $\rho(\tau) = \langle \delta\nu^*(t - \tau) \delta\nu(t) \rangle$ as the two-sided power spectral density $\tilde{S}_\nu(f)$. We

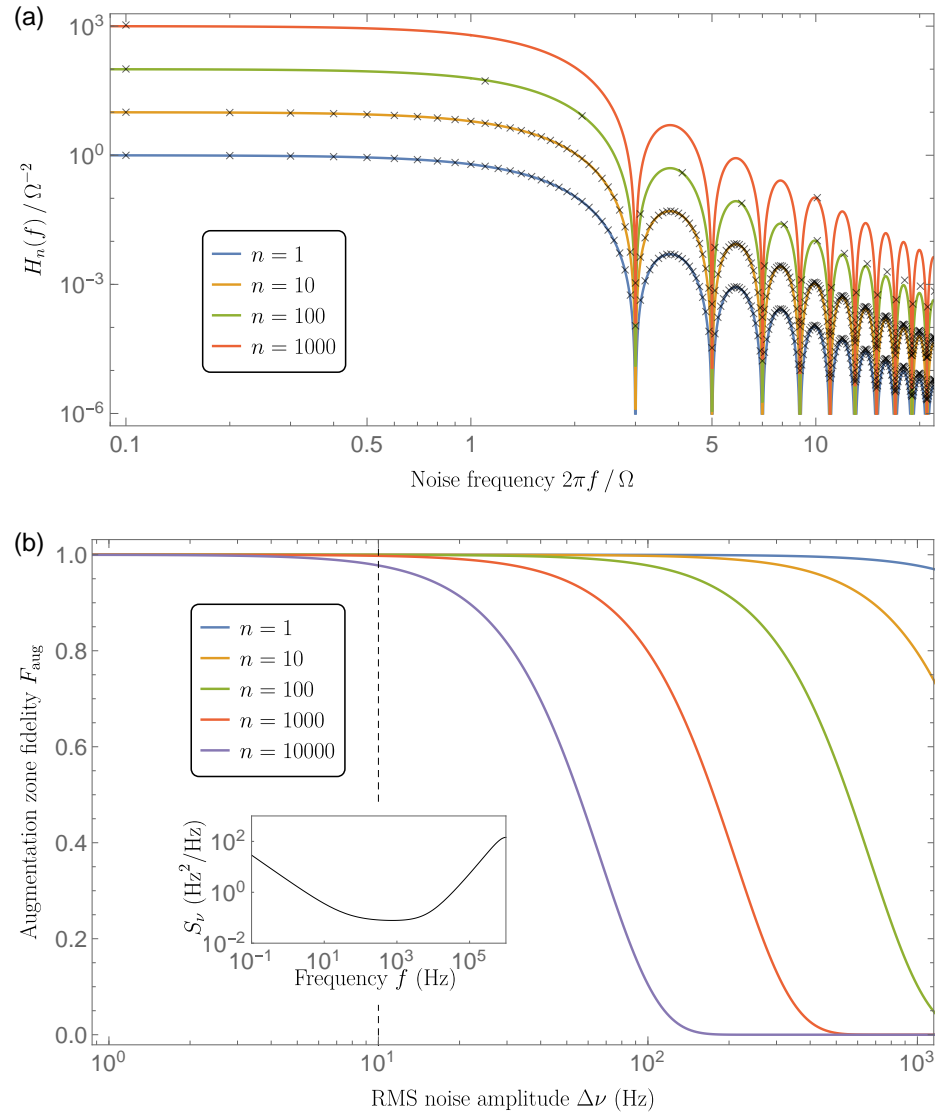


Figure 6.10: (a) Laser frequency noise transfer function $H_n(f)$ for an augmentation zone consisting of n pulses applied from alternating directions. The lines represent the analytic expression that scales linearly with n , and agree well with the black data points, which are numerically calculated by solving the Schrödinger equations in the Hilbert space with all possible external momentum. (b) The augmentation zone fidelity F_{aug} as a function of the RMS laser frequency noise $\Delta\nu$ for various sequence lengths n at Rabi frequency $\Omega = 2\pi \times 1\text{ kHz}$. The black dashed line is a guide to the eye at $\Delta\nu = 10\text{ Hz}$, where the corresponding noise model is shown in the inset.

apply Equation (6.90) to the ensemble average of Equation (6.86) and obtain

$$\langle \delta P \rangle = \int_{-\infty}^{+\infty} \int_{-\infty}^{+\infty} \hat{h}_1(f) \hat{h}_1^*(f') \langle \widehat{\delta\nu}^*(f) \widehat{\delta\nu}(f') \rangle df' df \quad (6.91)$$

$$= \int_{-\infty}^{+\infty} \hat{h}_1(f) \tilde{S}_\nu(f) df \int_{-\infty}^{+\infty} \hat{h}_1^*(f') \delta(f - f') df' \quad (6.92)$$

$$= \int_0^\infty |\hat{h}_1(f)|^2 S_\nu(f) df \quad (6.93)$$

where we have switched to the one-sided power spectral density $S_\nu(f) = 2\tilde{S}_\nu(f)$. We recognize $|\hat{h}_1(f)|^2$ as the single-pulse frequency noise transfer function $H_1(f)$, which we write analytically as

$$H_1(f) = \left(\frac{2\pi}{\Omega} \right)^2 \left(\frac{\Omega^2 \cos(\pi f \frac{\pi}{\Omega})}{\Omega^2 - (2\pi f)^2} \right)^2 \quad (6.94)$$

using Equation (6.87). Due to the linear scaling of population error with respect to the number of pulses, the transfer function for n sequential π -pulses applied from alternating directions is $H_n(f) = nH_1(f)$,

$$H_n(f) = n \left(\frac{2\pi}{\Omega} \right)^2 \left(\frac{\Omega^2 \cos(\pi f \frac{\pi}{\Omega})}{\Omega^2 - (2\pi f)^2} \right)^2 \quad (6.95)$$

6.4.2 Laser Stability Requirements

With the interference from parasitic paths ignored, we focus on a single augmentation zone of the interferometer and study the loss from n consecutive pulses applied from alternating directions. We use the laser noise transfer function given by Equation (6.95) to calculate the fidelity of the augmentation zone in the presence of laser frequency noise by numerically integrating the following equation

$$F_{\text{aug}} = 1 - \int_0^\infty H_n(f) S_\nu(f) df \quad (6.96)$$

for a given laser noise model described below. Figure 6.10 (b) shows the fidelity F_{aug} as a function of the RMS noise amplitude $\Delta\nu$, with the laser noise power spectral density $S_\nu(f)$ given by the inset and Rabi frequency $\Omega = 2\pi \times 1 \text{ kHz}$. We find that at a moderate laser stability requirement $\Delta\nu = 10 \text{ Hz}$, greater than 97% fidelity is maintained after 10^4 pulses, assuming that laser frequency noise is the only source of loss.

For this analysis, we vary the strength of the noise model but keep its structure fixed, which is pink below 100 Hz and white above. For the sake of completeness, we also include high-frequency noise above several ten-kHz due to limitation of the servo gain, which is observed in cavity-stabilized laser systems [44, 53]. Note, however, that this servo bump is outside the bandwidth of interest set by the Rabi frequency, and thus strongly suppressed by the roll-off of $H_n(f)$ when $2\pi f > \Omega$. The

low-frequency limit of the bandwidth is determined by the cycle time of the experiment, which is typically on the order of seconds.

Finally, we study a complete $n\hbar k$ interferometer sequence, which is constructed by inserting four augmentation zones of length $n - 1$ into a Mach-Zehnder interferometer. In addition to laser frequency noise, we include other loss mechanisms assuming a total contribution of 10^{-5} to the pulse inefficiency. The performance of the interferometer is evaluated by its LMT enhancement, defined as nC , which is proportional to the phase sensitivity of the interferometer. The existence of an optimal n for a given $\Delta\nu$ and Ω , as previously reported [44], is observed in Figure 6.11. However, since population loss scales linearly rather than quadratically with respect to n , a greater enhancement of sensitivity is expected at a much larger optimal n . For a laser with $\Delta\nu = 10$ Hz and $\Omega = 2\pi \times 1$ kHz, a peak LMT enhancement $nC = 7.5 \times 10^3$ is achieved at $n = 2.0 \times 10^4$. This is comparable to the targeted LMT order in the proposed final stage of MAGIS-100, as well as in future km-baseline MAGIS-style detectors [43]. Therefore, we identify laser frequency noise as not a fundamental limitation for the extreme-LMT applications in the next-generation long baseline atom interferometers.

6.5 Discussion

For narrowband clock atom interferometers, the population loss in the main paths is proportional to the LMT order n , and dominates over the interference background of the parasitic paths, which is bounded by a constant independent of n . The resulting loss of sequence fidelity grows linearly with n , and is a result of the momentum separation between the parasitic states and the correct states when driven by n pulses from alternating directions. This is in sharp contrast to the case of interrogating a two-level system n times from the same direction, where the amplitude error in the wave function is subject to all subsequent pulses and coherently accumulates over time, leading to a fidelity loss that grows as n^2 [181]. Note that spontaneous emission loss also scales linearly with n , with a magnitude similar to or larger than the loss induced by frequency noise at practical laser parameters $\Delta\nu = 10$ Hz and $\Omega = 2\pi \times 1$ kHz, considering narrowband transitions such as ${}^1S_0 - {}^3P_0$ in alkaline-earth(-like) elements. This suggests that laser frequency noise does not pose a fundamental constraint on the phase sensitivity of narrowband LMT clock atom interferometers.

It is possible to extend this analysis to broadband LMT clock atom interferometers [35], where each π -pulse is intentionally made velocity insensitive to impart momentum to both the upper and lower arms. In this scenario, the argument for a linearly growing population loss is still valid for the main paths. However, more parasitic paths will be generated as the pulses are not velocity-selective, leading to an increasing number of pulse error combinations for each m -term in Equation (6.45). Despite this, we note that if an error is made in an acceleration sequence, the resulting parasitic wave function will be decelerated by subsequent pulses, and vice versa, due to the alternation of pulse

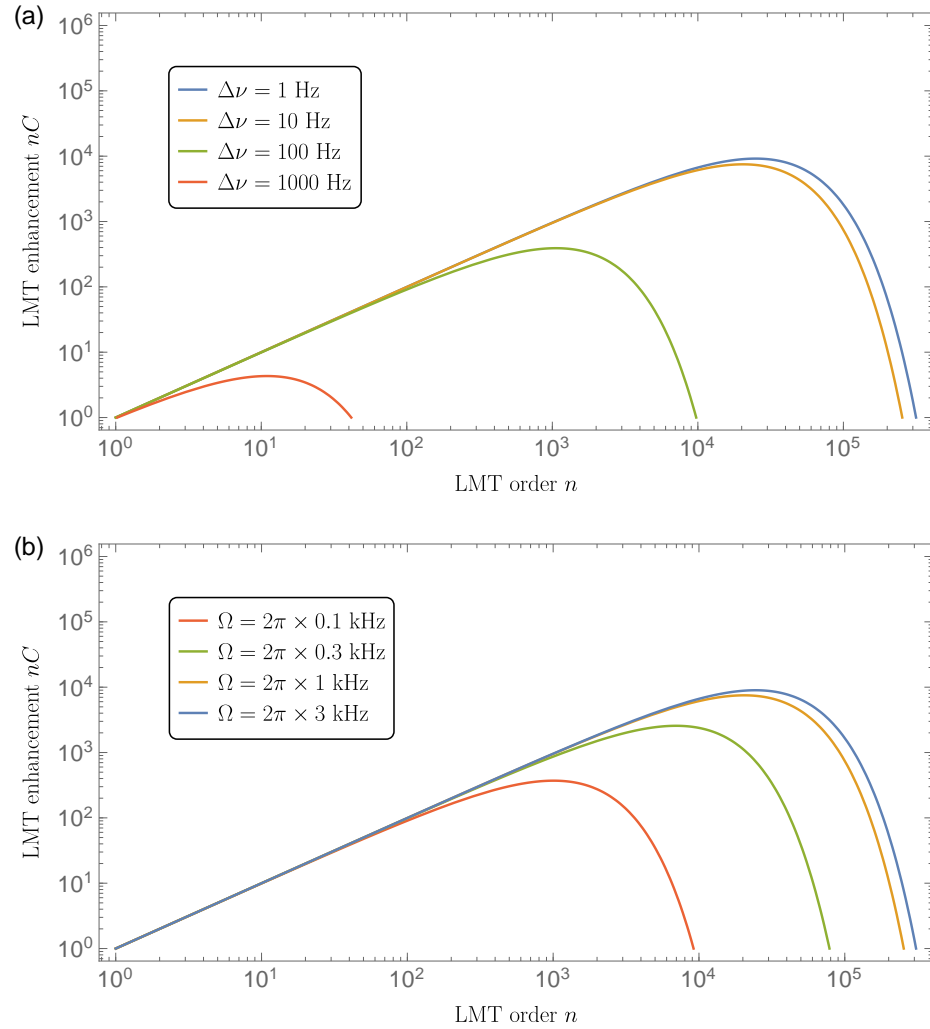


Figure 6.11: LMT enhancement nC of a clock atom interferometer in the presence of laser frequency noise. The other loss mechanisms are assumed to introduce an additional pulse inefficiency of 10^{-5} . Panel (a) compares different values of RMS laser frequency noise $\Delta\nu$, where the Rabi frequency is fixed at $2\pi \times 1 \text{ kHz}$. Panel (b) compares different values of Rabi frequency Ω , where the RMS noise is fixed at 10 Hz. In both panels, densely packed pulses and zero interrogation time are assumed.

direction. As a result, the majority of the parasitic paths lead to different momentum states from the main paths and terminate far away from the detection region. More importantly, as the LMT order n increases, the broadband assumption becomes less valid, and the interferometer will enter the intermediate-band [39] and eventually the narrowband regime. In this scenario, parasitic paths spawned many photon recoils away are sufficiently Doppler detuned to be treated by the formalism we have introduced here.

Beyond laser frequency noise, other sources of pulse inefficiency, such as beam intensity fluctuation [182], finite beam size [146], and magnetic field errors [183], induce transfer inefficiency at each pulse that decreases the population in the main paths and generates parasitic paths. The results here apply to these sources of error as well, leading to the same conclusion about fidelity loss scaling. For narrowband LMT clock atom interferometers with these noise sources, we expect the interference background from parasitic paths to not dominate over the amplitude loss in the main paths. Finally, many sources of pulse inefficiency, including laser frequency noise, can be alleviated by the implementation of composite pulse, optimal control, or pulse shaping techniques tailored to one or several specific types of errors, at the expense of a longer pulse duration [184–194]. Such techniques have the potential to suppress both main path losses and parasitic path amplitudes, thereby further relaxing the laser stability requirement beyond the results in this chapter.

Chapter 7

Outlook

In this dissertation, I summarized my Ph.D. work towards the development of long-baseline clock atom interferometry detectors. This led to a mature design of a 10-meter strontium atom interferometer tower at Stanford University, followed by the successful construction and characterization of the tower sections. In particular, I discussed two important components of the apparatus, namely a novel magnetic shield that screens the Earth's magnetic field in the tower sections and optical lattices that transport atoms over large distances as a preparation for atom interferometry. The knowledge obtained from the design and assembly of the 10-meter tower can be easily transferred to MAGIS-100 to realize the world's first 100-meter atom interferometer detector [43].

At the time of writing this dissertation, the tower construction is not yet complete. There is ongoing work that aims to finalize the mechanical structure and the vacuum system of the tower. In particular, the mezzanine structure shown in Figure 3.24 is currently under construction. The beam delivery tube and the retro chamber shown in Figures 3.28 and 3.30 has been assembled and will be added to the vacuum system in the near future, with the interferometry beam aligned with the alignment targets in and out of the vacuum tube. As a final step of vacuum assembly, the two atom sources will also be connected to the connection node chambers. The entire system will then be pumped down and baked to achieve the UHV environment necessary for atom interferometry experiments.

Once the tower is commissioned, it will serve as a platform for a variety of precision measurement experiments, including but not limited to the following. First, extreme LMT orders can be demonstrated even with broadband atom interferometry [35, 39], which will break our own record and extend the momentum separation between the interferometer arms to beyond $1000 \hbar k$. Second, narrowband LMT atom optics will be implemented on ^{87}Sr . In combination with the extremely long lifetime of the clock transition, an unprecedented LMT enhancement is expected, leading to a

gradiometer sensitivity of

$$\delta g_{zz} = 0.18 \text{ mE}/\sqrt{\text{Hz}} \times \left(\frac{1000}{n} \right) \left(\frac{1 \text{ s}}{T} \right)^2 \left(\frac{10^5}{N} \right)^{1/2} \left(\frac{t_{\text{cycle}}}{5 \text{ s}} \right)^{1/2} \quad (7.1)$$

where the baseline is $L = 167.66''$, taken as the distance between two connection nodes, t_{cycle} is the cycle time of the experiment, N is the atom number, and $1 \text{ mE} = 10^{-12}/\text{s}^2$.

The experience obtained by conducting experiments in the tower will be beneficial for the operation of MAGIS-100. As a MAGIS prototype, the tower will explore sequences that will be executed on the 100-meter detector. In this process, technical problems will be identified and solved in parallel to the construction of MAGIS-100. This will expedite the development of MAGIS-100, which once completed will be operated as a multi-purpose fundamental physics detector with unprecedented sensitivity in the mid-band.

The strain sensitivity of the initial phase of MAGIS-100 is expected to be $10^{-14}/\sqrt{\text{Hz}}$ [43]. This sensitivity can be improved by a few orders of magnitude through a series of future upgrades, including advanced LMT atom optics, as well as high-flux atom sources that incorporate spin squeezing for enhanced phase resolution [195–197]. Follow-on full-scale atom interferometers such as the km-scale terrestrial detector MAGIS-km and the satellite-based detector MAGIS-Space have also been envisioned to achieve a level that supports strain measurements in the scientifically interesting range below $10^{-20}/\sqrt{\text{Hz}}$ [43]. Meanwhile, an increasing number of large-scale atom interferometers aimed at gravitational wave and dark matter detection [198–201] are being built around the world, which leads to a promising direction to establish a global network of atom interferometer detectors [200].

Appendix A

Drawings for Custom Machining

This appendix includes drawings for several custom machined parts used in the tower, with the intention of possibly duplicating or modifying them for MAGIS-100.

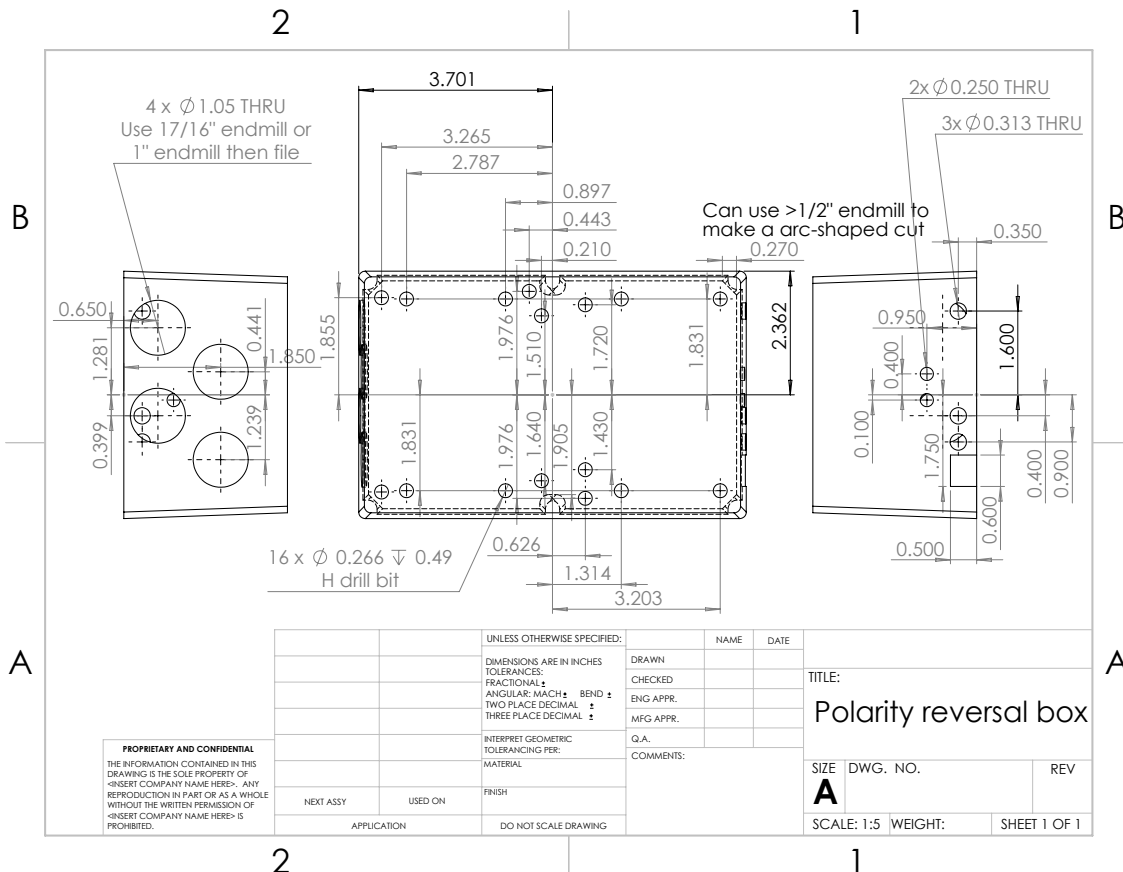


Figure A.1: Drawing of the polarity-reversal box.

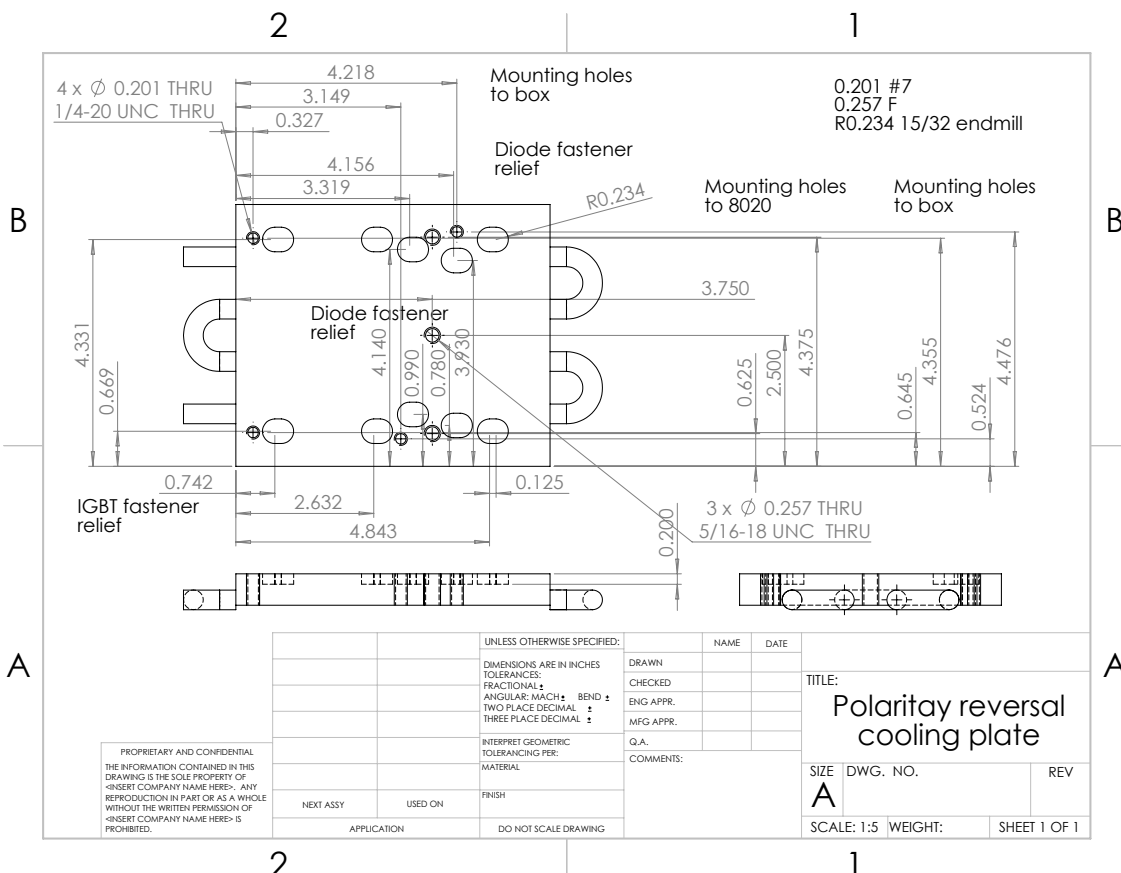


Figure A.2: Drawing of the water-cooling plate for the polarity-reversal box.

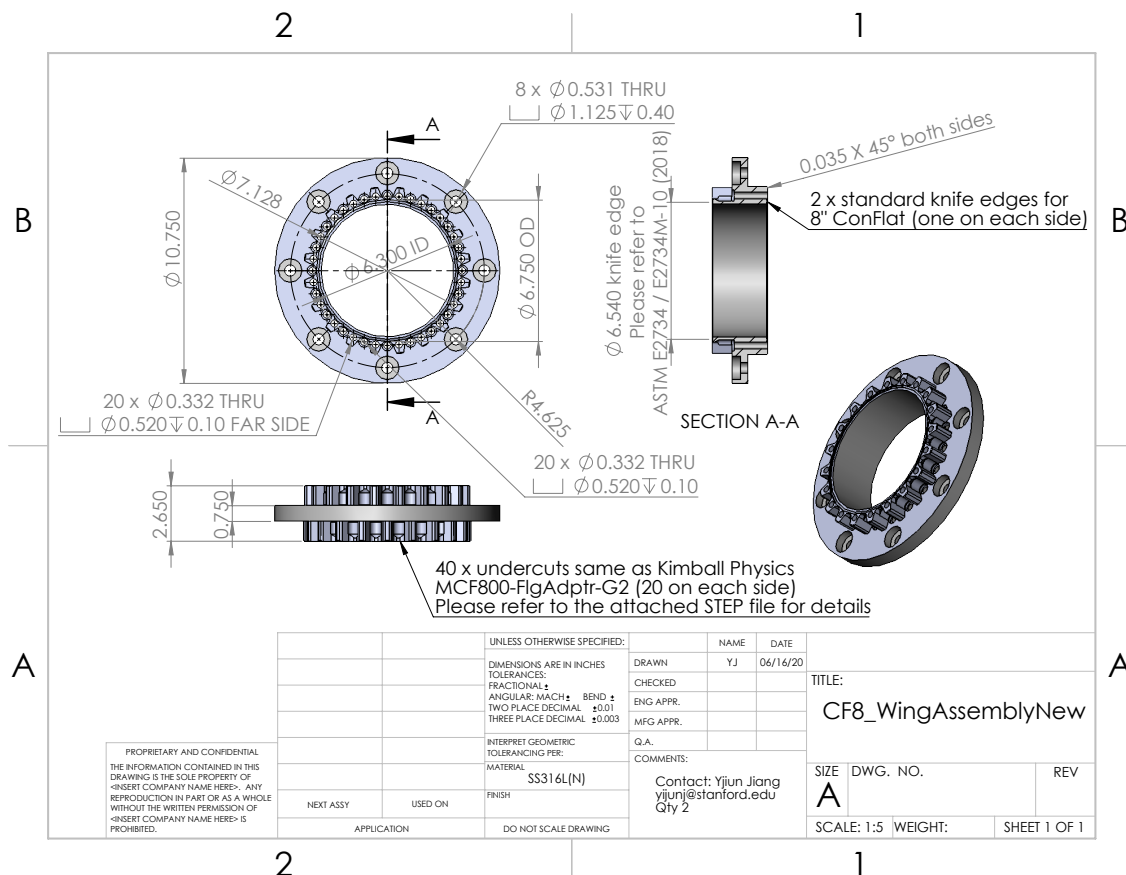


Figure A.3: Drawing of the “double crown” flange adapter.

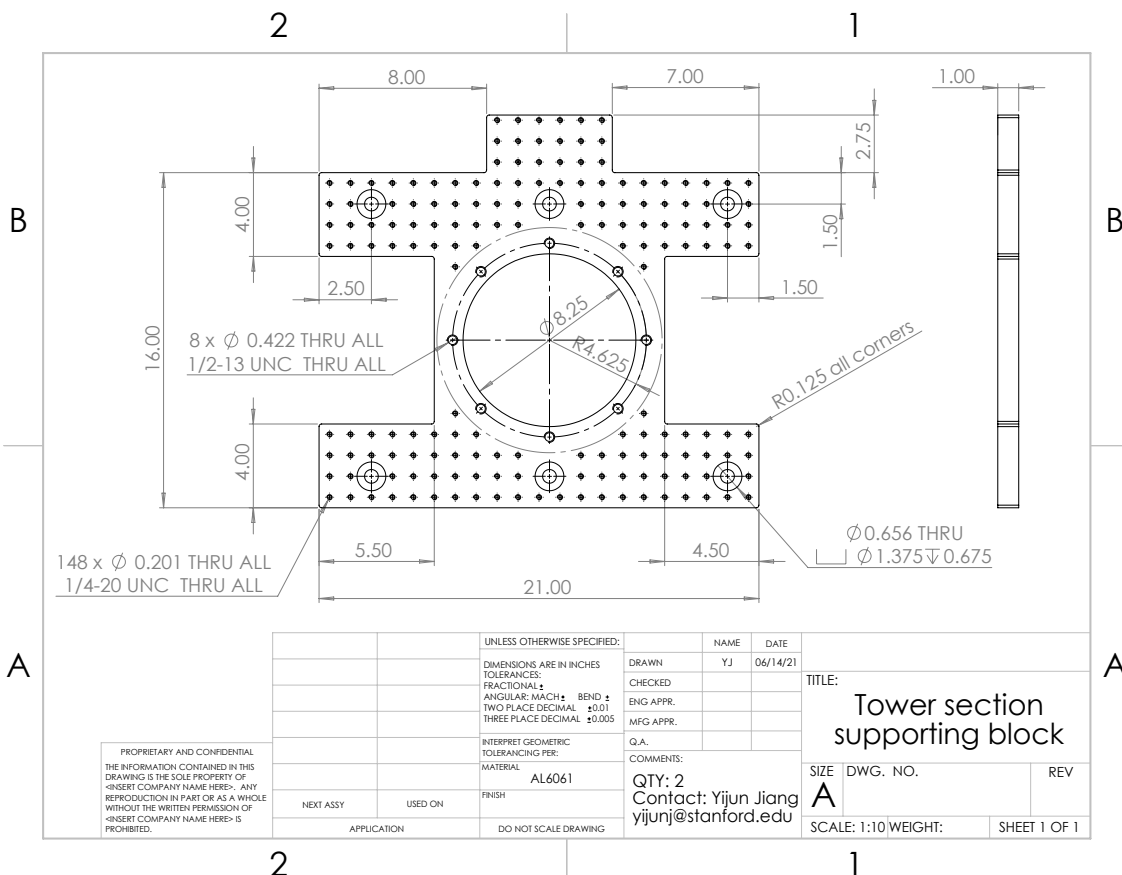


Figure A.4: Drawing of the “H-plate” adapter.

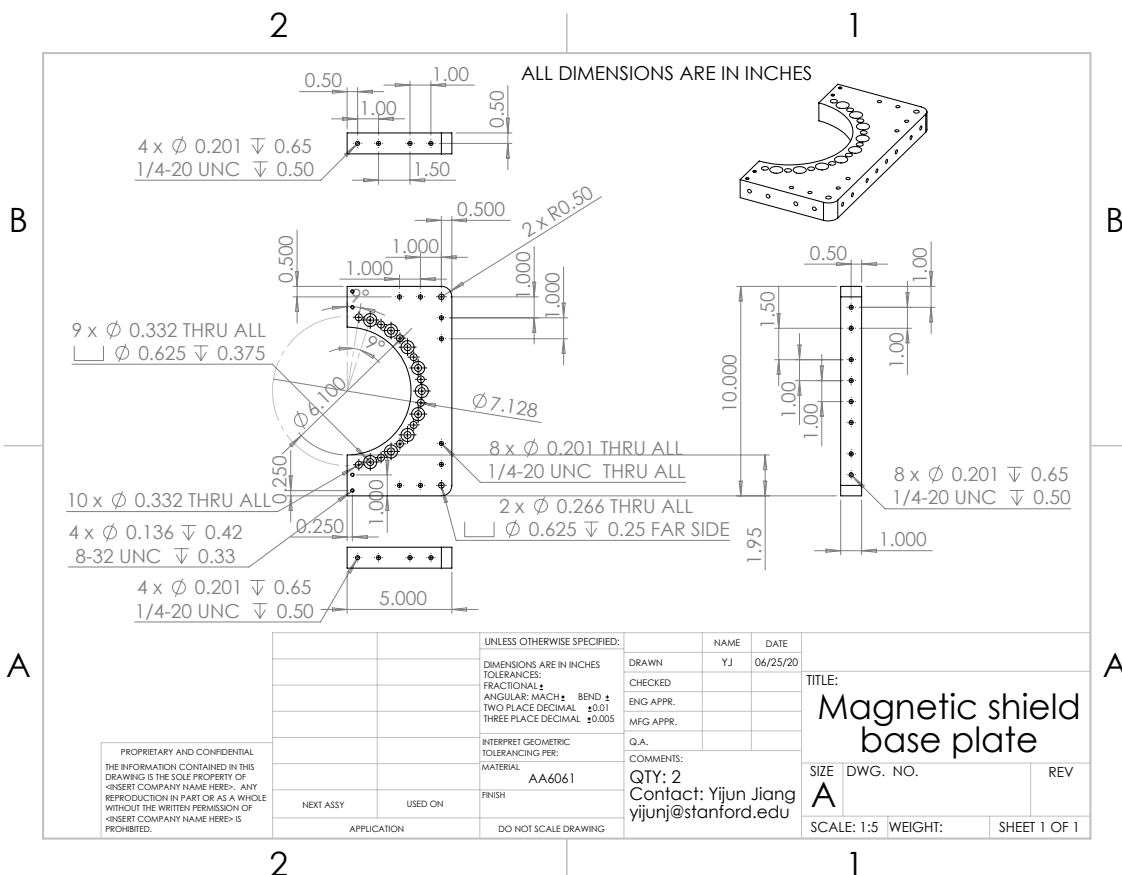


Figure A.5: Drawing of the magnetic shield base plate.

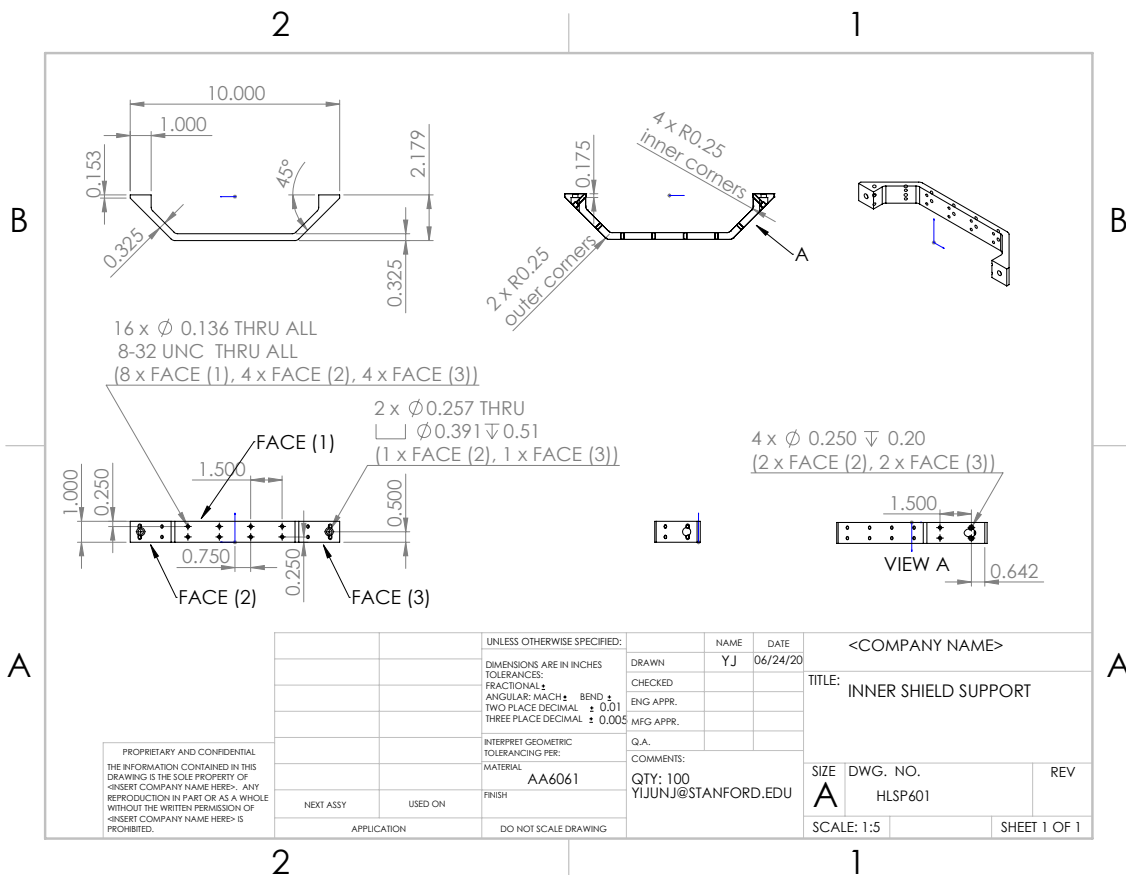


Figure A.6: Drawing of the magnetic shield supporting “rib”.

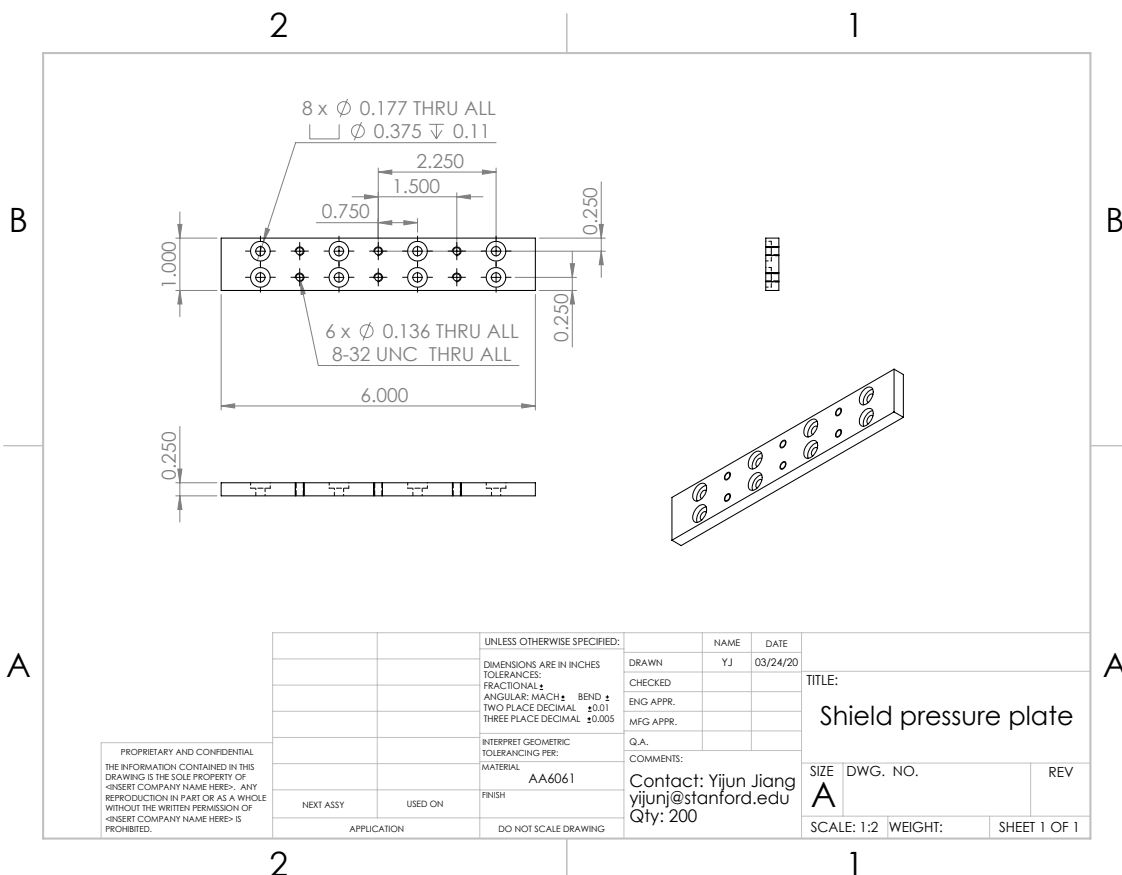


Figure A.7: Drawing of the magnetic shield pressure plate.

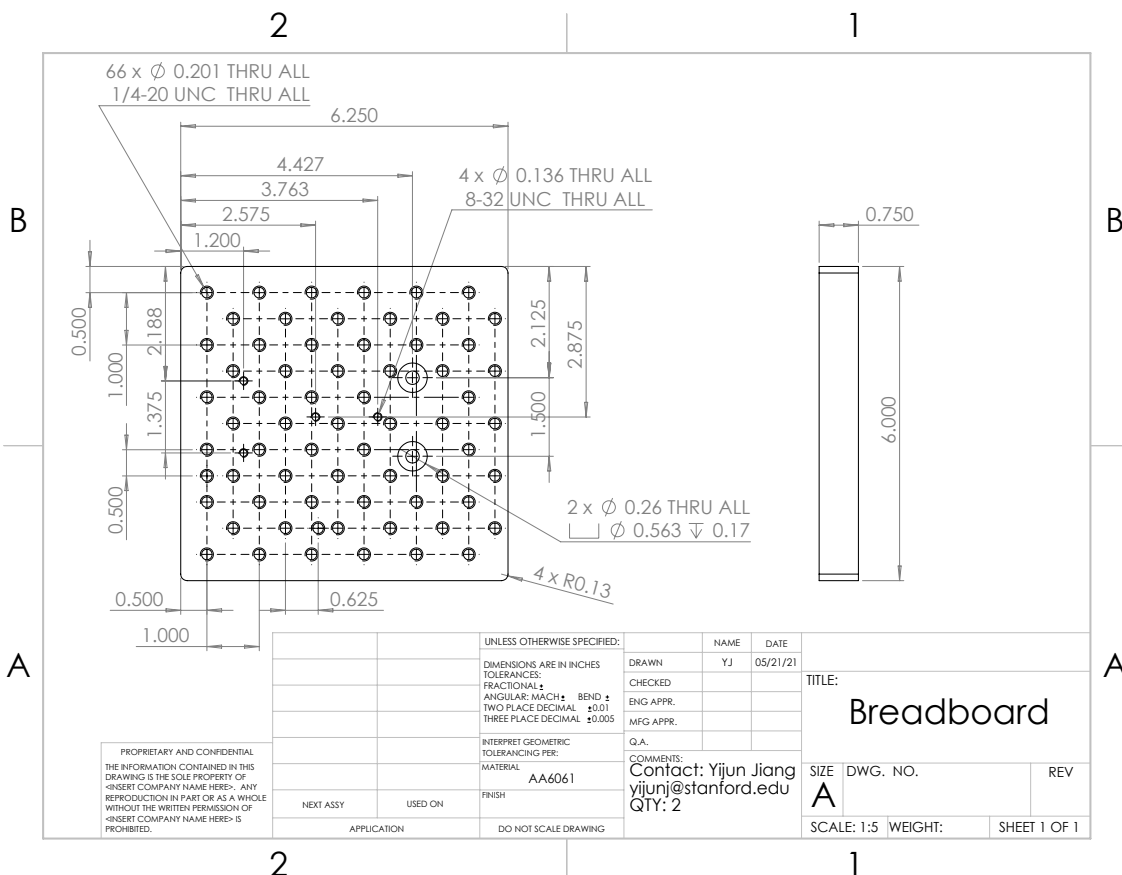


Figure A.8: Drawing of the shuttle lattice delivery breadboard.

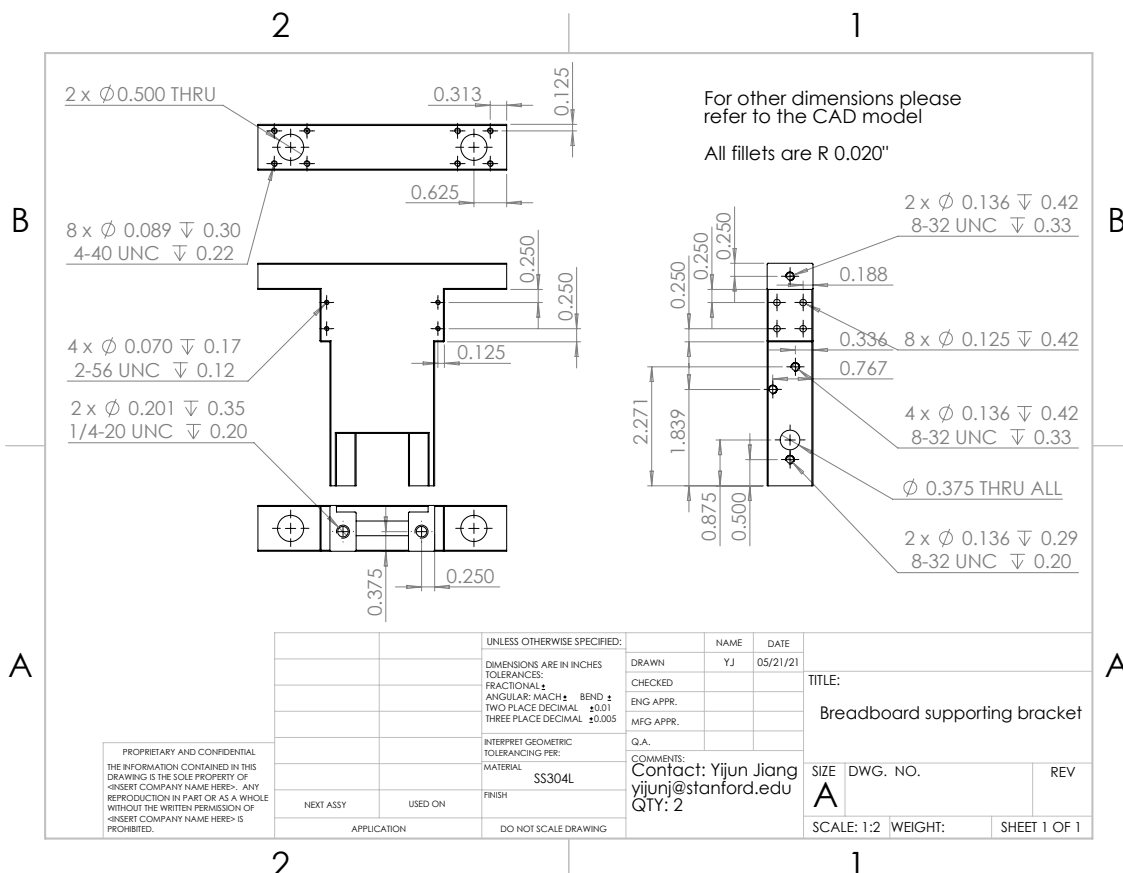


Figure A.9: Drawing of the block that extends from the shuttle lattice delivery breadboard.

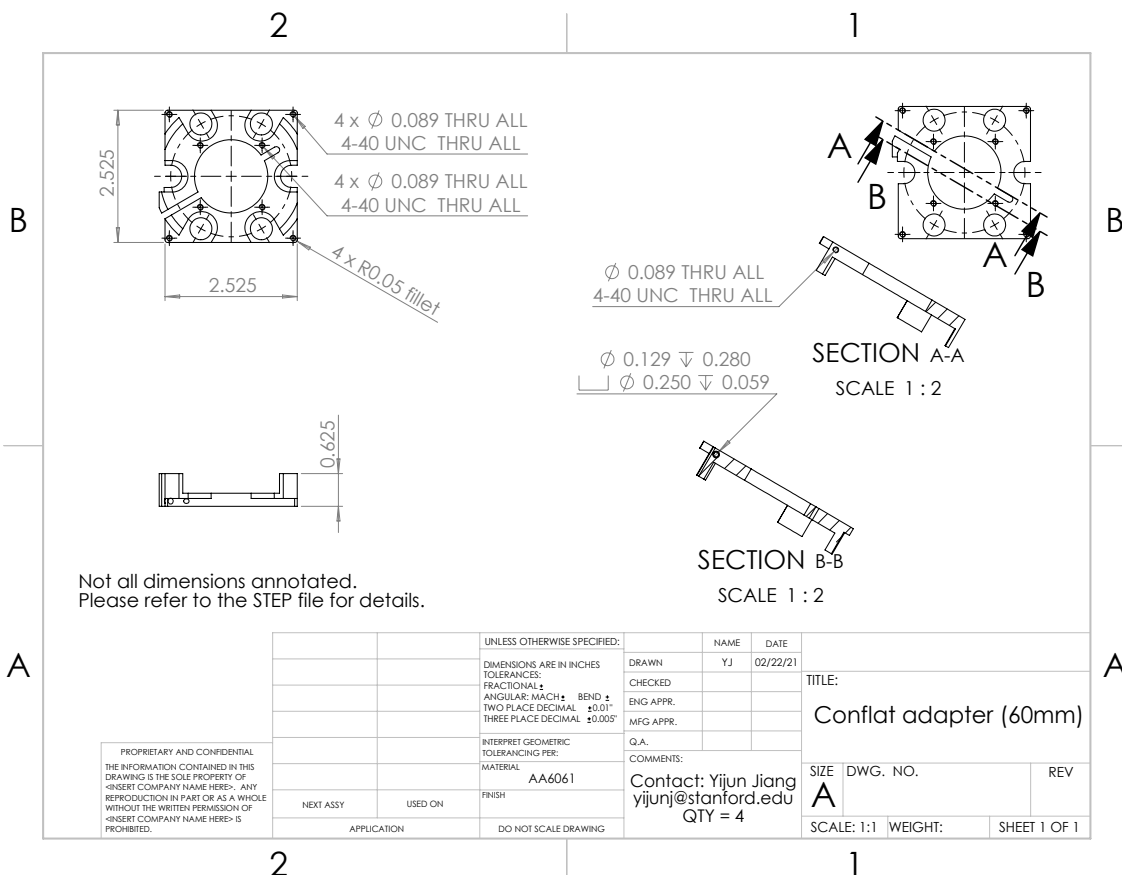


Figure A.10: Drawing of the CF 2.75" viewport adapter for shuttle lattice delivery optics.

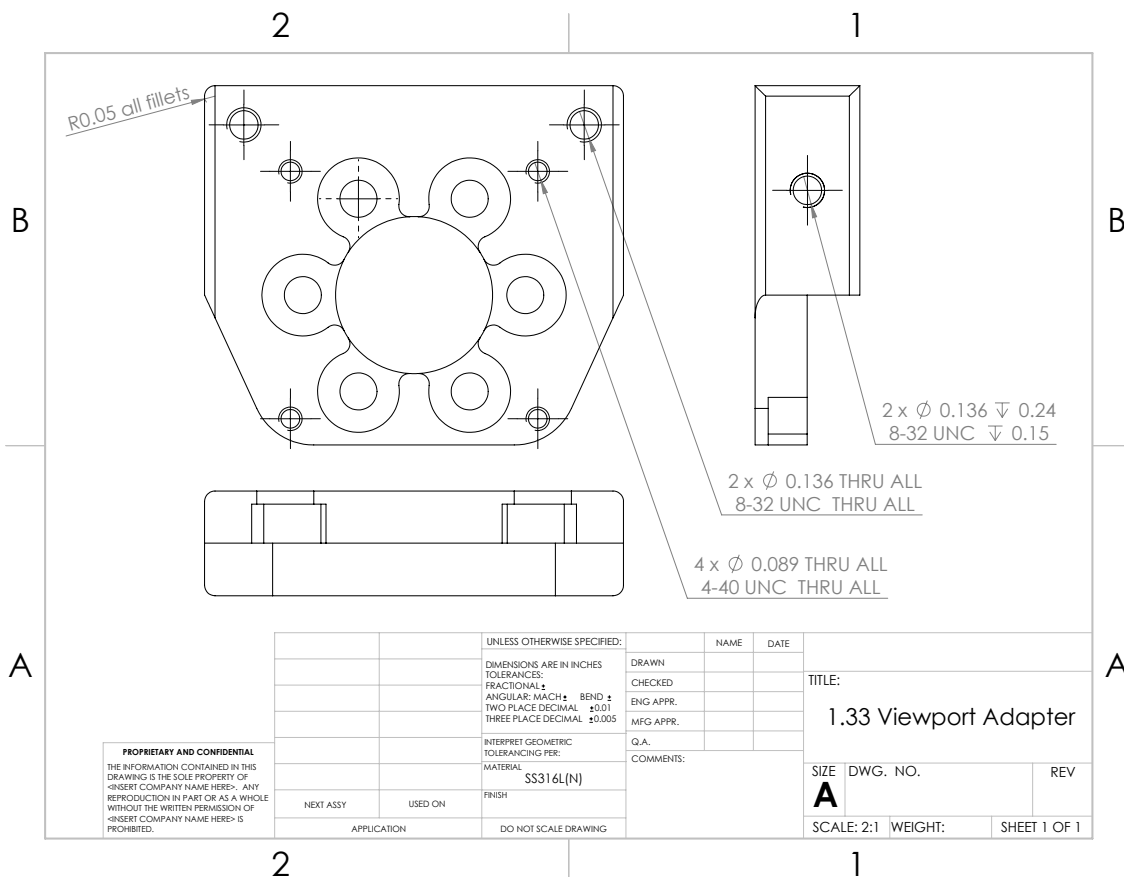


Figure A.11: Drawing of the CF 1.33" viewport adapter for launch lattice delivery optics.

Appendix B

Schematics for Custom PCBs

This appendix includes schematics for several custom PCBs used in the tower, with the intention of possibly duplicating or modifying them for MAGIS-100.

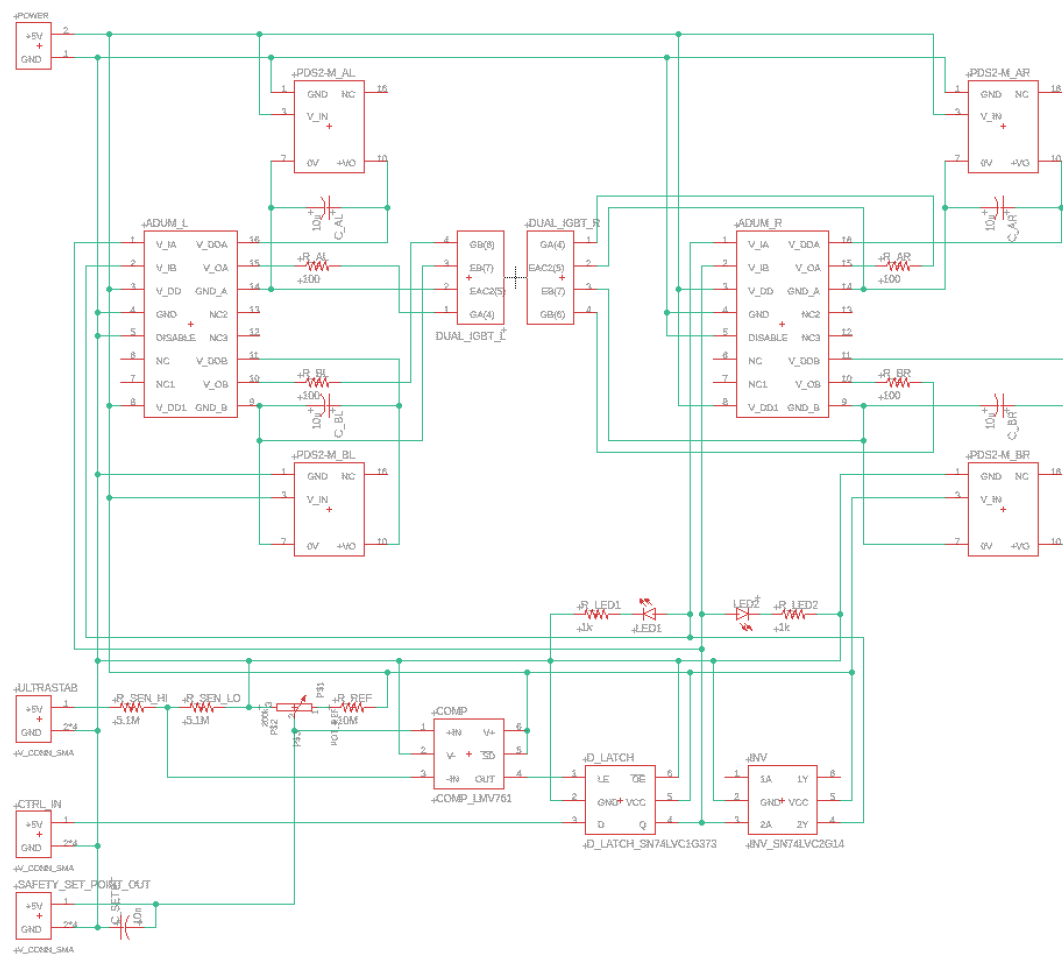


Figure B.1: Full schematic diagram of the H-bridge driver circuit.

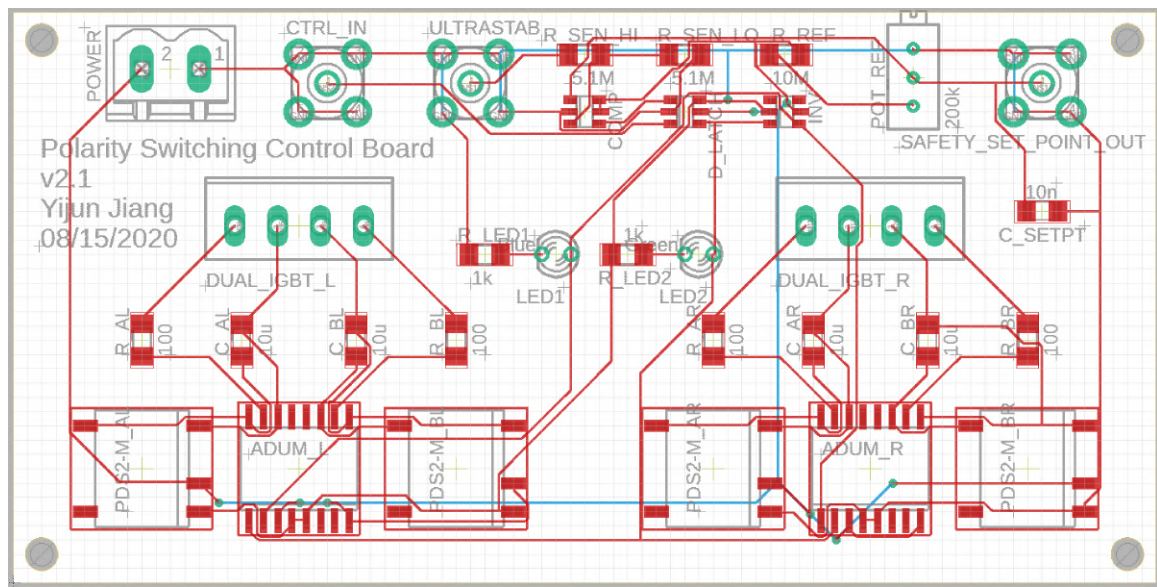


Figure B.2: PCB layout generated by EAGLE from the schematic diagram in Figure B.1.

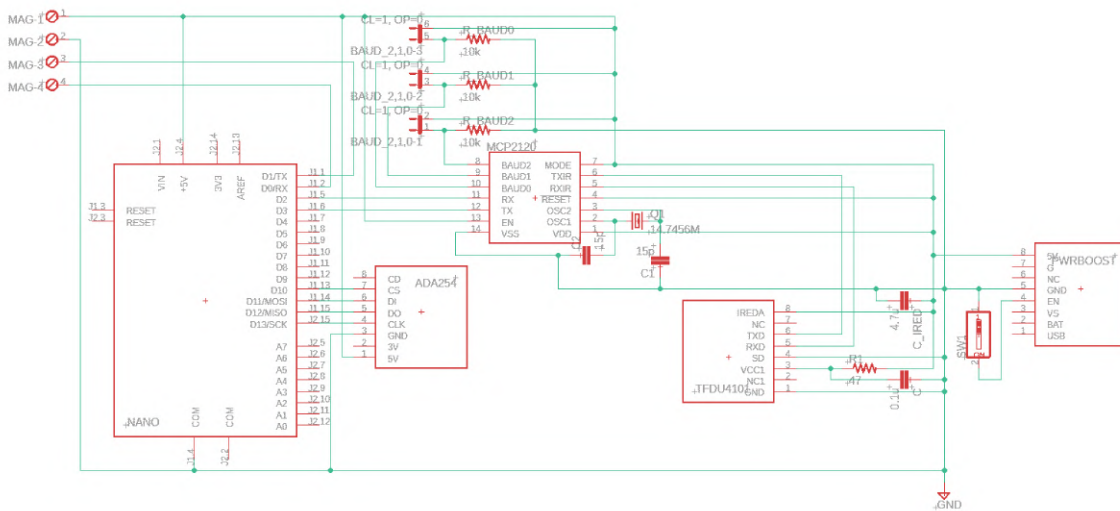


Figure B.3: Full schematic diagram of the magnetometry circuit inside the cart.

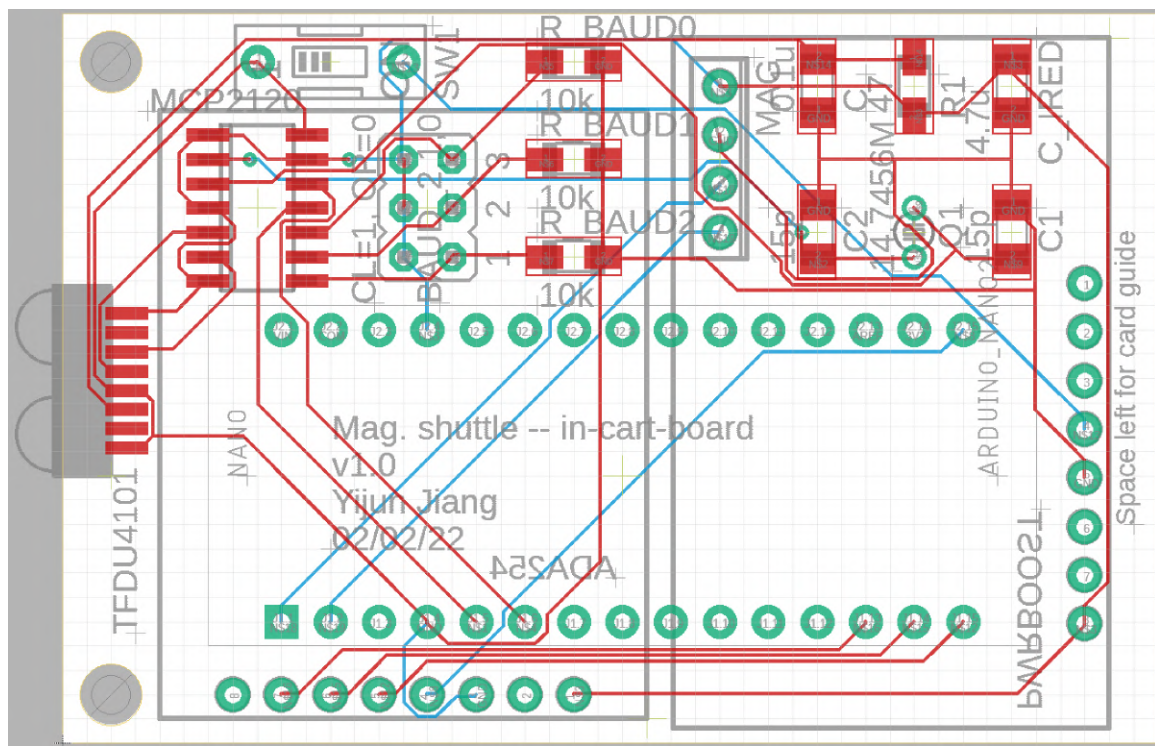


Figure B.4: PCB layout generated by EAGLE from the schematic diagram in Figure B.3.

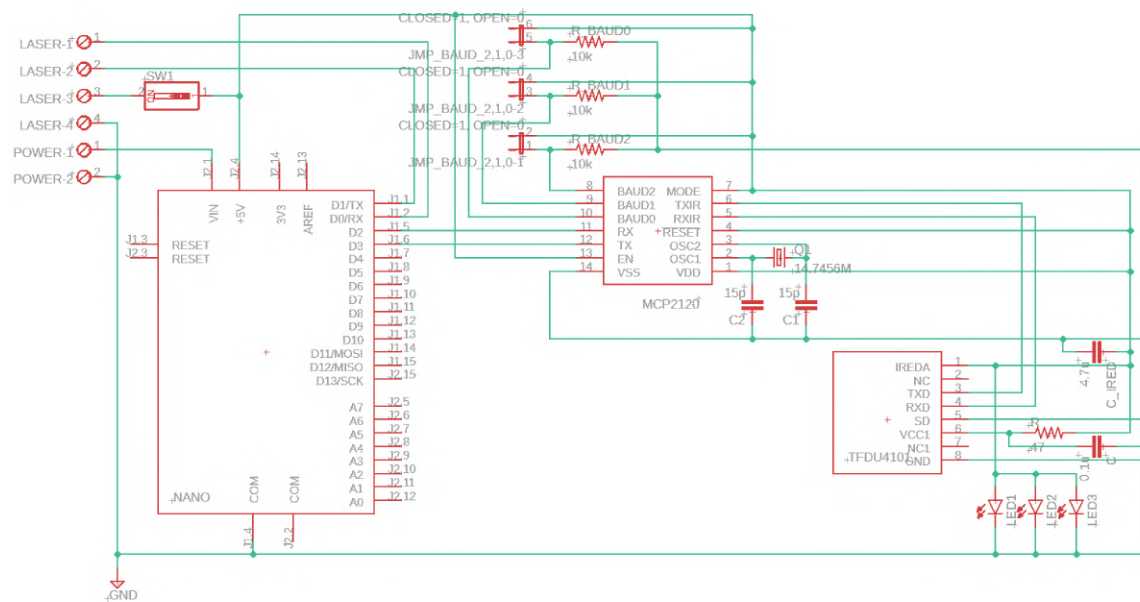


Figure B.5: Full schematic diagram of the magnetometry circuit on the laser distance sensor side.

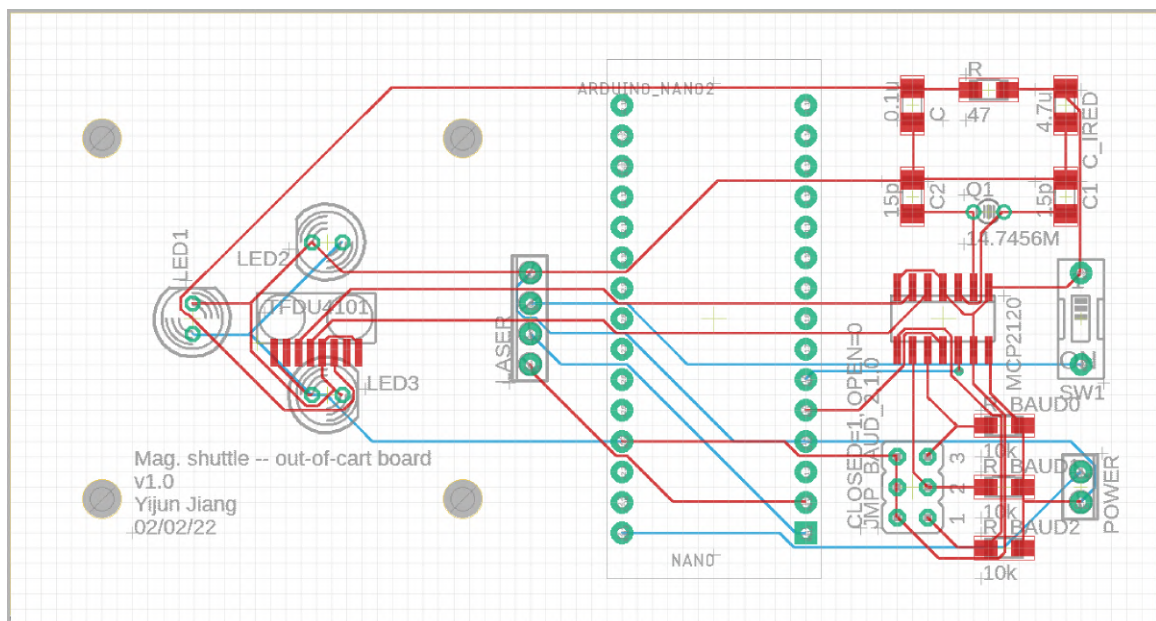


Figure B.6: PCB layout generated by EAGLE from the schematic diagram in Figure B.5.

Bibliography

- [1] J. B. Fixler, G. T. Foster, J. M. McGuirk, and M. A. Kasevich. “Atom interferometer measurement of the Newtonian constant of gravity”. *Science* **315**, 74–77 (2007). DOI: [10.1126/science.1135459](https://doi.org/10.1126/science.1135459)
- [2] G. Lamporesi, A. Bertoldi, L. Cacciapuoti, M. Prevedelli, and G. M. Tino. “Determination of the Newtonian gravitational constant using atom interferometry”. *Phys. Rev. Lett.* **100**, 050801 (2008). DOI: [10.1103/PhysRevLett.100.050801](https://doi.org/10.1103/PhysRevLett.100.050801)
- [3] G. Rosi, F. Sorrentino, L. Cacciapuoti, M. Prevedelli, and G. M. Tino. “Precision measurement of the Newtonian gravitational constant using cold atoms”. *Nature* **510**, 518–521 (2014). DOI: [10.1038/nature13433](https://doi.org/10.1038/nature13433)
- [4] R. Bouchendira, P. Cladé, S. Guellati-Khélifa, F. Nez, and F. Biraben. “New determination of the fine structure constant and test of the quantum electrodynamics”. *Phys. Rev. Lett.* **106**, 080801 (2011). DOI: [10.1103/PhysRevLett.106.080801](https://doi.org/10.1103/PhysRevLett.106.080801)
- [5] R. H. Parker, C. Yu, W. Zhong, B. Estey, and H. Müller. “Measurement of the fine-structure constant as a test of the Standard Model”. *Science* **360**, 191–195 (2018). DOI: [10.1126/science.aap7706](https://doi.org/10.1126/science.aap7706)
- [6] S. Fray, C. A. Diez, T. W. Hänsch, and M. Weitz. “Atomic interferometer with amplitude gratings of light and its applications to atom based tests of the equivalence principle”. *Phys. Rev. Lett.* **93**, 240404 (2004). DOI: [10.1103/PhysRevLett.93.240404](https://doi.org/10.1103/PhysRevLett.93.240404)
- [7] D. Schlippert, J. Hartwig, H. Albers, L. L. Richardson, C. Schubert, A. Roura, W. P. Schleich, W. Ertmer, and E. M. Rasel. “Quantum test of the universality of free fall”. *Phys. Rev. Lett.* **112**, 203002 (2014). DOI: [10.1103/PhysRevLett.112.203002](https://doi.org/10.1103/PhysRevLett.112.203002)
- [8] L. Zhou, S. Long, B. Tang, X. Chen, F. Gao, W. Peng, W. Duan, J. Zhong, Z. Xiong, J. Wang, et al. “Test of equivalence principle at 10^{-8} level by a dual-species double-diffraction raman atom interferometer”. *Phys. Rev. Lett.* **115**, 013004 (2015). DOI: [10.1103/PhysRevLett.115.013004](https://doi.org/10.1103/PhysRevLett.115.013004)

- [9] B. Barrett, L. Antoni-Micollier, L. Chichet, B. Battelier, T. Lévèque, A. Landragin, and P. Bouyer. “Dual matter-wave inertial sensors in weightlessness”. *Nat. Comm.* **7**, 13786 (2016). DOI: [10.1038/ncomms13786](https://doi.org/10.1038/ncomms13786)
- [10] C. C. N. Kuhn, G. D. McDonald, K. S. Hardman, S. Bennetts, P. J. Everitt, P. A. Altin, J. E. Debs, J. D. Close, and N. P. Robins. “A Bose-condensed, simultaneous dual-species Mach–Zehnder atom interferometer”. *New J. Phys.* **16**, 073035 (2014). DOI: [10.1088/1367-2630/16/7/073035](https://doi.org/10.1088/1367-2630/16/7/073035)
- [11] B. Barrett, L. Antoni-Micollier, L. Chichet, B. Battelier, P.-A. Gominet, A. Bertoldi, P. Bouyer, and A. Landragin. “Correlative methods for dual-species quantum tests of the weak equivalence principle”. *New J. Phys.* **17**, 085010 (2015). DOI: [10.1088/1367-2630/17/8/085010](https://doi.org/10.1088/1367-2630/17/8/085010)
- [12] M. G. Tarallo, T. Mazzoni, N. Poli, D. V. Sutyrin, X. Zhang, and G. M. Tino. “Test of Einstein equivalence principle for 0-spin and half-integer-spin atoms: search for spin-gravity coupling effects”. *Phys. Rev. Lett.* **113**, 023005 (2014). DOI: [10.1103/PhysRevLett.113.023005](https://doi.org/10.1103/PhysRevLett.113.023005)
- [13] A. Bonnin, N. Zahzam, Y. Bidel, and A. Bresson. “Simultaneous dual-species matter-wave accelerometer”. *Phys. Rev. A* **88**, 043615 (2013). DOI: [10.1103/PhysRevA.88.043615](https://doi.org/10.1103/PhysRevA.88.043615)
- [14] J. Hartwig, S. Abend, C. Schubert, D. Schlippert, H. Ahlers, K. Posso-Trujillo, N. Gaaloul, W. Ertmer, and E. M. Rasel. “Testing the universality of free fall with rubidium and ytterbium in a very large baseline atom interferometer”. *New J. Phys.* **17**, 035011 (2015). DOI: [10.1088/1367-2630/17/3/035011](https://doi.org/10.1088/1367-2630/17/3/035011)
- [15] P. Asenbaum, C. Overstreet, M. Kim, J. Curti, and M. A. Kasevich. “Atom-interferometric test of the equivalence principle at the 10^{-12} level”. *Phys. Rev. Lett.* **125**, 191101 (2020). DOI: [10.1103/PhysRevLett.125.191101](https://doi.org/10.1103/PhysRevLett.125.191101)
- [16] J. Williams, S.-w. Chiow, N. Yu, and H. Müller. “Quantum test of the equivalence principle and space-time aboard the International Space Station”. *New J. Phys.* **18**, 025018 (2016). DOI: [10.1088/1367-2630/18/2/025018](https://doi.org/10.1088/1367-2630/18/2/025018)
- [17] B. Battelier, J. Bergé, A. Bertoldi, L. Blanchet, K. Bongs, P. Bouyer, C. Braxmaier, D. Calonico, P. Fayet, N. Gaaloul, et al. “Exploring the foundations of the physical universe with space tests of the equivalence principle”. *Exp. Astron.* **51**, 1695–1736 (2021). DOI: [10.1007/s10686-021-09718-8](https://doi.org/10.1007/s10686-021-09718-8)
- [18] G. W. Biedermann, X. Wu, L. Deslauriers, S. Roy, C. Mahadeswaraswamy, and M. A. Kasevich. “Testing gravity with cold-atom interferometers”. *Phys. Rev. A* **91**, 033629 (2015). DOI: [10.1103/PhysRevA.91.033629](https://doi.org/10.1103/PhysRevA.91.033629)
- [19] A. Peters, K. Y. Chung, and S. Chu. “Measurement of gravitational acceleration by dropping atoms”. *Nature* **400**, 849–852 (1999). DOI: [10.1038/23655](https://doi.org/10.1038/23655)

- [20] T. L. Gustavson, P. Bouyer, and M. A. Kasevich. “Precision rotation measurements with an atom interferometer gyroscope”. *Phys. Rev. Lett.* **78**, 2046–2049 (1997). DOI: [10.1103/PhysRevLett.78.2046](https://doi.org/10.1103/PhysRevLett.78.2046)
- [21] M. Cadoret, E. de Mirandes, P. Cladé, S. Guellati-Khélifa, C. Schwob, F. ç. Nez, L. Julien, and F. ç. Biraben. “Combination of Bloch oscillations with a Ramsey-Bordé interferometer: new determination of the fine structure constant”. *Phys. Rev. Lett.* **101**, 230801 (2008). DOI: [10.1103/PhysRevLett.101.230801](https://doi.org/10.1103/PhysRevLett.101.230801)
- [22] A. Peters, K. Y. Chung, and S. Chu. “High-precision gravity measurements using atom interferometry”. *Metrologia* **38**, 25 (2001). DOI: [10.1088/0026-1394/38/1/4](https://doi.org/10.1088/0026-1394/38/1/4)
- [23] J. M. McGuirk, M. J. Snadden, and M. A. Kasevich. “Large area light-pulse atom interferometry”. *Phys. Rev. Lett.* **85**, 4498–4501 (2000). DOI: [10.1103/PhysRevLett.85.4498](https://doi.org/10.1103/PhysRevLett.85.4498)
- [24] H. Müller, S.-w. Chiow, Q. Long, S. Herrmann, and S. Chu. “Atom interferometry with up to 24-photon-momentum-transfer beam splitters”. *Phys. Rev. Lett.* **100**, 180405 (2008). DOI: [10.1103/PhysRevLett.100.180405](https://doi.org/10.1103/PhysRevLett.100.180405)
- [25] H. Müller, S.-w. Chiow, S. Herrmann, and S. Chu. “Atom interferometers with scalable enclosed area”. *Phys. Rev. Lett.* **102**, 240403 (2009). DOI: [10.1103/PhysRevLett.102.240403](https://doi.org/10.1103/PhysRevLett.102.240403)
- [26] P. Cladé, S. Guellati-Khélifa, F. ç. Nez, and F. ç. Biraben. “Large momentum beam splitter using Bloch oscillations”. *Phys. Rev. Lett.* **102**, 240402 (2009). DOI: [10.1103/PhysRevLett.102.240402](https://doi.org/10.1103/PhysRevLett.102.240402)
- [27] S.-w. Chiow, T. Kovachy, H.-C. Chien, and M. A. Kasevich. “ $102\hbar k$ large area atom interferometers”. *Phys. Rev. Lett.* **107**, 130403 (2011). DOI: [10.1103/PhysRevLett.107.130403](https://doi.org/10.1103/PhysRevLett.107.130403)
- [28] G. D. McDonald, C. C. N. Kuhn, S. Bennetts, J. E. Debs, K. S. Hardman, M. Johnsson, J. D. Close, and N. P. Robins. “ $80\hbar k$ momentum separation with Bloch oscillations in an optically guided atom interferometer”. *Phys. Rev. A* **88**, 053620 (2013). DOI: [10.1103/PhysRevA.88.053620](https://doi.org/10.1103/PhysRevA.88.053620)
- [29] T. Kovachy, P. Asenbaum, C. Overstreet, C. A. Donnelly, S. M. Dickerson, A. Sugarbaker, J. M. Hogan, and M. A. Kasevich. “Quantum superposition at the half-metre scale”. *Nature* **528**, 530–533 (2015). DOI: [10.1038/nature16155](https://doi.org/10.1038/nature16155)
- [30] T. Mazzoni, X. Zhang, R. Del Aguila, L. Salvi, N. Poli, and G. M. Tino. “Large-momentum-transfer Bragg interferometer with strontium atoms”. *Phys. Rev. A* **92**, 053619 (2015). DOI: [10.1103/PhysRevA.92.053619](https://doi.org/10.1103/PhysRevA.92.053619)
- [31] K. Kotru, D. L. Butts, J. M. Kinast, and R. E. Stoner. “Large-area atom interferometry with frequency-swept Raman adiabatic passage”. *Phys. Rev. Lett.* **115**, 103001 (2015). DOI: [10.1103/PhysRevLett.115.103001](https://doi.org/10.1103/PhysRevLett.115.103001)

- [32] B. Plotkin-Swing, D. Gochnauer, K. E. McAlpine, E. S. Cooper, A. O. Jamison, and S. Gupta. “Three-path atom interferometry with large momentum separation”. *Phys. Rev. Lett.* **121**, 133201 (2018). DOI: [10.1103/PhysRevLett.121.133201](https://doi.org/10.1103/PhysRevLett.121.133201)
- [33] M. Gebbe, J.-N. Siemß, M. Gersemann, H. Müntinga, S. Herrmann, C. Lämmerzahl, H. Ahlers, N. Gaaloul, C. Schubert, K. Hammerer, et al. “Twin-lattice atom interferometry”. *Nat. Commun.* **12**, 2544 (2019). DOI: [10.1038/s41467-021-22823-8](https://doi.org/10.1038/s41467-021-22823-8)
- [34] Z. Pagel, W. Zhong, R. H. Parker, C. T. Olund, N. Y. Yao, and H. Müller. “Symmetric Bloch oscillations of matter waves”. *Phys. Rev. A* **102**, 053312 (2020). DOI: [10.1103/PhysRevA.102.053312](https://doi.org/10.1103/PhysRevA.102.053312)
- [35] J. Rudolph, T. Wilkason, M. Nantel, H. Swan, C. M. Holland, Y. Jiang, B. E. Garber, S. P. Carman, and J. M. Hogan. “Large momentum transfer clock atom interferometry on the 689 nm intercombination line of strontium”. *Phys. Rev. Lett.* **124**, 083604 (2020). DOI: [10.1103/PhysRevLett.124.083604](https://doi.org/10.1103/PhysRevLett.124.083604)
- [36] L. Zhou, Z. Y. Xiong, W. Yang, B. Tang, W. C. Peng, K. Hao, R. B. Li, M. Liu, J. Wang, and M. S. Zhan. “Development of an atom gravimeter and status of the 10-meter atom interferometer for precision gravity measurement”. *Gen. Relativ. Gravit.* **43**, 1931–1942 (2011). DOI: [10.1007/s10714-011-1167-9](https://doi.org/10.1007/s10714-011-1167-9)
- [37] S. Abend, M. Gebbe, M. Gersemann, and E. M. Rasel. “Symmetric large momentum transfer for atom interferometry with BECs”. *Bull. Am. Phys. Soc.* **2017**, P9-005 (2017)
- [38] L. Hu, N. Poli, L. Salvi, and G. M. Tino. “Atom interferometry with the Sr optical clock transition”. *Phys. Rev. Lett.* **119**, 263601 (2017). DOI: [10.1103/PhysRevLett.119.263601](https://doi.org/10.1103/PhysRevLett.119.263601)
- [39] T. Wilkason, M. Nantel, J. Rudolph, Y. Jiang, B. E. Garber, H. Swan, S. P. Carman, M. Abe, and J. M. Hogan. “Atom interferometry with floquet atom optics”. *Phys. Rev. Lett.* **129**, 183202 (2022). DOI: [10.1103/PhysRevLett.129.183202](https://doi.org/10.1103/PhysRevLett.129.183202)
- [40] S. Chatterjee, D. DeMille, P. Graham, R. Falcone, E. Hu, M. Lukin, M. Kasevich, N. Mavalvala, C. Monroe, H. Mueller, et al. “Quantum sensors at the intersections of fundamental science, quantum information science and computing”. *DoE Community Report* (2016)
- [41] E. Farhi, S. Jordan, P. Hayden, M. Lukin, J. Maldacena, J. Preskill, P. Shor, J. Taylor, and C. Williams. “Grand challenges at the interface of quantum information science, particle physics, and computing”. *DoE Community Report* (2015)
- [42] M. Battaglieri, A. Belloni, A. Chou, P. Cushman, B. Echenard, R. Essig, J. Estrada, J. L. Feng, B. Flaugher, P. J. Fox, et al. “US cosmic visions: new ideas in dark matter 2017: community report”. *arXiv e-prints* (2017). arXiv: [1707.04591 \[hep-ph\]](https://arxiv.org/abs/1707.04591)

- [43] M. Abe, P. Adamson, M. Borcean, D. Bortoletto, K. Bridges, S. P. Carman, S. Chattopadhyay, J. Coleman, N. M. Curfman, K. DeRose, et al. “Matter-wave atomic gradiometer interferometric sensor (MAGIS-100)”. *Quantum Sci. Technol.* **6**, 044003 (2021). doi: [10.1088/2058-9565/abf719](https://doi.org/10.1088/2058-9565/abf719)
- [44] M. Chiarotti, J. N. Tinsley, S. Bandarupally, S. Manzoor, M. Sacco, L. Salvi, and N. Poli. “Practical limits for large-momentum-transfer clock atom interferometers”. *PRX Quantum* **3**, 030348 (2022). doi: [10.1103/PRXQuantum.3.030348](https://doi.org/10.1103/PRXQuantum.3.030348)
- [45] L. V. de Broglie. “Recherches sur la théorie des quanta”. Ph.D. dissertation. University of Paris, 1924
- [46] C. Davisson and L. H. Germer. “Diffraction of electrons by a crystal of nickel”. *Phys. Rev.* **30**, 705–740 (1927). doi: [10.1103/PhysRev.30.705](https://doi.org/10.1103/PhysRev.30.705)
- [47] C. Jönsson. “Electron diffraction at multiple slits”. *Am. J. Phys.* **42**, 4–11 (1974). doi: [10.1119/1.1987592](https://doi.org/10.1119/1.1987592)
- [48] P. G. Merli, G. F. Missiroli, and G. Pozzi. “On the statistical aspect of electron interference phenomena”. *Am. J. Phys.* **44**, 306–307 (1976). doi: [10.1119/1.10184](https://doi.org/10.1119/1.10184)
- [49] A. Tonomura, J. Endo, T. Matsuda, T. Kawasaki, and H. Ezawa. “Demonstration of single-electron buildup of an interference pattern”. *Am. J. Phys.* **57**, 117–120 (1989). doi: [10.1119/1.16104](https://doi.org/10.1119/1.16104)
- [50] C. Oshima, K. Mastuda, T. Kona, Y. Mogami, M. Komaki, Y. Murata, T. Yamashita, T. Kuzumaki, and Y. Horiike. “Young’s interference of electrons in field emission patterns”. *Phys. Rev. Lett.* **88**, 038301 (2002). doi: [10.1103/PhysRevLett.88.038301](https://doi.org/10.1103/PhysRevLett.88.038301)
- [51] F. Hasselbach. “Progress in electron- and ion-interferometry”. *Rep. Prog. Phys.* **73**, 016101 (2009). doi: [10.1088/0034-4885/73/1/016101](https://doi.org/10.1088/0034-4885/73/1/016101)
- [52] Y. Y. Fein, P. Geyer, P. Zwick, F. Kialka, S. Pedalino, M. Mayor, S. Gerlich, and M. Arndt. “Quantum superposition of molecules beyond 25 kDa”. *Nature* **15**, 1242–1245 (2019). doi: [10.1038/s41567-019-0663-9](https://doi.org/10.1038/s41567-019-0663-9)
- [53] U. Sterr, T. Legero, T. Kessler, H. Schnatz, G. Grosche, O. Terra, and F. Riehle. “Ultrastable lasers – new developments and applications”. In: *Time and Frequency Metrology II*. Vol. 7431. SPIE. 2009, 33–46
- [54] H. J. Metcalf and P. Van der Straten. *Laser cooling and trapping of neutral atoms*. Wiley Online Library, 2007
- [55] C. J. Foot. *Atomic physics*. Oxford University Press, 2005
- [56] J. M. Hogan, D. M. S. Johnson, and M. A. Kasevich. “Light-pulse atom interferometry”. In: *Proc. Int. Sch. Phys. “Enrico Fermi” Atom Opt. Sp. Phys.* IOS Press, 2009, 411–447

- [57] S. Dimopoulos, P. W. Graham, J. M. Hogan, and M. A. Kasevich. “General relativistic effects in atom interferometry”. *Phys. Rev. D* **78**, 042003 (2008). DOI: [10.1103/PhysRevD.78.042003](https://doi.org/10.1103/PhysRevD.78.042003)
- [58] J. M. McGuirk, G. T. Foster, J. B. Fixler, M. J. Snadden, and M. A. Kasevich. “Sensitive absolute-gravity gradiometry using atom interferometry”. *Phys. Rev. A* **65**, 033608 (2002). DOI: [10.1103/PhysRevA.65.033608](https://doi.org/10.1103/PhysRevA.65.033608)
- [59] N. Yu and M. Tinto. “Gravitational wave detection with single-laser atom interferometers”. *Gen. Relativ. Gravit.* **43**, 1943–1952 (2011). DOI: [10.1007/s10714-010-1055-8](https://doi.org/10.1007/s10714-010-1055-8)
- [60] P. W. Graham, J. M. Hogan, M. A. Kasevich, and S. Rajendran. “New method for gravitational wave detection with atomic sensors”. *Phys. Rev. Lett.* **110**, 171102 (2013). DOI: [10.1103/PhysRevLett.110.171102](https://doi.org/10.1103/PhysRevLett.110.171102)
- [61] A. Sugarbaker, S. M. Dickerson, J. M. Hogan, D. M. S. Johnson, and M. A. Kasevich. “Enhanced atom interferometer readout through the application of phase shear”. *Phys. Rev. Lett.* **111**, 113002 (2013). DOI: [10.1103/PhysRevLett.111.113002](https://doi.org/10.1103/PhysRevLett.111.113002)
- [62] J. M. Hogan, D. M. S. Johnson, S. Dickerson, T. Kovachy, A. Sugarbaker, S.-w. Chiow, P. W. Graham, M. A. Kasevich, B. Saif, S. Rajendran, et al. “An atomic gravitational wave interferometric sensor in low earth orbit (AGIS-LEO)”. *Gen. Relativ. Gravit.* **43**, 1953–2009 (2011). DOI: [10.1007/s10714-011-1182-x](https://doi.org/10.1007/s10714-011-1182-x)
- [63] W. Chaibi, R. Geiger, B. Canuel, A. Bertoldi, A. Landragin, and P. Bouyer. “Low frequency gravitational wave detection with ground-based atom interferometer arrays”. *Phys. Rev. D* **93**, 021101 (2016). DOI: [10.1103/PhysRevD.93.021101](https://doi.org/10.1103/PhysRevD.93.021101)
- [64] M. M. Boyd. “High precision spectroscopy of strontium in an optical lattice: towards a new standard for frequency and time”. Ph.D. dissertation. University of Colorado Boulder, 2007
- [65] J. A. Muniz, D. J. Young, J. R. K. Cline, and J. K. Thompson. “Cavity-QED measurements of the ^{87}Sr millihertz optical clock transition and determination of its natural linewidth”. *Phys. Rev. Res.* **3**, 023152 (2021). DOI: [10.1103/PhysRevResearch.3.023152](https://doi.org/10.1103/PhysRevResearch.3.023152)
- [66] M. Takamoto, F.-L. Hong, R. Higashi, Y. Fujii, M. Imae, and H. Katori. “Improved frequency measurement of a one-dimensional optical lattice clock with a spin-polarized fermionic ^{87}Sr isotope”. *J. Phys. Soc. Jpn.* **75**, 104302 (2006). DOI: [10.1143/JPSJ.75.104302](https://doi.org/10.1143/JPSJ.75.104302)
- [67] M. M. Boyd, T. Zelevinsky, A. D. Ludlow, S. Blatt, T. Zanon-Willette, S. M. Foreman, and J. Ye. “Nuclear spin effects in optical lattice clocks”. *Phys. Rev. A* **76**, 022510 (2007). DOI: [10.1103/PhysRevA.76.022510](https://doi.org/10.1103/PhysRevA.76.022510)
- [68] W. McGrew, X. Zhang, R. Fasano, S. Schäffer, K. Beloy, D. Nicolodi, R. Brown, N. Hinkley, G. Milani, M. Schioppo, et al. “Atomic clock performance enabling geodesy below the centimetre level”. *Nature* **564**, 87–90 (2018). DOI: [10.1038/s41586-018-0738-2](https://doi.org/10.1038/s41586-018-0738-2)

- [69] N. Hinkley, J. A. Sherman, N. B. Phillips, M. Schioppo, N. D. Lemke, K. Beloy, M. Pizzocaro, C. W. Oates, and A. D. Ludlow. “An atomic clock with 10^{-18} instability”. *Science* **341**, 1215–1218 (2013). DOI: [10.1126/science.1240420](https://doi.org/10.1126/science.1240420)
- [70] B. J. Bloom, T. L. Nicholson, J. R. Williams, S. L. Campbell, M. Bishof, X. Zhang, W. Zhang, S. L. Bromley, and J. Ye. “An optical lattice clock with accuracy and stability at the 10^{-18} level”. *Nature* **506**, 71–75 (2014). DOI: [10.1038/nature12941](https://doi.org/10.1038/nature12941)
- [71] G. E. Marti, R. B. Hutson, A. Goban, S. L. Campbell, N. Poli, and J. Ye. “Imaging optical frequencies with $100\text{ }\mu\text{Hz}$ precision and $1.1\text{ }\mu\text{m}$ resolution”. *Phys. Rev. Lett.* **120**, 103201 (2018). DOI: [10.1103/PhysRevLett.120.103201](https://doi.org/10.1103/PhysRevLett.120.103201)
- [72] T. L. Nicholson, S. L. Campbell, R. B. Hutson, G. E. Marti, B. J. Bloom, R. L. McNally, W. Zhang, M. D. Barrett, M. S. Safronova, G. F. Strouse, et al. “Systematic evaluation of an atomic clock at 2×10^{-18} total uncertainty”. *Nat. Commun.* **6**, 6896 (2015). DOI: [10.1038/ncomms7896](https://doi.org/10.1038/ncomms7896)
- [73] S. L. Campbell, R. B. Hutson, G. E. Marti, A. Goban, N. Darkwah Oppong, R. L. McNally, L. Sonderhouse, J. M. Robinson, W. Zhang, B. J. Bloom, et al. “A Fermi-degenerate three-dimensional optical lattice clock”. *Science* **358**, 90–94 (2017). DOI: [10.1126/science.aam5538](https://doi.org/10.1126/science.aam5538)
- [74] M. Schioppo, R. C. Brown, W. F. McGrew, N. Hinkley, R. J. Fasano, K. Beloy, T. H. Yoon, G. Milani, D. Nicolodi, J. A. Sherman, et al. “Ultrastable optical clock with two cold-atom ensembles”. *Nat. Photonics* **11**, 48 (2017). DOI: [10.1038/nphoton.2016.231](https://doi.org/10.1038/nphoton.2016.231)
- [75] M. D. Swallows, M. J. Martin, M. Bishof, C. Benko, Y. Lin, S. Blatt, A. M. Rey, and J. Ye. “Operating a ^{87}Sr optical lattice clock with high precision and at high density”. *IEEE Trans. Ultrason. Ferroelectr. Freq. Control* **59**, 416–425 (2012). DOI: [10.1109/TUFFC.2012.2210](https://doi.org/10.1109/TUFFC.2012.2210)
- [76] S. Falke, H. Schnatz, J. S. R. V. Winfred, T. Middelmann, S. Vogt, S. Weyers, B. Lipphardt, G. Grosche, F. Riehle, U. Sterr, et al. “The ^{87}Sr optical frequency standard at PTB”. *Metrologia* **48**, 399 (2011). DOI: [10.1088/0026-1394/48/5/022](https://doi.org/10.1088/0026-1394/48/5/022)
- [77] T. Ebisuzaki, H. Katori, J. Makino, A. Noda, H. Shinkai, and T. Tamagawa. “INO: interplanetary network of optical lattice clocks”. *Int. J. Mod. Phys. D* **29**, 1940002 (2020). DOI: [10.1142/S0218271819400029](https://doi.org/10.1142/S0218271819400029)
- [78] Y. Zhou, R. Ranson, M. Panagiotou, and C. Overstreet. “Ytterbium atom interferometry for dark matter searches”. *Phys. Rev. A* **110**, 033313 (2024). DOI: [10.1103/PhysRevA.110.033313](https://doi.org/10.1103/PhysRevA.110.033313)

- [79] J. S. Schelfhout, T. M. Hird, K. M. Hughes, and C. J. Foot. “Single-photon large-momentum-transfer atom interferometry scheme for Sr or Yb atoms with application to determining the fine-structure constant”. *Phys. Rev. A* **110**, 053309 (2024). DOI: [10.1103/PhysRevA.110.053309](https://doi.org/10.1103/PhysRevA.110.053309)
- [80] A. Abdalla, M. Abe, S. Abend, M. Abidi, M. Aidelsburger, A. Alibabaei, B. Allard, J. Antoniadis, G. Arduini, N. Augst, et al. “Terrestrial very-long-baseline atom interferometry: summary of the second workshop”. *EPJ Quantum Technol.* **12**, 1–79 (2025). DOI: [10.1140/epjqt/s40507-025-00344-3](https://doi.org/10.1140/epjqt/s40507-025-00344-3)
- [81] S. Stellmer. “Degenerate quantum gases of strontium”. Ph.D. dissertation. University of Innsbruck, 2013
- [82] P. G. Mickelson, Y. N. Martinez de Escobar, M. Yan, B. J. DeSalvo, and T. C. Killian. “Bose-Einstein condensation of ^{88}Sr through sympathetic cooling with ^{87}Sr ”. *Phys. Rev. A* **81**, 051601 (2010). DOI: [10.1103/PhysRevA.81.051601](https://doi.org/10.1103/PhysRevA.81.051601)
- [83] S. Stellmer, M. K. Tey, B. Huang, R. Grimm, and F. Schreck. “Bose-Einstein condensation of strontium”. *Phys. Rev. Lett.* **103**, 200401 (2009). DOI: [10.1103/PhysRevLett.103.200401](https://doi.org/10.1103/PhysRevLett.103.200401)
- [84] S. Stellmer, B. Pasquiou, R. Grimm, and F. Schreck. “Laser cooling to quantum degeneracy”. *Phys. Rev. Lett.* **110**, 263003 (2013). DOI: [10.1103/PhysRevLett.110.263003](https://doi.org/10.1103/PhysRevLett.110.263003)
- [85] A. V. Taichenachev, V. I. Yudin, C. W. Oates, C. W. Hoyt, Z. W. Barber, and L. Hollberg. “Magnetic field-induced spectroscopy of forbidden optical transitions with application to lattice-based optical atomic clocks”. *Phys. Rev. Lett.* **96**, 083001 (2006). DOI: [10.1103/PhysRevLett.96.083001](https://doi.org/10.1103/PhysRevLett.96.083001)
- [86] S. P. Carman, J. Rudolph, B. E. Garber, M. J. V. de Graaff, H. Swan, Y. Jiang, M. Nantel, M. Abe, R. L. Barcklay, and J. M. Hogan. “Collinear three-photon excitation of a strongly forbidden optical clock transition”. *arXiv e-prints* (2024). arXiv: [2406.07902 \[physics.atom-ph\]](https://arxiv.org/abs/2406.07902)
- [87] S. P. Carman. “Multi-photon clock atom interferometry for long-baseline atomic sensors”. Ph.D. dissertation. Stanford University, 2025
- [88] J. He, B. Pasquiou, R. G. Escudero, S. Zhou, M. Borkowski, and F. Schreck. “Coherent three-photon excitation of the strontium clock transition”. *Phys. Rev. Res.* **7**, L012050 (2025). DOI: [10.1103/PhysRevResearch.7.L012050](https://doi.org/10.1103/PhysRevResearch.7.L012050)
- [89] G. Panelli, S. C. Burd, E. J. Porter, and M. Kasevich. “Doppler-free three-photon spectroscopy on narrow-line optical transitions”. *Phys. Rev. A* **111**, 033112 (2025). DOI: [10.1103/PhysRevA.111.033112](https://doi.org/10.1103/PhysRevA.111.033112)
- [90] L. Hu, E. Wang, L. Salvi, J. N. Tinsley, G. M. Tino, and N. Poli. “Sr atom interferometry with the optical clock transition as a gravimeter and a gravity gradiometer”. *Class. Quantum Gravity* **37**, 014001 (2019). DOI: [10.1088/1361-6382/ab4d18](https://doi.org/10.1088/1361-6382/ab4d18)

- [91] M. Kasevich and S. Chu. “Atomic interferometry using stimulated Raman transitions”. *Phys. Rev. Lett.* **67**, 181–184 (1991). DOI: [10.1103/PhysRevLett.67.181](https://doi.org/10.1103/PhysRevLett.67.181)
- [92] B. P. Abbott, R. Abbott, R. Adhikari, P. Ajith, B. Allen, G. Allen, R. S. Amin, S. B. Anderson, W. G. Anderson, M. A. Arain, et al. “LIGO: the laser interferometer gravitational-wave observatory”. *Rep. Prog. Phys.* **72**, 076901 (2009). DOI: [10.1088/0034-4885/72/7/076901](https://doi.org/10.1088/0034-4885/72/7/076901)
- [93] B. P. Abbott, R. Abbott, T. D. Abbott, M. R. Abernathy, F. Acernese, K. Ackley, C. Adams, T. Adams, P. Addesso, R. X. Adhikari, et al. “Observation of gravitational waves from a binary black hole merger”. *Phys. Rev. Lett.* **116**, 061102 (2016). DOI: [10.1103/PhysRevLett.116.061102](https://doi.org/10.1103/PhysRevLett.116.061102)
- [94] B. P. Abbott, R. Abbott, T. D. Abbott, F. Acernese, K. Ackley, C. Adams, T. Adams, P. Addesso, R. X. Adhikari, V. B. Adya, et al. “Multi-messenger observations of a binary neutron star merger”. *Astrophys. J. Lett.* **848**, L12 (2017). DOI: [10.3847/2041-8213/aa91c9](https://doi.org/10.3847/2041-8213/aa91c9)
- [95] M. Punturo, M. Abernathy, F. Acernese, B. Allen, N. Andersson, K. Arun, F. Barone, B. Barr, M. Barsuglia, M. Beker, et al. “The Einstein Telescope: a third-generation gravitational wave observatory”. *Class. Quantum Gravity* **27**, 194002 (2010). DOI: [10.1088/0264-9381/29/12/124013](https://doi.org/10.1088/0264-9381/29/12/124013)
- [96] N. Bartolo, C. Caprini, V. Domcke, D. G. Figueroa, J. Garcia-Bellido, M. C. Guzzetti, M. Liguori, S. Matarrese, M. Peloso, A. Petiteau, et al. “Science with the space-based interferometer LISA. IV: probing inflation with gravitational waves”. *J. Cosmol. Astropart. Phys.* **2016**, 026–026 (2016). DOI: [10.1088/1475-7516/2016/12/026](https://doi.org/10.1088/1475-7516/2016/12/026)
- [97] T. A. Prince, M. Tinto, S. L. Larson, and J. W. Armstrong. “LISA optimal sensitivity”. *Phys. Rev. D* **66**, 122002 (2002). DOI: [10.1103/PhysRevD.66.122002](https://doi.org/10.1103/PhysRevD.66.122002)
- [98] C. Caprini, M. Hindmarsh, S. Huber, T. Konstandin, J. Kozaczuk, G. Nardini, J. M. No, A. Petiteau, P. Schwaller, G. Servant, et al. “Science with the space-based interferometer eLISA. II: gravitational waves from cosmological phase transitions”. *J. Cosmol. Astropart. Phys.* **2016**, 001 (2016). DOI: [10.1088/1475-7516/2016/04/001](https://doi.org/10.1088/1475-7516/2016/04/001)
- [99] C. Caprini, M. Chala, G. C. Dorsch, M. Hindmarsh, S. J. Huber, T. Konstandin, J. Kozaczuk, G. Nardini, J. M. No, K. Rummukainen, et al. “Detecting gravitational waves from cosmological phase transitions with LISA: an update”. *J. Cosmol. Astropart. Phys.* **2020**, 024 (2020). DOI: [10.1088/1475-7516/2020/03/024](https://doi.org/10.1088/1475-7516/2020/03/024)
- [100] S. Kawamura, T. Nakamura, M. Ando, N. Seto, K. Tsubono, K. Numata, R. Takahashi, S. Nagano, T. Ishikawa, M. Musha, et al. “The Japanese space gravitational wave antenna – DECIGO”. *Class. and Quantum Gravity* **23**, S125 (2006). DOI: [10.1088/0264-9381/23/8/S125](https://doi.org/10.1088/0264-9381/23/8/S125)

- [101] J. Crowder and N. J. Cornish. “Beyond LISA: exploring future gravitational wave missions”. *Phys. Rev. D* **72**, 083005 (2005). doi: [10.1103/PhysRevD.72.083005](https://doi.org/10.1103/PhysRevD.72.083005)
- [102] W.-T. Ni. “Gravitational wave detection in space”. *Int. J. Mod. Phys. D* **25**, 1630001 (2016). doi: [10.1142/S0218271816300019](https://doi.org/10.1142/S0218271816300019)
- [103] S. Dimopoulos, P. W. Graham, J. M. Hogan, M. A. Kasevich, and S. Rajendran. “Atomic gravitational wave interferometric sensor”. *Phys. Rev. D* **78**, 122002 (2008). doi: [10.1103/PhysRevD.78.122002](https://doi.org/10.1103/PhysRevD.78.122002)
- [104] A. Bertoldi, P. Bouyer, and B. Canuel. “Quantum sensors with matter waves for GW observation”. In: *Handbook of Gravitational Wave Astronomy*. Springer Nature Singapore, 2022, 199–241. doi: [10.1007/978-981-16-4306-4_5](https://doi.org/10.1007/978-981-16-4306-4_5)
- [105] P. W. Graham and S. Jung. “Localizing gravitational wave sources with single-baseline atom interferometers”. *Phys. Rev. D* **97**, 024052 (2018). doi: [10.1103/PhysRevD.97.024052](https://doi.org/10.1103/PhysRevD.97.024052)
- [106] P. W. Graham, J. M. Hogan, M. A. Kasevich, and S. Rajendran. “Resonant mode for gravitational wave detectors based on atom interferometry”. *Phys. Rev. D* **94**, 104022 (2016). doi: [10.1103/PhysRevD.94.104022](https://doi.org/10.1103/PhysRevD.94.104022)
- [107] P. W. Graham, J. M. Hogan, M. A. Kasevich, S. Rajendran, and R. W. Romani. “Mid-band gravitational wave detection with precision atomic sensors”. *arXiv e-prints* (2017). arXiv: [1711.02225 \[astro-ph.IM\]](https://arxiv.org/abs/1711.02225)
- [108] *aLIGO LHO logbook, Saturday 17 October 2015, how to process DELTAL_EXTERNAL at low frequency to get the calibration right.* <https://alog.ligo-wa.caltech.edu/aLOG/index.php?callRep=22591>. Accessed: 2025-04-29
- [109] J. Aasi, B. P. Abbott, R. Abbott, T. Abbott, M. R. Abernathy, K. Ackley, C. Adams, T. Adams, P. Addesso, R. X. Adhikari, et al. “Advanced LIGO”. *Classical and Quantum Gravity* **32**, 074001 (2015). doi: [10.1088/0264-9381/32/7/074001](https://doi.org/10.1088/0264-9381/32/7/074001)
- [110] J. Harms, F. Acernese, F. Barone, I. Bartos, M. Beker, J. F. J. van den Brand, N. Christensen, M. Coughlin, R. DeSalvo, S. Dorsher, et al. “Characterization of the seismic environment at the Sanford Underground Laboratory, South Dakota”. *Class. Quantum Gravity* **27**, 225011 (2010). doi: [10.1088/0264-9381/27/22/225011](https://doi.org/10.1088/0264-9381/27/22/225011)
- [111] A. Arvanitaki, P. W. Graham, J. M. Hogan, S. Rajendran, and K. Van Tilburg. “Search for light scalar dark matter with atomic gravitational wave detectors”. *Phys. Rev. D* **97**, 075020 (2018). doi: [10.1103/PhysRevD.97.075020](https://doi.org/10.1103/PhysRevD.97.075020)
- [112] P. Touboul, G. Métris, M. Rodrigues, Y. André, Q. Baghi, J. Bergé, D. Boulanger, S. Bremer, R. Chhun, B. Christophe, et al. “Space test of the equivalence principle: first results of the MICROSCOPE mission”. *Class. Quantum Gravity* **36**, 225006 (2019). doi: [10.1088/1361-6382/ab4707](https://doi.org/10.1088/1361-6382/ab4707)

- [113] R. Kolb, H. Weerts, N. Toro, R. Van de Water, R. Essig, D. McKinsey, K. Zurek, A. Chou, P. Graham, J. Estrada, et al. *Basic research needs for dark-matter small projects new initiatives: report of the Department of Energy's high energy physics workshop on dark matter*. Tech. rep. USDOE Office of Science (SC) (United States), 2018. doi: [10.2172/1659757](https://doi.org/10.2172/1659757)
- [114] P. W. Graham, D. E. Kaplan, J. Mardon, S. Rajendran, W. A. Terrano, L. Trahms, and T. Wilkason. “Spin precession experiments for light axionic dark matter”. *Phys. Rev. D* **97**, 055006 (2018). doi: [10.1103/PhysRevD.97.055006](https://doi.org/10.1103/PhysRevD.97.055006)
- [115] P. W. Graham, D. E. Kaplan, J. Mardon, S. Rajendran, and W. A. Terrano. “Dark matter direct detection with accelerometers”. *Phys. Rev. D* **93**, 075029 (2016). doi: [10.1103/PhysRevD.93.075029](https://doi.org/10.1103/PhysRevD.93.075029)
- [116] C. Overstreet, P. Asenbaum, T. Kovachy, R. Notermans, J. M. Hogan, and M. A. Kasevich. “Effective inertial frame in an atom interferometric test of the equivalence principle”. *Phys. Rev. Lett.* **120**, 183604 (2018). doi: [10.1103/PhysRevLett.120.183604](https://doi.org/10.1103/PhysRevLett.120.183604)
- [117] G. Rosi, G. D'Amico, L. Cacciapuoti, F. Sorrentino, M. Prevedelli, M. Zych, Č. Brukner, and G. M. Tino. “Quantum test of the equivalence principle for atoms in coherent superposition of internal energy states”. *Nat. Comm.* **8**, 15529 (2017). doi: [10.1038/ncomms15529](https://doi.org/10.1038/ncomms15529)
- [118] T. A. Wagner, S. Schlamming, J. H. Gundlach, and E. G. Adelberger. “Torsion-balance tests of the weak equivalence principle”. *Class. Quantum Gravity* **29**, 184002 (2012). doi: [10.1088/0264-9381/29/18/184002](https://doi.org/10.1088/0264-9381/29/18/184002)
- [119] P. Asenbaum, C. Overstreet, T. Kovachy, D. D. Brown, J. M. Hogan, and M. A. Kasevich. “Phase shift in an atom interferometer due to spacetime curvature across its wave function”. *Phys. Rev. Lett.* **118**, 183602 (2017). doi: [10.1103/PhysRevLett.118.183602](https://doi.org/10.1103/PhysRevLett.118.183602)
- [120] S. M. Dickerson, J. M. Hogan, A. Sugarbaker, D. M. S. Johnson, and M. A. Kasevich. “Multi-axis inertial sensing with long-time point source atom interferometry”. *Phys. Rev. Lett.* **111**, 083001 (2013). doi: [10.1103/PhysRevLett.111.083001](https://doi.org/10.1103/PhysRevLett.111.083001)
- [121] V. Xu, M. Jaffe, C. D. Panda, S. L. Kristensen, L. W. Clark, and H. Müller. “Probing gravity by holding atoms for 20 seconds”. *Science* **366**, 745–749 (2019). doi: [10.1126/science.aay6428](https://doi.org/10.1126/science.aay6428)
- [122] M. Arndt and K. Hornberger. “Testing the limits of quantum mechanical superpositions”. *Nat. Phys.* **10**, 271–277 (2014). doi: [10.1038/nphys2863](https://doi.org/10.1038/nphys2863)
- [123] A. Bassi, K. Lochan, S. Satin, T. P. Singh, and H. Ulbricht. “Models of wave-function collapse, underlying theories, and experimental tests”. *Rev. Mod. Phys.* **85**, 471–527 (2013). doi: [10.1103/RevModPhys.85.471](https://doi.org/10.1103/RevModPhys.85.471)
- [124] S. Nimmrichter and K. Hornberger. “Macroscopicity of mechanical quantum superposition states”. *Phys. Rev. Lett.* **110**, 160403 (2013). doi: [10.1103/PhysRevLett.110.160403](https://doi.org/10.1103/PhysRevLett.110.160403)

- [125] A. Bassi, A. Großardt, and H. Ulbricht. “Gravitational decoherence”. *Class. Quantum Gravity* **34**, 193002 (2017). DOI: [10.1088/1361-6382/aa864f](https://doi.org/10.1088/1361-6382/aa864f)
- [126] N. Altamirano, P. Corona-Ugalde, R. B. Mann, and M. Zych. “Gravity is not a pairwise local classical channel”. *Class. Quantum Gravity* **35**, 145005 (2018). DOI: [10.1088/1361-6382/aac72f](https://doi.org/10.1088/1361-6382/aac72f)
- [127] S. Weinberg. “Testing quantum mechanics”. *Ann. Phys.* **194**, 336–386 (1989). DOI: [10.1016/0003-4916\(89\)90276-5](https://doi.org/10.1016/0003-4916(89)90276-5)
- [128] A. Bertoldi, F. Minardi, and M. Prevedelli. “Phase shift in atom interferometers: corrections for nonquadratic potentials and finite-duration laser pulses”. *Phys. Rev. A* **99**, 033619 (2019). DOI: [10.1103/PhysRevA.99.033619](https://doi.org/10.1103/PhysRevA.99.033619)
- [129] C. Overstreet, P. Asenbaum, and M. A. Kasevich. “Physically significant phase shifts in matter-wave interferometry”. *Am. J. Phys.* **89**, 324–332 (2021). DOI: [10.1119/10.0002638](https://doi.org/10.1119/10.0002638)
- [130] *AOSense cold atomic beam system*. <https://aosense.com/wp-content/uploads/2024/01/AOSense-Cold-Atomic-Beam-System-2023.pdf>. Accessed: 2025-04-29
- [131] T. F. Wilkason. “Clock atom interferometry for precision measurements in fundamental physics”. Ph.D. dissertation. Stanford University, 2022
- [132] T. Kovachy, J. M. Hogan, A. Sugarbaker, S. M. Dickerson, C. A. Donnelly, C. Overstreet, and M. A. Kasevich. “Matter wave lensing to picokelvin temperatures”. *Phys. Rev. Lett.* **114**, 143004 (2015). DOI: [10.1103/PhysRevLett.114.143004](https://doi.org/10.1103/PhysRevLett.114.143004)
- [133] R. Roy, A. Green, R. Bowler, and S. Gupta. “Rapid cooling to quantum degeneracy in dynamically shaped atom traps”. *Phys. Rev. A* **93**, 043403 (2016). DOI: [10.1103/PhysRevA.93.043403](https://doi.org/10.1103/PhysRevA.93.043403)
- [134] GitHub repository of Yijun Jiang. <https://github.com/yijunj/DissertationSupplemental>. Accessed: 2025-04-29
- [135] S. L. Campbell. “A Fermi-degenerate three-dimensional optical lattice clock”. Ph.D. dissertation. University of Colorado Boulder, 2017
- [136] S. Schmid, G. Thalhammer, K. Winkler, F. Lang, and J. Hecker Denschlag. “Long distance transport of ultracold atoms using a 1D optical lattice”. *New J. Phys.* **8**, 159 (2006). DOI: [10.1088/1367-2630/8/8/159](https://doi.org/10.1088/1367-2630/8/8/159)
- [137] F. Gerbier and Y. Castin. “Heating rates for an atom in a far-detuned optical lattice”. *Phys. Rev. A* **82**, 013615 (2010). DOI: [10.1103/PhysRevA.82.013615](https://doi.org/10.1103/PhysRevA.82.013615)
- [138] A. Browaeys, T. Lahaye, T. Porto, M. Weidemüller, C. S. Adams, and L. F. Cugliandolo. *Current trends in atomic physics*. Oxford University Press, USA, 2019. DOI: [10.1093/oso/9780198837190.001.0001](https://doi.org/10.1093/oso/9780198837190.001.0001)

- [139] I. R. Solá, V. S. Malinovsky, and D. J. Tannor. “Optimal pulse sequences for population transfer in multilevel systems”. *Phys. Rev. A* **60**, 3081–3090 (1999). DOI: [10.1103/PhysRevA.60.3081](https://doi.org/10.1103/PhysRevA.60.3081)
- [140] M. Nantel. “Advances in clock atom interferometry for fundamental physics and precision inertial sensing”. Ph.D. dissertation. Stanford University, 2025
- [141] A. Arvanitaki, S. Dimopoulos, A. A. Geraci, J. Hogan, and M. Kasevich. “How to test atom and neutron neutrality with atom interferometry”. *Phys. Rev. Lett.* **100**, 120407 (2008). DOI: [10.1103/PhysRevLett.100.120407](https://doi.org/10.1103/PhysRevLett.100.120407)
- [142] B. E. Garber. “Strontium clock atom interferometry for fundamental physics”. Ph.D. dissertation. Stanford University, 2024
- [143] A. D. West, Z. Lasner, D. DeMille, E. P. West, C. D. Panda, J. M. Doyle, G. Gabrielse, A. Kryskow, and C. Mitchell. “An underappreciated radiation hazard from high voltage electrodes in vacuum”. *Health Phys.* **112**, 33–41 (2017). DOI: [10.1097/HP.0000000000000593](https://doi.org/10.1097/HP.0000000000000593)
- [144] A. E. Siegman. *Lasers*. University Science Books, 1986
- [145] A. Stockham and J. G. Smith. “Comparison between a super Gaussian and a “true” top hat”. In: *Laser Beam Shaping IX*. Vol. 7062. SPIE. 2008, 70620I. DOI: [10.1117/12.796074](https://doi.org/10.1117/12.796074)
- [146] N. Mielec, M. Altorio, R. Sapam, D. Horville, D. Holleville, L. A. Sidorenkov, A. Landragin, and R. Geiger. “Atom interferometry with top-hat laser beams”. *Appl. Phys. Lett.* **113**, 161108 (2018). DOI: [10.1063/1.5051663](https://doi.org/10.1063/1.5051663)
- [147] C. Bischoff, U. Rädel, U. Umhofer, E. Jäger, and A. F. Lasagni. “Integration of diffractive optics for top-hat generation and enhanced depth of focus”. *J. Laser Micro Nanoeng.* **17** (2022)
- [148] K. Gillen-Christandl, G. D. Gillen, M. J. Piotrowicz, and M. Saffman. “Comparison of Gaussian and super Gaussian laser beams for addressing atomic qubits”. *Appl. Phys. B* **122** (2016). DOI: [10.1007/s00340-016-6407-y](https://doi.org/10.1007/s00340-016-6407-y)
- [149] S.-Y. Lan, P.-C. Kuan, B. Estey, P. Haslinger, and H. Müller. “Influence of the Coriolis force in atom interferometry”. *Phys. Rev. Lett.* **108**, 090402 (2012). DOI: [10.1103/PhysRevLett.108.090402](https://doi.org/10.1103/PhysRevLett.108.090402)
- [150] S. Dickerson, J. M. Hogan, D. M. S. Johnson, T. Kovachy, A. Sugarbaker, S.-w. Chiow, and M. A. Kasevich. “A high-performance magnetic shield with large length-to-diameter ratio”. *Rev. Sci. Instrum.* **83**, 065108 (2012). DOI: [10.1063/1.4720943](https://doi.org/10.1063/1.4720943)
- [151] J. Hogan. “Towards precision tests of general relativity using an atom interferometer”. Ph.D. dissertation. Stanford University, 2010

- [152] E. Wodey, D. Tell, E. M. Rasel, D. Schlippert, R. Baur, U. Kissling, B. Kölliker, M. Lorenz, M. Marrer, U. Schläpfer, et al. “A scalable high-performance magnetic shield for very long baseline atom interferometry”. *Rev. Sci. Instrum.* **91**, 035117 (2020). DOI: [10.1063/1.5141340](https://doi.org/10.1063/1.5141340)
- [153] *Mu-metal properties from Magnetic Shield Corporation*. <http://www.mu-metal.com/faqs.html>. Accessed: 2025-04-29
- [154] *Mu-metal B–H curves from Magnetic Shield Corporation*. <http://www.mu-metal.com/shielding-fundamentals.html>. Accessed: 2025-04-29
- [155] C. P. Bidinosti and J. W. Martin. “Passive magnetic shielding in static gradient fields”. *AIP Adv.* **4**, 047135 (2014). DOI: [10.1063/1.4873714](https://doi.org/10.1063/1.4873714)
- [156] N. R. “Quenching and tempering of welded carbon steel tubulars”. *The Fabricator* (2001)
- [157] I. Bloch, J. Dalibard, and W. Zwerger. “Many-body physics with ultracold gases”. *Rev. Mod. Phys.* **80**, 885–964 (2008). DOI: [10.1103/RevModPhys.80.885](https://doi.org/10.1103/RevModPhys.80.885)
- [158] I. Bloch. “Ultracold quantum gases in optical lattices”. *Nat. Phys.* **1**, 23–30 (2005). DOI: [10.1038/nphys138](https://doi.org/10.1038/nphys138)
- [159] O. Morsch and M. Oberthaler. “Dynamics of Bose-Einstein condensates in optical lattices”. *Rev. Mod. Phys.* **78**, 179–215 (2006). DOI: [10.1103/RevModPhys.78.179](https://doi.org/10.1103/RevModPhys.78.179)
- [160] D. Jaksch, C. Bruder, J. I. Cirac, C. W. Gardiner, and P. Zoller. “Cold bosonic atoms in optical lattices”. *Phys. Rev. Lett.* **81**, 3108–3111 (1998). DOI: [10.1103/PhysRevLett.81.3108](https://doi.org/10.1103/PhysRevLett.81.3108)
- [161] M. Greiner, O. Mandel, T. Esslinger, T. W. Hänsch, and I. Bloch. “Quantum phase transition from a superfluid to a Mott insulator in a gas of ultracold atoms”. *Nature* **415**, 39–44 (2002). DOI: [10.1038/415039a](https://doi.org/10.1038/415039a)
- [162] S. Trotzky, P. Cheinet, S. Fölling, M. Feld, U. Schnorrberger, A. M. Rey, A. Polkovnikov, E. A. Demler, M. D. Lukin, and I. Bloch. “Time-resolved observation and control of superexchange interactions with ultracold atoms in optical lattices”. *Science* **319**, 295–299 (2008). DOI: [10.1126/science.1150841](https://doi.org/10.1126/science.1150841)
- [163] M. Endres, M. Cheneau, T. Fukuhara, C. Weitenberg, P. Schauß, C. Gross, L. Mazza, M. C. Bañuls, L. Pollet, I. Bloch, et al. “Observation of correlated particle-hole pairs and string order in low-dimensional Mott insulators”. *Science* **334**, 200–203 (2011). DOI: [10.1126/science.1209284](https://doi.org/10.1126/science.1209284)
- [164] W. S. Bakr, J. I. Gillen, A. Peng, S. Fölling, and M. Greiner. “A quantum gas microscope for detecting single atoms in a Hubbard-regime optical lattice”. *Nature* **462**, 74–77 (2009). DOI: [10.1038/nature08482](https://doi.org/10.1038/nature08482)

- [165] L. W. Cheuk, M. A. Nichols, M. Okan, T. Gersdorf, V. V. Ramasesh, W. S. Bakr, T. Lompe, and M. W. Zwierlein. “Quantum-gas microscope for fermionic atoms”. *Phys. Rev. Lett.* **114**, 193001 (2015). DOI: [10.1103/PhysRevLett.114.193001](https://doi.org/10.1103/PhysRevLett.114.193001)
- [166] S. Nascimbene, N. Goldman, N. R. Cooper, and J. Dalibard. “Dynamic optical lattices of subwavelength spacing for ultracold atoms”. *Phys. Rev. Lett.* **115**, 140401 (2015). DOI: [10.1103/PhysRevLett.115.140401](https://doi.org/10.1103/PhysRevLett.115.140401)
- [167] S. Kuhr, W. Alt, D. Schrader, I. Dotzenko, Y. Miroshnychenko, W. Rosenfeld, M. Khudaverdyan, V. Gomer, A. Rauschenbeutel, and D. Meschede. “Coherence properties and quantum state transportation in an optical conveyor belt”. *Phys. Rev. Lett.* **91**, 213002 (2003). DOI: [10.1103/PhysRevLett.91.213002](https://doi.org/10.1103/PhysRevLett.91.213002)
- [168] A. J. Matthes, J. M. Mortlock, L. A. McArd, A. P. Raghuram, A. D. Innes, P. D. Gregory, S. L. Bromley, and S. L. Cornish. “Long-distance optical-conveyor-belt transport of ultracold ^{133}Cs and ^{87}Rb atoms”. *Phys. Rev. A* **109**, 023321 (2024). DOI: [10.1103/PhysRevA.109.023321](https://doi.org/10.1103/PhysRevA.109.023321)
- [169] J. H. Denschlag, J. E. Simsarian, H. Häffner, C. McKenzie, A. Browaeys, D. Cho, K. Helmerson, S. L. Rolston, and W. D. Phillips. “A Bose-Einstein condensate in an optical lattice”. *J. Phys. B: At. Mol. Opt. Phys.* **35**, 3095 (2002). DOI: [10.1088/0953-4075/35/14/307](https://doi.org/10.1088/0953-4075/35/14/307)
- [170] X. Zhou, S. Jin, and J. Schmiedmayer. “Shortcut loading a Bose-Einstein condensate into an optical lattice”. *New J. Phys.* **20**, 055005 (2018). DOI: [10.1088/1367-2630/aac11b](https://doi.org/10.1088/1367-2630/aac11b)
- [171] L. D. Landau. “Zur Theorie der Energieübertragung. II”. *Phys. Z. Sowjetun.* (1932)
- [172] C. Zener. “Non-adiabatic crossing of energy levels”. *Proc. R. Soc. Lond. A* **137** (1932). DOI: [10.1098/rspa.1932.0165](https://doi.org/10.1098/rspa.1932.0165)
- [173] S. Schulz. “Tightly confined atoms in optical dipole traps”. Ph.D. dissertation. University of Innstruck, 2010
- [174] S. Baier. “An optical dipole trap for erbium with tunable geometry”. Master thesis. University of Innstruck, 2012
- [175] G.-B. Liao, K.-S. Wu, C.-Y. Shih, Y.-H. Cheng, L.-A. Sun, Y.-J. Lin, and M.-S. Chang. “Optimization of a crossed optical dipole trap for loading and confining laser-cooled atoms”. *J. Opt. Soc. Am. B* **34**, 869–876 (2017). DOI: [10.1364/JOSAB.34.000869](https://doi.org/10.1364/JOSAB.34.000869)
- [176] Y. Bao, S. S. Yu, L. Anderegg, S. Burchesky, D. Gonzalez-Acevedo, E. Chae, W. Ketterle, K.-K. Ni, and J. M. Doyle. “Fast optical transport of ultracold molecules over long distances”. *New J. Phys.* **24**, 093028 (2022). DOI: [10.1088/1367-2630/ac900f](https://doi.org/10.1088/1367-2630/ac900f)
- [177] G. Unnikrishnan, C. Beulenkamp, D. Zhang, K. P. Zamarski, M. Landini, and H.-C. Nägerl. “Long distance optical transport of ultracold atoms: a compact setup using a Moiré lens”. *Rev. Sci. Instrum.* **92**, 063205 (2021). DOI: [10.1063/5.0049320](https://doi.org/10.1063/5.0049320)

- [178] L.-S. Ma, P. Jungner, J. Ye, and J. L. Hall. “Delivering the same optical frequency at two places: accurate cancellation of phase noise introduced by an optical fiber or other time-varying path”. *Opt. Lett.* **19**, 1777–1779 (1994). doi: [10.1364/OL.19.001777](https://doi.org/10.1364/OL.19.001777)
- [179] K. Takahashi, M. Ando, and K. Tsubono. “Stabilization of laser intensity and frequency using optical fiber”. In: *J. Phys.: Conf. Ser.* Vol. 122. IOP Publishing. 2008, 012016. doi: [10.1088/1742-6596/122/1/012016](https://doi.org/10.1088/1742-6596/122/1/012016)
- [180] K. DeRose, T. Deshpande, Y. Wang, and T. Kovachy. “High-power, low-phase-noise, frequency-agile laser system for delivering fiber-noise-canceled pulses for strontium clock atom interferometry”. *Opt. Lett.* **48**, 3893–3896 (2023). doi: [10.1364/OL.493098](https://doi.org/10.1364/OL.493098)
- [181] T. J. Green, J. Sastrawan, H. Uys, and M. J. Biercuk. “Arbitrary quantum control of qubits in the presence of universal noise”. *New J. Phys.* **15**, 095004 (2013). doi: [10.1088/1367-2630/15/9/095004](https://doi.org/10.1088/1367-2630/15/9/095004)
- [182] J. Le Gouët, T. Mehlstäubler, J. Kim, S. Merlet, A. Clairon, A. Landragin, and F. Pereira Dos Santos. “Limits to the sensitivity of a low noise compact atomic gravimeter”. *Appl. Phys. B* **92**, 133–144 (2008). doi: [10.1007/s00340-008-3088-1](https://doi.org/10.1007/s00340-008-3088-1)
- [183] Q.-Q. Hu, C. Freier, B. Leykauf, V. Schkolnik, J. Yang, M. Krutzik, and A. Peters. “Mapping the absolute magnetic field and evaluating the quadratic Zeeman-effect-induced systematic error in an atom interferometer gravimeter”. *Phys. Rev. A* **96**, 033414 (2017). doi: [10.1103/PhysRevA.96.033414](https://doi.org/10.1103/PhysRevA.96.033414)
- [184] A. Dunning, R. Gregory, J. Bateman, N. Cooper, M. Himsworth, J. A. Jones, and T. Freegarde. “Composite pulses for interferometry in a thermal cold atom cloud”. *Phys. Rev. A* **90**, 033608 (2014). doi: [10.1103/PhysRevA.90.033608](https://doi.org/10.1103/PhysRevA.90.033608)
- [185] T. Zanon-Willette, D. Wilkowski, R. Lefevre, A. V. Taichenachev, and V. I. Yudin. “Generalized hyper-Ramsey-Bordé matter-wave interferometry: quantum engineering of robust atomic sensors with composite pulses”. *Phys. Rev. Res.* **4**, 023222 (2022). doi: [10.1103/PhysRevResearch.4.023222](https://doi.org/10.1103/PhysRevResearch.4.023222)
- [186] J. Saywell, M. Carey, M. Belal, I. Kuprov, and T. Freegarde. “Optimal control of Raman pulse sequences for atom interferometry”. *J. Phys. B: At. Mol. Opt. Phys.* **53**, 085006 (2020). doi: [10.1088/1361-6455/ab6df6](https://doi.org/10.1088/1361-6455/ab6df6)
- [187] F. Correia, G. Bichon, M. Guessoum, C. Cherfan, R. Geiger, A. Landragin, and F. P. Dos Santos. “Quantum optimal control for atom interferometry”. In: *Quantum 2.0 Conference and Exhibition*. Optica Publishing Group. 2022, QW4C.7. doi: [10.1364/QUANTUM.2022.QW4C.7](https://doi.org/10.1364/QUANTUM.2022.QW4C.7)
- [188] Z. Chen, G. Louie, Y. Wang, T. Deshpande, and T. Kovachy. “Enhancing strontium clock atom interferometry using quantum optimal control”. *Phys. Rev. A* **107**, 063302 (2023). doi: [10.1103/PhysRevA.107.063302](https://doi.org/10.1103/PhysRevA.107.063302)

- [189] B. Fang, N. Mielec, D. Savoie, M. Altorio, A. Landragin, and R. Geiger. “Improving the phase response of an atom interferometer by means of temporal pulse shaping”. *New J. Phys.* **20**, 023020 (2018). DOI: [10.1088/1367-2630/aaa37c](https://doi.org/10.1088/1367-2630/aaa37c)
- [190] J. C. Saywell, I. Kuprov, D. Goodwin, M. Carey, and T. Freegarde. “Optimal control of mirror pulses for cold-atom interferometry”. *Phys. Rev. A* **98**, 023625 (2018). DOI: [10.1103/PhysRevA.98.023625](https://doi.org/10.1103/PhysRevA.98.023625)
- [191] D. L. Butts, K. Kotru, J. M. Kinast, A. M. Radojevic, B. P. Timmons, and R. E. Stoner. “Efficient broadband Raman pulses for large-area atom interferometry”. *J. Opt. Soc. Am. B* **30**, 922–927 (2013). DOI: [10.1364/JOSAB.30.000922](https://doi.org/10.1364/JOSAB.30.000922)
- [192] M. H. Levitt. *Composite pulses*. Wiley Online Library, 2007. DOI: [10.1002/9780470034590.emrstm0086](https://doi.org/10.1002/9780470034590.emrstm0086)
- [193] M. H. Levitt. “Symmetrical composite pulse sequences for NMR population inversion. I. compensation of radiofrequency field inhomogeneity”. *J. Magn. Reson. (1969)* **48**, 234–264 (1982). DOI: [10.1016/0022-2364\(82\)90275-X](https://doi.org/10.1016/0022-2364(82)90275-X)
- [194] P. Berg, S. Abend, G. Tackmann, C. Schubert, E. Giese, W. P. Schleich, F. A. Narducci, W. Ertmer, and E. M. Rasel. “Composite-light-pulse technique for high-precision atom interferometry”. *Phys. Rev. Lett.* **114**, 063002 (2015). DOI: [10.1103/PhysRevLett.114.063002](https://doi.org/10.1103/PhysRevLett.114.063002)
- [195] O. Hosten, N. J. Engelsen, R. Krishnakumar, and M. A. Kasevich. “Measurement noise 100 times lower than the quantum-projection limit using entangled atoms”. *Nature* **529**, 505–508 (2016). DOI: [10.1038/nature16176](https://doi.org/10.1038/nature16176)
- [196] K. C. Cox, G. P. Greve, J. M. Weiner, and J. K. Thompson. “Deterministic squeezed states with collective measurements and feedback”. *Phys. Rev. Lett.* **116**, 093602 (2016). DOI: [10.1103/PhysRevLett.116.093602](https://doi.org/10.1103/PhysRevLett.116.093602)
- [197] N. J. Engelsen, R. Krishnakumar, O. Hosten, and M. A. Kasevich. “Bell correlations in spin-squeezed states of 500000 atoms”. *Phys. Rev. Lett.* **118**, 140401 (2017). DOI: [10.1103/PhysRevLett.118.140401](https://doi.org/10.1103/PhysRevLett.118.140401)
- [198] B. Canuel, A. Bertoldi, L. Amand, E. Pozzo di Borgo, T. Chantrait, C. Danquigny, M. Dovale Álvarez, B. Fang, A. Freise, R. Geiger, et al. “Exploring gravity with the MIGA large scale atom interferometer”. *Sci. Rep.* **8**, 14064 (2018). DOI: [10.1038/s41598-018-32165-z](https://doi.org/10.1038/s41598-018-32165-z)
- [199] B. Canuel, S. Abend, P. Amaro-Seoane, F. Badaracco, Q. Beaufils, A. Bertoldi, K. Bongs, P. Bouyer, C. Braxmaier, W. Chaibi, et al. “ELGAR – a European laboratory for gravitation and atom-interferometric research”. *Class. Quantum Gravity* **37**, 225017 (2020). DOI: [10.1088/1361-6382/aba80e](https://doi.org/10.1088/1361-6382/aba80e)

- [200] L. Badurina, E. Bentine, D. Blas, K. Bongs, D. Bortoletto, T. Bowcock, K. Bridges, W. Bowden, O. Buchmueller, C. Burrage, et al. “AION: an atom interferometer observatory and network”. *J. Cosmol. Astropart. Phys.* **2020**, 011 (2020). DOI: [10.1088/1475-7516/2020/05/011](https://doi.org/10.1088/1475-7516/2020/05/011)
- [201] M.-S. Zhan, J. Wang, W.-T. Ni, D.-F. Gao, G. Wang, L.-X. He, R.-B. Li, L. Zhou, X. Chen, J.-Q. Zhong, et al. “ZAIGA: Zhaoshan long-baseline atom interferometer gravitation antenna”. *Int. J. Mod. Phys. D* **29**, 1940005 (2020). DOI: [10.1142/S0218271819400054](https://doi.org/10.1142/S0218271819400054)